THE UNIVERSITY *of* EDINBURGH

On Structural Studies of High-Density Potassium and Sodium

Emma Elizabeth McBride

A thesis submitted in fulfilment of the requirements
for the degree of Doctor of Philosophy
to the
University of Edinburgh
August 2013

Abstract

The alkali elements at ambient conditions are well described by the nearly-free electron (NFE) model, yet show a remarkable departure from this "simple" behaviour with increasing pressure. Low-symmetry complex structures are observed in all, and anomalous melting has been observed in lithium (Li), sodium (Na), rubidium (Rb), and caesium (Cs). In this Thesis, static and dynamic compression techniques have been used to investigate the high-pressure high-temperature behaviour of the alkali elements potassium (K) and Na.

Utilising diamond anvil pressure cells and external resistive heating, both in-air and in-vacuum, the melting curve of K has been determined to 24 GPa and 750 K, and is found to be remarkably similar to that of Na, but strikingly different to that reported previously. Furthermore, there is some evidence to suggest that a change in the compressibility of liquid-K occurs at lower pressures than the solid-solid phase transitions, perhaps indicating structural transitions occurring in the liquid phase, similar to those in the underlying solid. This could suggest a mechanism to explain the anomalous melting behaviour observed. Previous *ab initio* computational studies indicate that the unusual melting curve of Na arises due to structural and electronic transitions occurring in the liquid, mirroring those found in the underlying solid at higher pressures. The discovery that the melting curve of K is very similar to that of Na suggests that the same physical phenomena predicted for Na could be responsible for the high-pressure melting behaviour observed in K.

The *tI*19 phase of K, observed above 20 GPa at 300 K, is a composite incommensurate host-guest structure consisting of 1D chains of guest atoms surrounded by a tetragonal host framework. Along the unique *c*-axis,

the host and guest are incommensurate with each other. During the melting studies described above, it was observed that with increasing temperature, the weaker-bonded guest chains become more disordered while the host structure remains unchanged. To investigate and characterise this order-disorder transition, *in situ* synchrotron X-ray diffraction studies were conducted on single-crystal and quasi-single crystal samples of *tI*19-K. An order-disorder phase line has been mapped out to 50 GPa and 650 K.

Perhaps the most striking departure from NFE behaviour in the alkali elements is observed in Na at pressures above 200 GPa where it transforms to a transparent electrical insulator. This phase is a so-called elemental "electride", which may be thought of as being pseudo-ionically bonded. Electrides are predicted to exist in many elements, but at pressures far beyond the current capabilities of static pressure techniques. Utilising laser-driven quasi-isentropic compression techniques, dynamic compression experiments were performed on Na to see if it is possible to observe this electride phase under the timescales of dynamic compression experiment (ns). Optical velocimetry and reflectivity of the sample were measured directly to determine pressure and monitor the on-set of the transparent phase, respectively.

Lay Summary

The alkali elements at ambient conditions are well described by the nearly-free electron model, a simple model, which nevertheless captures much of the essential physics of these systems. However, with increasing pressure, all the alkali elements lithium (Li), sodium (Na), potassium (K), rubidium (Rb) and caesium (Cs) undergo a marked departure from "simple" behaviour, crystallising into complex structures, and all but K exhibiting unusual melting behaviour.

Resistively heated diamond anvil cells (DACs), capable of achieving pressures like those at the centre of the Earth, and laser-compression techniques, capable of reaching pressure and temperature conditions orders of magnitude beyond those achieved by DACs, have been utilised to investigate the high-pressure high-temperature behaviour of K and Na.

The high-pressure high-temperature behaviour of K has been explored using DACs and X-ray diffraction, namely investigating its melting behaviour (demonstrated to be remarkably similar to that of Na), and investigating an order-disorder transition occurring in one of its high-pressure phases. At two-thirds of the pressure at the centre of the Earth, Na transforms to a transparent insulator. Laser-driven compression techniques were used to investigate the melting behaviour, the nature of the liquid (is it insulating?), and to determine whether this transparent phase could be observed on the nanosecond timescales that these laser experiments are conducted.

Declaration

Except where otherwise stated, the research undertaken in this thesis was the unaided work of the author. Where the work was done in collaboration with others, a significant contribution was made by the author.

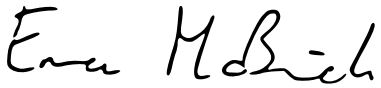

E. E. McBride
August 2013

Acknowledgements

This Thesis is dedicated to my parents, John and Veronica, my brothers, David and Stephen, and my sister(-in-law) Christine, for their unfailing love and support.

First and foremost I would like to thank my Ph.D. supervisor Malcolm McMahon. I should firstly thank him for his infectious enthusiasm for this subject. Furthermore, thanks to Malcolm not only for all he has taught me about high-pressure science, but also for all the support and encouragement, the opportunities he has given me, and the friendship over the last four years.

In addition to my supervisor I would like to thank my colleagues in CSEC for their advice, encouragement, and insightful questions over the last four years. Thanks in particular to Eugene Gregoryanz, John Loveday, Ingo Loa, and Chrystele Sanloup. Furthermore, thanks to Ingo Loa for permitting use of software which was vital for the single-crystal studies in this Thesis, and to Eugene Gregoryanz for use of his lab.

Thanks to the McMahon group past and present for all their help and friendship – in particular Graham Stinton, Rachel Husband, Wanaruk Chaimayo, Keith Munro, Richard Briggs and Martin Gorman. I was very fortunate to work with people who were not only great colleagues, but great friends as well. Special thanks to Keith Munro for growing the single-crystal, Olga Narygina for her help with the potassium melt experiments, and Lars Lundegaard, who left CSEC before I started, but who took the first high-temperature potassium data which spearheaded these studies. Thanks to Graham for teaching me how to use diamond anvil cells, and to Graham, Rachel and Wanaruk for their help on the innumerable beamtimes. Thanks to Simon Macleod of AWE for allowing use of his diamond anvil cells and

vacuum vessel.

Thanks to Gilbert "Rip" Collins and his group at LLNL for being such willing collaborators and for everything they have done and taught me. A special thanks to Jon Eggert for allowing use of his IgorPro code which was used to analyse the VISAR data in these studies, and to Ray Smith for taking me on my first ever laser experiment at OMEGA. Thanks to Jon Eggert, Ray Smith, Amy Lazicki, and Damian Swift for all their various contributions to this work and my knowledge. They are far to numerous to list here. A very special thanks to Amy Lazicki for all her help conducting the experiments and creating targets. Thanks to Cindy Bolme for taking a few shots of sodium during her own Janus time.

A very special thanks to the University of Edinburgh mechanical workshop staff for their excellent work. Thanks to the beamline staff at I15 (Diamond Light Source), ID09a (ESRF) and the ECB (Petra-III), and the facility staff at the Jupiter Laser Facility (LLNL). Thanks to Walt Unites for letting me use his lab and for all his advice in target preparation.

Thanks to the Scottish Doctoral Training Centre in Condensed Matter Physics and EPSRC for the Ph.D scholarship funding to conduct this research. In particular thanks to Andrew Mackenzie, Chris Hooley, Christine Edwards, Julie Massey, and of course Cohort 1. Thanks to Rachel Husband, Graham Stinton, Richard Briggs, and my father, John, who all proofread parts of this Thesis.

Thanks to all my friends both within and without The University of Edinburgh. There are far too many people to mention by name but particular thanks to Marialuisa Aliotta, Olga Degtyareva, Jane Patterson, Graham Stinton, Rachel Husband, Fred Farrell, Richard Briggs, and Katie Davies.

Finally, thanks to my parents, John and Veronica; my brothers, David and Stephen; and Christine. They cannot be thanked enough.

"That conquering matter is to understand it, and understanding matter is necessary to understanding the universe and ourselves: and that therefore Mendeleev's Periodic Table, which just during those weeks we were laboriously learning to unravel, was poetry, loftier and more solemn than all the poetry we had swallowed down in liceo; and come to think of it, it even rhymed!"

– Primo Levi

Contents

List of Figures

List of Tables

Chapter 1

Introduction

1.1 Complexity Under Pressure

The long-held view that with increasing pressure "simple" systems, such as the alkali elements, became more close-packed, and more simple, was contradicted, in the last decade, by various static compression studies (Alexander & McTague 1978) (Gregoryanz *et al.* 2008) (Ma *et al.* 2009). At ambient conditions, the alkali elements – lithium (Li), sodium (Na), potassium (K), rubidium (Rb), and caesium (Cs) – are characterised by one outer *s*-electron surrounding a closed-shell of tightly-bound core electrons. Their behaviour at ambient conditions is very well described by the nearly-free electron (NFE) model, a relatively simple model which never-the-less captures the fundamental physics of the system.

With increasing pressure, however, the alkali elements have been observed to depart from this simple behaviour, leading to the emergence of low-symmetry complex structures; unusual melting curves; and exotic electronic properties in all (McMahon & Nelmes 2006) (Gregoryanz *et al.* 2008) (Guillaume *et al.* 2011) (Boehler & Zha 1986). A detailed review of the complex structural phase transition sequences and anomalous melting curves that have been observed in the alkali elements with increasing pressure is given in Chapter 2. The high-pressure phases adopted by the alkali elements are summarised in Figure 1.1.

Under pressure, numerous elements have been observed to transform to low-symmetry complex structures, such as the composite incommensurate

Figure 1.1: Summary of the structural phase transitions observed in the alkali elements with increasing pressure. A detailed review of the phases adopted by the alkali elements is confined to Chapter 2.

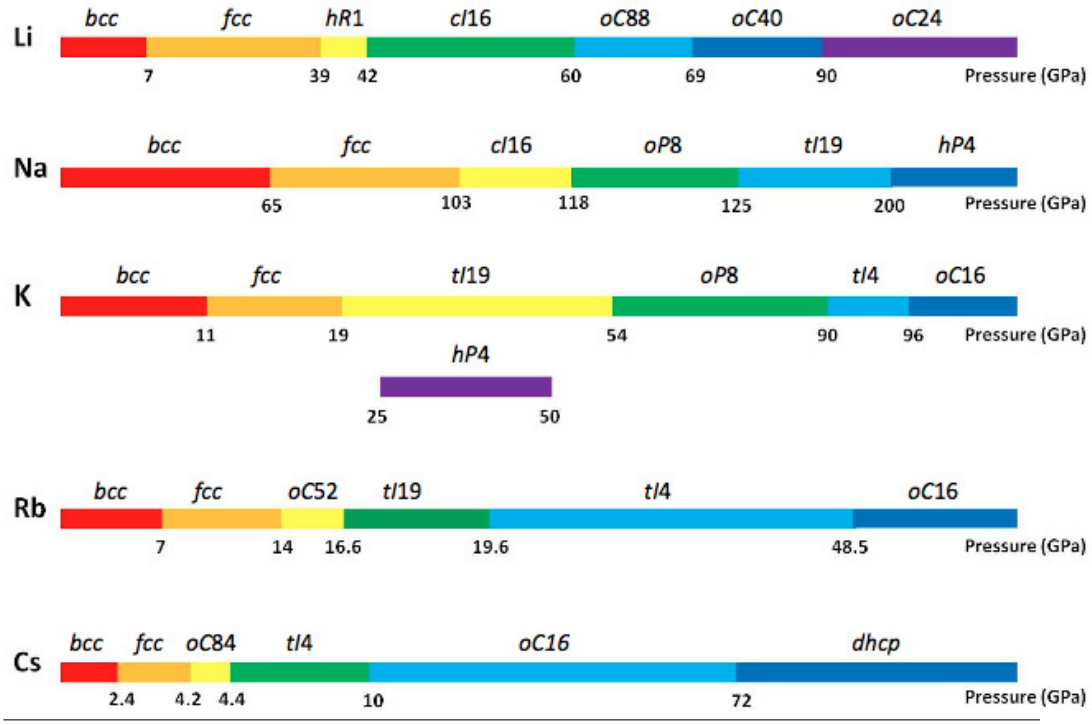

host-guest phases observed in Na, K, Rb, barium (Ba), and calcium (Ca), to name but a few (McMahon & Nelmes 2006). Na, in particular, exhibits a remarkable departure from simple behaviour with increasing pressure, undergoing numerous complex structural and electronic phase transformations (Gregoryanz *et al.* 2008) (Ma *et al.* 2009). At ambient conditions it is a shiny metal in the body-centred cubic phase, yet by 125 GPa, it has transformed to a black semi-metallic incommensurate host-guest structure (Gregoryanz *et al.* 2008). Furthermore, at 200 GPa, Na departs entirely from metallic behaviour, whereby it transforms to a transparent electrical insulator. This phase is characterised by having a large amount of electron localisation, whereby the extreme compression leads to valence electrons being forced to occupy interstitial regions of *hP*4-Na (Ma *et al.* 2009).

1.2 Static and Dynamic Compression Techniques

Static compression techniques have allowed the study of matter up to pressures of several megabar, and temperatures of order 10^4 K, recreating conditions found in the Earth's inner core (Tateno *et al.* 2010). Furthermore, numerous studies, in the last decade in particular, have illustrated that with increasing pressure seemingly simple systems at ambient conditions exhibit unusual structural and electronic properties (Ma *et al.* 2009) (Gregoryanz *et al.* 2008) (McMahon & Nelmes 2006). With particular relevance to the alkali elements, which are the focus of this Thesis research, by combining diamond anvil cell techniques with *in situ* synchrotron X-ray diffraction, low-symmetry complex structures have been observed in all (McMahon & Nelmes 2006) (Gregoryanz *et al.* 2005) (Gregoryanz *et al.* 2008) (Guillaume *et al.* 2011).

To achieve pressure states in excess of those reached by static compression techniques, one may utilise high-powered lasers to shock-compress matter. Furthermore, due to the generation of entropy on shock compression, materials can be heated to temperatures greater than 10^5 K (McWilliams *et al.* 2012). It is therefore typical that, due to the large amount of heating associated with shock compression, compressing to pressures above a few megabars means that most materials will be in the liquid or plasma state.

Recently, efforts have been made to utilise laser pulse-shaping techniques to more gradually compress matter, doing so on relatively long time scales (Bradley *et al.* 2009). By slowly compressing matter – slow when compared with the time scale of a shock-wave rise time – one avoids the large generation of entropy associated with shock-compression, and instead the sample will reach at point in P-T space which lies closer to the isentrope than the Hugoniot (Higginbotham *et al.* 2012). Such compression is often referred to as ramp- or quasi-isentropic (QI) compression. Therefore, QI-compression techniques make it possible to compress matter to pressures far beyond its shock-melting pressure, crucially remaining in the solid state. Rygg *et al.* have combined laser-driven QI-compression with *in situ* X-ray diffraction measurements to confirm that at 260 GPa tantalum (Ta) is in the solid state,

whereas it is known to shock-melt at 240 GPa (Rygg *et al.* 2012). By utilising QI-compression techniques it is possible to investigate the high-pressure *solid* behaviour of, say, the alkali elements at pressures far beyond the limits of static compression techniques.

1.3 Static and Dynamic Studies of the Alkali Elements

The work described in this Thesis utilises both static and dynamic compression techniques to study Na and K at extreme conditions, investigating their high-pressure melting behaviour and probing their high-pressure complex structures. The Thesis is therefore divided into two sections: Section I (Chapters 3, 4 and 5) which concerns the static compression studies performed on K using diamond anvil cell techniques; and, Section II (Chapter 6), which describes laser-driven dynamic compression studies on Na.

1.3.1 Section I: Static Studies of K

The structural phase transition sequence observed in K bears striking similarities to its immediate neighbours Na and Rb. Beyond the body-centred cubic (*bcc*) and face-centred cubic (*fcc*) phases common to all the alkali elements K has three phases isostructural with Na and three phases isostructural with Rb (McMahon & Nelmes 2006) (Marqués *et al.* 2009) (Lundegaard *et al.* 2009b) (Gregoryanz *et al.* 2008) (Ma *et al.* 2009). Despite the striking similarities in the high-pressure solid phases adopted by Na, K and Rb, the melting curve of K appears to be markedly different to its neighbours. Unlike Na and Rb, and Cs and Li, the melting curve of K, shown in Figure 1.2, was observed to increase continuously in both the *bcc* and *fcc* phases, with no maximum in the melting temperature determined, at least to 14.5 GPa and 650 K (Zha & Boehler 1985).

The static compression studies contained in this Thesis commence with a re-investigation of the melting behaviour of K to understand why, despite having such strikingly similar high-pressure structural phases, the melting behaviour of K should differ so dramatically from the trend common to all

Figure 1.2: The melting curve of K as measured by Zha & Boehler. The trend in the melting temperature of K is strikingly different to that reported in all the other alkali elements, with no maximum in the melting temperature observed, at least not to 14.5 GPa and 650 K (Zha & Boehler 1985).

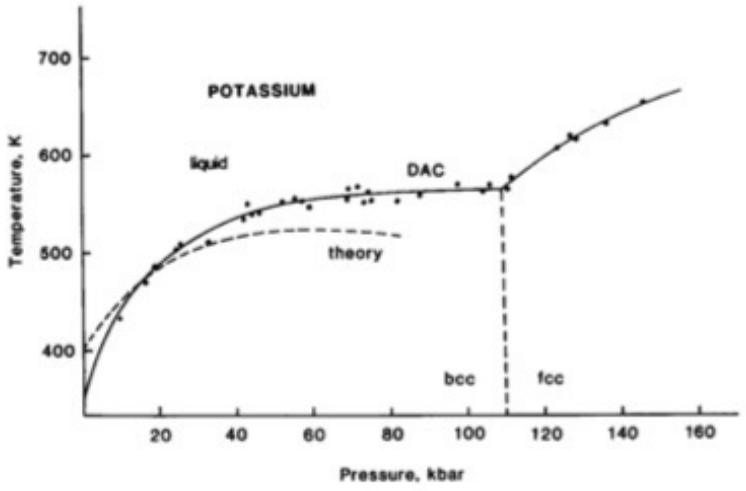

the other alkali elements.

1.3.2 Section II: Dynamic Studies of Na

The observation of the transparent insulating *hP*4 phase of Na was the most salient example of the alkali elements departing from NFE behaviour at extreme densities. Moreover, *ab initio* computational studies suggest that this phase is stable to at least 600 GPa, far beyond the limits of static compression techniques, with the band gap increasing with pressure (Ma *et al.* 2009). This begs the question of what is the nature of Na at such pressures, and what happens at further compression? Na is predicted to undergo another phase transform at 10 TPa (Pickard & Needs 2010). Does Na remain insulating at this pressure, or does it return to a metallic state?

Furthermore, what is the nature of the liquid at these pressures? Does the transparent insulating solid melt to a transparent insulating liquid? Using static compression techniques, Marqués *et al.* used temperature-dependent *in situ* Raman spectroscopy measurements to determine the C_{44} elastic constant in the *hP*4 phase of Na, and used this to predict the melting temperature at P$\sim$200 GPa (Marqués *et al.* 2011b). They concluded that to melt *hP*4-Na at

this pressure would require temperatures in excess of 3,500 K. The melting curve of Na as determined by static compression techniques may be seen in Figure 1.3, and it is clear that following the melting minimum, the gradient of the melting temperature increases steeply.

Figure 1.3: The melting curve of Na as determined using static compression techniques. It is predicted that it would require temperatures in excess of 3,500 K to melt Na at ∼200 GPa (Marqués *et al.* 2011b).

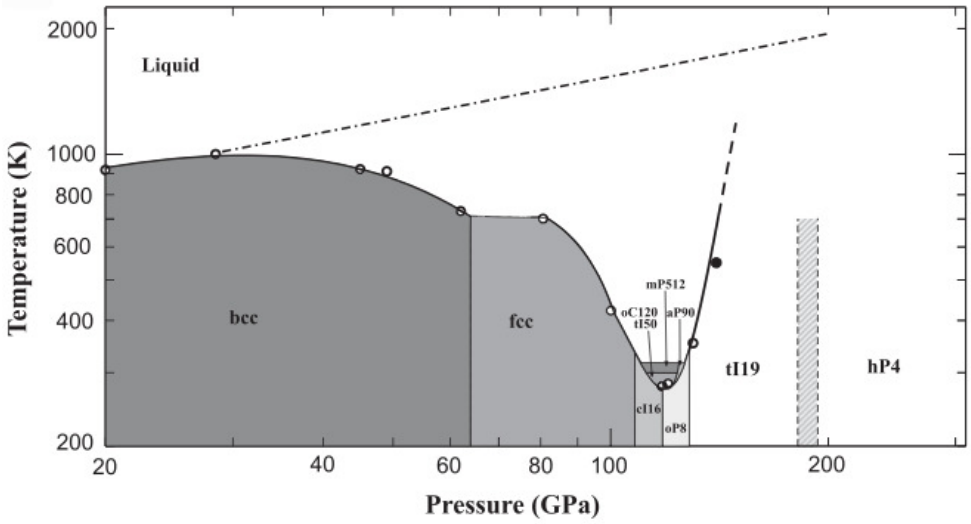

To perform a high-temperature melting study on Na using static compression techniques would require laser heating a highly-reactive substance at megabar pressures, which is currently at the limit of static compression techniques. Laser driven QI- and shock-compression techniques allow access to this P-T regime, and may be the only way to explore the high-pressure melting behaviour of such highly reactive materials at multi-megabar pressures. Furthermore, as it is predicted to require temperatures in excess of 3,500 K to melt *hP*4-Na at 200 GPa, it could be possible to QI-compress Na to pressures beyond 200 GPa, yet remain in the solid state, allowing studies of the solid at extreme compressions (Marqués *et al.* 2011b).

The focus of Section II is the combination of laser-driven compression techniques, available at the Janus laser at the Jupiter Laser Facility, with optical velocimetry, streaked optical pyrometry, and optical reflectivity diagnostics, to QI- and shock-compress Na into the stability field of the transparent insulating phase, monitoring the onset of the transparent phase

transition. These preliminary experiments are a proof-of-principle. In future campaigns, using higher-powered lasers with pulse shaping capabilities, it will be possible to compress Na to TPa pressures.

1.4 Thesis Outline

This Thesis contains 6 Chapters in addition to this introductory Chapter. Following a literature review (Chapter 2), Section I contains the techniques (Chapter 3) and results (Chapters 4 and 5) concerning the static compression experiments conducted on K. Section II is a self-contained Chapter (Chapter 6), which reports the techniques used, and some preliminary results obtained, in dynamic compression studies performed on Na. Chapter 7 contains the conclusions of this Thesis work. A more detailed outline of this Thesis is summarised below:

Chapter 2: The Alkali Elements at Extreme Conditions

This Chapter is a review of the structural phase transition sequences and melting behaviour of each of the alkali elements at extreme conditions. Also included is a brief explanation of Pearson notation, which is used throughout this Thesis to describe the different crystal structures adopted by the alkali elements at high pressure.

Section I: Static Compression Studies on K

Chapter 3: Techniques for Static Compression Experiments

Diamond anvil pressure cells were used to exert pressure, and their constitution and operation are described here. Means for determining pressure in the cell, such as fluorescence techniques, and the equation-of-state of an X-ray diffraction pressure-standard, are discussed. External resistive heating techniques, including in-vacuum heating, are described. Finally, X-ray diffraction techniques are discussed, in addition to a brief description

of the third generation synchrotron light sources at which all *in situ* X-ray diffraction measurements were made.

Chapter 4: The Melting Curve of Potassium

In situ X-ray diffraction techniques were used to re-investigate and extend the high-pressure melting behaviour of K up to 24 GPa and 750 K. Similarities between the melting curve of Na and K are described, and evidence for a change in the liquid compressibility ahead of phase changes in the underlying solid is presented and discussed.

Chapter 5: Chain "Melting" in the Incommensurate Host-Guest Structure of K-III

The high-pressure high-temperature melting studies of K (Chapter 4) unveiled a temperature-dependent order-disorder transition occurring in the guest chains of composite incommensurate host-guest K-III. As the temperature of the sample was increased, the Bragg peaks arising from scattering from the guest chains were observed to decrease in intensity before disappearing entirely, whereas the Bragg reflections from the host structure remained unchanged. To investigate this phenomenon, high-pressure high-temperature single-crystal and powder diffraction studies were conducted using *in situ* X-ray diffraction.

Single-crystal studies of *tI*19-K were performed at 21 GPa as a function of temperature, up to 365 K. Changes in correlation length of the host and guest with increasing temperature are presented and discussed, and the atomic displacement parameters are extracted from refinement of the single-crystal datasets. An interpretation of these results is discussed in the context of the Lindemann criterion for melting. Furthermore, to investigate the pressure and temperature dependence of this phenomenon over the stability field of the *tI*19 phase, powder and quasi-single crystal X-ray diffraction studies were conducted up to 50 GPa and 650 K. The order-disorder transition temperature was observed to undergo distinct changes in gradient at particular pressures, and an interpretation of this phenomenon in terms of intra-phase transitions occurring the host and guest structures is

discussed.

Section II: Dynamic Compression Studies on Na

Chapter 6: Dynamic Compression of Sodium

This Chapter describes both the techniques used and results obtained in a preliminary study using laser-compression techniques to shock and QI-compress Na. The differences between shock and QI-compression are discussed, with particular attention paid to the difference in temperatures achieved using the two techniques. Furthermore, optical velocimetry techniques (VISAR), streaked optical pyrometry (SOP), and the optical reflectivity techniques were used to determine the pressure, temperature and the onset of phase transitions, respectively, and these techniques are also described.

Preliminary results from this campaign are presented, and an interpretation of the results is discussed, alongside suggested improvements for future campaigns.

Chapter 7: Conclusions

The observations made in this Thesis are summarised, and future avenues of research is discussed.

1.5 Role of the author

The experiments contained within this Thesis are collaborative works. This Section describes the role of the author. All data in this Thesis were analysed by the author. Data analysed by others for publication were re-analysed in this work.

Chapter 4: The Melting Curve of Potassium

This Chapter contains four different studies. The data from Study A were collected by L. F. Lundegaard, G. W. Stinton and M. I. McMahon prior the the commencement of this Thesis research. The data from Study B were

collected by the author, W. Chaimayo, G. W. Stinton and M. I. McMahon. The data from Study C were collected by the author, O. Narygina, G. W. Stinton and M. I. McMahon. Finally, the data from Study D were collected by the author, G. W. Stinton, R. J. Husband and M. I McMahon. Data for publication were analysed by the author and O. Narygina, and those analysed by O. Narygina were re-analysed by the author for inclusion in this Chapter.

Chapter 5: Chain "Melting" in the Incommensurate Host-Guest Structure of K-III

The single crystal was grown by K. A. Munro during his Masters Thesis. Data were collected by the author, R. J. Husband and M. I. McMahon. Data were analysed by the author. In the powder and quasi-single crystal studies, data were collected by the author, R. Briggs and M. I. McMahon. Once more, all data were analysed by the author.

Chapter 6: Dynamic Compression of Sodium

The experiment was design by the author and M. I. McMahon in close collaboration with A. Lazicki, R. F. Smith, and J. H. Eggert at Lawrence Livermore National Lab. Targets for laser-driven compression studies of the alkali elements were designed and constructed by the autho following hydrodynamic simulations performed by D. Swift to determine target thickness. Additional targets were constructed by A. Lazicki. The target chamber set-up was performed, and experimental data were collected, by the author, A. Lazicki, and M. I. McMahon. Data were analysed by A. Lazicki and the author; data analysed by A. Lazicki were re-analysed by the author.

Chapter 2

The Alkali Elements at Extreme Conditions

2.1 Structural Transitions and Melting Behaviour of the Alkali Elements

The alkali elements – lithium (Li), sodium (Na), potassium (K), rubidium (Rb), and caesium (Cs) – are "simple" elements at ambient conditions, whose electronic structure is well described by the nearly-free electron model. Consequently, their behaviour under high-pressure conditions has been the focus of static compression experiments for decades, e.g. Young, and references therein (Young 1991), providing a direct test of theory. Extremes of pressure reveal the emergence of low-symmetry complex structures in all of the alkali elements and anomalous melting behaviour in Li, Na, Rb and Cs (McMahon & Nelmes 2006) (Gregoryanz *et al.* 2008) (Guillaume *et al.* 2011) (Boehler & Zha 1986).

At ambient conditions, all of the alkali elements crystallise into the 8-fold co-ordinated body-centred cubic (*bcc*) crystal structure. With increasing pressure they initially become more close-packed, transforming to a 12-fold co-ordinated face-centred cubic (*fcc*) structure. By furthering increasing pressure, however, complex structures with lower atomic co-ordination are observed in all.

What follows is a review of the melting curves of, and structures adopted

by, the alkali elements at high-pressures. Initially focussing on the structural phase transition sequences for each element, this Section begins by describing the high-pressure phases adopted by the heavy alkali element Rb and Cs, the behaviour of which is dominated by *s*-to-*d* electron transfer at modest compressions. Following Rb and Cs, the phase transition sequences of the light alkali elements Na and Li are described – *s*-to-*p* electron transfer initially dominates the behaviour of each. Finally, the phase transition sequence of K is discussed, the sequence of which is intermediate between the heavy and light alkali elements, perhaps unsurprisingly given its position in the group.

Following the review of the high-pressure crystal structures, the melting curves are described. This Section again begins with the heavy alkali elements – anomalous melting behaviour was first observed in Cs and Rb – followed by a review of the melting behaviour of the light alkali elements, and once more finishing with K which is reported to exhibit a, surprisingly, different trend in its melting temperature compared with its neighbours.

2.1.1 Pearson Notation

Throughout this Thesis, Pearson notation will be used to describe different crystal structures. This notation is composed of two letters, one lower-case and one upper-case which indicate the Bravais lattice. The lower-case letter indicates the crystal class, and the upper-case letter indicates the lattice type. These letters are followed by a number that indicates the number of atoms in the conventional unit cell. For example, the well-known diamond structure in Pearson notation is $cF8$ – c, as the crystal system is cubic; F, as the lattice type is face-centred, and 8 as there are 8 atoms in the unit cell. A summary of the Pearson symbols for the 14 Bravais lattices in 3D may be seen in Table 2.1.1.

2.2 Structural Studies

2.2.1 Caesium

Although francium (Fr) is the heaviest of the alkali elements, its most stable isotope has a half-life of just twenty minutes, so consequently it has not

Table 2.1: Pearson Notation describing the 14 Bravais lattices in 3D. Following the two italicised letters comes a number which indicates the number of atoms in the unit cell.

Crystal Class	**Lattice Type**	**Pearson Symbol**
Triclinic	Primitive	*aP*
Monoclinic	Primitive	*mP*
	Base-centred	*mA, mB, mC*
Orthorhombic	Primitive	*oP*
	Base-centred	*oA, oB, oC*
	Face-centred	*oF*
	Body-centred	*oI*
Tetragonal	Primitive	*tP*
	Body-centred	*tI*
Hexagonal	Primitive	*hP*
Rhombohedral	Primitive	*hR*
Cubic	Primitive	*cP*
	Face-centred	*cF*
	Body-centred	*cI*

been studied at high pressure. For the purposes of this review, we do not consider it and begin with Cs. The second-heaviest alkali element, Cs, undergoes a series of structural transitions, which may be interpreted in terms of pressure-induced *s*-to-*d* electron transfer (6*s*-to-5*d*). Due to the occurrence of relatively low phase-transition pressures, Cs has been studied extensively for many decades, and has been used as a simple system to explore this electron-transfer phenomenon. At 2.4 GPa, Cs transforms from *bcc* to *fcc* (Young 1991). At 4.2 GPa, there is a further transformation to Cs-III, which exists over an extremely narrow pressure range. Initially, this phase was reported as an isostructural phase transformation to *fcc*, but with a 9 % volume decrease (Hall *et al.* 1964); this transformation was initially supported with computational studies (Glötzel & McMahan 1979).

However, a subsequent synchrotron X-ray diffraction study could not confirm the *fcc* structure of Cs-III (Schwarz *et al.* 1998). Furthermore, Schwarz *et al.* noted the observation of Bragg peaks appearing at large *d*-spacings – 7.5 Å and 35 Å – which they suggested indicated the transformation to a large-period supercell (Schwarz *et al.* 1998). Subsequent *ab initio* calculations

also suggest that an isostructural transition does *not* occur, and that the *fcc* phase becomes unstable at ∼4.3 GPa due to phonon-softening (Christensen *et al.* 2000).

In 2001, McMahon *et al.* (McMahon *et al.* 2001a) successfully grew several high-quality single-crystals of Cs-III, which, combined with a synchrotron X-ray source, which produces brilliant X-rays, allowed the structural solution of Cs-III to be found; it is remarkably complex. Denoted $oC84$ in Pearson notation (spacegroup $C222_1$), Cs-III forms an 84-atom orthorhombic unit cell with lattice parameters a=9.2718(1) Å, b=13.3013(3) Å, and c=34.2025(7) Å at 4.3 GPa, as shown in Figure 2.1. Consequently, the decrease in volume upon transforming from Cs-II to Cs-III is now 6.4 %, as opposed to the previously reported 9 % (Hall *et al.* 1964). Accompanying this transition is the reduction in co-ordination number, from 12 in the *fcc* phase to approximately 10 in the $oC84$ phase (McMahon *et al.* 2001a).

Upon further increase of pressure, at 4.4 GPa, Cs undergoes yet another structural phase transformation, this time to a tetragonal structure with 4 atoms per unit cell ($tI4$) (Takemura *et al.* 1982). This is again an open-packed structure, with a local atomic co-ordination number of 8. Between 10 and 12 GPa, Cs undergoes a further phase transformation to a phase denoted Cs-V. In the pressure ranger where the Cs-IV to Cs-V transition was observed, the calculated *d*-orbital occupation has reached a value of 0.8, indicating the near completion of the *s*-to-*d* electron transfer discussed above. This electron-transfer is completed by 15 GPa, and so Cs-V may therefore be considered a monovalent metal with one outer *d*-electron.

Using laboratory based X-ray sources Takemura & Syassen (Takemura *et al.* 1982) suggested three different possible interpretations of their diffraction data from Cs-V. However, a subsequent energy-dispersive synchrotron X-ray diffraction study by Badding *et al.* (Badding *et al.* 1991) concluded that the previous suggestions were inconsistent with their study, though they (Badding *et al.*) did not provide a solution. The structure of Cs-V remained unsolved until a study by Schwarz *et al.* (Schwarz *et al.* 1998), in which they utilised a third generation synchrotron light source (3GLS) to perform angle-dispersive X-ray diffraction measurements. This technique provided peak intensities that lacked the ambiguity associated with the energy-dispersive

Figure 2.1: Crystal structures of Rb-III and Cs-III viewed on the same scale along the a-axis of the $C222_1$ unit cell. One may see how both structures are related. Both structures may be considered to consist of 8- and 10-atom a-b layers stacked along the c-axis. The black atoms represent the 10-atom layers and are related by symmetry – both structures have two such layers. The grey and white atoms represent two different sets of 8-atom layers, again related by symmetry. Cs-III has 4 of each type of 8-atom layers, whereas Rb-III has four of the grey set only. (McMahon *et al.* 2001a)

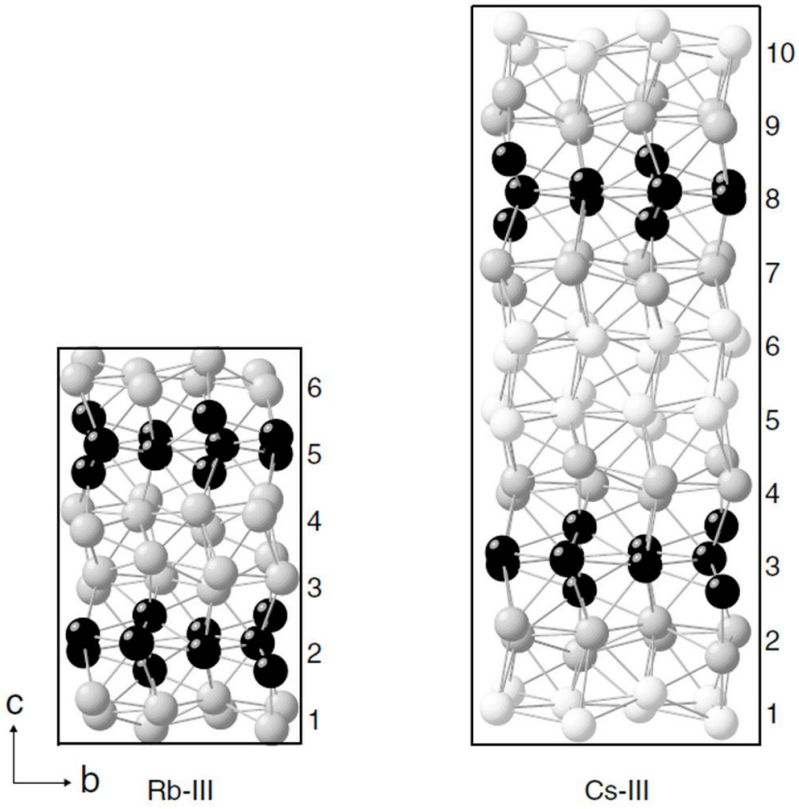

technique used by Badding *et al.* (Badding *et al.* 1991). The structure was found to be a 16-atom orthorhombic structure ($oC16$), with atoms occupying two unique Wyckoff positions: $8d$ and $8f$ (Schwarz *et al.* 1998). Interestingly, here the structure is more close-packed than that of Cs-IV, with the atoms occupying the $8d$ and $8f$ positions being 11-fold and 10-fold co-ordinated, respectively. Furthermore, the appearance of this structure approximately coincides with the end of the s-to-d electron transfer, entering a p-d hybridisation regime, and one where core-core interactions play an

increasing role (McMahan 1984).

Finally, at 72 GPa, Cs undergoes a transition to a double hexagonal close-packed (*dhcp*) structure, and no additional structural transitions have been observed up to pressures of 184 GPa (Takemura *et al.* 2000).

2.2.2 Rubidium

Moving vertically up the periodic table from Cs one reaches Rb. Rb also undergoes a series of phase transformations from high-symmetry close-packed structures to low-symmetry complex ones. Similar to the driving mechanism in Cs, the phase transformations in Rb are initially ascribed to a $5s$-to-$4d$ electronic transition under pressure. The *bcc* to *fcc* transition in Rb occurs at higher pressures than the equivalent one in Cs – in Rb it takes place at 7 GPa (Young 1991). In the early 1980s, at higher compressions, a transformation to a complex phase, Rb-III, was reported at ∼14 GPa (Olijnyk & Holzapfel 1983), but this structure remained unsolved until the development of synchrotron angle-dispersive X-ray diffraction techniques. It was finally determined in 2002 by Nelmes *et al.* (Nelmes *et al.* 2002).

Rb-III crystallises into a complex orthorhombic structure, $oC52$, and has 52 atoms per unit cell. It is, in fact, very similar to the structure of Cs-III, described above and the two structures are closely related, as shown in Figure 2.1. The b/a ratio of Rb-III (1.43) is very similar to that of Cs (1.435), yet the c-lattice parameters for each are notably different (Nelmes *et al.* 2002). For Cs-III, c=34.023 Å at 4.3 GPa, whereas for Rb-III c=18.42 Å at 14.3 GPa. This significant difference in the c-lattice parameter is further illustrated by the fact that Rb-III has fewer atoms in the unit cell. Figure 2.1 illustrates how both structures may be considered to consist of 8- and 10-atom a-b layers stacked along the c-axis. The black atoms in Figure 2.1 represent the 10-atom layers and are related by symmetry – both structures have two such layers. The grey and white atoms represent two different sets of 8-atom layers, again related by symmetry. Cs-III has 4 of each type 8-atom layers, whereas Rb-III has four of the grey set only.

Upon further compression, Rb transforms into a phase which has *not* been observed in Cs, Rb-IV. Again, Rb-IV was observed in 1983 (Olijnyk & Holzapfel 1983). Due to limitations arising from data quality, however, the

structural solution did not emerge for decades. Revisited in 1999 by Schwarz *et al.* (Schwarz *et al.* 1999a), angle-dispersive synchrotron powder X-ray diffraction techniques were used to determine a structural solution. They suggested that the structure was a composite host-guest (H-G) structure consisting of two inter-penetrating structures, one comprised of a 16-atom tetragonal framework – the host structure – and the other composed of quasi-1D chains which run along the *c*-axis, residing in channels formed by the tetragonal host framework – the guest structure. An example of a composite H-G structure may be seen in Figure 2.2.

Figure 2.2: An example of a composite host-guest structure as viewed in the *a*-*b* plane. The host atoms are represented by the light grey atoms and form a tetragonal framework, forming channels along the *c*-axis. The guest atoms are represented by the dark grey atoms.

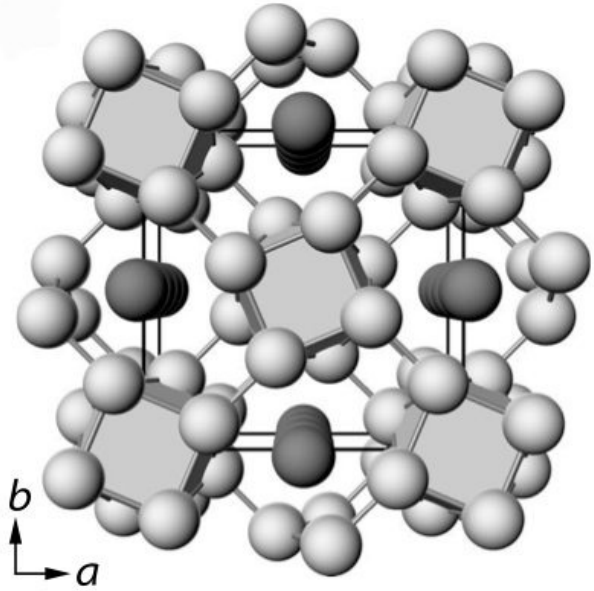

However, McMahon *et al.* (McMahon *et al.* 2001b), and indeed Schwarz *et al.* (Schwarz *et al.* 1999a), point out difficulties in interpreting the data as a *commensurate* H-G phase. In particular Schwarz *et al.* point to the emergence of a peak at $2\theta \sim 8.8^{\circ}$, as seen in Figure 2.3 and indicated by the triangle below the peak, which fits neither to the basic tetragonal cell, nor to simple supercells. Schwarz *et al.* tentatively ascribe it to a mixture of Rb-IV and Rb-V (Rb-IV transforms to Rb-V at 20 GPa; the structure of Rb-V will

be discussed below) (Schwarz *et al.* 1999a).

Figure 2.3: X-ray diffraction patterns of Rb-IV taken from the study of Schwarz *et al.* (Schwarz *et al.* 1999a). The unidentified peak in this study is highlighted by the black triangle. Schwarz et al. tentatively ascribe this peak a mixture of two phases – Rb-IV and Rb-V. This peak, and all other peaks in these diffraction patterns were later accounted for by a composite incommensurate host-guest structure, solved by McMahon *et al.* (McMahon *et al.* 2001b). See text for details.

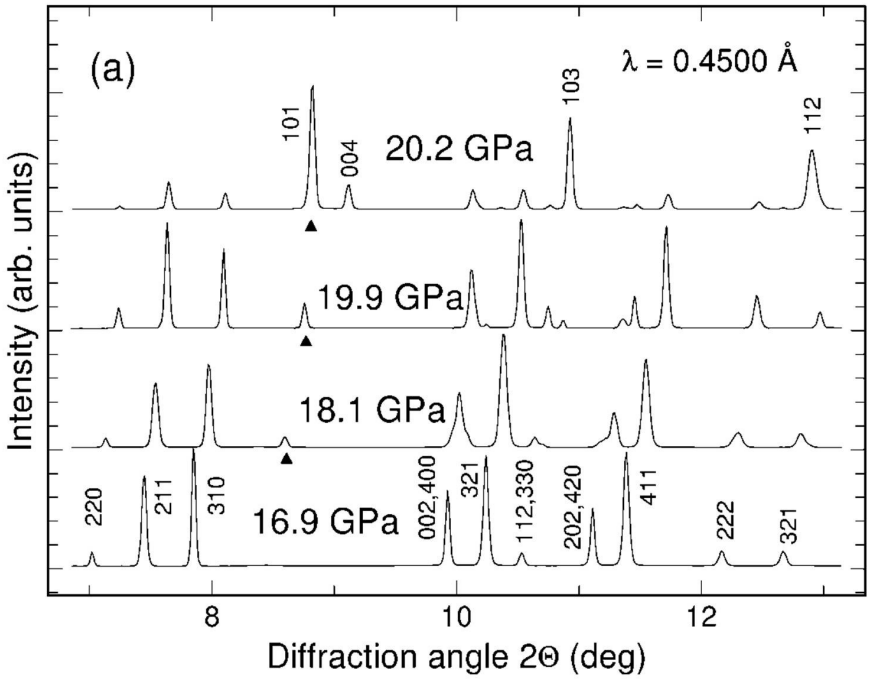

In fitting this additional peak to the appropriate reflection, (*101*), in Rb-V, McMahon *et al.* discovered a discontinuity of ∼0.02 Å between the observed and expected position of the reflection, concluding that the additional reflection is not due to a mixed phase of Rb-IV and Rb-V, and instead must be accounted for by the Rb-IV structure (McMahon *et al.* 2001b). They performed detailed powder diffraction measurements over a wide range of pressures, and observed additional reflections that are not accounted for by the tetragonal host framework, and, in fact, indicated that the guest structure was *incommensurate* with that of the host. They successfully indexed the additional reflections with spacegroup $I4/mmm$, but with a c-lattice parameter 1.631 times smaller than that of the host at 16.8

GPa; this c_{Host}/c_{Guest} ratio was found to vary continuously with pressure, approaching a commensurate value of 5/3 close to the transition to the Rb-V phase. Furthermore, on decreasing pressure below 16.5 GPa, McMahon *et al.* observed the (reversible) broadening of the guest reflections, which was later interpreted as a pressure-induced order-disorder transition in the guest structure (McMahon *et al.* 2001b). This phenomenon will be discussed further in Chapter 5.

At 20 GPa, the incommensurate H-G phase of Rb-IV transforms to the *tI*4 structure that was previously observed in Cs. In Rb, the *tI*4 structure is stable up to 48 GPa (Olijnyk & Holzapfel 1983), where, once more, Rb transforms to a structure previously observed in Cs – it transforms to a phase isostructural with *oC*16-Cs. The appearance of *oC*16-Rb marks the end of the pressure induced *s*-to-*d* electron transfer, entering a regime where core-core interactions play an increasing role (Schwarz *et al.* 1999b). The *oC*16 phase is stable up to at least 50 GPa, the maximum pressure to which Rb has been compressed to date.

2.2.3 Sodium

The pressure-induced changes in the lighter alkali elements, Na and Li, are initially driven by *s*-to-*p* electron transfer. In Na, with increasing pressure, *d*-states play an increasing role. Na is one of the best examples of a nearly-free electron metal. It remains in the *bcc* phase up to 65 GPa, where it transforms to the *fcc* phase (Hanfland *et al.* 2002). Due to the experimental difficulties in working with Na, and the difficulties associated with obtaining high-quality X-ray diffraction data from such a low-scattering sample in a diamond anvil cell at megabar pressures, Na remained largely unstudied until 3GLSs such as the ESRF, Grenoble, came online.

Consequently, for many years, studying Na under extreme compressions was the reserve of theorists. Neaton & Ashcroft, in their seminal paper in 2000, used density functional theory to treat the $3s$, $2p$ and $2s$ electrons as valence, leaving the $1s$ electron as an essentially frozen core (Neaton & Ashcroft 2001). They predict that at 71 GPa, the *bcc* structure would become unstable with respect to an *fcc* structure – this is very similar to the experimental value of 65 GPa obtained by Hanfland *et al.* (Hanfland

et al. 2002). Upon compression above a megabar, in a regime where core-core interactions play an increasing role, and the valence electrons are increasingly forced away from the cores into interstitial regions, Neaton & Ashcroft predicted that Na would transform to low-symmetry structures (Neaton & Ashcroft 2001). Interestingly, they also note an increase in *d*-states below the Fermi level, indicating that upon further compression, *s*-to-*d* hybridisation, in addition to *s*-to-*p* hybridisation, plays a role. Additionally, they suggest the possibility of a pressure-induced metal-to-insulator transition at multi-megabar pressures, sparking renewed experimental interest in Na. Similar predictions were also made by Siringo *et al.* (Siringo *et al.* 1997).

On direct compression from the *fcc* phase, Na undergoes a series of transitions to low-symmetry structures (Hanfland *et al.* 2002). At 105 GPa, Na recrystallises into a body-centred cubic structure, *cI*16, with 16 atoms per unit cell (McMahon *et al.* 2007). This structure is considerably less complex than the phases of Cs and Rb that immediately follow the *fcc* phase, and may be considered a 2×2×2 superstructure of a distorted *bcc* structure. In 2008, however, remarkable complexity was demonstrated in Na. Gregoryanz *et al.* (Gregoryanz *et al.* 2008) exploited the remarkable melting curve of Na (Gregoryanz *et al.* 2005) (discussed in detail in Section 2.3.3) whereby, at a megabar, Na melts at just 300 K to grow single-crystals of, an incredible, seven different structures at pressures close to 118 GPa.

Gregoryanz *et al.* (Gregoryanz *et al.* 2008) discovered that the *cI*16 phase was stable to 118 GPa whereupon three of their four samples transformed to an *oP*8 phase, which has a primitive orthorhombic structure with 8 atoms per unit cell. The remaining sample transformed to a structure with truly remarkable complexity. Denoted *mP*512, it is a monoclinic structure with an incredible 512 atoms in the unit cell, one of the most complex phase uncovered in an element, second only to the 768-atom commensurate host-guest structure recently solved in barium by Loa *et al.* (Loa *et al.* 2012). Interestingly, Gregoryanz *et al.* (Gregoryanz *et al.* 2008) noted strongly-modulated intensity distributions in this *mP*512 phase in reciprocal space, reminiscent of observations made in Cs-III (McMahon *et al.* 2001a), suggesting there may be some connection between these phases. Furthermore, at this pressure (118 GPa), Gregoryanz *et al.* detail that the

Figure 2.4: Representation of high-pressure polymorphs of Na. Lattices and unit cells of seven of the known phases are shown, with their crystallographic axes labelled. The green atoms represent the atomic arrangement for the *cI*16, *oP*8, and the host framework of the *tI*19 phases. In the *tI*19 structure, the letter G marks channels in the host structure that are occupied by linear chains of guest atoms. (Gregoryanz *et al.* 2008)

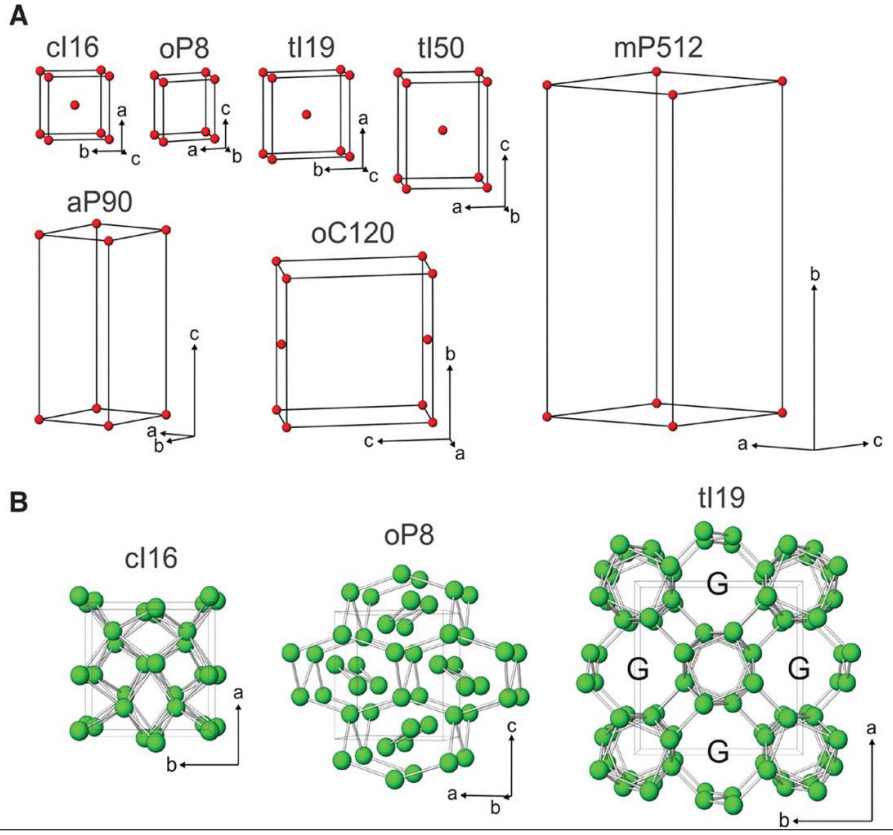

*mP*512 structure was observed repeatedly upon melting and recrystallisation, and, additionally, three other metastable phases are observed: *tI*50 (a body-centred tetragonal structure with 50 atoms per unit cell), *oC*120 (a *C*-centred orthorhombic structure with 120 atoms per unit cell) and *aP*90 (a triclinic structure with 90 atoms per unit cell). Phases *tI*50 and *oC*120 were observed at 117 GPa, and phase *aP*90 was observed at a slightly higher pressure, at around 120 GPa.

In addition to the six phases detailed above, Gregoryanz *et al.* (Gregoryanz *et al.* 2008) observed a seventh phase, a composite incommensurate H-G phase, observed to be stable above 125 GPa. The 16-atom host structure of

this phase is identical to that of Rb-IV, and is described above. The guest structure, however, is unique to Na.

Despite sharing the same host structure, a study by Lundegaard *et al.* in 2009 (Lundegaard *et al.* 2009a) revealed that the guest structure of *tI*19-Na is different to that of *tI*19-Rb. Rather than having a body-centred structure like that observed in Rb, the guest chains in Na adopt a monoclinic structure, though it should be noted that in the study of *tI*19-Na the guest reflections were broad and very weak, indicating that the guest chains were nearly disordered at room temperature, making their refinement very difficult. This will be discussed in greater detail in Chapter 5. Figure 2.4 illustrates the structural information for the seven phases of Na at megabar pressures.

Furthermore, the transformation to the *tI*19 phase is characterised by a significant drop in the reflectivity of the sample, whereby optically it appears black, indicating a departure from metallic behaviour (Lazicki *et al.* 2009), (Marqués *et al.* 2011b). See Figure 2.5 for an example of photomicrographs of Na at high pressure.

Figure 2.5: Photomicrographs of Na at different pressures in a diamond anvil cell. Images (a) and (b) illustrate that Na is still a reflective metal in the *cI*16 phase at 120 GPa (a) and the *oP*8 phase at 124 GPa (b). When Na undergoes a transition to the *tI*19 phase (c), the sample becomes black indicating a departure from metallic behaviour. Finally, at 199 GPa, Na is observed to be a transparent insulator (d) (Ma *et al.* 2009).

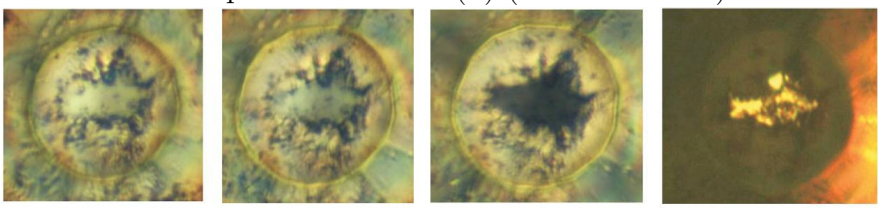

a) 120 GPa b) 124 GPa c) 156 GPa d) 199 GPa

Beyond 180 GPa, Na transforms once more, exhibiting the most striking departure from nearly-free electron behaviour of all the alkali elements to-date. Ma *et al.* (Ma *et al.* 2009) have reported that at 5-fold compression Na transforms to a transparent electrical insulator. A photomicrograph of Na in this phase may be seen in Figure 2.5 (d). Due to the difficulties associated with obtaining high-quality diffraction data from low-Z elements at multi-

megabar pressures, diffraction data alone was insufficient to identify this phase. A combined approach of extensive computational structure searching and *in situ* X-ray diffraction data, allowed them to identify this phase as $hP4$, a structure which may be described as a double hexagonal close-packed structure with 4 atoms per unit cell. At 320 GPa, calculations reveal that the c/a ratio is far from the ideal value of c/a=3.266, predicted instead to be c/a=1.391. At 200 GPa, this transparent insulator has a measurable band gap of 1.3 eV. Moreover, Ma *et al.* (Ma *et al.* 2009) predict that $hP4$-Na is stable up to at least 600 GPa, with the band gap expected to reach 6.5 eV.

As Neaton & Ashcroft (Neaton & Ashcroft 2001), and Siringo *et al.* (Siringo *et al.* 1997), suggested in their theoretical studies, Na transforms to a transparent insulating state due to increasing p-d hybridisation with increasing pressure. In this regime electrons are forced to occupy interstitial regions and so $hP4$-Na may be thought of as analogous to an electride, whereby the interstitial electrons play the role of essentially massless anions, a truly exotic form of matter.

2.2.4 Lithium

With only three electrons, Li is the lightest and simplest of all the alkali elements, making it an ideal candidate to test theoretical predications at high pressures. In keeping with the general trend observed in the alkali elements, Li transforms from *bcc* to *fcc* at 7 GPa (Young 1991) (Hanfland *et al.* 1999). However, it has been observed that at room temperature, Li is highly corrosive resulting in diamond anvil failure on a time scale of 12 hours at pressures above 21 GPa (Hanfland *et al.* 1999). Consequently, almost all high-pressure structural studies conducted on Li above this pressure have been performed below room temperature, and the following Section is concerned with phase transitions occurring at temperatures close to 200 K.

Li, like Na, has been the focus of intense theoretical study, and again is predicted to undergo transitions to low-symmetry structures with increasing pressure. In 2000, Hanfland *et al.* (Hanfland *et al.* 2000) performed *in situ* X-ray diffraction measurements on cold dense Li. By keeping their samples cooled below 200 K, they found that they could compress Li up to 50 GPa. In doing so they discovered two phases: $hR1$, a rhombohedral structure stable

above 39 GPa, and upon further compression the *cI*16 phase, stable above 42 GPa. This *cI*16 phase is the same as that found in Na above 105 GPa. Like Na, the emergence of this phase with a lower symmetry than *fcc* is due to *s*-to-*p* electron transfer (Hanfland *et al.* 2000).

The *cI*16 phase endures up to 60 GPa at 200 K, after which Li goes through various phase transformations to lower-symmetry structures. Marqués *et al.* (Marqués *et al.* 2011a) utilised *ab initio* random structure searching techniques, combined with *in situ* X-ray diffraction measurements, to determine the structure of three low-symmetry phases of Li above 60 GPa. At 60 GPa, Li transforms to the *oC*88 phase, a low-symmetry orthorhombic structure, determined to be a poor metal. At 65 GPa, Li transforms to the *oC*40 phase which has been found to be semi-conducting; Marqués *et al.* suggest this is due to increased electron localisation in interstitial regions, similar to the case of *hP*4-Na described above. Finally, above 95 GPa, Li transforms to the metallic *oC*24 phase. In fact, all three phases are characterised by electron localisation, and, to-date, are unique to Li.

2.2.5 Potassium

K resides in the middle of the group-I elements, between Na and Rb, and the different structures it adopts at high-pressure reflect this position. At 11 GPa, K transforms from *bcc* to *fcc* (Young 1991). At further compressions – 19 GPa – there is a transition to a complex structure. Using energy-dispersive X-ray diffraction techniques, this phase was originally indexed as a *tI*16 structure by Winzenick *et al.* (Winzenick *et al.* 1994). However, due to the background associated with their measurements, Winzenick *et al.* were unable to observe the additional weak reflections that would later be revealed in the angle dispersive synchrotron X-ray diffraction study of McMahon *et al.* (McMahon *et al.* 2006). In all the diffraction patterns collected, additional peaks were observed which were inconsistent with the *tI*16 solution. McMahon *et al.* identified this phase as another composite incommensurate H-G structure, with the same host structure as the H-G (*tI*19) phases of Rb and Na, but, yet again with a unique guest component; in *tI*19-K, the guest chains assume a *C*-centred tetragonal arrangement.

The incommensurate H-G phase of K is further complicated at higher

pressures by the occurrence of intra-phase transitions in both the host and guest components (Lundegaard 2013). As in Rb and Na, the host structure adopts a body-centred tetragonal arrangement, and a raw diffraction pattern of this phase may be seen in Figure 2.6 (a), with the host reflections indicated by the Miller indices with the "H" subscript. At 27 GPa, however, the host loses the c-glide symmetry, signified most obviously by the emergence of the $(101)_H$ reflection, highlighted by the $*$ symbol in Figure 2.6 (b).

Moreover, by increasing the pressure slightly, at 30 GPa, the guest reflections, indicated by the Miller indices with the "G" subscript, reduce in intensity, and additional peaks emerge in their vicinity. At this point there is no change in the host structure, and therefore this marks a phase transition occurring in the guest chains *only*. At 30 GPa, the guest atoms form an A-centred orthorhombic structure, which endures up to 40 GPa, at which point the guest structure transforms *back* to the C-centred tetragonal structure that it adopted at lower pressures. Further complications arise in the H-G phase as the host regains the previously lost c-glide symmetry at P $\sim$43 GPa, 3 GPa above the guest transition pressure. The guest structures in Figure 2.6 (a) and (b), denoted by the † and ‡ symbols are in the C-centred tetragonal and A-centred orthorhombic phases respectively. Evidence for such intra-phase transitions will be detailed in Chapter 5.

The incommensurate H-G phases are stable up to 54 GPa where K transforms to the orthorhombic $oP8$ phase, previously observed only in Na (Lundegaard *et al.* 2009b). Following this phase there is a transition at 90 GPa to the $tI4$ structure observed in Rb and Cs, and, finally, at 96 GPa to the $oC16$ structure, again observed at high pressures in Rb and Cs (Schwarz *et al.* 1998) (Schwarz *et al.* 1999b). Furthermore, a metastable phase has been observed in K. Marqués *et al.* detected the $hP4$ structure, previously observed in Na at pressures over 180 GPa, to exist as a metastable phase in K in the pressure region 25-35 GPa (Marqués *et al.* 2009).

Moreover, Marqués *et al.* (Marqués *et al.* 2009) calculate that the metastable $hP4$ phase is a semi-conductor, not an insulator like the isostructural phase of Na. Furthermore, they (Marqués *et al.*) proceed to calculate the electronic structure of the high-pressure phases of K and determine that, like $oP8$-K, $hP4$-K is an "electride", exhibiting behaviour which marks a

Figure 2.6: X-ray diffraction pattern from *tI*19-K illustrating intra-phase transitions occurring in the host and guest substructures. The host and guest peaks are indexed with their (*hkl*) indices and "*H*" and "*G*" subscripts, which indicate peaks belonging to the host and guest structures respectively. Profile (a) is at 25.3 GPa and the guest reflections which have been indexed as tetragonal are highlighted by the † symbol. Profile (b) is at 33.6 GPa. Here, the host substructure has undergone a slight change in symmetry, signified by the emergence of the $(101)_H$ reflection at low angle, highlighted by the $*$ symbol. At this pressure the guest substructure has also undergone a phase transition. The guest peaks are now indexed using an orthorhombic lattice, and the peaks are highlighted by the ‡ symbols.

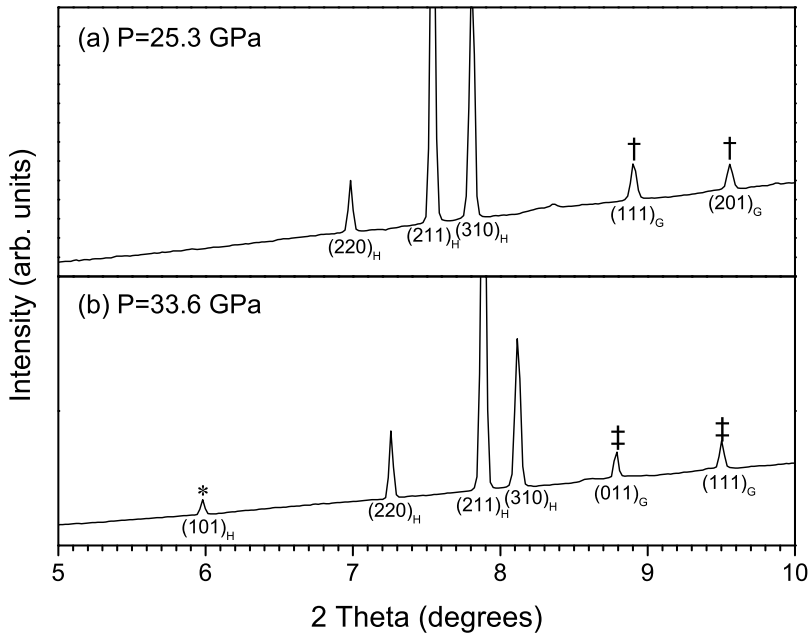

departure from metallic behaviour. The emergence of the *tI*4 and *oC*16 phases marks a return to metallic behaviour (Marqués *et al.* 2009).

The phase transition sequence in K appears to be somewhat intermediate between that of Na and the higher-Z alkali elements Rb and Cs, which is perhaps unsurprising given its location in the group. At lower pressures it follows the expected *bcc*-to-*fcc* phase transition observed in all the alkali elements. At moderate compressions, the *tI*19 phase is observed and this structure is also observed in Na and Rb. In the stability field of *tI*19, a metastable phase, *hP*4-K, is observed, the same phase observed in Na,

which has been ascribed to a growing *p*-*d* hybridisation in Na at extreme compressions (Ma *et al.* 2009). The occurrence of *oP*8 and *tI*19 (and *hP*4) in a reverse order in Na and K could be due to the relative increase or decrease of, say, *p*-electron character (Gregoryanz *et al.* 2008) (Ma *et al.* 2009) (McMahon *et al.* 2006) (Lundegaard *et al.* 2009b) (Marqués *et al.* 2009). Structural phase transitions in K are, at first, dominated by an *s*-to-*d* transition, and at higher pressures a *p*-*d* hybridisation. Na is, at first, dominated by *s*-to-*p* electron transfer, and then at further compressions an increase in *d* character.

Figure 2.7 summarises the different high-pressure structures adopted by the alkali elements.

2.3 Melting Curves

2.3.1 Caesium

Due to the low phase-transition pressures, Cs has long been studied at high pressure. From these earliest studies, the melting behaviour of Cs has been shown to be unusual. In their 1962 study, Kennedy *et al.* utilised a tungsten carbide piston-cylinder apparatus, combined with differential thermal analysis (DTA), to detect the onset of melting (Kennedy *et al.* 1962). In the DTA method, temperature is measured relative to a known reference. At a first-order phase transition, like melting, the reference temperature continues to rise, whereas the temperature of the sample plateaus as energy is stored as latent heat. Kennedy *et al.* (Kennedy *et al.* 1962) discovered two maxima in the melting curve of Cs, one in the *bcc* phase at 2.25 GPa and 470 K, and a second in the *fcc* phase at 3.05 GPa and 471 K. Furthermore, they noted a negative gradient in the melting temperature following the maximum in the *fcc* phase, where the melting temperature decreases to 360 K at the II-III-liquid triple point. The melting temperature remains essentially horizontal over the narrow pressure region that Cs-III is stable. At the Cs-III-to-Cs-IV phase transition, the melting temperature regains a positive slope.

This melting behaviour was confirmed and extended by Boehler & Zha in their 1986 work (Boehler & Zha 1986). Rather than tungsten carbide piston cylinders, they utilised diamond anvil pressure cells, allowing visual

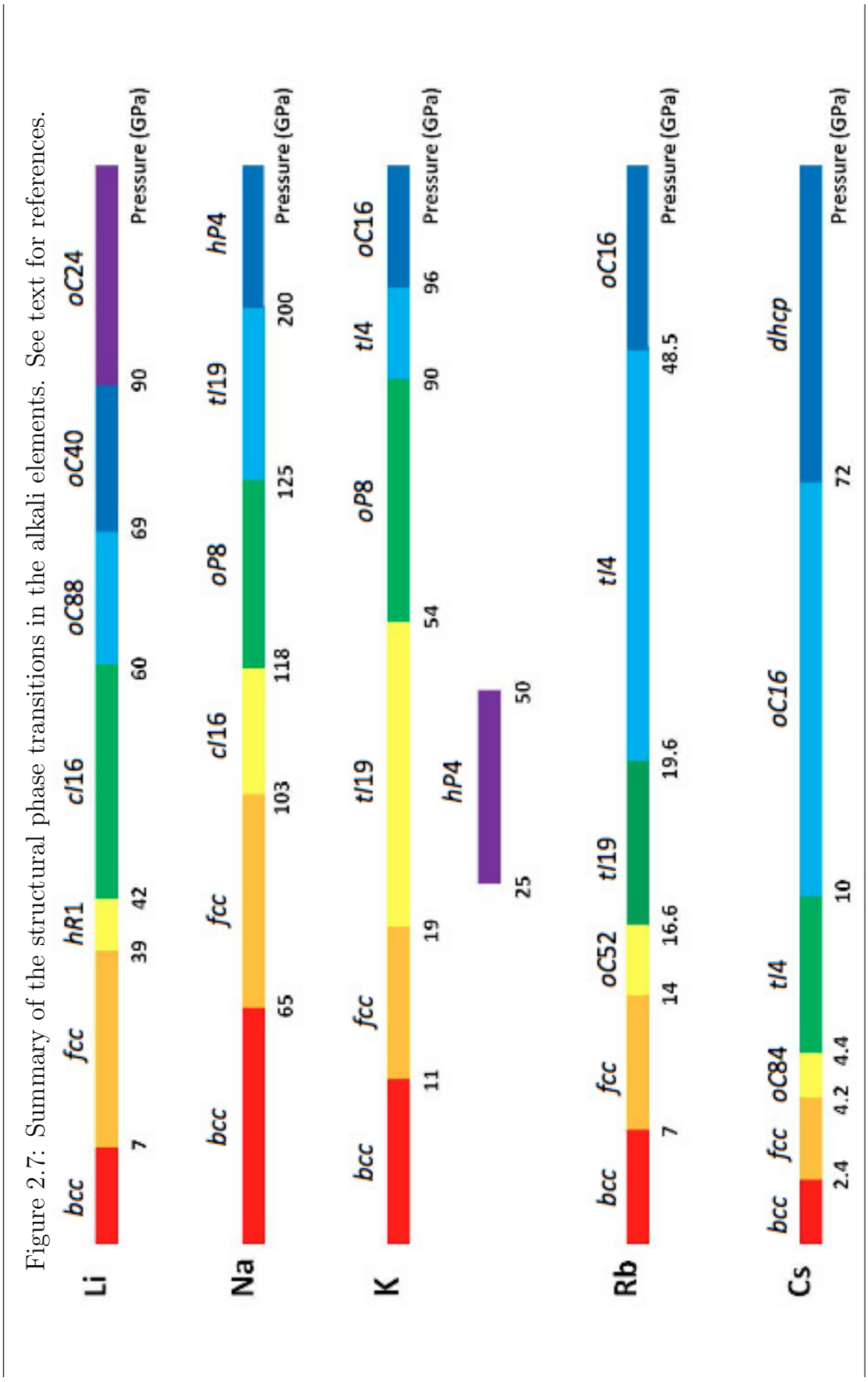

Figure 2.7: Summary of the structural phase transitions in the alkali elements. See text for references.

Figure 2.8: The melting curve of Cs as determined using visual observation techniques of sample in diamond anvil cells to determine the onset of melting (Boehler & Zha 1986).

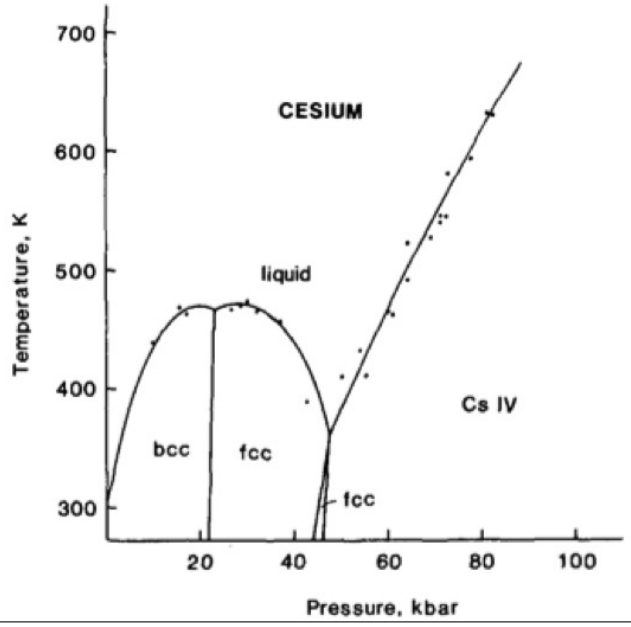

observation of the sample. They detected melting in both reflected and transmitted light by monitoring changes in shape, surface texture, and reflectivity of small samples of alkali metals surrounded by mineral oil. Furthermore, they extended the melting curve of Cs to 9 GPa, demonstrating that following the melting minimum, when the underlying solid was in the Cs-IV phase, there is a continual rise in the melting temperature. See Figure 2.8 for the current melting curve of Cs.

2.3.2 Rubidium

Like Cs, Rb has long been the focus of high-pressure melting studies. In 1959, Bundy used changes in resistivity to detect the onset of melting, which was determined by a sharp discontinuity of the sample resistance with increasing temperature (Bundy 1959). He concluded that there exists, a perhaps unsurprising, sharp maximum in the melting temperature in the Rb-I phase at $\sim$4 GPa and 553 K. Following this maximum, the gradient of the melting temperature becomes negative, decreasing down to melt at

∼14 GPa and 420 K. In 1968, Ludemann & Kennedy re-investigated the unusual melting behaviour of Rb using DTA method described above for Cs (Luedemann & Kennedy 1968). In disagreement with Bundy, they could not confirm the maximum in the melting temperature at 4.0 GPa, and suggested instead that their data demonstrated a plateau in the melting temperature at P∼8 GPa.

Figure 2.9: The melting curve of Rb as determined using visual observations of the sample to determine the onset of melting (Boehler & Zha 1986).

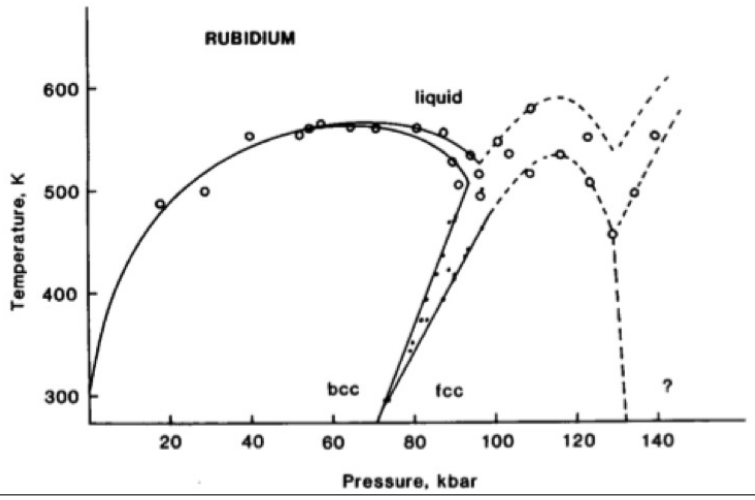

The most recent melting study of Rb was again conducted by Boehler & Zha (Boehler & Zha 1986), who used visual observations to detect the onset of melting. They concluded that there existed a melting maximum in the *bcc* phase at 7 GPa and 550 K, and located the *bcc*-*fcc*-liquid triple point at 9.5 GPa and 500 K. Moreover, they suggested that, as in Cs, the melting temperature briefly rises to a second maximum at 11 GPa and 520 K, before decreasing down to a minimum at the *fcc*-Rb-III-liquid triple point, which they tentatively suggest occurs at 13 GPa and 500 K. Following this, the melting temperature may once more continue to rise, as has been observed in Cs, though to-date there is little experimental data confirming this. See Figure 2.9 for the melting curve according to Boehler & Zha. A detailed experimental determination of the melting curve of Rb above 8 GPa is still required.

2.3.3 Sodium

The unexpected observation of a melting maximum in Cs and Rb led to numerous theoretical studies attempting to explain this phenomenon. One such study is that by Dass (Dass 1995), which suggested that there is a maximum in the melting temperature of all the alkali elements, occurring in Na in the *bcc* phase at 37 GPa. At the time the study by Dass was published, the melting curve of Na had only been determined up to 12 GPa (Boehler & Zha 1986).

The Na melting curve data from the 1968 Luedemaan & Kennedy study, and those from the several studies conducted by Zha & Boehler in the 1980s are largely in agreement (Luedemann & Kennedy 1968) (Boehler & Zha 1986) (Zha & Boehler 1985). They observe a continual rise in the melting temperature with increasing pressure, but were unable to reach the pressure at which the *bcc*-to-*fcc* transformation takes place (Hanfland *et al.* 2002). It was not until the development of diamond anvil cells capable of reaching megabar pressures, and also the development of sufficient probes such as the high intensity focussed X-rays at third generation synchrotron sources, that the melting behaviour of Na was extended further.

Gregoryanz *et al.* (Gregoryanz *et al.* 2005) demonstrated that Na has perhaps the most striking melting behaviour of all the alkali elements. Using a combination of resistively-heated diamond anvil pressure cells and *in situ* synchrotron diffraction to *directly* observe the onset of melting, they observed a maximum in the melting temperature in the *bcc* phase. To locate the melting maximum, they performed a fit to their data using the Kechin equation, a phenomenological equation which has been demonstrated to capture the behaviour of (relatively) simple systems under pressure (Kechin 2001). The melting maximum was determined to be at 31 GPa and 1,000 K. The melting temperature then proceeds to drop a remarkable 700 K over a wide pressure range, to melt just above room temperature at megabar pressures (P 115 GPa). See Figure 2.10. Beyond this remarkable minimum, the melting temperature regains a positive slope, increasing monotonically (Gregoryanz *et al.* 2005).

A recent study by Marqués *et al.* (Marqués *et al.* 2011b) places a minimum bound on the gradient of the increasing melt line. They compressed

Figure 2.10: The melting curve of Na as determined using a combination of diamond anvil cells and *in situ* X-ray diffraction techniques to directly determine the onset of melting. The melting curve is striking with a minimum at 115 GPa and just 300 K (Gregoryanz *et al.* 2005).

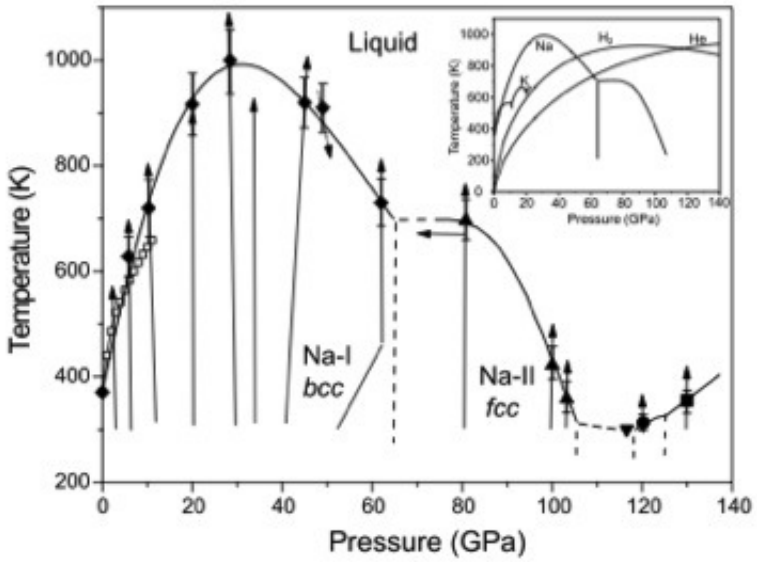

Na to 140 GPa and heated it to 550 K, where they continued to observe the solid phase. Moreover, they report calculations which suggest that at 200 GPa it would require temperatures in excess of 3,500 K to melt Na.

This dramatic melting behaviour prompted a wealth of theoretical investigations into the origin of both the melting maximum and the melting minimum. Martinez-Canales & Bergara (Martinez-Canales & Bergara 2008) have suggested that the melting maximum is due to the collapse of the shear modulus under pressure, and predict the existence of a melting maximum and minimum, but at less dramatic temperatures.

In their computational study, Raty *et al.* (Raty *et al.* 2007) suggest that the melting maximum is due to a change in density or structure that occurs in the liquid phase, similar to the phase changes which take place in the underlying solid, but at lower pressures. Moreover, they proceed to suggest that the melting minimum at 115 GPa and 300 K is due to structural and electronic changes taking place in liquid, that once more mirror the significant changes occurring in the underlying solid.

It is interesting to note that neither of the theoretical studies mentioned

above predict a second maximum, or even a shoulder in the melting temperature in the *fcc* phase. Closer inspection of the melting curve from Gregoryanz *et al.* reveals this prediction would not be inconsistent with the experimental determination of the melting temperature as there is a lack of data in this pressure region (Gregoryanz *et al.* 2005). The melting behaviour of Na is somewhat qualitatively similar with that of Rb and Cs, but with notable differences, such as the dramatic temperatures at which the solid-liquid transitions occur.

2.3.4 Lithium

Due to the difficulties concerned with performing experimental studies on Li (e.g. diamond failure), particularly on hot Li (T$\geq$ 300 K), its melting curve had only been investigated up to 8 GPa until a few years ago (Hanfland *et al.* 1999). The gradient of the melting temperature was determined to flatten out approaching 8 GPa and 530 K, and Luedemann & Kennedy suggest their data points to a maximum at 10 GPa at this temperature (Luedemann & Kennedy 1968).

Lazicki *et al.* (Lazicki *et al.* 2010) extended these measurements in 2010 to pressures of 15 GPa. Like Luedemann & Kennedy, they also used DTA methods to detect the onset of melting, and determined there to be a slight maximum in the *bcc* phase at 10 GPa and 520 K, in broad agreement with the previous study (Luedemann & Kennedy 1968). Li, therefore, appeared to behave in a similar manner to Rb and Cs, despite being considerably lower-Z and lacking *d*-electrons, with a slight positive slope in the melting temperature, culminating in a maximum at relatively modest pressures and temperatures.

The publication of work by Guillaume *et al.* in 2011 (Guillaume *et al.* 2011) revealed the melting behaviour of Li to be arguably much more remarkable than Rb or Cs. Using diamond anvil cells combined with cryostat cooling and *in situ* X-ray diffraction, they determined the melting curve of Li to pressures of 60 GPa, and studied solid-Li in the temperature range 75-300 K. Their results indicate that the melting temperature becomes negative following the solid undergoing a phase transition to the *fcc* phase. The melting temperature decreases to a deep broad minimum beginning at

40 GPa and 190 K, suggesting that perhaps quantum effect play a role in the melting curve of Li. Furthermore, this minimum exists over a broad pressure range – melting at T∼200 K between 40 and 60 GPa. This makes Li the element with the lowest melting temperature at high pressure.

Importantly, it should be noted here that due to Li being such a low-Z element it was impossible to observe the diffuse halo of scattering from the liquid phase in the X-ray diffraction experiments, and so melting was quantified by the disappearance of crystalline Bragg reflections (Guillaume *et al.* 2011). In their 2012 study, Schaeffer *et al.* called in to question the depth of the melting minimum (Schaeffer *et al.* 2012). They determined melting by the observation of discontinuities in resistance-temperature measurements at constant pressure. They found no indications of a discontinuity in resistivity at 40-60 GPa and 200 K, and instead place the melting minimum at 300 K. They do, however, agree with the general trend uncovered by Guillaume *et al.*, but their study suggests little evidence for quantum effects influencing the melting curve. Finally, they observe a maximum in the melting temperature at P∼18 GPa and 550 K, occurring in the *fcc* phase, rather than the *bcc* phase. Their results are broadly consistent with the simulated melting curve by Tamblyn *et al.* (Tamblyn *et al.* 2008). Figure 2.11 is taken from the work of Guillaume *et al.* (Guillaume *et al.* 2011), and shows the melting curve of Li as determined using *in situ* X-ray diffraction techniques.

It is key to note that in the study of Schaeffer *et al.* (Schaeffer *et al.* 2012), no evidence is provided that the sample they measure is actually Li. Melting was determined through indirect methods, such as visual observation of the sample in mineral oil, and discontinuities in resistivity measurements. Equally, the absence of Bragg reflections, used to determine the solid-liquid phase transition in the study of Guillaume *et al.* (Guillaume *et al.* 2011), is itself not sufficient to determine a liquid state. The observation of the diffuse scattering from the molten state is also required, currently impossible in Li due to how weakly it scatters X-rays. Further work is required to reconcile these two studies.

Figure 2.11: The melting curve of Li as determined using *in situ* X-ray diffraction techniques. The melting temperature decreases steeply when the underlying solid is in the *fcc* phase, down to a minimum which is, remarkably, 100 K below room temperature, reaching 190 K at 40 GPa (Guillaume *et al.* 2011).

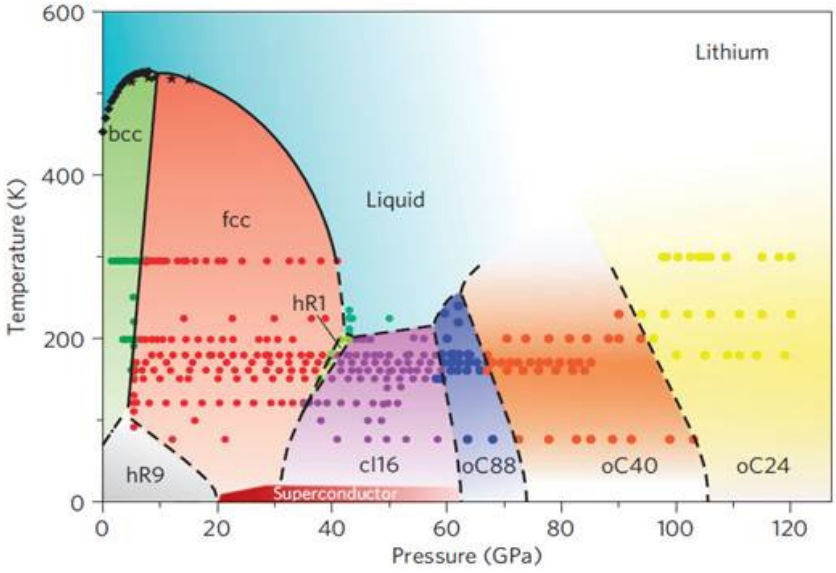

2.3.5 Potassium

The melting curve of K has been studied using the DTA method by Luedemaan & Kennedy in a multi-anvil press to 8 GPa (Luedemann & Kennedy 1968). They determined that the gradient of the melting temperature plateaued above 5 GPa, to melt at 550 K. Furthermore, they drew comparisons between K and Cs, suggesting that above 8 GPa the melting temperature would decrease over a particular period.

In the 1980s, several experimental studies were performed on the melting of K. The studies conducted by Zha & Boehler (Zha & Boehler 1985) (Boehler & Zha 1986) focussed on visual observations of sample contained within a diamond anvil cell to determine the transition from the solid to the liquid state. As described above for Na, K was suspended in mineral oil in a diamond anvil cell and heated externally. Size, shape, texture, and reflectivity of the sample were all considered. Zha & Boehler extend the melting curve of K to 14.5 GPa. What they observed was a continual rise

in the melting temperature, and, in fact, at the *bcc-fcc* transition they note an increase in the gradient of the melting temperature (Zha & Boehler 1985) (Boehler & Zha 1986).

From Zha & Boehler's study, shown in Figure 2.12, it appears that the melting behaviour of K is different to that of its neighbours. Some comparisons could be drawn between the studies of K by Zha & Boehler and that of Li by Schaeffer *et al.* (Schaeffer *et al.* 2012), where Schaeffer *et al.* also describe an increase in the gradient of the melting temperature at the *bcc-fcc* phase transition. This observation, however, is in disagreement with a previous Li melting study by Lazicki *et al.* (Lazicki *et al.* 2010).

Figure 2.12: The melting curve of K as measured by Zha & Boehler using visual observation of the sample to determine the onset of melting (Zha & Boehler 1985).

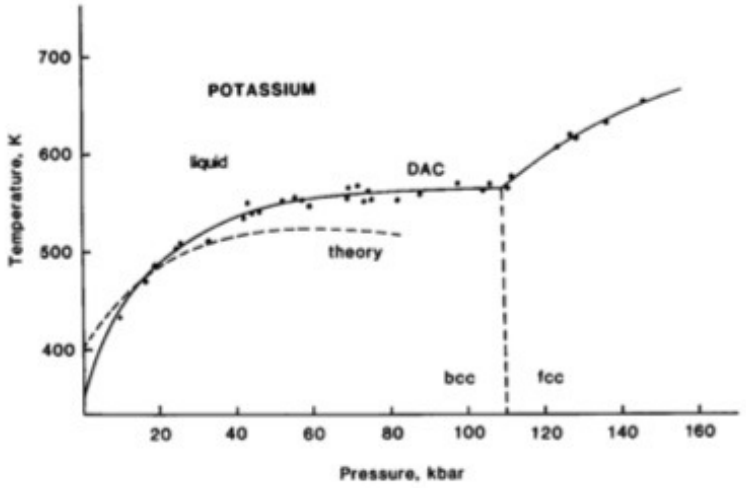

Moreover, this observation raises the question of why K would behave like Li and not like Na, Rb or Cs, with which it has demonstrably more in common – see Section 2.1. The low-pressure phase transition sequence in K is dominated by an *s*-to-*d* electron transfer, as in Rb and Cs, and then at higher pressures by *p*-*d* hybridisation. The low-pressure phase-transition sequence bears striking similarities with that of Na. The *tI*19, *hP*4, and *oP*8 phases are observed in both K and Na, though notably in a different order, possibly due to the degree of *p*- and *d*-electron character influencing K and Na with increasing pressure. At further compressions K transforms to phases

observed at extreme compression in Rb and Cs.

Given the remarkable structural similarities between K, Rb and Na, it is most surprising that the melting behaviour should be so markedly different. The majority of this Thesis focuses on exploring the high-pressure high-temperature behaviour of K with static compression techniques and *in situ* X-ray diffraction. The next Chapter describes experimental techniques that have been employed in the study of K, and the two subsequent Chapters concern the results of the static compression studies. The penultimate Chapter of this Thesis focuses on exploring the high-density behaviour of the alkali elements, namely Na, with dynamic compression techniques. Experimental techniques relevant to that study are found ahead of the results for ease of reading.

Section I

Static Compression Studies on Potassium

Chapter 3

Techniques for Static Compression Experiments

This Chapter contains the experimental techniques used in the static compression experiments contained in Chapters 4 and 5 of this Thesis. It begins with a description of diamond anvil cells, the devices used to generate pressure. Following this is a discussion of techniques used to determine sample pressure, and then a description of external resistive heating techniques. Finally, the Chapter ends with a description of X-ray diffraction theory, a summary of how a synchrotron works, and a brief description of data analysis techniques used.

3.1 Diamond Anvil Pressure Cells

The diamond anvil cell (DAC) is an indispensable tool in high-pressure research. Developed by Weir *et al.* in 1959, as cited by Jayaraman (Jayaraman 1983), it uses the same principle as Bridgman's tungsten carbide opposed anvils, but, crucially, utilises diamonds as the anvil material. Diamond possesses several properties that make it an ideal anvil material. Not only does it have a large compressive strength and hardness, it is also transparent to a wide-range of the electromagnetic spectrum. The use of diamond anvils allows the implementation of optical diagnostic techniques *in situ*, such as visual observation of the sample, infra-red spectroscopy techniques, and Raman scattering, to name but a few. Furthermore, due

to the large thermal conductivity of diamond, it may be ideally combined with external resistive heating techniques to raise the sample temperature. See Section 3.3 for further details on external resistive heating.

The DAC itself operates on a very simple principle. Pressure is generated by compressing samples between the flat tips of two opposing diamond anvils. By using this technique, pressures like those at the centre of the Earth (P∼370 GPa) have been achieved (Tateno *et al.* 2010). A schematic of a typical diamond anvil cell may be seen in Figure 3.1. A sample is contained within a (typically) metallic gasket, and the material used to create the gasket depends on a number of factors, such as sample reactivity and the pressure that is desired to be reached. Typical gasket materials used are rhenium (Re), tungsten (W), or stainless steel. The static compression studies contained in this Thesis focus on high-pressure high-temperature studies of potassium. W was used as a gasket material as it was discovered that Re reacted readily with liquid potassium. See Chapter 4 for further details.

Figure 3.1: A schematic of a diamond anvil pressure cell. Samples are placed between the flat opposing tips of two diamond anvils, contained within a gasket. Pressure is generated by forcing the diamonds together. Use of diamond as the anvil material allows the coupling of high pressure and optical diagnostic techniques.

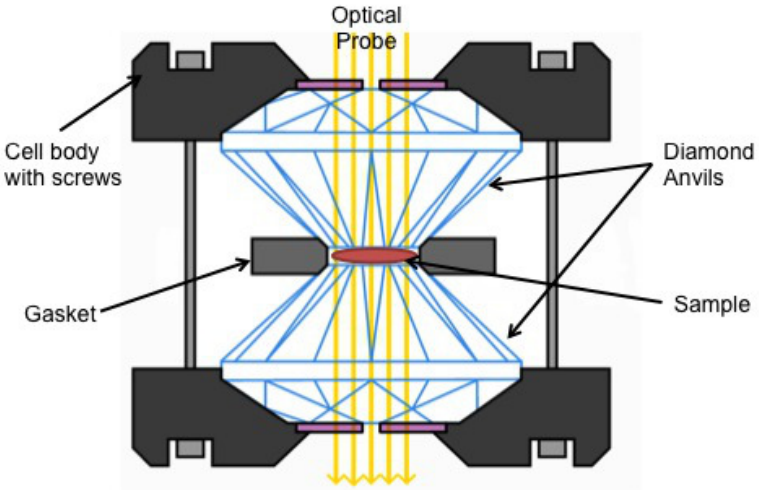

Two types of cell have been used throughout this Thesis: a Merrill-Bassett (MB) cell and a Livermore cell. A MB cell, developed by Merrill and Bassett in 1974, is a compact design, with three screws that pull together the plates

on which the diamonds sit (Merrill & Bassett 1974). An illustration of this type of cell may be seen in Figure 3.2, and images of a typical cell may be seen in Figures 3.3 (a) and (b). This cell was specifically designed for single-crystal X-ray diffraction studies. Its light, miniature body allowed it to be mounted on a standard goniometer setup, and its large opening angle allows access to a wide-range of reciprocal space, making it ideal for single-crystal X-ray diffraction studies.

Figure 3.2: A schematic of a Merrill-Bassett diamond anvil cell. The small cell body and wide opening angles make it ideal for single-crystal X-ray diffraction studies. The cell body (1), seats (2), gasket (3), and diamond anvils (4), are labelled (Merrill & Bassett 1974).

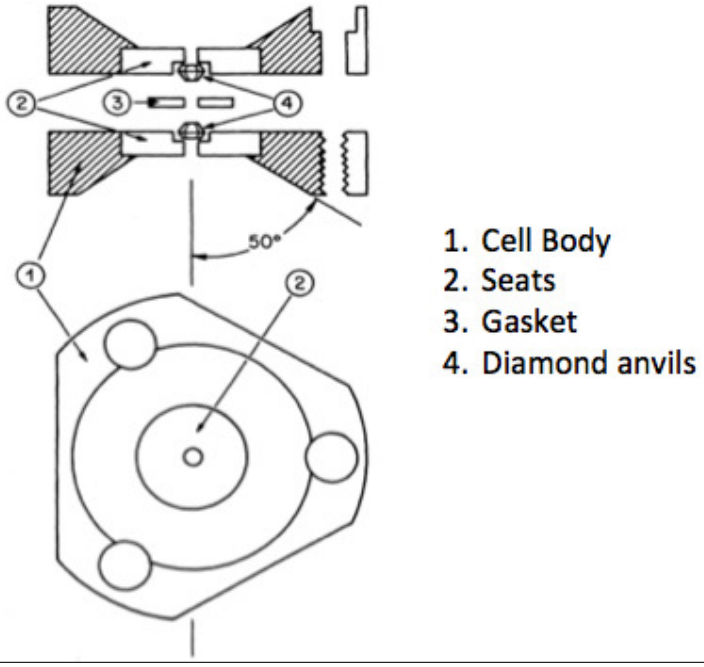

A Livermore cell is a gas membrane driven piston-cylinder cell (Jenei *et al.* 2009). Image of an example cells may be seen in Figures 3.3 (c) and (d), and a schematic of a Livermore cell may be seen in Figure 3.4. Membrane-driven diamond anvil cells are frequently used in high-pressure studies, and have been described in detail by Letoullec *et al.* (LeToullec *et al.* 1988). The advantage of using a membrane to control pressure changes is that unlike, screws and other hand tools used to exert pressure, the gas-driven membrane exerts uniform pressure across the cell body as it pushes the piston further

Figure 3.3: Images of diamond anvil pressure cells: (a) an open Merrill-Bassett cell illustrating the tungsten carbide seats and diamond anvils, (b) a closed Merrill-Bassett cell, (c) an open Livermore cell illustrating the piston and cylinder, and (d) a closed Livermore cell.

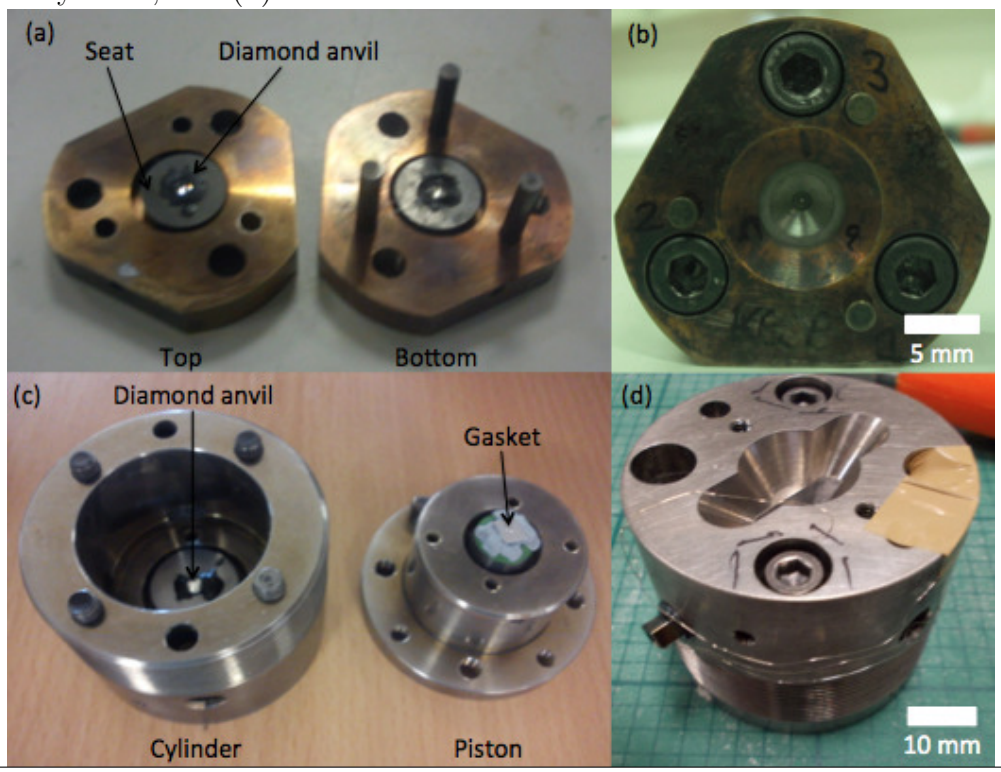

into the cylinder. Furthermore, use of a membrane allows remote-control of pressure when samples are being heated or cooled. This is particularly relevant to the highest temperature studies detailed in this Thesis, where a vacuum vessel, combined with external resistive heaters, was used to achieve T>650 K. This vessel is described in Section 3.3, and was designed to be used in conjunction with Livermore cells. Note that the MB cells used in this Thesis were all placed in a purpose-built adaptor so that they too could be driven by a gas-filled membrane, increasing pressure uniformly, and further, could be used in conjunction with the vacuum vessel.

In this Thesis research, the MB cells used were equipped with Boehler-Almax (BA) cut diamonds and seats composed of tungsten carbide. The BA cut for diamond anvils was developed by Boehler & De Hansetters, and is extremely useful in high-pressure diffraction studies (Boehler &

Figure 3.4: A schematic of the Livermore diamond anvil cell. This cell is designed to operate in conjunction with a vacuum vessel. It is a gas membrane driven piston-cylinder cell, allowing remote and uniform control of changes in pressure. Illustrated on this Figure are (a) the cylinder, (b) the piston, (c) the membrane, (d) the membrane gap, (e) seats, (f) diamond anvils, and (g) the gas inlet to drive the membrane. (Jenei *et al.* 2009)

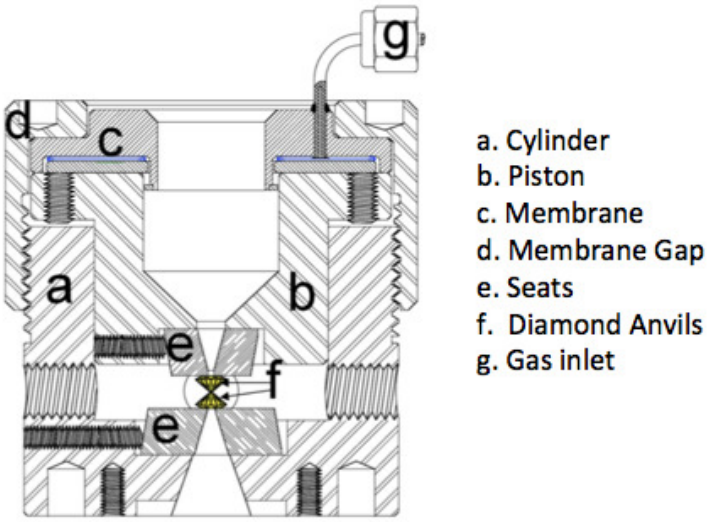

De Hantsetters 2004). The large opening angle afforded by the BA cut, illustrated in Figure 3.5 (b), offers access to a large amounts of reciprocal space. This is particularly useful for high-pressure single-crystal studies, as with a large opening angle one gains access to many more reflections when one rotates the cell. More generally, in X-ray diffraction experiments conducted at high-pressures, the Bragg peaks are shifted to higher 2θ with increasing pressure, and so a cell with a large opening angle will yield more information than the conventional anvils shown in Figure 3.5 (a).

Furthermore, the seat, or backing disc, used to support the BA cut diamonds is composed of tungsten carbide. These seats, which are machined such that the conical anvils sit within them (Figure 3.5 (b)), provide greater mechanical stability than conventional anvil, which sit atop their associated backing disc (Figure 3.5 (a)). The seats optimised for use with BA cut diamonds have the added advantage that they do not require the X-ray beam to pass through any of the supporting material until the cell is rotated

through a very large angle. With conventional diamond anvils, the seats were composed of beryllium (Be), or, later, cubic boron nitride (BN), which greatly increased the background in X-ray diffraction experiments as the cell was rotated. Clearly, using BA cut diamonds, with their accompanying seat design means that the cell may be rotated through a much larger angle before the backing disc material contributes to the background.

Figure 3.5: Schematic of (a) conventional and (b) Boehler-Almax cut diamond anvils. The Boehler-Almax cut diamonds have a larger opening angle and so allow access to a larger volume of reciprocal space (Boehler & De Hantsetters 2004)

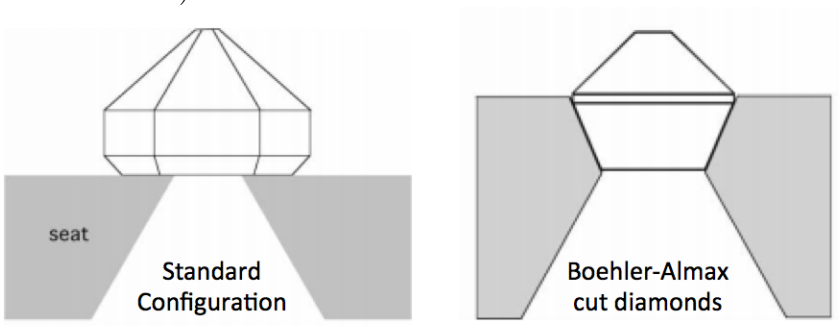

The BA diamonds used in several of the studies detailed in Chapters 4 and 5 have an opening angle of $\pm 37°$, and were particularly useful in the single-crystal study detailed in Chapter 5. The Livermore cells were equipped with conventional diamond anvils (Figure 3.5 (a)), which additionally have a slot in the backing disc of the cylinder-side of the cell, which matches the window in the vacuum vessel (see Section 3.3). This provides greater stability when heating at multi-megabar pressures, but further reduces the 2θ-range accessible when using this cell, and so these cells were used only for the highest temperature melting studies, which required use a vacuum vessel (see Chapter 4). They were also used in some, but not all, of the high-temperature powder diffraction studies described in Chapter 5.

3.2 Determining Pressure

Throughout this Thesis, pressure was determined using either optical spectroscopy techniques, or by using the Equation of State (EoS) of a high-

pressure diffraction standard, namely tantalum (Ta).

3.2.1 Fluorescence Techniques

The ruby (α-Al_2O_3:Cr^{3+}) fluorescence technique was developed by Piermaini *et al.* (Piermarini *et al.* 1975), and extended to 100 GPa in 1978 by Mao *et al.* (Mao *et al.* 1978). This technique is based on the observation that a pair of electronic transitions, caused by the Cr^{3+} dopant in the Al_2O_3 (the R_1 and R_2 fluorescence lines), shift in wavelength under pressure. An example of the shift in the R_1 and R_2 fluorescence lines under pressure may be seen in Figure 3.6.

Figure 3.6: An example of ruby R_1 and R_2 fluorescence lines shifting in wavelength as pressure is increased. This is an example of an optical spectroscopy technique used to determine the sample pressure in diamond anvil cell experiments.

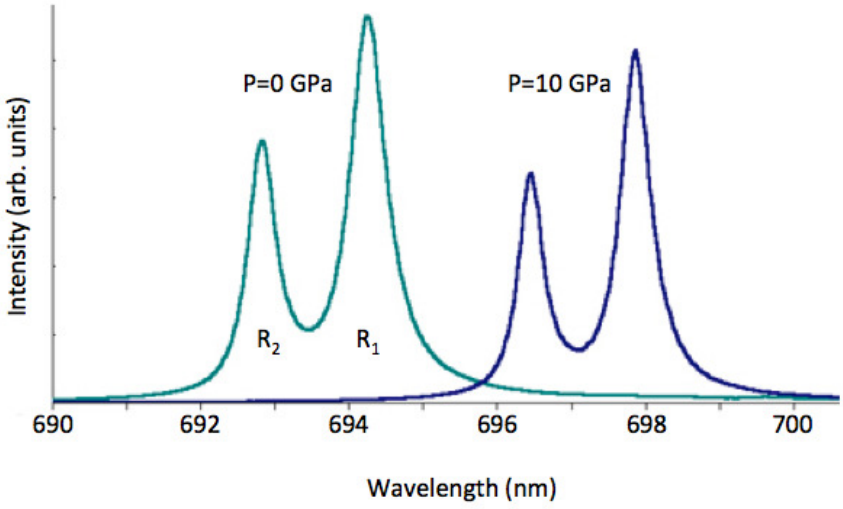

Piermaini *et al.* derived the wavelength-pressure relation to be:

$$P = \frac{19.04}{5}\left[\left(\frac{\lambda_0 + \Delta\lambda}{\lambda_0}\right)^5 - 1\right] \tag{3.1}$$

where pressure, P, is in Mbar, λ is in nm and λ_0 is the ambient pressure ruby wavelength, often assumed to be 694.34 nm (Piermarini *et al.* 1975).

The data of Mao *et al.* and an extrapolation of the data from Piermarini *et al.* are in good agreement to ∼30 GPa (Mao *et al.* 1978).

Ruby fluorescence is a very useful, and hence widely used technique, yet it does have several limitations. At pressures above 100 GPa, the fluorescence from the R_1 line has diminished significantly, making pressure determination extremely difficult. Furthermore, at high temperatures (∼500 K), the ruby R_1 fluorescence line broadens, once more making pressure determination extremely difficult and inaccurate (Datchi *et al.* 2007). This temperature effect is particularly relevant to this Thesis research, where studies have been performed at relatively modest pressures (ambient pressure to 50 GPa), yet high temperatures (up to 750 K). In such instances the ruby fluorescence technique becomes difficult to use.

An alternative pressure calibrant to ruby is samarium doped strontium borate – SrB_4O_7:Sm^{2+}. Datchi *et al.* studied the wavelength pressure shift of the $^7D_0 \rightarrow {}^5F_0$ fluorescence line up to 124 GPa (Datchi *et al.* 1997). By coupling fluorescent luminescence techniques and *in situ* X-ray diffraction, Datchi *et al.* calibrated the wavelength shift of the $^7D_0 \rightarrow {}^5F_0$ line in SrB_4O_7:Sm^{2+}, to the R_1 line in ruby, and to the EoS of gold – a high-pressure diffraction standard. They determined that this pressure-wavelength relation could be described as:

$$P = 4.032\Delta\lambda(1 + 9.29 \times 10^3\Delta\lambda)/(1 + 2.32 \times 10^{-2}\Delta\lambda) \qquad (3.2)$$

where pressure, P, is in GPa and $\Delta\lambda = \lambda - 685.41$ is in nm. The value of 685.41 nm is the ambient-pressure wavelength of the $^7D_0 \rightarrow {}^5F_0$ line (Datchi *et al.* 1997). Crucially, Datchi *et al.* discovered that not only did the width of the fluorescence line have a negligible temperature dependence up to 900 K, but that the shift in peak position with increasing temperature was also very small, making it an excellent pressure calibrant for high-pressure high-temperature studies.

3.2.2 Diffraction Standards

An alternative and often more precise technique to determine pressure is the use of diffraction standards, which are internal to the DAC sample chamber.

Pressure is measured by determining the volume of the unit cell using *in situ* diffraction, and use of the EoS of the standard.

In certain studies contained in this Thesis, small pieces of Ta foil or a few grains of Ta powder were used to determine pressure. The Vinet EoS, as determined by Dewaele *et al.* (Dewaele *et al.* 2004), was used to calculate the pressure at room temperature, P_{RT}:

$$P_{RT} = 3K_0 x^{-2}(1-x)e^{(1.5(K_0'-1)(1-x))} \tag{3.3}$$

where $x = (V/V_0)^{(1/3)}$; the V_0 is the ambient-pressure volume, 18.033 Å^3; K_0 is the bulk modulus, 194 GPa; and the pressure derivative of the bulk modulus is $K_0' = 3.25$. Note that the ambient pressure lattice parameters of Ta depend on how much hydrogen has dissolved into the lattice (Taxak *et al.* 2012). Therefore, in every experiment using Ta as a pressure calibrant, the ambient-pressure lattice parameter, and hence volume, were measured and used to calculate V_0. K_0 and K_0' where assumed to be as above. The $P-V$ plot of the EoS of Ta as determined by Dewaele *et al.* (Dewaele *et al.* 2004) is shown in Figure 3.7.

The EoS of Ta was used to determine pressure not only at room temperature, but also at elevated temperatures. To account for the thermal expansion of the lattice, an additional factor was added to the room-temperature pressure. Cohen & Gülseren (Cohen & Gülseren 2001) performed first-principles calculations on the thermal EoS of Ta up to 300 GPa and 1,000 K. They describe that the thermal EoS for Ta can be determined simply by adding a thermal pressure P_{Th} to the room-temperature pressure, P_{RT}. Cohen & Gülseren suggest that the high temperature contribution to the pressure may be written as:

$$P_{Th} = aT \tag{3.4}$$

where $a = 0.00442$ GPa/K. The pressure of the sample, P_S, is therefore simply:

$$P_S = P_{RT} + P_{Th} \tag{3.5}$$

In this Thesis, the ruby fluorescence technique was only used in the single-

Figure 3.7: The Equation of State of the high-pressure diffraction standard tantalum from a study by Dewaele *et al.* (Dewaele *et al.* 2004). The circles represent the experimental data and the solid line is a fit using the Vinet EoS. This EoS was used to determine sample pressure in some of the high-pressure high-temperature studies detailed in this Thesis.

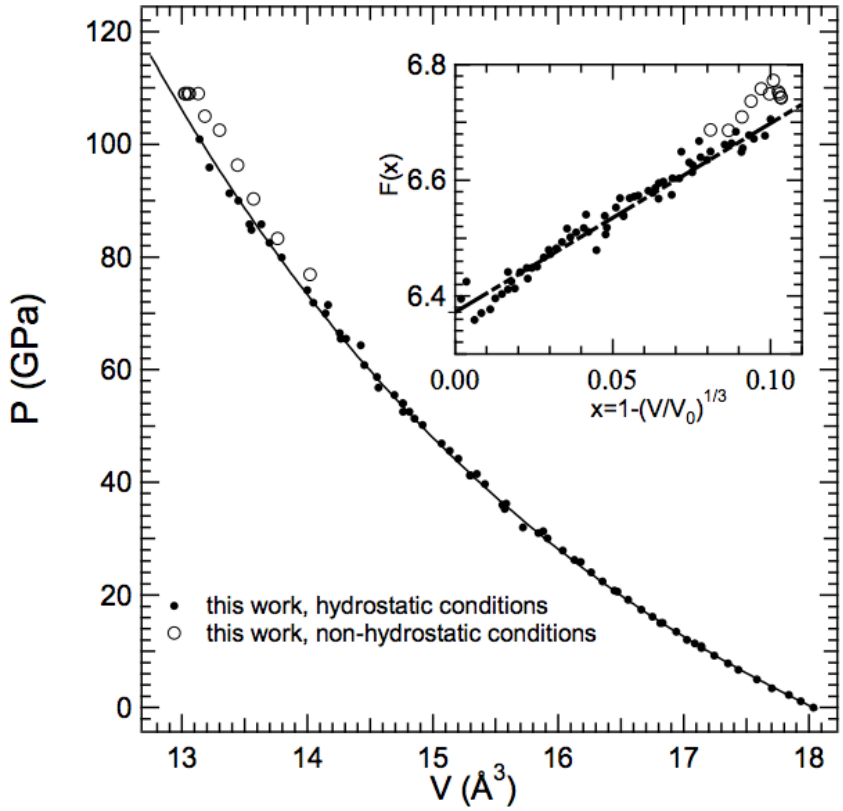

crystal experiment detailed in Chapter 5. In this experiment, the maximum temperature reached was 365 K. Furthermore, it was key that the pressure calibrant could be easily avoided with a narrowly focused X-ray beam, as the experiment relied on the analysis of a number of weak reflections, meaning SrB_4O_7:Sm^{2+} was not used as it is a fine powder. In the melting studies (Chapter 4) conducted up to a maximum of T$\sim$650 K, SrB_4O_7:Sm^{2+} was used as a pressure calibrant for the reasons detailed above in Section 3.2.1. At higher temperatures, use of a vacuum vessel was required, which did not permit the use of spectroscopic techniques. Here, as in the powder diffraction studies in Chapter 5, Ta foil or powder was used.

3.3 Heating

There are many methods which may be utilised to heat samples in a DAC, such as continuous wave and pulsed laser heating, and internal and external resistive heating (Briggs *et al.* 2012) (Goncharov *et al.* 2008) (Falconi *et al.* 2006) (Jenei *et al.* 2009). Throughout the work detailed in Chapters 4 and 5, samples were heated using external resistive heating only. Two types of heating set-up were used. For temperatures up to and including 650 K, K-type external resistive heating rings (Watlow Ltd.) were used in air, to heat both MB cells and Livermore cells.

For temperatures in excess of 650 K, samples were heated in a small purpose-built vacuum chamber, as heating diamonds to temperatures in excess of ∼650 K in air leads to the diamond burning, or subliming, and to eventual failure and hence the end of the experiment. The vacuum vessel used was developed by S. Macleod (AWE). It is an adaptation of a vessel designed by Jenei *et al.* at LLNL (Jenei *et al.* 2009). During the development and testing stages of the AWE vessel, use of the vessel was kindly permitted in exchange for testing ongoing modifications, and to adapt the vessel for use at beamline ID09a at the European Synchrotron Radiation Facility (ESRF).

The Livermore cell body is surrounded by 675 W coiled cable heaters (Watlow Ltd.). An example of a cell being set up in the heating vessel may be seen in Figure 3.8 (a). The closed vacuum vessel may be seen in Figure 3.8 (b), complete with a kapton window for use in X-ray diffraction experiments. A photograph of the vacuum vessel setup for use on the high-pressure X-ray diffraction beamline, I15, at the Diamond Light Source (DLS), may be seen in Figure 3.9. Using in-vacuum heating, samples were heated to temperatures of ∼800 K, which is by no means the upper limit of this technique. This temperature-limit was chosen to avoid damage to the cells and the vessel during the early testing stages of the vessel. As an example of the high temperatures that are capable of being reached using in-vacuum heating, Jenei *et al.* heated molecular CO_2 at 96 GPa to 1,000 K. Furthermore, they were capable of heating to such temperatures for extended periods of time, heating to 1,000 K for between 8-12 hours (Jenei *et al.* 2009).

In all heating experiments the sample temperature was measured using a K-type thermocouple, either on the rear of one of the diamond anvils, or

Figure 3.8: An example of a Livermore cell being mounted in a vacuum vessel. Shown in (a) is the cell, surrounded by a cable heater, and mounted on the vessel. Image (b) illustrates the front face of the vessel, which faces the detector, with a narrow kapton window for X-ray diffraction measurements.

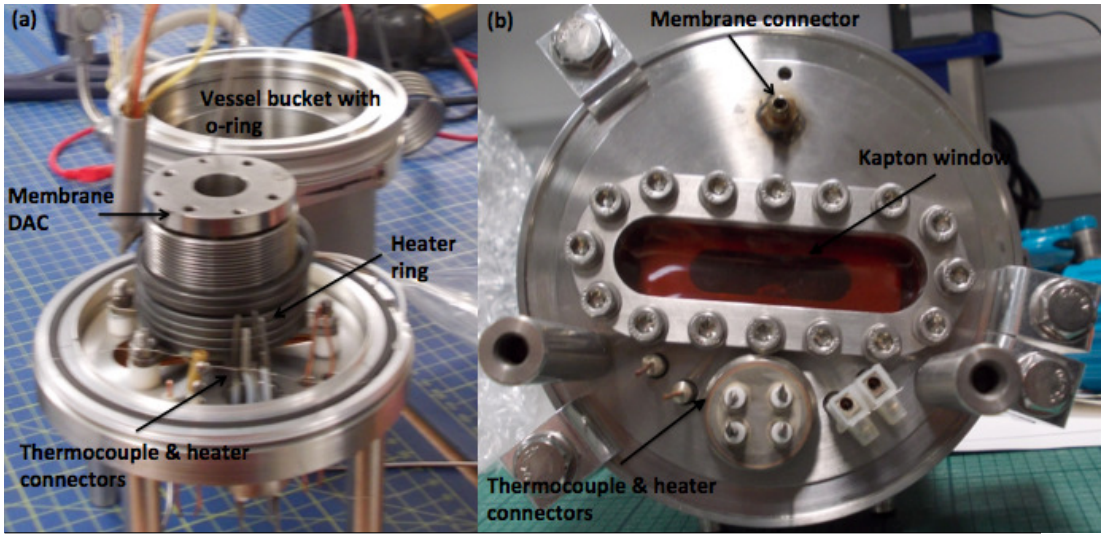

attached directly to a diamond anvil inside the pressure cell, located close to the sample. Due to the high thermal conductivity of the diamond anvils, it was discovered that measuring the sample on the rear surface or closer to the sample made a difference of only 2-3 K at 600 K.

3.4 X-ray Scattering

One of the most fundamental properties of a solid is its structure, and knowledge of this is essential to our understanding of the high-pressure behaviour of materials. Determination of crystal structures is most commonly based on analysis of diffraction phenomena caused by the interaction of the crystal with, for example, X-rays. The interaction of X-rays with matter occurs in two common processes, either through scattering or absorption. The majority of the work in this thesis utilises X-ray scattering techniques as the main investigative tool.

In certain processes, incident photons may be scattered elastically, and so the scattered photon will have the same wavelength as the incident photon.

Figure 3.9: The closed vacuum vessel mounted on beamline I15 at the Diamond Light Source for *in situ* X-ray diffraction measurements.

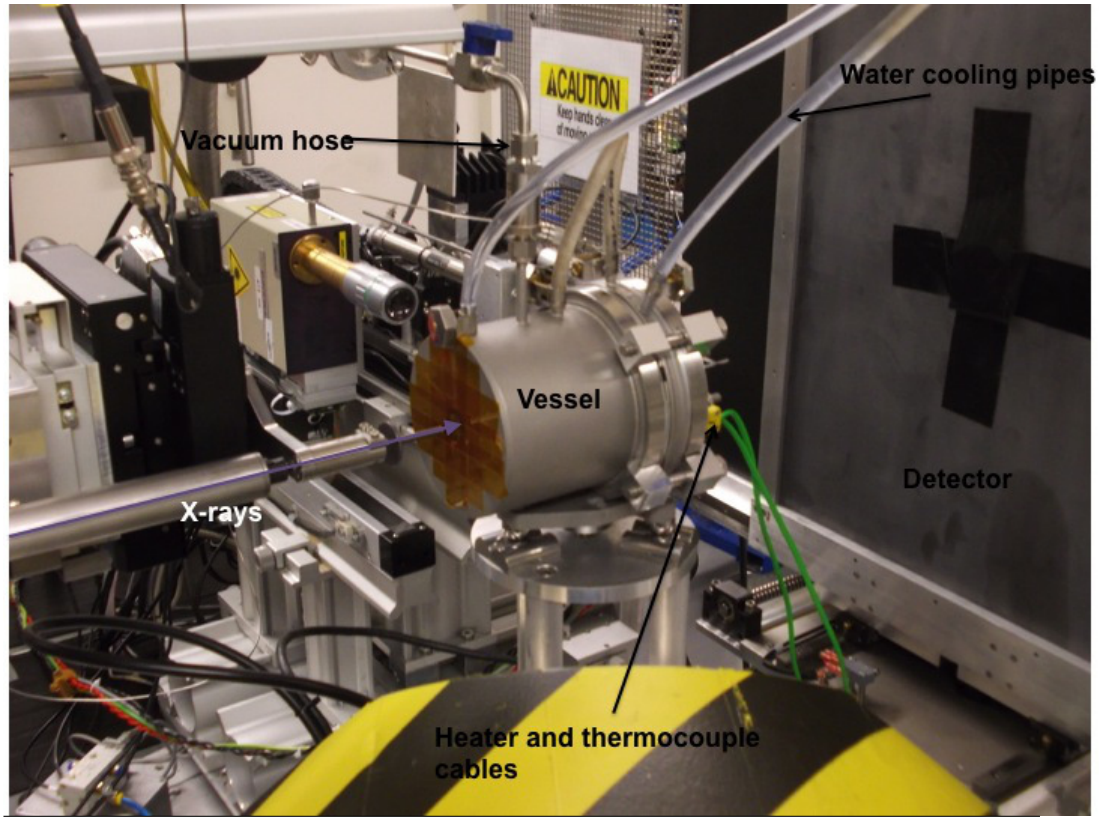

Other photons may be inelastically scattered, losing energy and consequently having a longer wavelength than the incident photon. This constitutes Compton scattering. Compton scattering is incoherent, and such scattering from the diamond anvils, which are considerably larger than the sample, contributes to a considerable background in DAC experiments. This becomes particularly important when treating liquid-diffraction data. This will be discussed further in Chapter 4.

Prior to a discussion of X-ray diffraction from crystals, it is important to introduce some crystallographic nomenclature. Any crystal may be described in terms of a unit cell, an arbitrary choice of a representative repeating unit that describes the crystal. A unit cell is described, generally, in terms of the cell lengths a, b and c in three dimensions, and the angles between said lengths: α, the angle between b and c; β, the angle between a and c; and γ,

the angle between a and b.

When discussing X-ray diffraction, it is often convenient to think of X-rays as scattering from different planes in a crystal. This is particularly useful when thinking about X-ray diffraction in terms of the Bragg formalism.

3.4.1 Bragg Formalism

In 1915 W.H. and W.L. Bragg were awarded the Nobel Prize in Physics for determining the structure of NaCl using X-ray diffraction. The Bragg formalism considers X-rays reflecting from successive crystal planes. X-rays scatter off a set of parallel planes of atoms, described by Miller indices (hkl), resulting in sharp, intense peaks (Bragg peaks), formed by the constructive interference of the reflecting X-rays. For simplicity, we will consider scattering from an orthogonal unit cell, where $\alpha = \beta = \gamma = 90°$. Indeed, all the crystal structures treated in this Thesis have orthogonal unit cells.

The crystal planes are described in terms of the axes of the crystal unit cell, such that if one plane member passes through the origin, the next intercepts at a/h along x, b/k along y, and c/l, along z, where h, k and l are integers, known as the Miller indices. The spacing between subsequent planes is thus denoted d, as illustrated in Figure 3.10. For an orthogonal unit cell d has the form $1/d^2 = h^2/a^2 + k^2/b^2 + l^2/c^2$.

On inspection of Figure 3.10, it is clear that the path difference between the two rays is equal to $2d\sin\theta$, and that the angle between the incident and scattered ray is 2θ. Hence, for rays to interfere constructively they satisfy:

$$m\lambda = 2d\sin\theta \tag{3.6}$$

where m is an integer.

What should be clear from the Bragg formalism is that a diffraction pattern is not a representation of the direct crystal lattice, but rather each point represents a plane of atoms off which incident X-rays scatter. A diffraction pattern is instead a representation of what is called the reciprocal lattice.

For a group of direct lattice planes separated by a distance d there are

Figure 3.10: An illustration of the Bragg formalism for X-ray diffraction. X-rays scatter elastically off a set of parallel planes of atoms separated by a distance **d**.

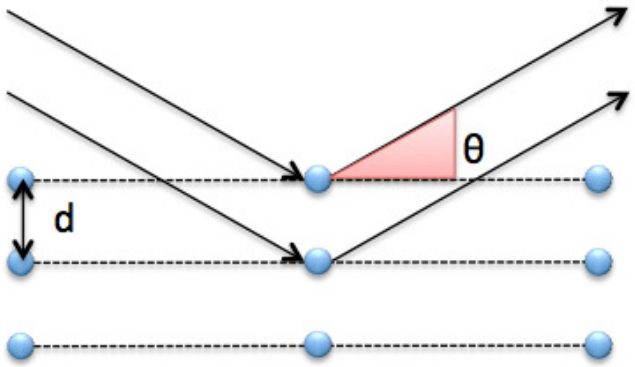

corresponding reciprocal space vectors which are perpendicular to the direct lattice planes, and the shortest one has length $2\pi/d$. In general, any direct lattice may be defined as:

$$\mathbf{R} = u\mathbf{a} + v\mathbf{b} + w\mathbf{c} \tag{3.7}$$

where u, v, and w are integers, and $\mathbf{a}$, $\mathbf{b}$ and $\mathbf{c}$ are the direct lattice vectors. The corresponding reciprocal lattice is defined as:

$$\mathbf{G} = h\mathbf{a}^* + k\mathbf{b}^* + l\mathbf{c}^* \tag{3.8}$$

where h, k and l are the Miller indices described above, and the reciprocal lattice vectors are: $\mathbf{a}^* = 2\pi\frac{\mathbf{b}\times\mathbf{c}}{\mathbf{a}\cdot(\mathbf{b}\times\mathbf{c})}$, $\mathbf{b}^* = 2\pi\frac{\mathbf{c}\times\mathbf{a}}{\mathbf{b}\cdot(\mathbf{c}\times\mathbf{a}}$), and $\mathbf{c}^* = 2\pi\frac{\mathbf{a}\times\mathbf{b}}{\mathbf{c}\cdot(\mathbf{a}\times\mathbf{b})}$.

The direct and reciprocal lattices are related by:

$$e^{i\mathbf{G}\cdot\mathbf{R}} = 1 \tag{3.9}$$

3.4.2 The von Laue Formalism

Awarded the 1914 Nobel Prize in Physics for his work on the scattering of X-rays from a crystalline lattice, von Laue devised an alternative to the Bragg

formalism. Unlike the Bragg formalism, it does not assume that crystals are sectioned into planes, but rather they are composed of a series of point scatterers (atoms), connected by a displacement vector, **d**, as illustrated in Figure 3.11.

Figure 3.11: An illustration of the von Laue formalism of X-ray diffraction. X-rays are scattered from point-like objects (atoms) separated by a displacement vector **d**. Unlike the Bragg formalism, this construction does not assume that crystals are sectioned into planes.

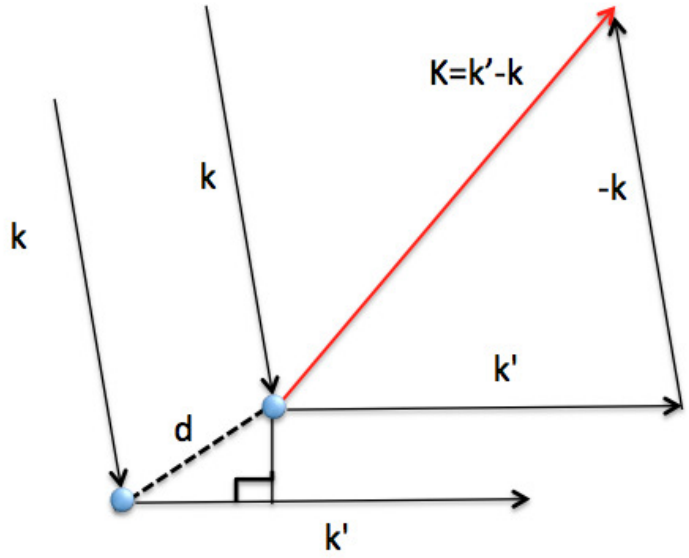

The incident X-ray has wavelength λ and is travelling along the same direction as its associated wavevector $\mathbf{k}$, where the magnitude of vector $\mathbf{k}$ is $k = 2\pi/\lambda$. An X-ray is scattered from a point-like object (an atom) and the scattered X-ray, again with wavelength λ, has a wavevector $\mathbf{k}'$. The magnitude of $\mathbf{k}'$ is $k' = 2\pi/\lambda$. A scattered X-ray will be observed provided that the path difference between the incident and scattered ray is an integral number of wavelengths - the path length difference is simply $\mathbf{d} \cdot (\mathbf{k}' - \mathbf{k}) = 2\pi m$, where m is an integer.

Extending this argument to an array of scattering atoms, a crystal, where the atoms are separated from each other on lattice sites by a set of lattice vectors $\mathbf{R}$, the condition for constructive interference is therefore: $\mathbf{R} \cdot (\mathbf{k} - \mathbf{k}') = 2\pi m$, which may equivalently be written as $e^{i(\mathbf{k}-\mathbf{k}')\cdot\mathbf{R}} =$

1. Now, appealing to Equation 3.9, the Laue condition for constructive interference will be achieved provided that the change in wavevector, $\mathbf{K} = \mathbf{k} - \mathbf{k}'$, is a vector of the reciprocal lattice i.e. $\mathbf{K}$=$\mathbf{G}$, or $\mathbf{K}$=$\mathbf{G}m$, where m is an integer.

3.4.3 The Ewald Construction & Equivalence of the Bragg and von Laue Formalisms

The Ewald construction is a useful tool for visualising reflection conditions, and is particularly useful for single-crystal diffraction experiments. It is also an elegant demonstration of the equivalence of the Bragg and von Laue formalisms. Figure 3.12 illustrates the so-called Ewald sphere, depicted here in two-dimensions by a circle of radius $2\pi/\lambda$, with a crystal placed at the centre. A Bragg peak occurs if and only if $\mathbf{K}$ gives a reciprocal lattice point which intersects the surface of the sphere (circle). Importantly, for a monochromatic X-ray source and a single-crystal sample, rotating the crystal allows additional reciprocal lattice points to pass through the surface of the Ewald sphere.

Here, as in the von Laue formalism, the incident X-ray has wavevector $\mathbf{k}$, and the reflected ray has wavevector $\mathbf{k}'$. It should be clear from Figure 3.12 that the angle between the incident and reflected X-rays is 2θ, and we may write:

$$K = 2k \sin\theta \tag{3.10}$$

Recall that the magnitude of $\mathbf{k}$ is $k = 2\pi/\lambda$, and that vector $\mathbf{K}$ must be an integer multiple of the reciprocal lattice vector. If we assume the crystal is constructed of planes separated by a distance d, then the magnitude of vector $\mathbf{K}$ is $K = 2\pi m/d$. Therefore Equation 3.10 may be rewritten as:

$$2\pi m/d = 2(2\pi/\lambda)\sin\theta \tag{3.11}$$

By cancelling out a factor of 2π on each side, and by performing some simple rearrangement, one recovers the Bragg condition, Equation 3.6.

Figure 3.12: The Ewald construction illustrating the equivalence of the Bragg and von Laue formalisms. X-rays are incident on a crystal at the centre of an Ewald sphere (circle) of radius $2\pi/\lambda$. The wavevectors of the incident and reflected X-rays are **k** and **k'**, respectively.

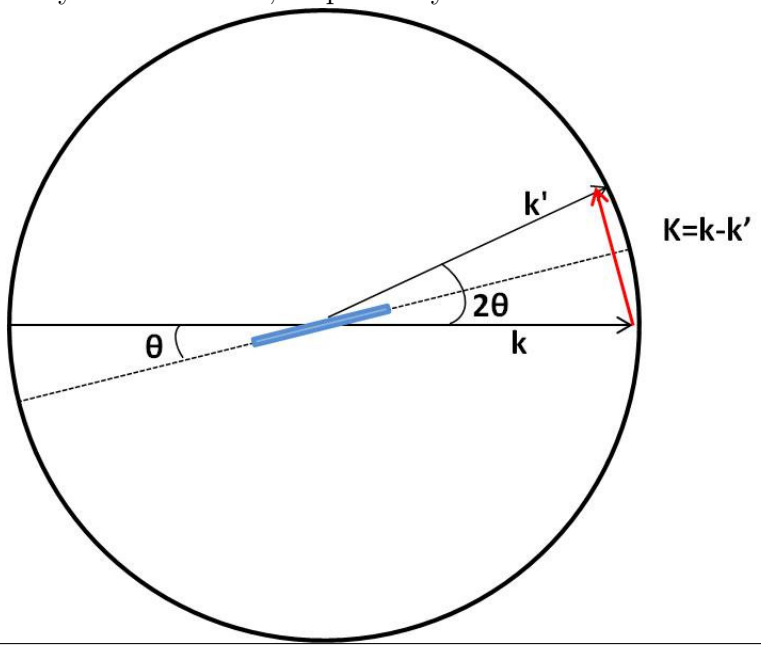

3.4.4 Scattering from Atoms and Crystals

Typically in X-ray scattering process, the incident X-rays are scattered by atomic electrons, and the same is assumed here. The total amplitude arising from a volume $d\mathbf{r}$, which contains a certain number of electrons $\rho(\mathbf{r})d\mathbf{r}$, where $\rho(\mathbf{r})$ is the electron density, is given by:

$$f(\mathbf{S}) = \int_V \rho(\mathbf{r}) e^{i\mathbf{S}\cdot\mathbf{r}} d\mathbf{r} = T[\rho(\mathbf{r})] \tag{3.12}$$

where $T[\rho(\mathbf{r})]$ is the Fourier Transform of the electron density, and **r** and **S** are generic position vectors of the direct and reciprocal lattice, respectively. Likewise, by performing an inverse Fourier Transform on the scattering factor, $T^{-1}[f(\mathbf{S})]$, one obtains the electron density:

$$\rho(\mathbf{r}) = \int_{V^*} f(\mathbf{S}) e^{-i\mathbf{S}\cdot\mathbf{r}} d\mathbf{S} = T^{-1}[f(\mathbf{S})] \tag{3.13}$$

where V^* is a volume in reciprocal space.

To a good approximation, the atomic electron density function, ρ_a, may be considered to be a spherically symmetric function. Assuming that the centre of the atom is located at the origin, one may write the atomic electron density function as $\rho_a = \rho(\mathbf{r})$. Likewise, the Fourier transform of this function, f_a, is also a spherically symmetric function, and is called the atomic scattering factor.

Now consider scattering from a unit cell containing N atoms. The electron density of a unit cell may be written as: $\rho_U(\mathbf{r}) = \Sigma_{i=1}^{N} \rho_i(\mathbf{r} - \mathbf{r}_i)$, where $\mathbf{r}_i$ is the position, and ρ_i is the density, of the i^{th} atom. The structure factor, or scattering factor of the unit cell, is

$$f_U(\mathbf{S}) = \int_{\chi} \sum_{i=1}^{N} \rho_i(\mathbf{r} - \mathbf{r}_i) e^{i\mathbf{S}\cdot\mathbf{r}} d\mathbf{r} = \sum_{i=1}^{N} f_i(\mathbf{S}) e^{i\mathbf{S}\cdot\mathbf{r}} \tag{3.14}$$

where $f_i(\mathbf{S})$ is the atomic form factor for the i^{th} atom and χ is a region of space where the probability of finding an electron is non-zero. It should be noted that there can be more than one species of atom in each unit cell, and furthermore that the unit cell is not necessarily the primitive unit cell, but rather a conventional one. The difference between a primitive and conventional unit cell may be easily understood in the context of a lattice which describes the periodicity of the crystal system.

The repetitive geometry of a crystal may be represented in three dimensions by a periodic sequence of points. The position vector $\mathbf{r_i}$, may be defined such that it ranges over all possible positions within the unit cell, with its origin at $x = y = z = 0$. One may write $\mathbf{r_i}$ as:

$$\mathbf{r_i} = x_i\mathbf{a} + y_i\mathbf{b} + z_i\mathbf{c} \tag{3.15}$$

where $\mathbf{a}$, $\mathbf{b}$ and $\mathbf{c}$ are the lattice vectors defined above, and x_i, y_i and z_i are fractional co-ordinates within the unit cell.

If any lattice point is chosen as the origin, then the position of any other lattice point is defined by the direct lattice vector $\mathbf{R} = u\mathbf{a} + v\mathbf{b} + w\mathbf{c}$, where u, v, and w are integers and $\mathbf{a}$, $\mathbf{b}$, and $\mathbf{c}$ are the basis vectors. A primitive unit cell is one with the smallest possible volume, containing just one lattice point. A conventional unit cell is typically a more convenient representation of the crystal, and can contain more than one lattice point.

An example of a conventional unit cell is the well known face-centred cubic cell, which contains 4 lattice points, one at each of the eight corners of the unit cell, and one on each of the six faces. The entire cell, therefore, contains 4 complete lattice points, with the corners each contributing $\frac{1}{8}$ of a lattice point, and each of the six faces contributing $\frac{1}{2}$ of a lattice point.

One may write:

$$\mathbf{S} \cdot \mathbf{r_i} = (h\mathbf{a}^* + k\mathbf{b}^* + l\mathbf{c}^*) \cdot (x_i\mathbf{a} + y_i\mathbf{b} + z_i\mathbf{c}) = 2\pi(hx_i + ky_i + kz_i) \quad (3.16)$$

A consequence of the choice of a conventional unit cell, containing more lattice points than within a primitive unit cell, is that there exist systematic absences in the reflection conditions, that is the absence of any diffraction intensity at specific sets of reciprocal lattice points. For example, for a face-centred cubic lattice, there exists diffraction intensity only when (hkl) are all odd or all even.

The electron density of a 3D crystal, therefore, may be described as the convolution of the electron density of the basis, that is the electron density of the set of atoms associated with each lattice point, $\rho_M(\mathbf{r})$, with some function that describes a 3D lattice (Giacovazzo *et al.* 2002). The lattice may be represented by:

$$L(\mathbf{r}) = \sum_{u,v,w=-\infty}^{\infty} \delta(\mathbf{r} - \mathbf{R}) \quad (3.17)$$

where $\mathbf{R}$ is the direct lattice vector $\mathbf{R} = u\mathbf{a} + v\mathbf{b} + w\mathbf{c}$. The electron density of an infinite 3D crystal, ρ_C is therefore:

$$\rho_C = \rho_M(\mathbf{r}) * L(\mathbf{r}) \quad (3.18)$$

and so the amplitude of scattering from a crystal may be written:

$$f_C(\mathbf{S}) = T[\rho_M(\mathbf{r})] \cdot T[L(\mathbf{r})] = f_M(\mathbf{S})\frac{1}{V}\sum_{h,k,l=-\infty}^{\infty} \delta(\mathbf{S} - \mathbf{G}) \quad (3.19)$$

where $\mathbf{G}$ is the generic reciprocal lattice vector $\mathbf{G} = h\mathbf{a}^* + k\mathbf{b}^* + l\mathbf{c}^*$.

The structure factor may also be written in the polar form:

$$f_C(\mathbf{S}) = |f_C|e^{i\phi} \tag{3.20}$$

where $|f_C|$ is the amplitude of the structure factor, and ϕ is the phase. Therefore, to determine the electron density, and hence the structure, of a crystal, it is essential to have knowledge of both the amplitude and the phase. However, what is measured in diffraction experiments is the intensity, I, of the scattered X-rays, which is the square of the structure factor: $I = f_C(\mathbf{S})^2$. Measuring the diffracted intensity allows one to determine the relative magnitude of each (hkl) reflection, but does not give knowledge of the phase. Therefore, to construct the electron density and hence determine crystal structures, a model is constructed that accurately describes the observed diffraction intensity, and therefore allows a structural solution (Giacovazzo *et al.* 2002).

3.5 Synchrotron Sources

Synchrotrons are very brilliant sources of X-rays that are extremely useful in the field of high-pressure X-ray diffraction. Essentially, they operate by accelerating charged particles (electrons) to relativistic velocities in a circular path using a series of magnets. Particles travelling in a circular path at relativistic velocities emit radiation tangentially to the circular path they travel in.

This Thesis work was conducted at three different synchrotron sources: the European Synchrotron Radiation Facility (ESRF) in France; the Diamond Light Source (DLS) at Rutherford Appleton Laboratories, UK; and the Petra-III facility at the Deutsches Elektronen-Synchrotron, Germany. This Section describes the basics of synchrotron operation and expands in some detail on the beamlines used at each facility.

In its most simple terms, a synchrotron may be thought of as being composed of four essential components: a linear accelerator; a small pre-accelerator ring; a storage ring; and, finally, the beamlines where the experiments are conducted. A schematic of a synchrotron may be seen in Figure 3.13. The linear accelerator produces bunches of electrons, which are accelerated such that they have an energy of ∼200 MeV. These rapidly

Figure 3.13: An illustration of a typical third generation synchrotron light source showing the main constituent components – a linear accelerator, a booster ring, a storage ring, and beamlines

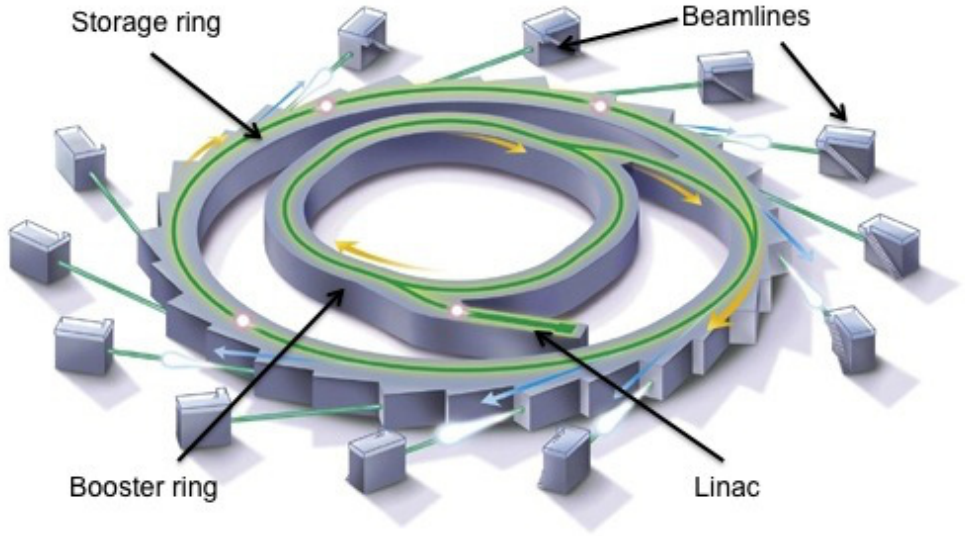

moving electron bunches are then injected into the so-called "booster" synchrotron, where they are accelerated further, to the desired operating energy of the facility. For the ESRF and Petra-III this is ∼6 GeV. For the DLS it is 3 GeV.

Following the "booster" synchrotron the electron bunches are sent to the storage ring, designed such that the kinetic energy of the electrons is kept constant. In their journey around the storage ring the electron bunches pass through a variety of magnets – bending magnets, wigglers, undulators – and emit X-ray radiation characteristic of the particular device. This X-ray radiation is directed towards beamlines, which house various optics, focussing the X-rays towards an end station where the experiment is conducted. Figure 3.14 illustrates a beamline setup, where experiments are conducted in transmission through diamond anvils.

Bending magnets cause the electrons to form a circular orbit. As the electrons are deflected from a straight path they emit a wide, continuous spectrum, of X-rays. To produce a more focussed and brilliant X-ray source, insertion devices such as wigglers or undulators may be used. A wiggler is a series of magnets that causes the electron to move in a periodic path lateral

Figure 3.14: An example of a beamline setup for diamond anvil cell experiments. This beamline is ID09a at the ESRF. The MB diamond anvil cell is in a membrane adaptor and is surrounded by an external resistive heater. The MAR555 flat panel detector is also pictured.

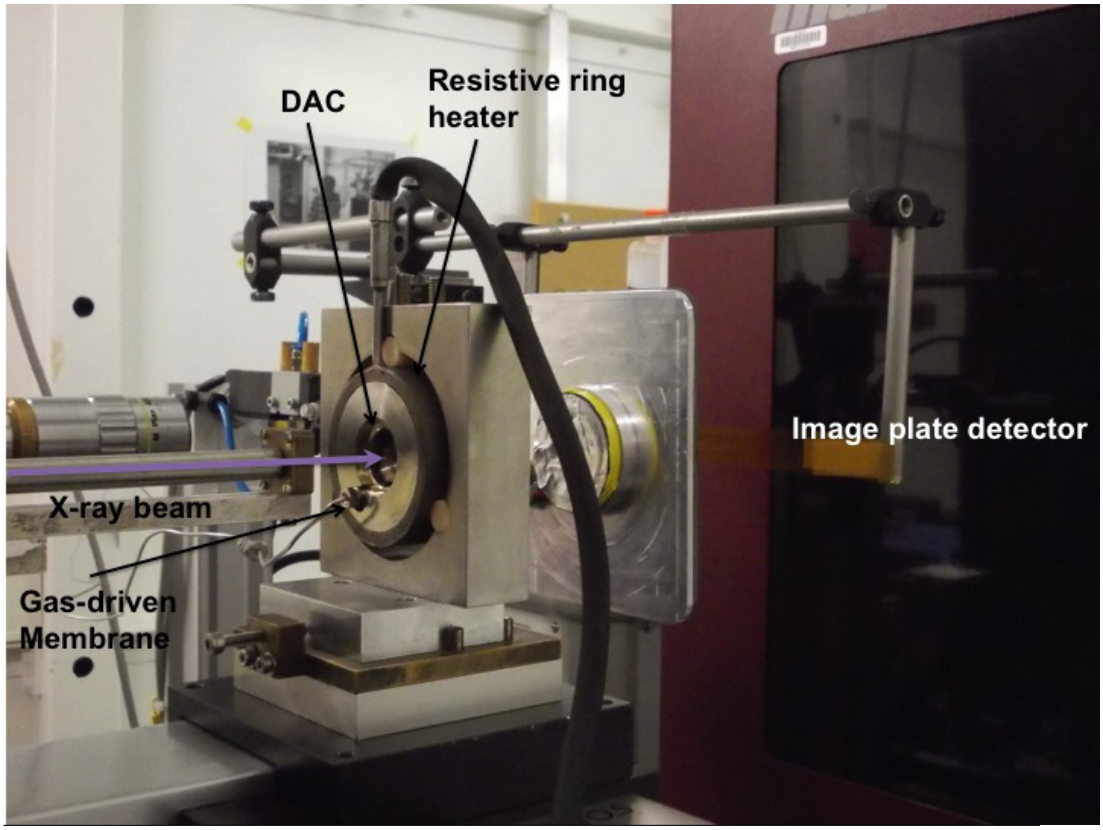

to its motion, a so-called "wiggle". Essentially the electron path through the wiggler may be thought of as a series of small circular arcs, and so at each arc X-ray radiation is emitted. The contribution of X-rays from a series of arcs caused by the magnets in a wiggler setup means that the spectrum of emission is considerably brighter than that of a bending magnet.

To obtain an even narrower and more intense X-ray energy spectrum, one has to appeal to undulator technology. An undulator operates in a similar manner to a wiggler, in that they are composed of periodic magnetic structures, which force the electrons to oscillate periodically about their direction of motion. What differs significantly between a wiggler and an undulator is the K-parameter, a dimensionless parameter that characterises

the deflection angle of the electrons. In an undulator, K≪1, meaning that the electrons do not undergo a large deviation perpendicular to their forward trajectory. At some point downstream of the magnets, the cones of emitted radiation from difference source points – different arcs – will interfere constructively resulting in narrow, intense energy bands. For a wiggler, K≫1, causing little overlap in the cones of emitted radiation, therefore every arc produces a cone of radiation which do not interfere with each other. Instead there is a superposition, and so the spectrum from a wiggler with K≫1 is more intense than a bending magnet, but the energy spectrum it produces is wide. Figure 3.15 illustrates the different X-ray energy spectra produced by bending magnets, wigglers and undulators.

Figure 3.15: An example of the different X-ray energy spectra produced by bending magnets, wigglers, and undulators.

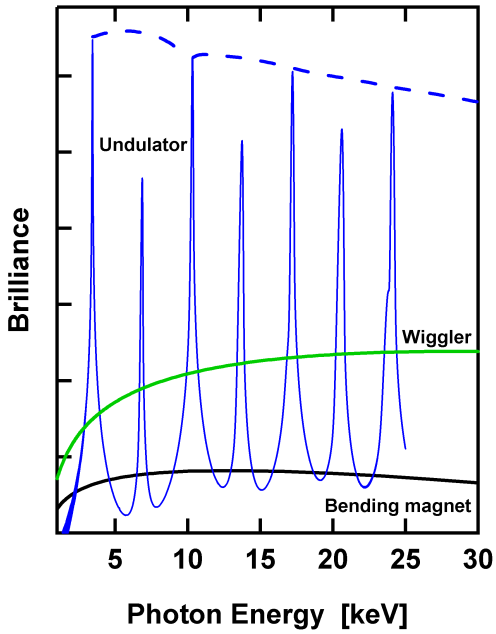

Having briefly covered the operation of a synchrotron the rest of this Section is devoted to the specifics of different beamlines at which this Thesis research was conducted.

3.5.1 ID09a, ESRF

Beamline ID09a at the ESRF is composed of an in-vacuum undulator, after which the produced radiation is focussed by a spherical mirror and a single silicon (*111*) monochromator. Due to the glancing angle of the silicon monochromator the incident beam energy of ID09a is fixed at ∼30 keV. Here, the beamsize is typically focussed to 30×30 μm^2 but it is possible to focus further to a minimum size of 10×10 μm^2 for megabar experiments. The detector used at ID09a throughout this Thesis work was the MAR555, a large flatpanel detector ideal for both powder and single crystal diffraction experiments. A major advantage of this detector is that X-rays are converted to signal directly, as opposed to, say, CCD detectors which count photons, and so there is no point-spreading, and hence no associated signal degradation. A further advantage is the extremely fast read-out time of the detector on the order of 1200 ms.

3.5.2 I15, Diamond Light Source

Unlike ID09a, I15 at the Diamond Light Source utilises a wiggler magnet, not an undulator. Furthermore, the synchrotron operates at a significantly lower energy – 3 GeV, as opposed to 6 GeV. Both these factors contribute to a lower X-ray flux. Following the wiggler magnet, the beam is made monochromatic by a double crystal monochromator, composed of two silicon (*111*) crystals. The glancing angles of these crystals may be tuned, and so an advantage of this beamline over ID09a is that X-ray beam energy is tunable between 20-80 keV. This is particularly useful if one wishes, say, to conduct liquid diffraction experiments where accessing as large a q-range as possible is advantageous – one way to achieve this is to use a higher X-ray energy. The beam is then focussed using Kirkpatrick-Baez (KB) mirrors, a pair of mirrors, one operating horizontally, the other vertically, which are curved to have a common focal point. Using this system it is possible to focus X-rays to spot sizes of a few microns at full-width at half-maximum, though there are usually large tails associated with the beam, whereby the beam profile extends outwards by 10s of microns.

There are two detectors that were used at this beamline in this Thesis

research: the MAR345 image plate detector, and the Perkin Elmer flatpanel detector. The MAR345 is a phosphor image plate equipped with a read-out laser. This detector has a readout time of ∼34 s. The Perkin Elmer flatpanel detector is an amorphous silicon detector, with a rapid read out capability able to output up to 15 frames per second.

3.5.3 ECB, Petra-III

The Extreme Conditions Beamline, or ECB, at Petra-III is the newest of the three beamlines, and was opened to users in late 2011. Like ID09a, the insertion device at this beamline is an undulator rather than a wiggler. Here the X-rays may be at one of three fixed energy positions: 25.7 keV, 42.9 keV, and 60 keV. Following the undulator, the remainder of the beamline set-up differs from that of ID09a. The X-ray beam is first made monochromatic at a silicon (*111*) and (*311*) double crystal monochromator, and then focussed using a compound refractive lens, and KB mirrors. The focussed X-ray spot size may be as small as 5 μm horizontally and 2 μm vertically at the beam full-width at half-maximum. The detectors used at this beamline were the MAR345 image plate and Perkin Elmer flatpanel detector mentioned above.

3.6 Data Analysis

The data contained in Chapters 4 and 5 were collected at the beamlines mentioned above, and treated using either single-crystal or powder diffraction analysis techniques. Single-crystal data analysis is specific to one Section of Chapter 5, and so is contained within that Chapter. This Section focuses on the powder diffraction integration and analysis techniques used throughout Chapters 4 and 5.

Azimuthal Integrations

Diffraction from polycrystalline or powder samples form Debye-Scherrer rings. The data analysis techniques utilised in powder diffraction experiments – such as Le Bail fitting or Rietveld refinement, require the azimuthal integration of this 2D data, producing a 1D output in 2θ, d-spacing, or

q-space, for example. The software used to perform these integrations was Fit2D (Hammersley *et al.* 1996).

The first step in performing such integrations is to accurately calibrate the detector positions, and to determine the experimental geometry, such as the beam centre i.e. the position of the straight-through X-ray beam; the detector tilt; and, the detector rotation angle. The x and y co-ordinates of the beam centre on the detector, the tilt, and the rotation angle, may all be refined by use of a standard calibrant, provided the pixel size, X-ray wavelength and sample-to-detector distance are known; the X-ray wavelength and sample-to-detector distance is often also freely refined. Silicon is often used as a calibrant. The lattice parameters, and hence d-spacings, are well known, and so by relating certain pixel positions to the silicon (*111*) peak, choosing at least five positions around the Debye-Scherrer ring, Fit2d can perform an interpolation relating every pixel on the detector to a d-spacing (Hammersley *et al.* 1996).

Now that the pixels have been converted to d-spacing, it is relatively simple to integrate the 2D data and produce 1D diffraction profiles. In all the data discussed in Chapters 4 and 5, unless explicitly stated otherwise, was integrated azimuthally and converted into units of 2θ. This data may be output in a convenient format, i.e. chiplot, and analysed using crystallographic refinement software. In this Thesis, analysis was performed using Jana2006 (Petricek *et al.* 2006).

Fit2D is an extremely diverse tool for image processing, and includes many features that were not used in this Thesis research. One feature that was particularly useful, however, was the masking tool, which was crucial in the analysis of liquid diffraction patterns (Chapter 4). Specifics of the analysis performed are contained in that Chapter, but the advantage of the Fit2D masking tool was that it allowed the masking, and hence removal from the azimuthal integration, of Bragg reflections arising from, for example, the diamond anvils. This allowed the creation of a background profile from the diamond anvil cell, which could then be subtracted from the liquid profile. This technique was described in detail by Sanloup *et al.* (Sanloup *et al.* 2008), and is explained in Chapter 4.

Refining the Data

Analysis of the data in Chapters 4 and 5, which was not expressly described as performed using single-crystal analysis techniques, was analysed using a least-squares method. As all the solid phases of potassium treated in Chapters 4 and 5 are already known, the spacegroup and approximate lattice parameters were established. The data were therefore treated using the Le Bail method, often referred to as a Le Bail decomposition. This was performed using the crystallographic analysis software Jana2006 (Petricek *et al.* 2006).

In the Le Bail method, individual integrated peak intensities and shapes are treated as free least squares parameters. The peak shapes are modelled as Gaussian, Lorentzian or Pseudo-Voigt profiles – Pseudo-Voigt peak profiles are a convolution of a Gaussian and a Lorentzian peak. Furthermore, the individual Bragg peak positions are obtained through refinement of the unit cell dimensions i.e. the lattice parameters a, b, and c, and the angles between them α, β, and γ. Finally, a polynomial profile describing the background to the diffraction profile is calculated, and this too is refined using a non-linear least squares method (Pecharsky & Zavalij 2009).

A point to note is that the Le Bail method provides key information concerning the lattice parameters and the peak shape, but does not take into account the atomic positions, site occupancies, atomic displacements, scale factors, or preferred orientation of the sample. To do this a Rietveld refinement is required. A Rietveld refinement requires good-quality powder data, continuous rings that would give reliable intensities for each integrated peak (Pecharsky & Zavalij 2009). In the data collected in Chapters 4 and 5, the powder diffraction data was quasi-single crystal like, and so it was not possible to perform Rietveld refinements. All diffraction profiles were therefore analysed using the Le Bail method.

Chapter 4

The Melting Curve of Potassium

4.1 Anomalous Melting in the Alkali Elements

The high-pressure phase transformation sequences and melting behaviour observed in the alkali elements have been described in detail in Chapter 2. To briefly summarise: the alkali elements are relatively simple elements at ambient conditions, well described by the nearly-free electron model. With increasing pressure, however, a remarkable departure from this simple behaviour has been observed. Complex, low-symmetry, open-packed structures have been observed in all, and anomalous melting has been reported in lithium (Li), sodium (Na), rubidium (Rb), and caesium (Cs) (McMahon & Nelmes 2006) (Gregoryanz *et al.* 2008) (Guillaume *et al.* 2011) (Boehler & Zha 1986). However, the melting behaviour of K appears to strongly disagree with this trend, with no maximum in the melting temperature observed, at least to 14.5 GPa and 650 K (Zha & Boehler 1985), a striking anomaly, particularly when considering how structurally similar K is to its neighbours.

This Chapter describes several experiments conducted to re-investigate the low pressure melting behaviour of K, and to extend measurements of the melting temperature to pressures in excess of 14.5 GPa. For ease of reading, the studies described here will be referred to as Study A, Study B, Study

C, and Study D. Study A was conducted prior to the commencement of this Thesis research, and prompted the subsequent thorough re-investigations of the melting curve, as detailed in Studies B and C. Study D, the final study in this Chapter, focussed on extending the melting curve to higher pressures and temperatures. The experimental details of studies A, B and C were similar, and will be detailed in Section 4.2 whereas the experimental details of Study D were slightly different and so will be confined to their own Section (Section 4.5.1).

4.2 Experimental Details of Studies A, B and C

High-purity samples of K (99.95 % Alfa Aesar) were loaded in Merrill-Bassett (MB) diamond anvil cells which had been adapted so as to be driven by a gas membrane. See Chapter 3 for further details on diamond anvil cells. The cells were equipped with diamonds with culets 300-400 μm in diameter. All samples were loaded without a pressure-transmitting medium to avoid contamination of the sample, and were loaded in a dry, oxygen-free environment to prevent oxidation. In Study A, rhenium (Re) was used as a gasket material. In subsequent studies either iridium lined Re gaskets or tungsten (W) gaskets were used as liquid-K was observed to react with Re. The gaskets were typically indented to an initial thickness of 20-25 μm prior to loading, and the sample chamber diameter was typically 80-125 μm, depending on the material used. The shift of the fluorescence line of samarium-doped strontium borate (SrB_4O_7:Sm^{2+}) was used for pressure calibration. The shift of the $^7D_0 - ^5F_0$ line has been shown to have a very small temperature dependence – several orders of magnitude less than that of the more commonly used ruby R_1 line, making it ideal for pressure calibration in high-pressure high-temperature studies (Datchi *et al.* 1997). See Chapter 3 for additional details.

In order to heat the sample to the desired temperatures, external resistive heating K-rings (Watlow Ltd.) were used, allowing sustained, stable, and homogeneous heating of the sample up to 650 K. A K-type (chromel-alumel) thermocouple, placed on the back of the diamond anvils, was used for

temperature measurements; the uncertainty in temperature was estimated to be not more than 10 K. At each experimental point, the temperature before and after the X-ray exposure was the same to within 2-3 K.

Melting of the sample was determined both by the complete disappearance of the Bragg reflections from the crystalline-solid phase, and by the appearance of a diffuse halo of scattering from the liquid phase. Typical 2D diffraction images from the liquid and solid phases are shown in Section 4.4. *In situ* high-pressure X-ray diffraction measurements were performed on beamline I15 at the Diamond Light Source (DLS), and on beamline ID09a at the European Synchrotron Radiation Facility (ESRF). The incident X-ray wavelengths were 0.4140 Å and 0.4143 Å, and the beam diameters were approximately 30 μm and 10 μm, respectively. On I15 the data were collected on a MAR345 image plate detector, and on ID09a the data were collected on a MAR555 flatpanel detector. In both cases, the detectors were placed approximately 350 mm from the sample. During each X-ray exposure, the sample was oscillated $\pm 7^{\circ}$ around a vertical axis in order to improve the powder-averaging of the diffraction patterns from polycrystalline samples, and to obtain a sufficient number of reflections to identify the crystal structure when the sample had annealed into a single-crystal, frequently observed to occur in the body-centred cubic (*bcc*) and face-centred cubic (*fcc*) phases upon heating.

The resulting two-dimensional (2D) X-ray diffraction images were integrated azimuthally using Fit2D (Hammersley *et al.* 1996), and subsequent analysis was performed using Jana2006 (Petricek *et al.* 2006). In all experimental runs, the K samples were initially pre-compressed to a desired pressure at room temperature and then heated until melting was observed. The pressure and/or temperature of the sample were then changed to bring it back into a crystalline phase (*bcc*, *fcc*, or *tI*19 depending on the pressure).

In several runs, once the melting point of K was first reached, the fluorescence signal from the SrB_4O_7:Sm^{2+} became very weak or disappeared entirely. Here, pressure was determined from the room-temperature K equation-of-state (EoS) (McMahon *et al.* 2006) and included a correction for the effects of thermal expansion, obtained from the high-pressure, high-temperature measurements of the crystalline phases when the pressure could

be directly determined from SrB_4O_7:Sm^{2+}. In these cases, the maximum correction that needed to be applied to the pressure determined from the room-temperature EoS was 0.5 GPa.

4.3 Initial Studies A & B

Prior to the commencement of this Thesis research, high-pressure, high-temperature data were taken on K (Diamond Light Source (EE741)). This initial study will hereafter be referred to as Study A. The aim of Study A was to grow a single-crystal of the metastable phase *hP*4 at P∼30 GPa (Marqués *et al.* 2009). Interestingly, rather than growing a single-crystal, it was observed that K melted at 33.0 GPa and 423 K. Unfortunately, upon melting, the highly-reactive liquid-K reacted readily with the Re gasket material, dissolving it, and resulting in the loss of the sample and failure of the diamond anvils, bringing the experiment to an abrupt end. Combining the observation that K melts at 33 GPa and 423 K with data from previous melting studies, in particular those conducted by Zha & Boehler (Zha & Boehler 1985), suggested the presence of a melting maximum. The melting curve as determined from a combination of data from Study A and data from Zha & Boehler (Zha & Boehler 1985) may be seen in Figure 4.1.

To further investigate this melting minimum, and to perform a comprehensive study of the melting behaviour of K up to 40 GPa, in October 2009 an additional *in situ* X-ray diffraction study was performed at the ESRF, ID09a – Study B. Numerous X-ray diffraction profiles were taken on increase and decrease of both pressure and temperature between 23 GPa and 40 GPa, and 295 K and 625 K, as indicated by the open and closed diamonds, respectively, in Figure 4.2. No indication of melting was observed in this region of P-T space, and the only phase observed was that of the incommensurate host-guest phase, denoted *tI*19. These observations are in clear disagreement with Study A.

Briefly, the *tI*19 phase may be thought of as being composed of two inter-penetrating 3D substructures, a host and a guest. The tetragonal host framework forms channels along the *c*-axis in which the guest atoms reside, and the host and guest incommensurate with each other along the

Figure 4.1: The suggested melting curve of K, constructed by combining data from a previous study by Zha & Boehler (Zha & Boehler 1985), and the high-pressure high-temperature melting point at 33 GPa and 423 K determined from Study A, denoted by the blue star. The dot-dash line indicates the melting curve as determined by Zha & Boehler, and the dotted line is a tentative extension of this melting curve.

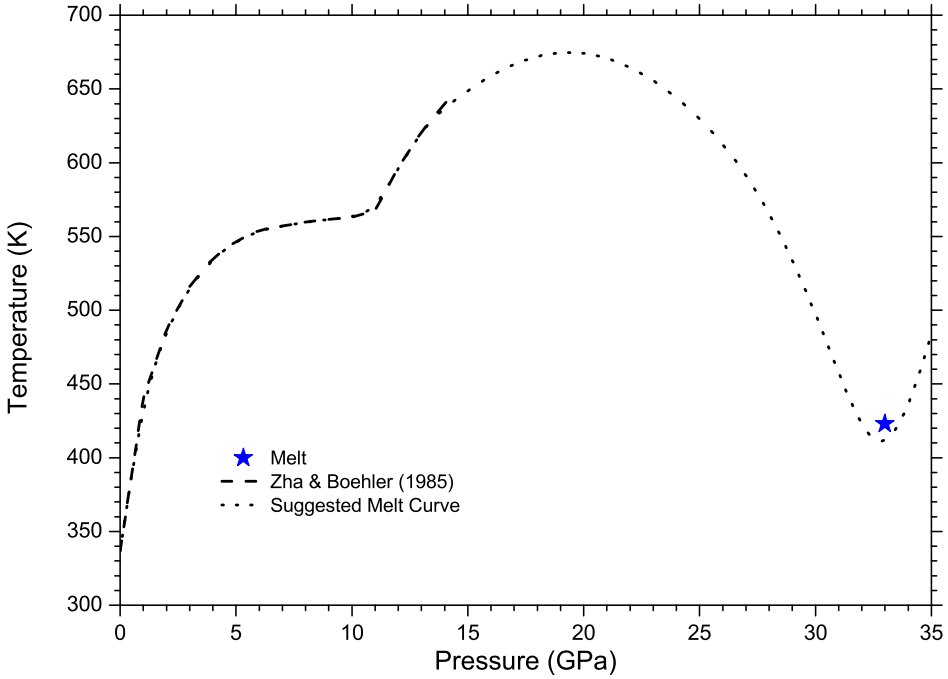

c-axis. Interestingly, in the *tI*19 phase, Bragg reflections belonging to the guest substructure were observed to reduce in intensity, and even disappear entirely, while the host substructure remained unchanged. This phenomenon will be discussed comprehensively in Chapter 5.

Following the unsuccessful melting above 25 GPa, it was decided to investigate the phase boundary between the *fcc*-solid and the *tI*19-solid at pressures below 25 GPa. The sample was initially compressed to 19.5 GPa, and diffraction patterns were taken upon changing pressure and temperature in small increments. Significantly, melting and re-crystallisation of K into the *tI*19-solid phase at pressures between 17 GPa and 21 GPa in the temperature

range 410 K to 475 K was observed. The blue circles represent the liquid phase in Figure 4.2, and the *tI*19 solid is represented by the orange diamonds. On pressure decrease, the sample, below 17 GPa, was observed to transform from the liquid phase into the *fcc*-solid phase. Study B, therefore, suggests the presence of a melting minimum at approximately 19 GPa and 400 K, 14 GPa lower than that observed in Study A (see Figure 4.1).

Figure 4.2: The melting curve of K as constructed from a combination of data from Study B and the previous experimental data from Zha & Boehler. Closed symbols indicate data taken on pressure increase and open symbols indicate data taken on pressure decrease. The orange diamonds denote the incommensurate host-guest solid phase *tI*19, the blue circles indicate the liquid phase, and the green squares indicate the face-centred cubic phase. The previous study by Zha & Boehler (Zha & Boehler 1985) is shown by the dot-dash line, and the extension to the melting curve determined by combining the data from Study B with that of Zha & Boehler is indicated by the dotted line.

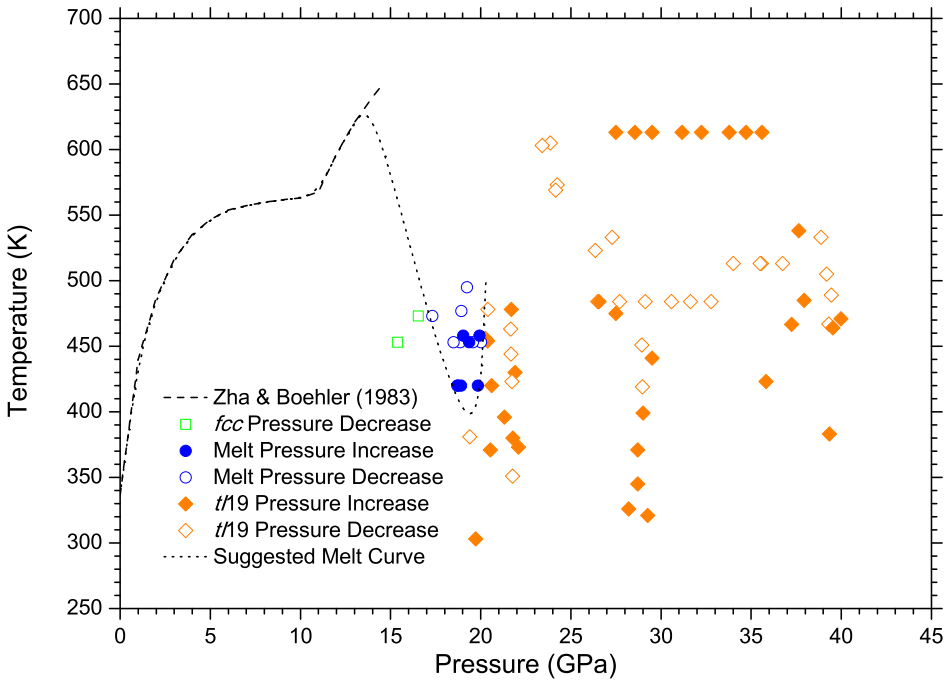

4.3.1 Reconciling Studies A & B

The suggested melting curves as determined in Study A (Figure 4.1) and in Study B (Figure 4.2) are very different – in Study A melting was observed a remarkable 14 GPa higher than in Study B, in a region of P-T space where in Study B only a solid crystalline phase was observed. To reconcile these two studies, careful re-analysis of the data from Study A was required.

Azimuthally integrated 1D X-ray diffraction profiles obtained during Study A may be seen in Figure 4.3. Figure 4.3 (a) is an X-ray diffraction profile at 33.0 GPa and 325 K, and Figure 4.3 (b) is an X-ray diffraction profile when the temperature was increased by 150 K, collected immediately prior to the observation of melting, and loss of the sample. The data were analysed by performing Le Bail fits to the profiles, and the tick marks below each peak in the diffraction profiles indicate where a calculated peak should occur. Both diffraction profiles indicate that K is in the incommensurate host-guest phase, and here the tick marks below the peaks correspond to the host structure only. Note that the high-pressure behaviour of *tI*19-K is complex, as the host and guest undergo a series of intra-phase transitions – the $*$ symbols in Figure 4.3 (a) indicate peaks which emerge due to such phase transitions. The complex intra-phase transitions observed in *tI*19-K are described in Chapter 5. For this study it is sufficient to note that the sample is in the incommensurate host-guest phase in Figures 4.3 (a) and (b).

It was presumed that pressure remained stable at 33.0 GPa throughout Study A. However, following inspection of the diffraction profiles in Figure 4.3, it is clear that pressure has dropped significantly between diffraction patterns (a) and (b) being collected, demonstrating the vital importance of *in situ* pressure measurement. In fact, upon closer inspection of Figure 4.3 (b), the broad bump associated with a liquid state may be seen to be emerging at $2\theta \sim 9°$, indicating that the sample will soon melt, or is in the process of melting during the X-ray exposure time – typically 10s of seconds at Diamond Light Source (DLS). Furthermore, the large reduction in the intensity of the crystalline Bragg peaks, particularly of the (*310*) reflection in Figure 4.3 (b), is a further indication that the sample would soon melt.

The Le Bail fits performed to the diffraction profiles in Figure 4.3 (a) and (b) give host-structure lattice parameters a=9.291 Å and c=4.414 Å,

and a=9.935 Å and c=4.854 Å, respectively. By comparing the volume of the unit cells obtained for each profile – 381 Å^3 and 479 Å^3 for Figure 4.3 (a) and (b) respectively – it is clear that a large volume increase occurs in the sample between the two patterns being taken, indicating that the sample was at significantly lower pressure when profile (b) was collected (just prior to melting). Comparing this data with that obtained during Study B, where pressure was measured *in situ* for every data point, it was determined that the pressure of the K sample in Figure 4.3 (b) was in fact 20.5 GPa. Consequently, all data taken above 17 GPa in Studies A and B are in good agreement.

Figure 4.2 illustrates the suggested melting curve from the combination of data from the now reconciled Studies A and B with data from previous melting studies conducted by Zha & Boehler (Zha & Boehler 1985). The data imply a remarkably sharp turnaround in the melting temperature. To further quantify the melting behaviour of K, to investigate the nature of this seemingly extremely sharp melting maximum, and to map out more precisely the observed minimum in the melting temperature at ∼19 GPa, a systematic study of the melting temperature was made between ambient pressure and 22 GPa – Study C.

4.4 Study C: The Melting Curve between Ambient pressure and 22 GPa

A total of ten samples were used to re-examine and extend the melting curve of K to 22 GPa, and consistent results were obtained in all. The experimental details in Study C are described in Section 4.2. Furthermore, as again detailed in Section 4.2, melting was determined both by the disappearance of crystalline Bragg reflections and by the appearance of a diffuse halo of scattering characterising the liquid phase. Figure 4.4 shows typical 2D diffraction images where the crystalline Bragg reflections from the *fcc* and *tI*19 solid phases may be clearly seen in images (a) and (c). Bragg reflections are absent in Figure 4.4 (b), where K is in the liquid phase.

Typical integrated 1D diffraction profiles may be seen in Figure 4.5. These profiles are the azimuthal 1D integrations of the 2D images shown in Figure

Figure 4.3: Azimuthally integrated 1D diffraction profiles obtained in Study A. Both integrated diffraction profiles indicate that K is in the incommensurate host-guest phase, and the diffraction profiles have been fitted using the Le Bail method. The tick marks below each profile indicate where predicted peaks of the host structure should occur. The $*$ in profile (a) indicate peaks which appear due to a change of symmetry in the host-guest structure. These phase transitions will be described in Chapter 5. Profile (b) is the diffraction pattern taken immediately prior to melting of the sample, and by eye one can clearly see that a large decrease in pressure has occurred between profile (a) and profile (b), as the peaks shift to lower 2θ.

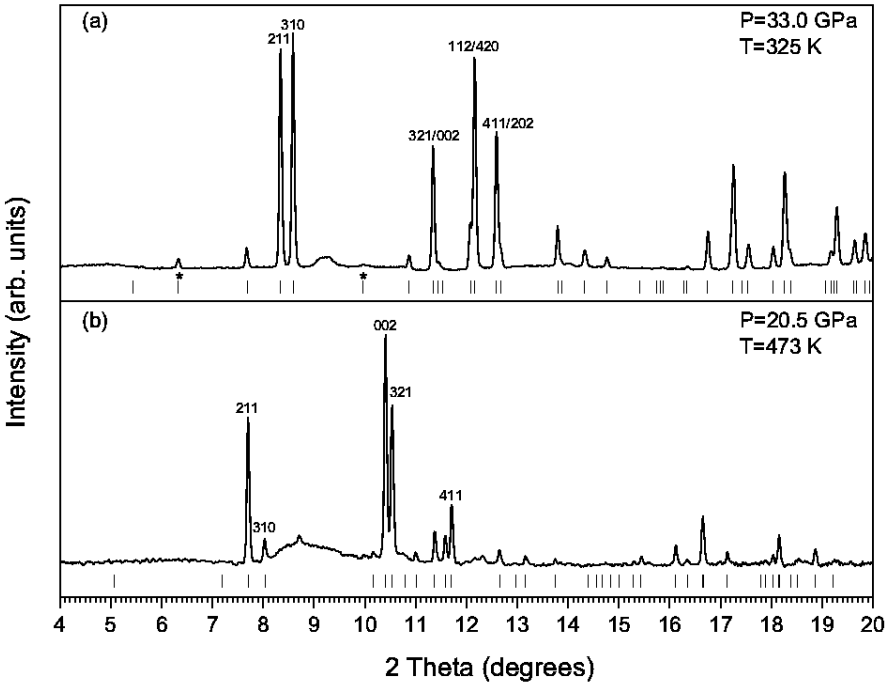

4.4. Here, a distinct difference between the scattering from the crystalline phases and the liquid phase may be clearly seen. The integrated peaks in Figure 4.5 (a) and (b) are sharp, well-defined Bragg peaks, as expected from scattering from a crystalline solid. Figure 4.5 (b) illustrates a typical 1D diffraction profile from the liquid, characterised by the broad first peak. Here, the cell background, including the thermal diffuse scattering from the diamond anvils, has been subtracted so one may clearly see the liquid.

Figure 4.4: Typical sections of 2D X-ray diffraction images: (a) *fcc*-solid at 18.3 GPa and 403 K, (b) liquid at 18.3 GPa and 408 K, and (c) *tI*19-solid at 22.3 GPa and 408 K. In image (a) the Bragg peaks belonging to the *fcc* solid are highlighted by the red squares and their accompanying (*hkl*) indices are listed. In image (b) the diffuse halo of scattering arising from the liquid phase is highlighted by the white arrow. Note that in this image there are no Bragg reflections present. Image (c) is the incommensurate host-guest phase. The scattering from the host and guest substructures are distinctly different. A line of diffuse scattering arising from the guest structure is highlighted by the red arrow. Scattering from the host structure form structured rings due to the large degree of preferred orientation of the sample. Several of the (*hkl*) indices belonging to the host structure are listed on the image.

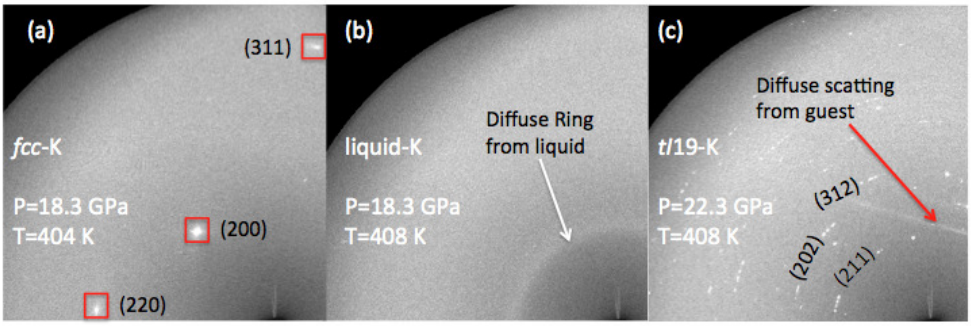

Due to the large background caused by the diamond anvil cell, analysis of the liquid diffraction data required careful treatment. For each liquid diffraction pattern, the background arising from the cell and the diamond anvils has been subtracted following the method devised by Sanloup *et al.* (Sanloup *et al.* 2008). X-ray diffraction patterns of the solid immediately prior to and following melting were taken. A baseline for the liquid pattern at each pressure was created by masking the crystalline-solid diffraction peaks from the sample and the diamond anvils immediately prior to melting. This results in a background from the cell at a temperature very close to the melting point. This baseline includes the Compton scattering and the thermal diffuse scattering from the diamond anvils. An example of a liquid profile without background subtraction may be seen in Figure 4.6 (a) and is represented by the red line; the background created from the masked solid is represented by the blue line. The subsequent liquid profile with background subtraction may be seen in Figure 4.6 (b). This liquid diffraction pattern

Figure 4.5: Typical integrated 1D X-ray diffraction profiles: (a) *fcc*-solid, (b) liquid, (c) *tI*19-solid. For the solid profiles the tick marks underneath indicate where a predicted peak for that structure should appear as determined by performing Le Bail fits to the data. Note the distinct peak absences in profile (a). This is due to the high temperature annealing of K in this phase. Profile (b) is an example of the liquid after careful background subtraction.

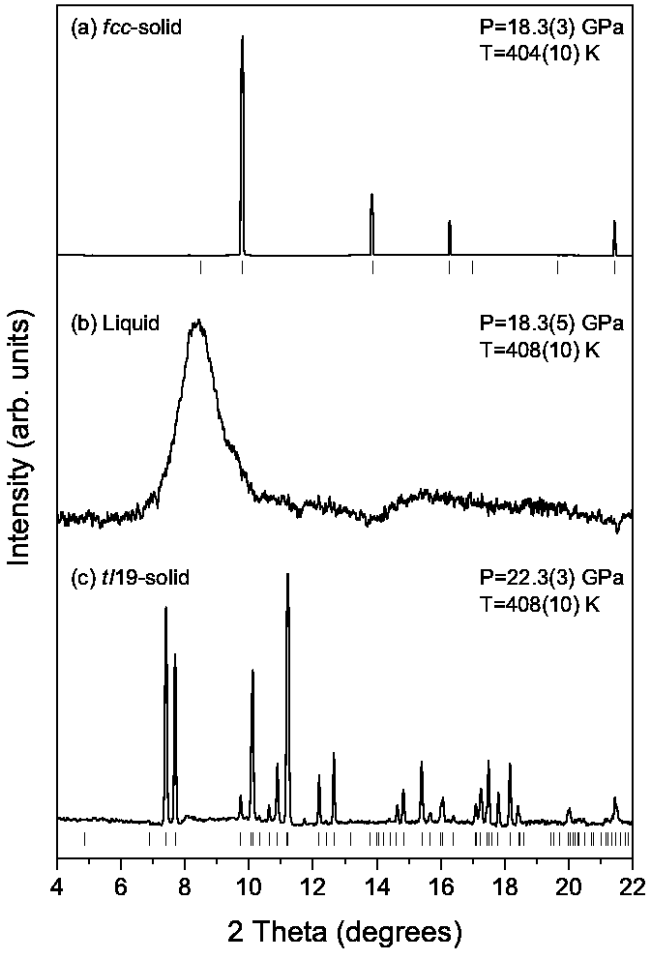

was taken at 12.8 GPa and 476 K.

Crystalline diffraction patterns were analysed using Jana2006 (Petricek *et al.* 2006). Due to a large degree of preferred orientation in the powder samples it was not possible to perform Rietveld refinements on the data.

Figure 4.6: An example of the background subtraction technique performed on all liquid diffraction patterns: (a) The red line indicates the raw integrated liquid diffraction pattern, and the blue line indicates the baseline as constructed from the masked solid just prior to melting. The profile shown in (b) is the resultant liquid pattern following background subtraction.

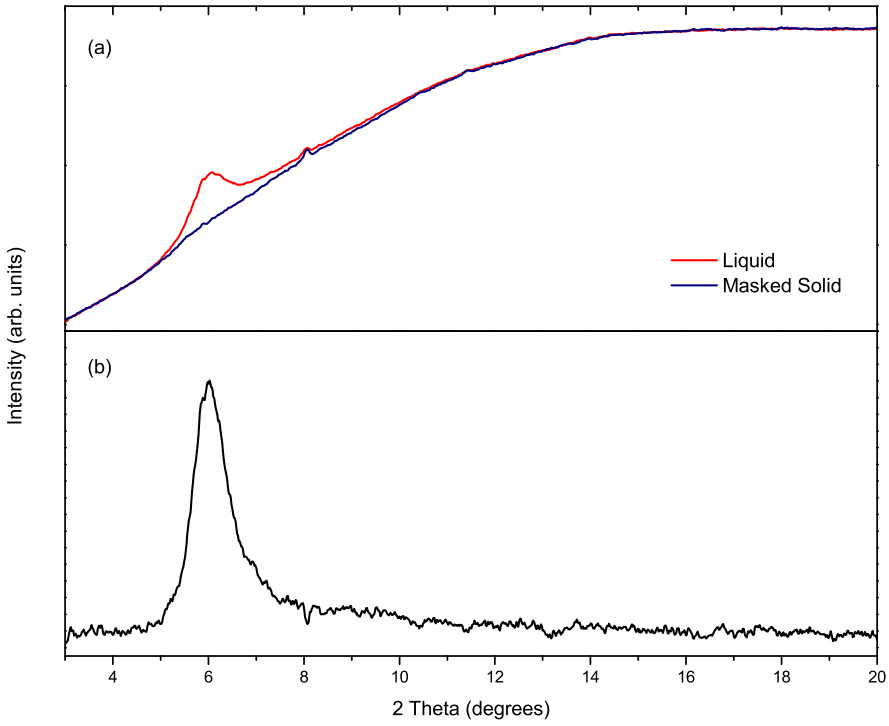

Therefore, data were analysed by performing Le Bail fits to the integrated profiles, and the tick marks underneath each crystalline diffraction pattern in Figure 4.5 indicate where the calculated peaks should be. There are clear peak-absences in Figure 4.5 (a); this is due to the *fcc*-solid annealing into a single-crystal upon heating, as may be clearly seen in the corresponding 2D diffraction image in Figure 4.4 (a).

Figures 4.4 and 4.5 illustrate that by holding pressure constant at 18.3 GPa and increasing temperature from 404 K to 408 K, the sample transforms from the *fcc*-solid phase (a), to the liquid (b). Furthermore, by holding temperature constant at 408 K and increasing pressure to 22.3 GPa, liquid-

K recrystallises into the *tI*19-solid phase. Note that in Figure 4.5 (c) the Bragg reflections associated with the guest structure, typically most obvious between 2θ ∼8-10° at these wavelengths, are broad or do not appear. This disappearance of the guest is a temperature-dependent phenomenon, previously observed in the alkali elements in Rb (McMahon & Nelmes 2004). Chapter 5 describes a comprehensive study of this phenomenon in *tI*19-K.

Diffraction data were taken upon small increases of pressure and/or temperature, and the melting curve, as determined using *in situ* X-ray diffraction, may be seen in Figure 4.7. When the underlying solid was determined to be *bcc*-K, indicated by the red triangles in Figure 4.7, the melting curve was traversed five times: at 0 GPa and 338 K, 2.3 GPa and 498 K, 4.5 GPa and 536 K, 7.4 GPa and 526 K, and 11.5 GPa and 498 K. These data suggest the presence of a melting maximum in the stability field of the *bcc* solid. By further increasing pressure, the melting temperature was determined to decrease down to the *bcc*-*fcc*-liquid triple point, determined to be at 13.6 GPa and 462 K.

To locate the maximum in the melting temperature in the *bcc* phase, the data up to the *bcc*-*fcc*-liquid triple point were combined with those of previous studies (Zha & Boehler 1985) and (Luedemann & Kennedy 1968) up to 3 GPa (the open symbols in Figure 4.7), where the trends in the melting temperature were determined to be in good agreement with Study C. A fit to these data was performed using the Kechin equation, a phenomenological equation which has been demonstrated to capture the melting behaviour of several systems, such as Rb, Cs and Te (tellurium)(Kechin 2001).

The Kechin fit to these data yielded parameters a=0.57(4) GPa, b=0.310(13), and c=0.049(2) GPa^{-1}, and hence determined the melting maximum to be at 5.6 GPa and 534 K, in good agreement with theoretical calculations by Young & Ross (Young & Ross 1984) – see Figure 4.8 for a comparison of the melting data from Study C with previous experiments and theoretical models.

Beyond the *bcc*-*fcc*-liquid triple point the melting temperature plateaus over several GPa, before once more adopting a negative gradient at 15.6 GPa, decreasing to a melting minimum at 19 GPa and 390 K at the *fcc*-*tI*19-liquid triple point. This minimum is very sharp, existing over a very narrow

Figure 4.7: The melting curve of K as determined using *in-situ* X-ray diffraction. Red triangles denote the *bcc*-solid phase, green squares denote the *fcc*-solid phase and purple diamonds denoted the *tI*19-solid phase. The melt is represented by the blue circles. Open circles are data from references (Zha & Boehler 1985) and (Luedemann & Kennedy 1968), with which data from Study C are in good agreement. The solid black curve below the *bcc*-*fcc*-liquid triple point at 13.6 GPa is a fit to the data from Study C and the open circles using the Kechin equation (Kechin 2001). The solid black line above the triple point is drawn as a guide to the eye. Phase boundaries between the solid phases are drawn using dashed lines, and the yellow stars are the room temperature phase transition pressures as taken from McMahon *et al.*(McMahon *et al.* 2006)

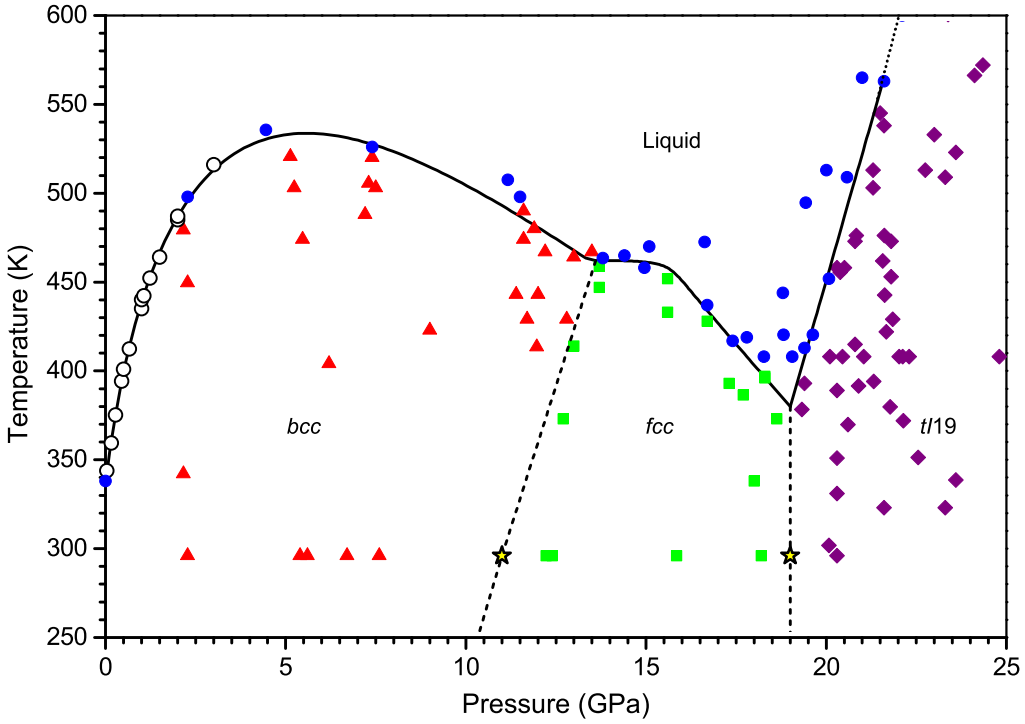

pressure region, in contrast to that observed, for example, in Na (Gregoryanz *et al.* 2005). Following the melting minimum, the melting temperature with increasing pressure regains a positive gradient, and increases steeply at a rate of 65 K/GPa. Moreover, the combination of the high-pressure high-temperature data from Study C with data from previous room temperature studies by McMahon *et al.* (McMahon *et al.* 2006) allowed the determination

Figure 4.8: Comparisons of theoretical and experimental melting curves of K. The solid black line is the melting curve of K as determined in Study C. The red dashed line is from the experimental study by Zha & Boehler (Zha & Boehler 1985), and the blue dashed line from an experimental study by Luedemann & Kennedy (Luedemann & Kennedy 1968). The calculated melting curve by Young & Ross (Young & Ross 1984) is shown with the purple dot-dashed line, and the green dotted line is the theoretical melting curve as calculated by Katsnelson *et al.* (Katsnelson *et al.* 2000)

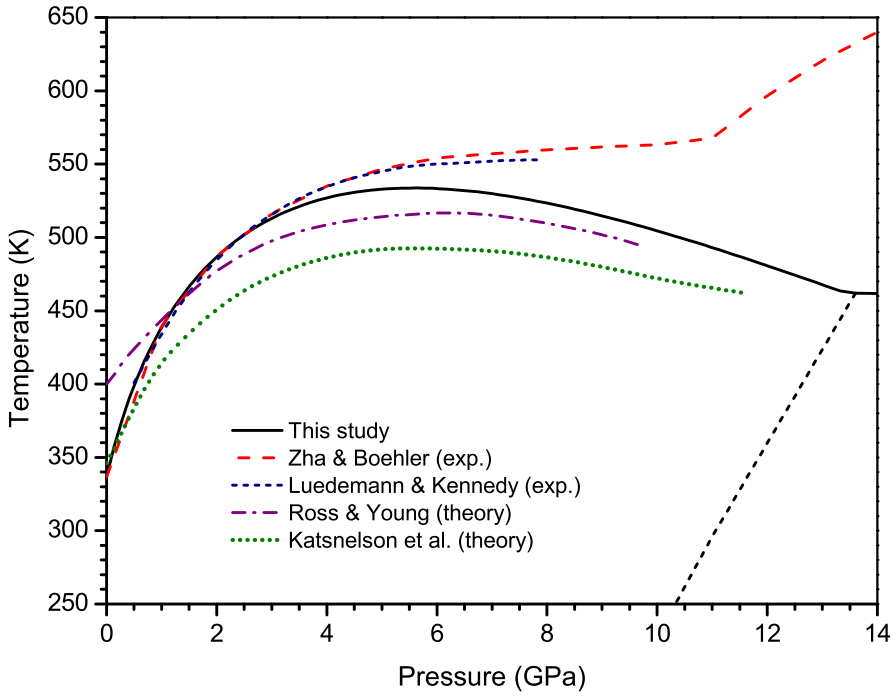

of the phase boundaries between the *bcc* and *fcc* phases, and the *fcc* and *tI*19 phases. The gradient of the *bcc-fcc* phase boundary was calculated to be ∼65 K/GPa, and the *fcc-tI*19 phase boundary was determined to be essentially vertical.

4.5 Study D: Extension of the Melting Curve Beyond 22 GPa

The final study on the melting curve of K aimed to extend the high-pressure high-temperature studies of K to pressures in excess of 50 GPa and temperatures of ∼800 K. The experimental details of this study are broadly similar to Studies A, B and C (Section 4.2), but with slight differences which will be described below. A major difference in the experimental method used in this Study was the use of a Livermore diamond anvil cell, equipped with smaller diamonds. The design of this cell is such that it is considerably more stable than a MB-type cell when heated, and is therefore capable of achieving higher pressure and temperature states. In addition to use of a different type cell, a vacuum vessel was used to contain the heated cell to prevent the diamonds burning when heating to extreme temperatures i.e. temperatures in excess of 650 K. See Chapter 3 for further details on this cell.

4.5.1 Experimental Details

High-purity samples of K were loaded under argon, as described in Section 4.2, into membrane-driven Livermore-type diamond anvil cells equipped with 200 μm culets. W gaskets were used and were typically indented to an initial thickness of 18-20 μm prior to loading. The sample chamber diameter was typically 80 μm. A small piece of Ta foil or a few grains of Ta powder were used to calibrate pressure, and the EoS used, including a high temperature correction, is discussed in Chapter 3. Heating was achieved by using 675 W coiled cable heaters (Watlow Ltd.) which surround the cell, and the entire apparatus was placed in a small vacuum vessel. Temperature was determined using a K-type thermocouple attached to one of the diamond anvils, internal to the cell body.

Once more, melting was determined both by the complete disappearance of the Bragg reflections from the crystalline-solid phase, and by the appearance of a diffuse halo of scattering from the liquid phase. *In situ* high-pressure X-ray diffraction measurements were performed on beamline I15 at the Diamond Light Source (DLS), with an X-ray wavelength of 0.311 Å and

a beam diameter of approximately 40 μm. Data were collected on a MAR345 image plate detector placed approximately 400 mm from the sample. During each X-ray exposure, the sample was oscillated $\pm 3^{\circ}$ around a vertical axis – the oscillation angle in this study was limited by the opening angle of the vacuum vessel, and its freedom of movement on the beamline. Analysis of the collected diffraction data was performed in an identical manner to that described for Studies A, B and C.

4.5.2 The Extended Melting Curve

The extended melting curve of K using *in situ* X-ray diffraction combined with in-vacuum heating and membrane-driven diamond anvil cells may be seen in Figure 4.9. In addition to data extending the melting curve to higher pressures, data were taken to more carefully map out the plateau in the melting temperature at the *fcc*-liquid phase transition above 13.6 GPa. Furthermore, included on Figure 4.9 are previous data acquired in Studies A, B and C. Before briefly expanding on the extension of the melting temperature above 22 GPa, one should note the slight change in the line drawn as a guide to the eye below the melting minimum.

Study C details that following the *bcc*-*fcc*-liquid triple point at 13.6 GPa and 462 K the melting temperature plateaus, before reducing further at 15.6 GPa down to the melting minimum. In this most recent Study, following the acquisition of additional melting data in this region of P-T space, instead of determining that the melting temperature plateaus over 2 GPa, it appears that a better fit to the data would require the gradient of the melting temperature to be negative, decreasing slightly to 15.6 GPa and 452 K, before becoming more negative at pressures above 15.6 GPa, decreasing down to the minimum at the *fcc*-*tI*19-liquid triple point at 19 GPa and 390 K.

The melting curve of has been extended to 24 GPa and 750 K, and the gradient of the melting temperature increases linearly from the *fcc*-*tI*19-liquid triple point at a rate of 65 K/GPa. There appears to be no evidence of the melting temperature becoming more gradual, and there is no evidence of melting at 750 K at pressures between 24 and 47 GPa. It is important to note here that at elevated temperatures, T>700 K, K was observed to react over a period of a few hours, suggesting that if one wished to extend the

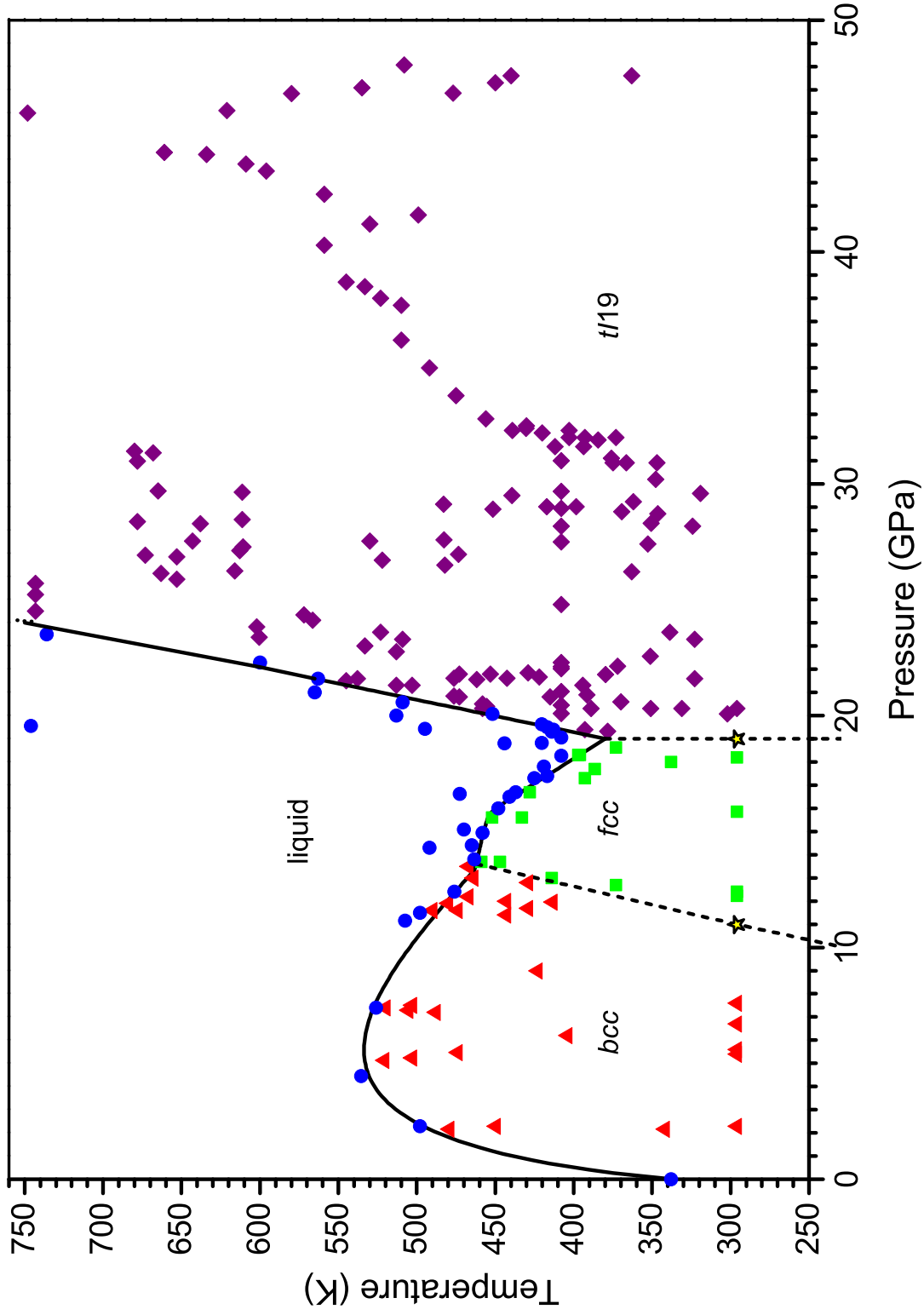

Figure 4.9: The melting curve of K displaying all data from Studies A-D. The red triangles represent the *bcc*-solid phase, the green squares represent the *fcc*-solid phase, and the purple diamonds represent the *tI*19-solid phase. The blue circles represent the liquid phase. The solid black curve below the *bcc*-*fcc*-liquid triple point at 13.6 GPa is a fit to these data using the Kechin equation (Kechin 2001), as described in Section 4.4. The solid black line above the triple point is drawn as a guide to the eye. There is a slight reduction in the gradient of the melting temperature following the *bcc*-*fcc*-liquid triple point, reducing to 15.6 GPa and 452 K, before decreasing further to the minimum at 19 GPa and 390 K. Following the melting minimum, the melting temperature regains a positive slope, increasing at ∼65 K/GPa, up to 24 GPa and 750 K. Phase boundaries between the solid phases are drawn using dashed lines, and the yellow stars are the room temperature phase transition pressures as taken from McMahon *et al.* (McMahon *et al.* 2006)

melting curve further time-resolved techniques may be required.

4.6 Disagreement with Literature Studies

The melting curve of K, as determined using *in situ* X-ray diffraction, is different from that previously reported by Zha & Boehler (Zha & Boehler 1985). See Figure 4.8 for a comparison of the melting curve as determined by Studies A-D to 14 GPa with previous experimental studies (Zha & Boehler 1985), (Luedemann & Kennedy 1968) and theoretical works (Young & Ross 1984), (Katsnelson *et al.* 2000). The significant differences between the melting temperatures as determined by Studies A-D, and those determined by Zha & Boehler could be due to a variety of factors. The most likely cause of disagreement in the data sets is due to the method used to determine the onset of melting.

In the studies conducted for this Thesis research, melting was observed directly, and determined by the disappearance of crystalline-solid diffraction peaks and by the simultaneous appearance of the broad amorphous signature of the liquid phase. Zha & Boehler inferred melting through visual observation of the sample, through studying changes in sample shape; surface texture; and reflectivity in transmitted and reflected light (Zha & Boehler 1985). Furthermore, they used the ruby pressure scale to determine pressure, which broadens significantly upon heating making it difficult to obtain accurate pressure measurements (Datchi *et al.* 1997). To avoid this issue, in Studies A-D, (SrB_4O_7:Sm^{2+}) or small pieces of Ta powder or foil were used as a pressure maker. Finally, Zha & Boehler loaded their samples in mineral oil to ensure hydrostaticity, yet provide no evidence that K does not react with the mineral oil – sample contamination could have led to a misinterpretation of their data (Zha & Boehler 1985).

In Studies A-D, no pressure-transmitting medium was used to limit the possibility of a reaction taking place in the sample. However, it should be mentioned that in diamond anvil cell experiments hydrostaticity is an important consideration, and that deviations from hydrostatic pressure may give results which are difficult to interpret. Therefore, the choice *not* to use a pressure-transmitting medium must be carefully considered. The pressures

Figure 4.10: Representative gamma plots for K data under pressure indicating hydrostatic behaviour. Plot (a) is at 17.5 GPa and room temperature; plot (b) is at 17.5 GPa and 375 K. The slight deviatoric stress present at 17.5 GPa and room temperature (a) is clearly alleviated at 375 K (b), where, within error, the data points lie on a straight line.

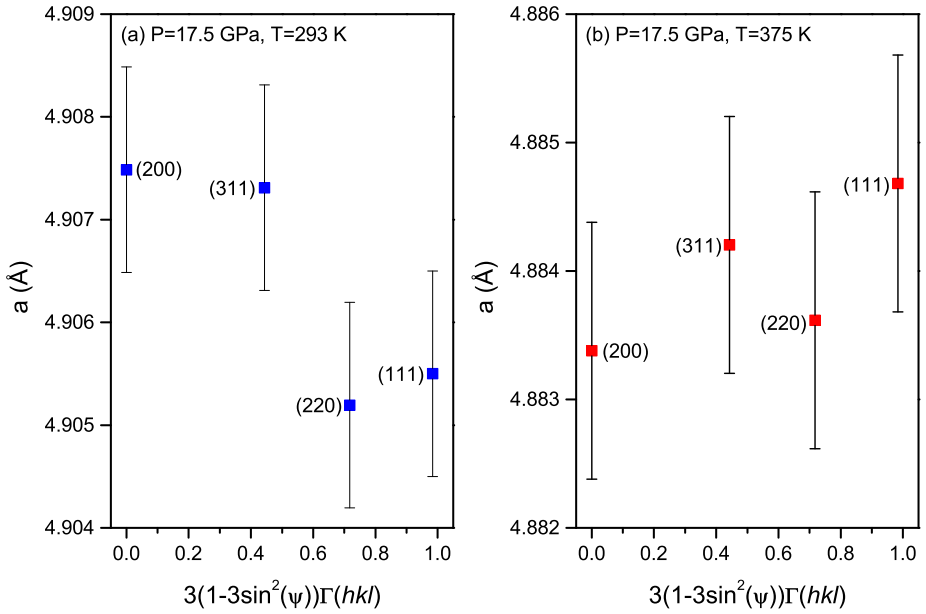

at which K was determined to melt in Studies A-D are relatively modest, and one must also consider that K is highly compressible, and so it is reasonable to expect that the absence of a pressure-transmitting medium would cause little deviation from hydrostatic behaviour. For a more quantitative analysis of hydrostaticity, following analysis devised by Singh & Kenichi (Singh & Kenichi 2001), gamma plots were constructed for different pressure and temperature states. In these plots, deviation from a straight line indicates a deviation from hydrostatic pressure. Examples of such plots may be seen in Figure 4.10. Figure 4.10 (a) illustrates that at 17.5 GPa and room temperature, K exhibits a slight deviation from hydrostatic behaviour, which is alleviated when the sample is heated to 375 K, some 50 K below the melting temperature at this pressure, as shown by Figure 4.10 (b).

4.7 Similarities with Na and the other Alkali Elements

The melting curve of K is remarkably different to that reported previously, and, moreover, the re-examined melting curve fits in with the general trend of anomalous melting observed in the other alkali elements. The presence of a maximum in the melting temperature, which does not coincide with structural changes occurring in the underlying solid, is often described as anomalous melting.

According to Clausius-Clapyeron, the negative gradient in the melting temperature indicates that the liquid phase is more dense than the underlying solid. The turnover in the gradient of the melting temperature occurs in the stability field of the *bcc* phase, and one interpretation to explain this phenomenon is that a phase transition occurs in the liquid phase, similar to that taking place in the underlying solid. The coincidence with the melting minimum and a transformation from a close-packed *fcc* structure to a low-symmetry open-packed structure is not unique to K. The melting minima in Li, Na, Rb and Cs also involve a transformation from an *fcc* structure to low symmetry structures (Guillaume *et al.* 2011) (Gregoryanz *et al.* 2005) (Boehler & Zha 1986) (McMahon & Nelmes 2006).

Not only does the melting curve of K fit with the trend observed in the other alkali elements, it is also strikingly similar to that of Na in particular, as illustrated in Figure 4.11 (Gregoryanz *et al.* 2005). The melting behaviour of K, however, occurs at significantly lower, and hence more experimentally accessible, pressures and temperatures. The melting temperature of Na reaches a maximum at 30 GPa and 1,000 K, again in the stability field of the *bcc*-solid phase, before becoming negative over a large pressure region. Over a pressure range spanning 70 GPa, the melting temperature of Na decreases significantly, melting just above room temperature at a megabar. Here, the melting temperature regains a positive slope, increasing steeply; not that the underlying solid here is *tI*19, as it is in K. As a brief aside, the experimentally determined melting curve of Na contains no melting data in the region between 60-80 GPa, and one could imagine a slight negative gradient in the melting temperature in this region rather than a plateau.

Figure 4.11: Comparison of the melting curves of K and Na. The melting curves exhibit remarkably similar trends, but with the melting curve of K occurring at significantly lower pressures and temperatures pressure. The melting curve of Na is adapted from references (Gregoryanz *et al.* 2005) and (Marqués *et al.* 2011b)

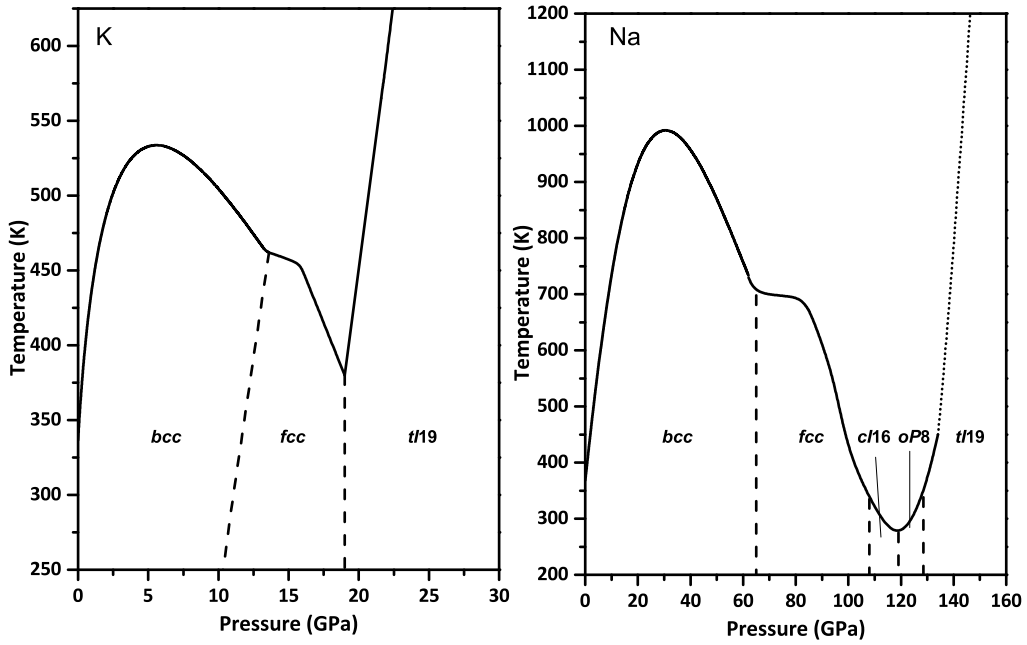

In an attempt to understand the unusual melting behaviour observed in Na, Martinez-Canales & Bergara performed *ab initio* calculations on the elastic moduli, and demonstrated the existence of a maximum in, and subsequent decay of, the shear modulus (Martinez-Canales & Bergara 2008). Associated with this is a maximum in the Debye temperature, θ_D, at pressures above 43 GPa. Interpreting this through the Lindemann criterion, $T_m = Cv^{2/3}\theta_D^2$, suggests the presence of a melting maximum. Importantly, this interpretation does not require a change in liquid structure or co-ordination. It should be noted, however, that although this view reconstructs the general trend observed in the melting behaviour, it dramatically underestimates the melting temperature.

Theoretical calculations on the shear moduli of K were performed by

Katsnelson *et al.* (Katsnelson *et al.* 2000), and a softening of the shear moduli was revealed. The calculated melting curve from this study may be seen in Figure 4.8, where once more the melting temperature is underestimated. Importantly, Katsnelson *et al.* predicted the existence of a maximum in the melting temperature at 5 GPa, in good agreement with Studies C and D, as shown in Figure 4.8.

Alternatively, Hernández & Íñiguez (Hernández & Íñiguez 2007), performed molecular dynamics simulations on Na at pressure and temperature conditions close to the experimentally determined melting maximum. Their work suggests that there is a change of compressibility of the liquid with respect to the underlying solid, and, in fact, that the liquid becomes more dense than the underlying solid, resulting in a maximum in the melting temperature and regions where the melting temperature has a negative gradient.

Furthermore, Raty *et al.* (Raty *et al.* 2007) suggest a mechanism to explain the melting behaviour beyond the *bcc*-like to *fcc*-like liquid transition proposed by Hernández & Íñiguez (Hernández & Íñiguez 2007). At 65 GPa, corresponding to where the melting temperature plateaus before further decreasing down to the melting minimum, Raty *et al.* predict that liquid-Na undergoes a change in co-ordination from an *fcc*-like liquid to one with a lower co-ordination, to a *cI*16-like liquid (Raty *et al.* 2007). Moreover, alongside these structural transitions occur electronic transitions, which above 60 GPa are manifested in a three-fold drop in conductivity. Similar electronic transitions have been observed occur in solid-Na but, once more, at higher pressures (Ma *et al.* 2009) (Marqués *et al.* 2011b).

Given the marked similarities in the melting behaviour of Na and K, it is suggested that the same mechanism responsible for the melting of Na is responsible for the melting of K. Between 13.6 GPa and 15.6 GPa (or indeed between 13.6 GPa and 19 GPa), finite temperature fluctuations in the liquid may cause it to undergo a gradual *fcc*-like to *tI*19-like liquid transition. The *fcc*-*tI*19 solid-solid transition has an associated volume collapse of 4 %, and so if a similar change occurs in the liquid, a significant density increase of the liquid may be expected. However, since this transition is not expected to be first order, the density increase is not expected to be sharp. Beyond

19 GPa, the melting curve regains a positive slope, which may be associated with the solid once more acquiring the same co-ordination as the liquid.

Figure 4.12: As an indication of the compressibility of the liquid phase, the d-spacings of the first liquid peak, the blue closed circles, are plotted alongside the d-spacing of the (110) *bcc*-solid peak, the red triangles, and the d-spacing of the *fcc*-solid peak, the green squares. The dashed red and green lines are polynomial fits to the *bcc*-solid and *fcc*-solid data, and the black dashed line is drawn as a guide to the eye. Between ∼2 and 5 GPa, close to the maximum in the melting temperature, there is a shift in the liquid peak away from a *bcc*-like position towards an *fcc*-like position. At higher pressure, at ∼15 GPa, there is a shift away from an *fcc*-like position. This corresponds to a change in gradient in the melt curve.

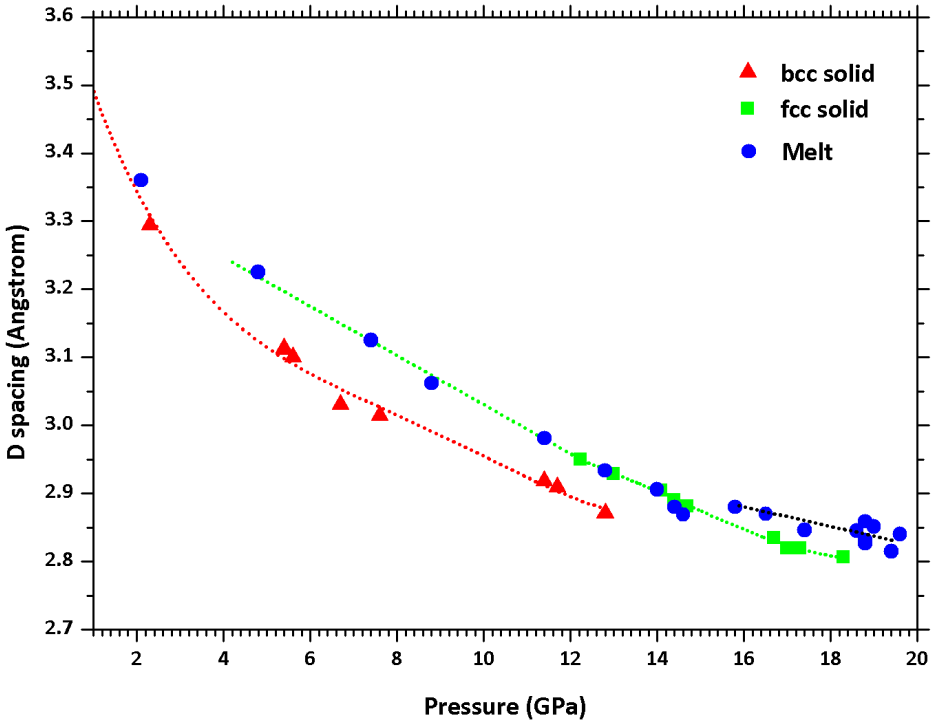

An indication of the compressibility of the liquid phase may be obtained by plotting the pressure dependence of the first liquid peak position. This may be seen in Figure 4.12, where the d-spacing of the liquid peak with increasing pressure is represented by the blue closed circles. The d-spacings

of the (*110*) *bcc* peak and the (*111*) *fcc* peak just prior to melting are also plotted, and the dashed lines polynomial fits drawn as a guide to the eye. Clearly, from Figure 4.12, at very low pressures the liquid peak appears to have a *bcc*-like position, yet at higher pressure it shifts to an *fcc*-like position. What is of particular interest is the shift from a *bcc*-like position to an *fcc*-like position of the first liquid peak at a pressure where the underlying solid is in the stability field of the *bcc* phase. Indeed, the shift in the first liquid peak towards an *fcc*-like position occurs close to the maximum observed in the melting temperature – the melting maximum was determined to be at 5.6 GPa and 534 K, and the shift in the liquid peak occurs between 2.2 GPa and 4.8 GPa. This observation is indicative, but not demonstrative, of a change in the liquid structure, similar to the phase change occurring in the underlying solid, but at lower pressure.

Solid-K, like solid-Na, exhibits electronic changes with increasing pressure, as demonstrated by the optical reflectivity studies conducted by Takemura & Syassan (Takemura & Syassen 1983), and is further illustrated by the photomicrographs shown in Figure 4.13, whereby K becomes less reflecting in visible light with increasing pressure. Figure 4.13 is an image of a sample of K in a diamond anvil cell in the *bcc* and the *fcc* phases. It is clear that the *fcc* phase is significantly less reflecting than the *bcc* phase. It should be noted, however, that should electronic transitions occur in liquid-K, they would be significantly less dramatic than those expected in liquid-Na – the *tI*19 phase of Na is a black semi-conductor (Ma *et al.* 2009), whereas *tI*19-K is still metallic, though less reflecting than the *bcc* and *fcc* phases (Takemura & Syassen 1983).

If one wished to observe electronic transitions in liquid-K, one could imagine performing resistivity measurements in the liquid phase. Careful attention would need to be paid to materials used for the resistivity probes, however, as K is highly reactive – for instance a typical resistivity probe material is Au, which K reacts with readily. Detailed reflectivity measurements on liquid-K over a broad spectrum, from the infra-red to the visible, would also be challenging, but should provide insight into whether electronic transitions occur in the liquid. A comparative study would be required of the underlying solid, and indeed one could compare the data to the

Figure 4.13: Photomicrographs of K under pressure at room temperature. Image (a) is K at 6.2 GPa and is highly reflective. Increasing pressure at room temperature, K transforms to the *fcc*-solid phase at 11.5 GPa and is visually characterised by a change in reflectivity of the sample.

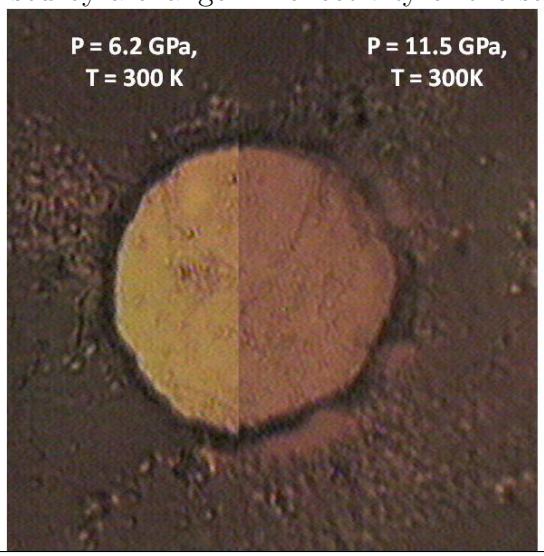

room temperature study of Takemura & Syassan (Takemura & Syassen 1983).

4.8 Revised Melting Curve of Potassium

The melting curve of K has been determined using diamond anvil cells combined with external resistive heating and *in situ* X-ray diffraction. It has been shown to be remarkably different to that reported previously, and strikingly similar to that of Na. Furthermore, the melting curve of K has been determined to be in keeping with the general trend observed in all the alkali elements.

In many of the high-temperature experiments conducted throughout Studies A-D an interesting phenomenon was noticed to occur in the *tI*19 phase – the composite incommensurate host-guest phase. Bragg reflections which were determined to arise from scattering from the guest substructure only became increasingly weak and diffuse with increasing temperature before disappearing entirely, while the Bragg scattering from the host structure remained unchanged. This observation is indicative of a loss of long-range

order in the guest structure. The discovery that a minimum in the melting temperature occurs close to the *tI*19-K phase boundary allowed the growth of a small single-crystal of this phase. Chapter 5 concerns single-crystal, quasi-single crystal, and powder diffraction studies of this phenomenon.

Chapter 5

Chain "Melting" in the Incommensurate Host-Guest Structure of K-III

5.1 Motivation

During the investigation of the melting temperature of K at high pressure detailed in the previous Chapter, an interesting observation was made. Above 19 GPa, K crystallises into the incommensurate host-guest phase. Upon heating a sample in this phase with pressure held constant at 33 GPa, it was observed that the Bragg peaks arising from the guest structure significantly broaden and reduce in intensity before disappearing entirely. The disappearance of Bragg scattering arising from the guest structure while the scattering from the host structure remained unchanged indicates a loss of long-range ordering in the guest structure. This Chapter utilises single-crystal and powder diffraction techniques to investigate the nature of the chain disordering in incommensurate host-guest K. In previous studies, i.e. studies of Rb which will be discussed below, the chain order-disorder transition has been denoted chain "melting". To distinguish this phenomenon from the solid-liquid phase transition described in the previous Chapter, throughout this study chain "melting" will be referred to as an order-disorder transition.

5.1.1 Incommensurate Host-Guest Structures in the Alkali Elements

As discussed in Chapter 2, there exist isostructural phases in several of the alkali elements. The composite incommensurate host-guest (H-G) structure is one such phase, and is found in Na, K and Rb. This structure comprises of two inter-penetrating substructures, a "host" and a "guest". The host structure is common to all three elements listed, yet the guest structure is unique to each (McMahon *et al.* 2006), (McMahon *et al.* 2001b), (Lundegaard *et al.* 2009a).

Figure 5.1: An example of a composite incommensurate host guest structure. This is *tI*19-K, comprised of a 16-atom tetragonal host structure, represented by the light grey atoms, and a tetragonal *C*-centred guest structure, represented by the dark grey atoms. The host structure forms channels in which the guest atoms reside, where they form linear chains along the incommensurate *c*-axis (McMahon *et al.* 2006).

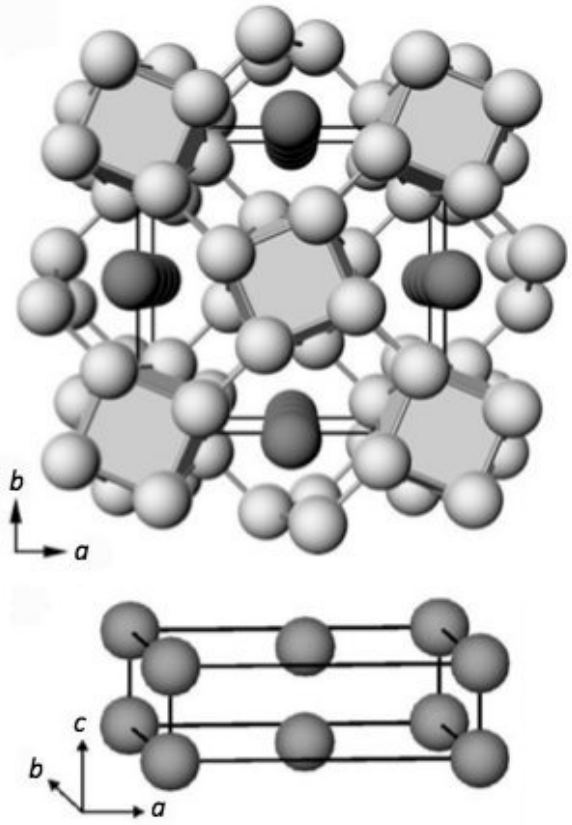

An example of an incommensurate H-G structure may be seen in Figure 5.1. The tetragonal host substructure, represented by the light grey atoms, has spacegroup $I4/mcm$ and consists of a 16-atom tetragonal framework, forming non-intersecting channels along the c-axis. Residing in these channels are the guest atoms, the dark grey atoms. The guest is a 2-atom substructure, which form 1D linear chains along the c-axis. The host and guest structures are incommensurate with each other along the c-axis. The guest structure depicted here is unique to K, and may be described using spacegroup $P4/mmm$ (McMahon *et al.* 2006). However, to highlight the close relationship between the host and guest structures, the guest is instead described using the non-standard spacegroup setting $C4/mmm$, which is chosen such that the a and b lattice parameters of the host and the guest substructures are the same.

Throughout this Chapter this phase will be referred to as $tI19$, using Pearson notation. "t" and "I" refer to the tetragonal and body-centred nature of the H-G structure, and 19 refers to the number of atoms in the unit cell. As detailed above, the host and guest substructures contain 16 and 2 atoms respectively. The incommensurate nature of the host and guest substructures result in a non-integer number of atoms in the unit cell, and is related to the c_{Host}/c_{Guest} ratio, which varies with pressure. The number of atoms in the unit cell is $16+2\times c_{Host}/c_{Guest}$. For example, K crystallises into the H-G structure at 19 GPa where there are $\sim$19.3 atoms in the unit cell. As pressure is increased the c_{Host}/c_{Guest} ratio initially decreases so that at 25 GPa there are $\sim$19.2 atoms per unit cell. The fractional part is excluded for convenience of notation.

An example of X-ray scattering from an incommensurate H-G structure may be seen in Figure 5.2. This particular example is a quasi-single crystal of $tI19$-K at 27.2 GPa and room temperature, oscillated about a vertical axis $\pm5^\circ$ during a single exposure. Scattering from the host and guest substructures is distinctly different, as can be clearly seen in Figure 5.2. Several host and guest reflections that arise from scattering from one of larger crystallites in this sample are highlighted by the upper (downwards) and lower (upwards) arrows, respectively. The host reflections are sharp Bragg spots as expected when scattering from a 3D crystal. Scattering from

the guest structure may be thought of as consisting of two components: a line of diffuse scattering arising from scattering from a linear chain of atoms, and Bragg spots arising from interchain ordering. The diffuse line of scattering is caused by the intersection of a diffuse sheet of scattering from the 1D guest structure intersecting the Ewald sphere.

Figure 5.2: X-ray diffraction from a composite incommensurate host-guest structure. This particular sample is a quasi-single crystal of incommensurate host-guest K at 27 GPa and room temperature. The arrows in the upper region indicate scattering from the host component and the lower arrows indicate scattering from the guest component. The host structure gives sharp Bragg spots as expected from a 3D crystal. The guest scattering is composed of two components: a line of diffuse scattering arising from the 1D nature of the chains, overlain with Bragg spots which arise from interchain ordering.

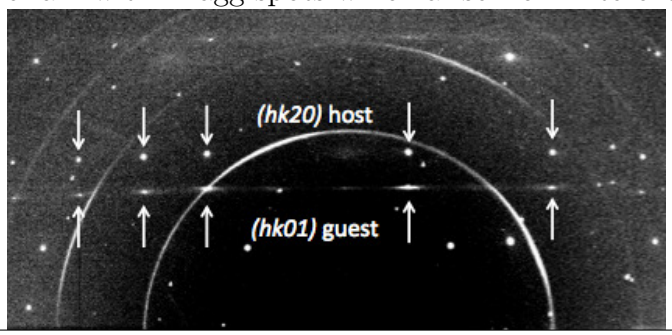

As mentioned above, the *tI*19 structures are found in Na, K, and Rb, and have a common host structure, yet unique guest substructures. The *tI*19 phase was first observed in the alkali elements in Rb by McMahon *et al.* (McMahon *et al.* 2001b)– Rb-IV, stable between 16 and 20 GPa. The guest structure is body-centred tetragonal and is indexed with spacegroup $I4/mmm$ (McMahon *et al.* 2001b). In a subsequent study, McMahon and Nelmes (McMahon & Nelmes 2004) noted an interesting phenomenon: the sharp Bragg reflections arising from scattering from the guest structure, observed at 18.5 GPa, grow increasingly broad and reduce in intensity as pressure is decreased. Below 16.2 GPa, the guest reflections have almost entirely disappeared, as shown in Figure 5.3. This increase in peak-width upon pressure decrease indicates that the correlation length between the guest chains is reducing significantly, demonstrating a loss of long-range order. On decreasing pressure from 17 GPa down to 16.2 GPa, the correlation

length decreases from values in excess of ∼300 Å down to ∼30 Å, only 4 times the interchain spacing at this pressure. The guest chains at 16.2 GPa may therefore be thought of as being a 1D liquid, having no long-range order; hence the authors of this study referring to this phenomenon as chain "melting".

Figure 5.3: Pressure-induced chain "melting" in *tI*19-Rb. The (*1001*) guest reflection appears sharp at 18.5 GPa and clearly broadens as pressure is decreased from (a) to (f), disappearing entirely at 16.2 GPa. This transition is reversible, as scattering from the guest structure returns as pressure is increased (f)-(i). Figure taken from McMahon & Nelmes (McMahon & Nelmes 2004)

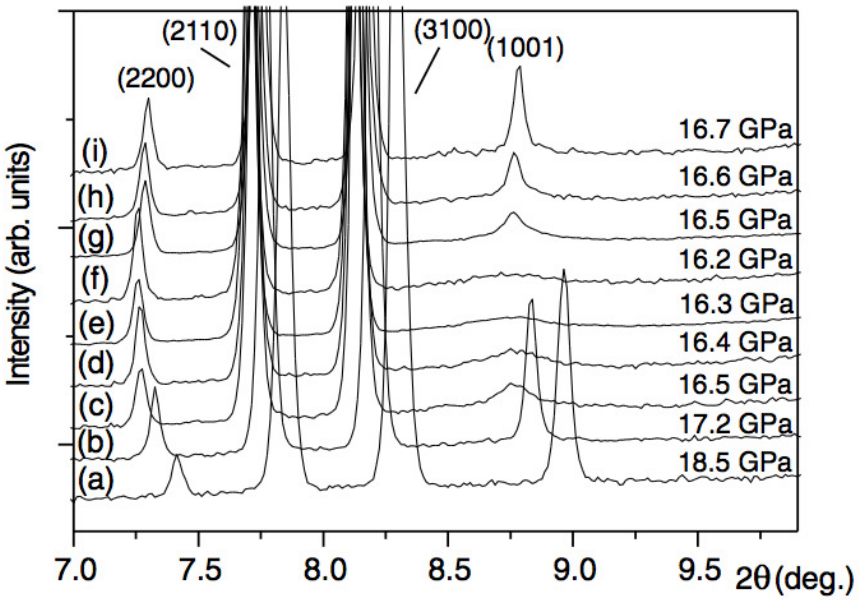

This phenomenon is similar to a temperature-dependent one observed at ambient pressure in the $Hg_{3-\delta}AsF_6$ system (Emery & Axe 1978). This system crystallises into a composite incommensurate structure consisting of tetrahedra of 1D chains of Hg atoms contained within channels formed by an AsF_6 framework. Considering a single-crystal of this material, at room temperature, scattering from the chains of Hg atoms gives only diffuse lines of scattering, arising from fact that the Hg atoms form a 1D structure with no interchain correlations. As temperature is cooled to 120 K, well-defined Bragg peaks begin to appear as the interchain correlations increase.

In Na, the *tI*19 phase is stable between 125 GPa and 180 GPa (Gregoryanz *et al.* 2008). The guest structure in this pressure range at room temperature has been noted to be highly disordered, with the Bragg peaks from the guest component characterised by broad diffuse discs of scattering. Despite the small amount of Bragg scattering from the guest chains at room temperature, the *tI*19-Na guest structure has been indexed as a having a primitive monoclinic structure (spacegroup $P2/m$)(Lundegaard *et al.* 2009a). Interestingly, unlike the guest chains in Rb, the broadened Bragg peaks from the guest phase observed in Na do *not* sharpen on pressure increase. Lundegaard *et al.* (Lundegaard *et al.* 2009a) calculated the interchain correlation length at 147 GPa, nearly 20 GPa above the *oP*8-to-*tI*19 phase transition pressure, to be ∼30 Å. In *tI*19-Rb, the guest-chain correlation length was ∼30 Å at the lower pressure limit of the stability field of this phase (McMahon *et al.* 2001b). Lundegaard *et al.* (Lundegaard *et al.* 2009a) suggested that the absence of pressure-induced ordering may be due to the proximity of the room temperature study of the *tI*19 phase to the melting curve of Na – as described in Chapter 2, the melting curve of Na has a minimum close to 110 GPa and 300 K (Gregoryanz *et al.* 2005).

As previously described, the guest structure of K is also unique (McMahon *et al.* 2006). However, the *tI*19-K phase shows further complexity on increasing pressure as it undergoes a series of intra-phase transitions. At 19 GPa, following the minimum in the melting curve, K transforms from *fcc* to the *tI*19 phase (Chapter 4). Here, the guest structure crystallises into a *C*-centred tetragonal arrangement (spacegroup $C4/mmm$). On increasing pressure, at 27 GPa the host structure loses its *c*-glide symmetry, and then at 30 GPa, the guest structure undergoes a transition to an *A*-centred orthorhombic structure ($Ammm$). The guest structure remains in this *A*-centred orthorhombic phase up to 39.5 GPa, after which it undergoes a re-entrant phase transition, transforming back to the *C*-centred structure it adopted at lower pressure. A few GPa above this re-entrant transition, at 43 GPa, the *c*-glide symmetry of the host structure returns, and K remains in this phase up to the transition to *oP*8-K at ∼54 GPa (Lundegaard 2013). Above 43 GPa the H-G phase is structurally identical to that below 27 GPa, but the evolution of the c_{Host}/c_{Guest} ratio with pressure has a different trend –

below 27 GPa c_{Host}/c_{Guest} decreases with pressure, whereas above P$\sim$40 GPa the c_{Host}/c_{Guest} ratio increases with pressure.

At room temperature, the guest chains in K appear to be long-range ordered and no pressure-induced order-disorder transition has been reported. This Chapter investigates the high-temperature behaviour of the guest structure of *tI*19-K over a wide range of P-T space.

5.2 Experimental Details

All experiments were conducted with high-purity (99.95 % Alfa Aesar) K, loaded without a pressure-transmitting medium under argon, in a dry, oxygen-free atmosphere (O_2<1 ppm, H_2O<1 ppm). Membrane-driven diamond anvil cells equipped with 200-300 μm culets were used, with either a small piece of Ta powder or foil, or a small ruby sphere ($\sim$5 μm) for pressure calibration. The temperature was controlled using external resistive heating rings which surrounded the diamond anvil cells, and measured using a K-type thermocouple attached to one of the diamond anvils. The data analysis techniques used for the single-crystal analysis are contained within Section 5.4.5. Powder diffraction analysis techniques are described in Chapter 3.

5.3 Notation for Describing Host and Guest Reflections

The host-guest structures may be described in terms of one 4D structure, described by a superspace-group, or by two 3D structures, each described by their own spacegroups. In this Chapter, the data has been treated as two inter-penetrating 3D structures. However, to discern which reflections belong to the host structure, which belong to the guest structure, and which reflections form from contributions from both the host and guest structures, the 4D superspace-group index notation will be used. Instead of the traditional h, k, l Miller indices, the host and guest structures will be described by four indices – h, k, l, and m. The (*hkl0*) reflections belong to the host structure only, the (*hk0m*) reflections belong to the guest structure only, and the (*hk00*) reflections are from contributions from both the host

and guest structures. Higher order ($hklm$) reflections with l and $m \neq 0$ are weak reflections, which arise from interactions between the host and guest structure.

5.4 Single-Crystal Studies

5.4.1 Crystal Growth

The extension of the melting curve of K to 24 GPa and 750 K, and the discovery of a melting minimum at the *fcc*-*tI*19-liquid triple point at 19 GPa and 380 K, as discussed in Chapter 4, allowed the growth of a single-crystal of *tI*19-K. The gradient of the melting temperature following this triple point rises steeply at ∼65 K/GPa, and so growth of a single-crystal was non-trivial. K.A. Munro, as part of his Masters Thesis grew a small yet high-quality single-crystal of *tI*19-K at 21 GPa.

5.4.2 Data Collection

Single-crystal diffraction data were collected at P02.2, Petra-III. The incident X-ray wavelength was 0.29 Å and the beam size was 2×5 μm^2 at full-width at half-maximum. Data were collected on a MAR345 image plate detector operating in the 2300 mode, and sample to detector distance and tilt were calibrated using a cerium dioxide diffraction standard.

The diamond anvil cell – Merrill-Bassett type with 300 μm culets – was equipped with Boehler-Almax type diamond anvils and seats, which provided an opening angle of 75°. Data were collected by rotating the diamond anvil cell in a sequence of contiguous 1° oscillations over a total scan range of ω=56° around a vertical axis. The angle ω is indicated in Figure 5.4.

A complete single-crystal data set was initially collected at room temperature (RT) and indexed fully. By obtaining the orientation matrix it was possible to orient the crystal in such a manner so as to access guest reflections of interest for longer exposures. Such exposures were necessary for the interchain correlation length measurements described below. Complete single-crystal data sets, and long exposures of reflections of interest, were collected in temperature increments of 10 K, up to 345 K.

Figure 5.4: Depiction of goniometer angles and X, Y, Z positions used to define the orientation of a single-crystal. Note that in the single-crystal data sets collected angles χ and ϕ were set to zero and so are absent from this diagram for clarity. Angles 2θ and ω are shown.

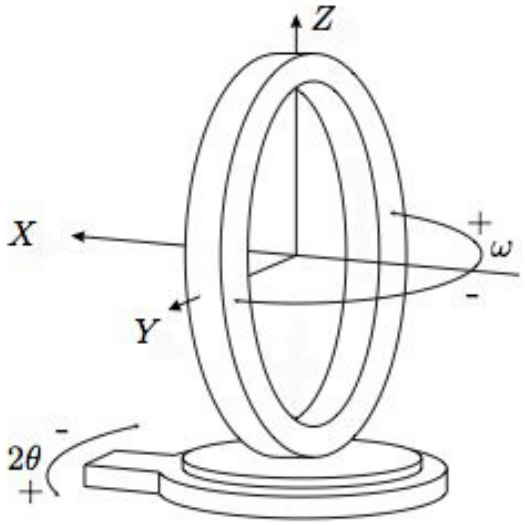

5.4.3 Diffraction Observations

The difference in scattering between the host and guest reflections at RT may be seen in a 2D slice of the single-crystal data set in Figure 5.5. The $(\bar{1}\,3\,20)$ and $(0\,\bar{2}\,20)$ host reflections and the $(\bar{1}\,3\,01)$ and $(0\,\bar{2}\,01)$ guest reflections are highlighted by the rectangle, and expanded for clarity. The host reflections are clearly-defined, sharp Bragg reflections, as one would expect from the 3D host. The guest reflections, however, are markedly different. Each may be understood as consisting of a Bragg spot at the centre of an elongated disc of diffuse scattering, stretching out along the unique c-axis, along which the guest is incommensurate with the host. This indicates that even at room temperature the guest chains exhibit some degree of disorder.

Pressure was held constant at 21 GPa as temperature was increased in increments of 10 K. 2D diffraction images of the $(\bar{1}\,3\,20)$ and $(0\,\bar{2}\,20)$ host, and the $(\bar{1}\,3\,01)$ and $(0\,\bar{2}\,01)$ guest reflections from Figure 5.5, and the effect of temperature on the guest may be seen in Figure 5.6. With increasing temperature, the Bragg reflections at the centre of the discs of diffuse scattering disappear, and the discs become increasingly elongated.

Figure 5.5: A 2D diffraction image of a 1° slice through a single-crystal data set at 21 GPa and 295 K. Pairs of host and guest reflections are highlighted by the red rectangle and expanded for clarity. Guest reflections are indicated by "G" and host reflections by "H", and their $(hklm)$ indices are included on the diagram. The letters "D" indicate Bragg reflections from the diamond anvils.

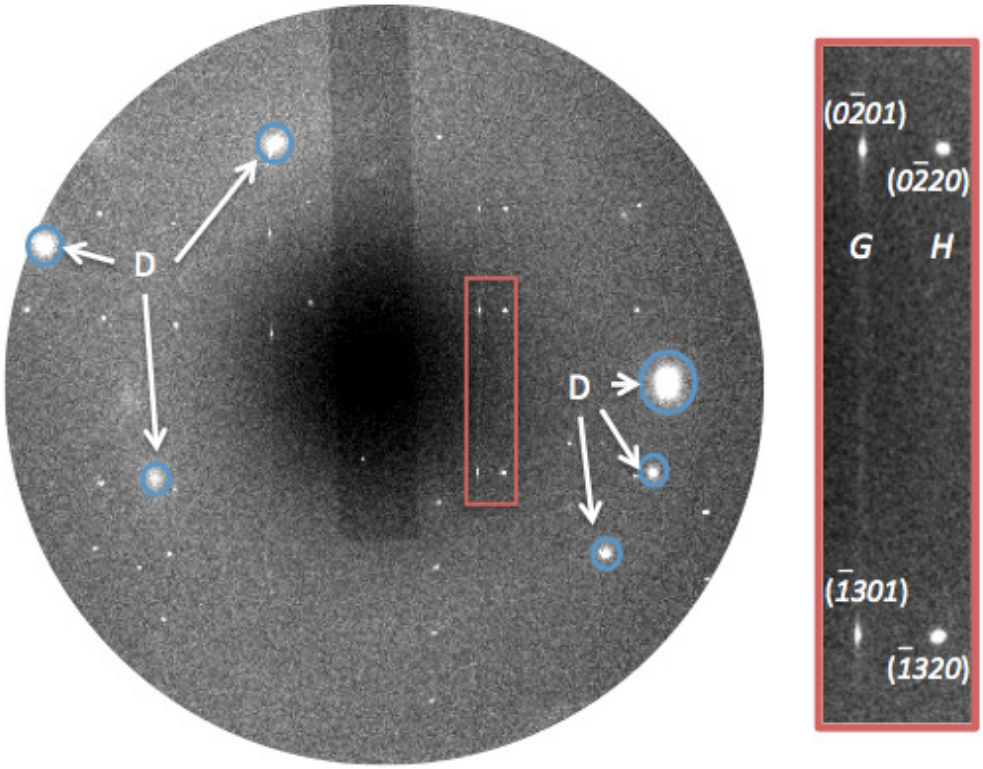

Indeed, at 345 K the discs appear to have disappeared entirely leaving instead a near uniform sheet of diffuse scattering, indicating a complete loss of interchain order, and a sharp order-disorder transition. Despite the significant change that occurs in the guest, inspection of the host reflections reveals no discernible change in the host structure with increasing temperature.

The relative behaviour of the host and the guest structures may be further demonstrated by inspection of 1D azimuthally integrated diffraction patterns as shown in Figure 5.7, where the $(0\bar{2}20)$ and $(\bar{1}320)$ host, and the $(0\bar{2}01)$ and $(\bar{1}301)$ guest peaks are expanded. There is a clear broadening and

Figure 5.6: An example of 2D diffraction images of the $(0\bar{2}20)$ and $(\bar{1}320)$ host, and the $(0\bar{2}01)$ and $(\bar{1}301)$ guest peaks from a 1° slice through a single-crystal data set at 21 GPa as temperature is increased in 10 K steps, beginning at room temperature. The host reflections remain unchanged with increasing temperature whereas the guest reflections reduce significantly in intensity, disappearing at 340 K.

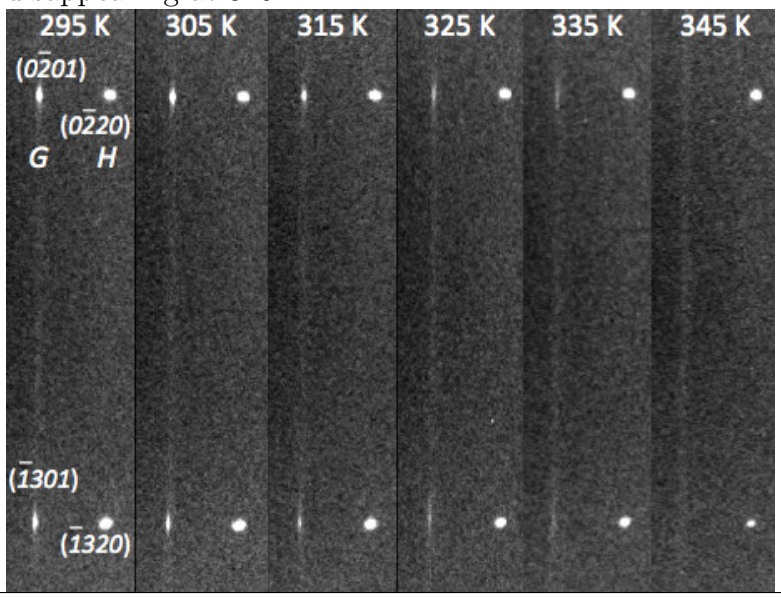

reduction in intensity of the $(0\bar{2}01)$ guest peak with increasing temperature, and yet there is no broadening or reduction in intensity of the accompanying host reflection. This indicates temperature-induced disordering occurs only in the guest structure. The following Sections endeavour to provide a quantitative understanding of this order-disorder transition.

5.4.4 Interchain Correlation Length

The interchain correlation length may be quantified by analysing the increasing width of the guest reflections perpendicular to the *c*-axis as temperature is increased. Importantly, for this analysis to be performed the integration must be a) performed along the line of diffuse scattering (perpendicular to c) and b) transformed to reciprocal space. Once the data are integrated and transformed, the correlation length is estimated as:

$$2\pi/\Delta_{FWHM} \tag{5.1}$$

Figure 5.7: Azimuthally integrated 1D diffraction images of a host and guest peak under the influence of increasing temperature. The $(0\bar{2}01)$ guest reflection is indicated by the "*G*" and the $(0\bar{2}20)$ host reflection is indicated by the "*H*". The host reflection remains unchanged whereas the guest reflection noticeably broadens before disappearing entirely, indicating a loss of long-range correlations between the 1D guest chains.

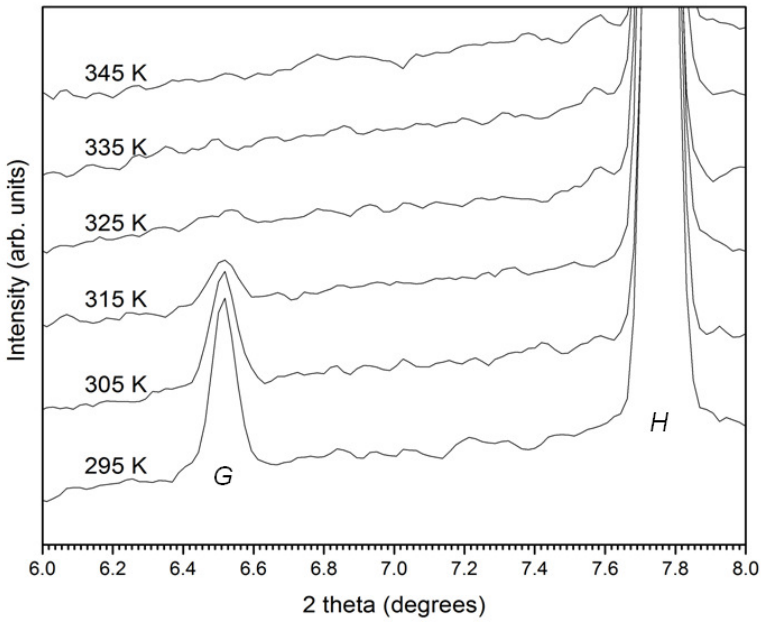

where Δ_{FWHM} is the difference in the full-width at half-maximum of the guest peak relative to the corresponding host reflection. The host reflections are treated similarly to the guest reflections, and their width in reciprocal space gives the resolution limit of this correlation length measurement.

Transforming the Data

To perform the integration along the line of diffuse scattering, a careful choice of the centre of integration must be made. Moreover, it is important to restrict the area over which the integration is performed, so that we are integrating over only the line of scattering. To do this, Fit2D (Hammersley *et al.* 1996) was used to mask everything in the 2D diffraction images except a narrow strip, as shown in Figure 5.8. The centre of integration, shown by the green X in Figure 5.8, was chosen such that the integration was performed along the line of diffuse scattering. It should be noted that as a consequence,

these integrations are not azimuthal, and so the x-axis is now arbitrary i.e. the units of our integration are in real space but are no longer in degrees. See Chapter 3 for details on azimuthal integrations.

Figure 5.8: To extract a correlation length from the 2D diffraction images a careful choice of the centre and the region of the image included in the integration were required. Such a choice would allow transformation of the real space integrated data into reciprocal lattice units and allow the extraction of a correlation length. A typical example of the region over which an integration was performed may be seen here. Large regions of the 2D image have been masked (excluded) so as to perform the integration only along the line of diffuse scattering which intersects the two guest reflections.

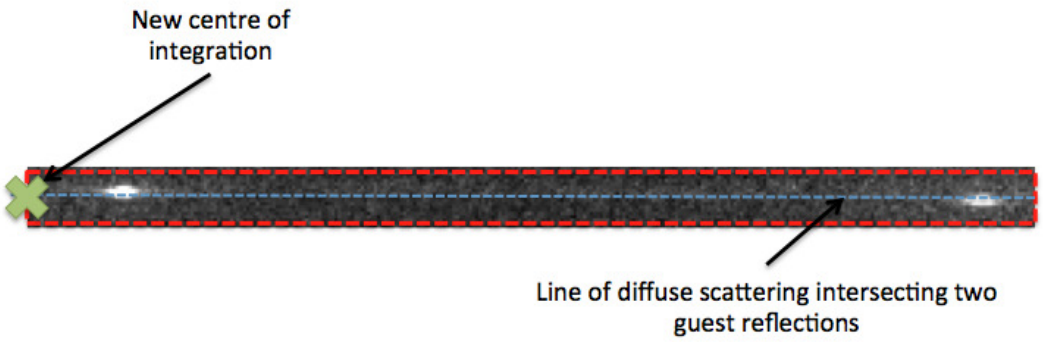

Now that an integration along the line of diffuse scattering has been performed, to extract the correlation length one needs to transform the data from real-space units to reciprocal-space units. To do this several approximations are required. As shown in Figure 5.5, due to the orientation of the crystal and the wavelength of the incoming X-ray beam, at a particular 1° slice through the single-crystal dataset, the $(0\bar{2}01)$ and the $(\bar{1}301)$ guest reflections simultaneously intersect the Ewald sphere.

The real-space co-ordinates obtained from the integration were transformed to reciprocal lattice co-ordinates by approximating the distance between the two guest reflections as a straight line. The analysis depends on the widths of the peaks themselves, not the empty space between, and so

Figure 5.9: The Ewald sphere at λ=0.29 Å intersecting two guest reflections simultaneously. The radius of the Ewald sphere is ∼22 Å^{-1} whereas the distance between the two reflections is ∼3.4 Å^{-1}. The distance between the Bragg reflections along the Ewald sphere was approximated as a straight line. Each point along the line of diffuse scattering connecting the two Bragg reflections, was interpolated and was converted to reciprocal lattice space units.

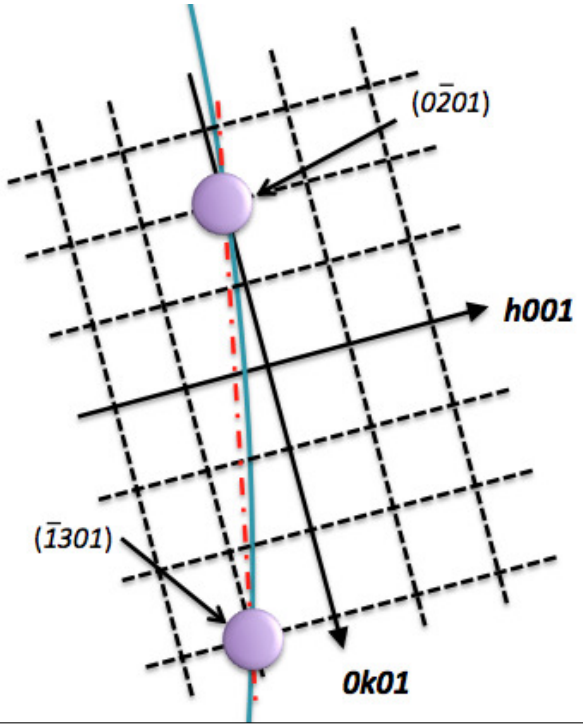

a linear interpolation was determined to be sufficient. This analysis was repeated for the two accompanying host reflections ($\bar{1}320$) and ($0\bar{2}20$). Figure 5.9 illustrates a scaled drawing of the Ewald sphere intersecting the two guest reflections, and one may see that the approximation to a straight line is reasonable. The radius of the Ewald sphere is ∼22 Å^{-1} whereas the distance between the two reflections is ∼3.4 Å^{-1}. Each point along the line of diffuse scattering connecting the two Bragg reflections was interpolated, and was converted to reciprocal lattice space units.

Identical analysis was performed for the accompanying host reflections (Figure 5.5), and the width of the host reflections in reciprocal space (perpendicular to the c direction) gave the resolution-limit of this measurement. The width of the host peak depends on numerous factors, such as the size

of the single-crystal, the point-spread function of the detector, the incident X-ray beam size, and the beam divergence. By taking the width of the host peak as the resolution limit of this measurement one may take these factors in to account. No change in the host peak-width was observed as temperature was increased.

Changing Correlation Length

A plot of the additional peak width of the guest reflection minus that of an average of the accompanying host reflection may be seen in Figure 5.10. There is little difference in the width of the guest reflections at RT (295 K) and at 305 K. However, at 345 K it was impossible to discern any peak at all in the integrated profile i.e. there is a complete loss in long-range order, and hence the guest chains at this temperature may be considered to be liquid-like.

The temperature-dependence of the guest interchain correlation length may be seen in Figure 5.11. The resolution limit of these measurements was determined by the width of the accompanying host reflections along the same direction in reciprocal space. This was determined to be ∼300 Å. At 295 K (RT) and 305 K, both guest peaks exhibit long range correlations on the scale of the host structure, with no discernible difference in the correlation length observed. At 335 K, the interchain correlation length is approximately twice the interchain spacing – interchain spacing was determined to be 7.00 Å as a=9.906 Å at 21 GPa, and the interchain correlation length is ∼15 Å. The complete disappearance of any discernible peak at 345 K indicates that the chains become completely disordered between these two temperatures.

Interestingly, at 315 K, the loss in long-range order becomes significant, dropping by a few hundred ångströms, reaching the RT value reported for the chains in *tI*19-Na at 325 K (∼30 Å) (Lundegaard *et al.* 2009a). Although the structure in which the chains order in Na is different, the fact that an order-disorder transition is present in both Rb and K may suggest that by cooling Na below RT, the chains could become ordered. To-date, no single-crystal diffraction studies have been performed on Na below room temperature.

Furthermore, in the single-crystal dataset, only the (*hk01*) guest reflections were observable, even at RT. Careful analysis of the diffraction data

Figure 5.10: The additional peak-width, in reciprocal space units, of the guest reflections of *tI*19-K at 21 GPa with increasing temperature. The additional peak width was determined by subtracting the host peak peak-width from the guest reflection peak-width. The variation of the width of the host reflection was determined to be negligible.

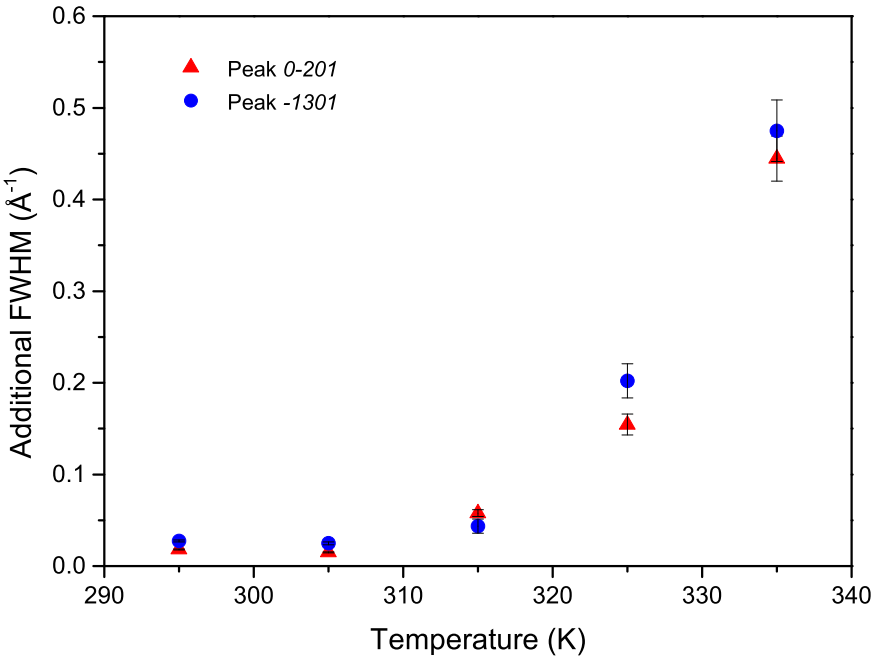

revealed no (*hk0l*) guest reflections with *l*>*1*. The lack of these additional higher order guest reflections in K, even at RT, indicate that there is a large degree of disorder within the guest chains, i.e. the guest structure has a larger thermal motion along the *c*-axis than along *a*/*b*. To quantify this thermal motion, the atomic displacement parameters of the host and guest atoms may be extracted following a full single-crystal refinement. This will be the subject of the subsequent Section.

5.4.5 Single-Crystal Data Reduction

Although the data analysis in Section 5.4.4 was performed on single-crystal data sets, the analysis techniques used – 1D integrations using Fit2D – are

Figure 5.11: The effect of temperature on the interchain correlation length of the guest chains in *tI*19-K at 21 GPa. The interchain correlation length was determined using Equation 5.1 and the resolution of this measurement is determined from the peak width of the host reflection, determined to be ~300 Å. The guest reflections exhibit a significant reduction in correlation length above 315 K.

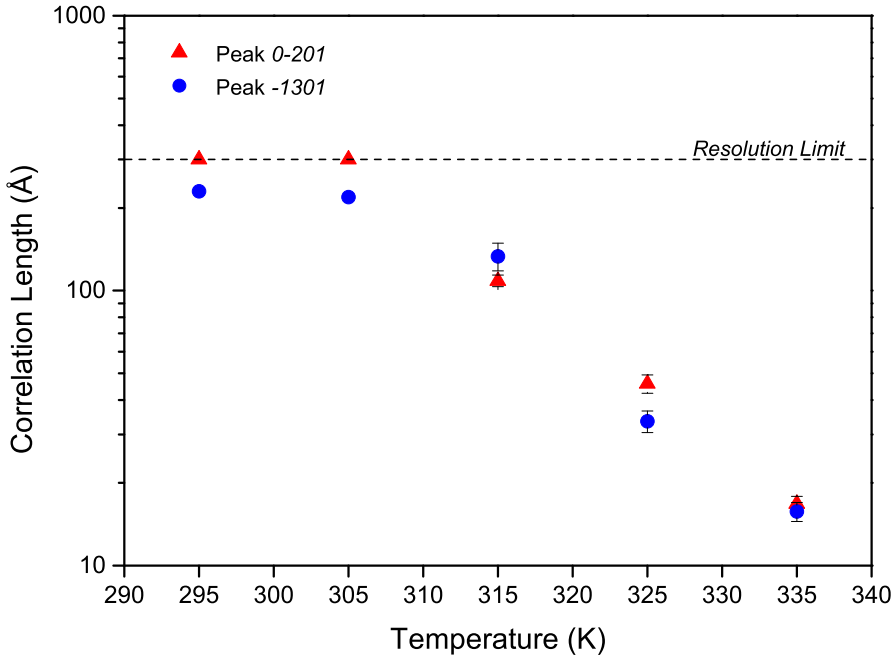

more akin to powder diffraction, rather than single-crystal, analysis. This Section describes the reduction and integration of full single-crystal data sets, with the aim of quantifying the thermal motion of the guest chains.

The first step in data reduction for the single-crystal data sets involves determining the unit cell and acquiring an orientation matrix that will be used for the subsequent integrations. It should be noted that the first step in the single-crystal data reduction process was conducted prior to the analysis to extract the interchain correlation length, described in the previous Section, and is how the host and guest reflections were indexed. Recall that the host and guest are treated as two 3D substructures.

The preferred program for performing single-crystal analysis is SMART

v5.62 (Bruker). It should be noted that the SMART software assumes a detector of size 512×512 pixels. However, the data sets were collected on a MAR345 image plate detector, operating in the 2300 mode, meaning that there are 2300×2300 pixels on the active detector area. It was therefore necessary to re-bin the data and convert it to an appropriate format. This was done using a program developed by I. Loa & L.F. Lundegaard (Lundegaard 2007). Furthermore, it is also important to perform careful masking of each frame. The diamond anvil cell body shadows an increasing amount of the individual frame as the cell is rotated, as highlighted in Figure 5.12. If reflections in the shadowed region were included in the final integration they would give inaccurate peak intensities. Therefore, again using a program developed by L.F. Lundegaard & I. Loa, a mask was applied to the data which excluded reflections from these regions (Lundegaard 2007).

Figure 5.12: A 1° section of the single-crystal data set that is shadowed by the diamond anvil cell body. A mask is required to remove the highlighted section of this image as, if included, the peaks in this shadowed region would give unreliable intensities. Use of masking software kindly permitted by L.F. Lundegaard & I. Loa (Lundegaard 2007).

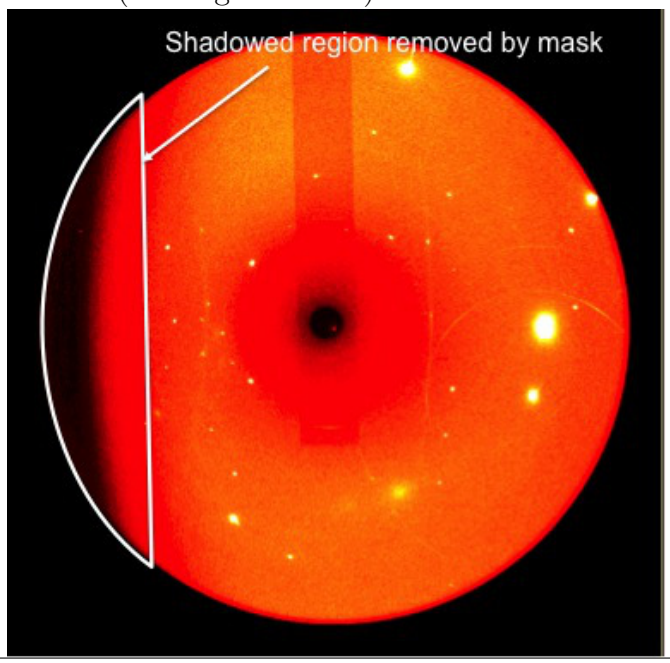

Upon converting the data to the appropriate format for SMART, it is simple to identify non-sample reflections when browsing through the data

frames. For example, the K reflections are considerably less intense than the reflections from the diamond anvils. The hand-picked K reflections were next viewed in a reciprocal space viewer – RLATT (Bruker) – which allows the easy identification and exclusion of any accidental non-sample reflections acquired, as illustrated in Figure 5.13 – the reflections shown in this Figure belong to the host structure and one may see that they form well spaced lines in reciprocal space. Non-host reflections are readily identified, as they do not line up in reciprocal space.

Figure 5.13: The reciprocal lattice of the host structure of *tI*19-K at 21 GPa as viewed using the RLATT (Bruker) software. Reflections that do not fit the host lattice are easily identified by eye and removed within RLATT. As seen here the reflections all line up extremely well in reciprocal space indicating they belong to the same crystal.

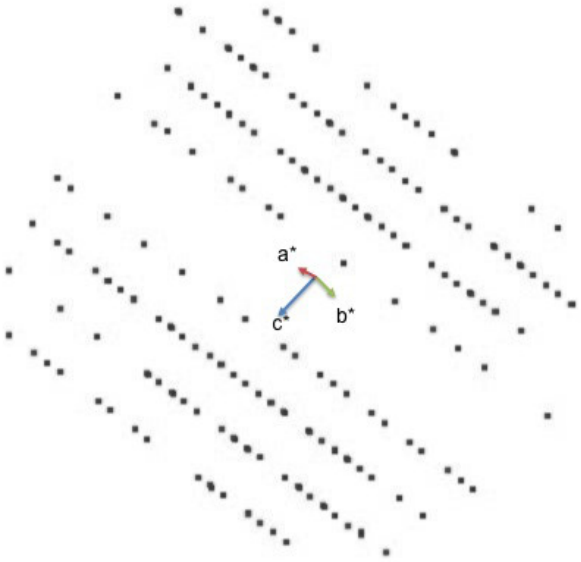

The adjusted list of reflections, containing only host reflections, is then read into SMART and the reflections indexed, the unit cell determined, and a least squares fit performed to acquire the most accurate orientation (UB) matrix – a 3×3 matrix which describes the dimensions and orientation of the reciprocal cell. At each temperature point the host structure was determined independently.

Indexing the guest reflections proved more difficult due to fact that

they are considerably less intense than the host reflections, even at RT. As discussed in Section 5.4.4, the large thermal motion of the guest is indicated by the fact that no (*hk0l*) guest reflections with *l>1* were observed, which additionally made indexing the guest structure difficult. The guest UB matrix was therefore determined at RT through a combination of hand-picking the guest reflections, and by manual adjustment of the host UB matrix. Powder diffraction studies conducted by McMahon *et al.* (McMahon *et al.* 2006), determined that at 21 GPa the c_{Host}/c_{Guest} ratio was 1.61 with the *a* and *b* host and guest lattice parameters having a 1:1 correspondence. The guest UB matrix was obtained by pre-multiplying a column (*hkl*) vector formed from each host reflection by a matrix:

$$\begin{pmatrix} 1 & 0 & 0 \\ 0 & 1 & 0 \\ 0 & 0 & \frac{c_{Guest}}{c_{Host}} \end{pmatrix}$$

This gives a column vector which contains the transformed (*hkl*) values i.e. the guest reflections. The guest UB matrix may then be more accurately acquired by performing a least-squares refinement on these adjusted reflections.

5.4.6 Atomic Displacement Parameters

Diffraction studies reveal not only the mean atomic positions, but also the probability density functions of atomic displacements from these mean positions. It is taken as understood that atoms in a crystalline lattice vibrate, and that these vibrations increase as temperature increases. As discussed previously, for example in Section 5.4.4, there is qualitative evidence that the guest structure exhibits larger thermal motion along the incommensurate *c*-axis, than along axes *a* or *b*. The advantage of having high-quality single-crystal data is that atomic displacement parameters may be refined as part of a structural solution.

The host and guest lattice parameters and orientation matrices were obtained using SMART. The host and guest were indexed on a tetragonal lattices, and lattice parameters of the host were determined to be a=9.9055(7) Å and c=4.820(5) Å and those of the guest were determined to be a=9.9055(15)

Table 5.1: A table of the refined atomic positions and atomic displacement parameters of the host and guest structures. The host atom occupies the 16*k* Wyckoff site at (x, y, 0.5) and the guest atom occupies the 2*a* Wyckoff position at (0.5, 0, 0). In each refinement the host and guest U_{11} and U_{22} ADPs were determined to refine to similar values, and so to obtain an accurate value of the U_{33} guest parameter, the U_{11} and U_{22} guest parameters were fixed at 0.03 Å^2, approximately equal to that of the host.

Host *I4/mcm*	
x	0.7893(1) Å
y	0.0860(1) Å
U_{11}	0.0324(9) Å^2
U_{22}	0.0270(8) Å^2
U_{33}	0.0339(8) Å^2
Guest *C4/mmm*	
U_{11}	Fixed at 0.03 Å^2
U_{33}	0.17(3) Å^2

Å and c=2.989(3) Å. The intensities of both the host and guest structures were integrated in SAINT+ (Bruker), and corrected for absorption due to the diamond anvils. Symmetry equivalent reflections were then averaged.

Least-squares refinement of the structures were performed using Jana2006 (Petricek *et al.* 2006), using only the (*hkl0*), $l \neq 0$ for the host structure and (*hk0m*), $m \neq 0$ for the guest structure, as these reflections are unique to the host and guest respectively.

The host converged to an excellent fit, with a weighted R-factor (wR) of 4.4 %. The guest structure, with fewer observed reflections, proved more difficult to refine, converging to a fit with wR=6.7 %. The host atoms are located on the 16*k* Wyckoff sites of spacegroup $I4/mcm$, at positions (x, y, 0.5) with x=0.7892(1), and y=0.0860(1), in reasonable agreement with the previous study of McMahon *et al.*, where the positions were determined to be x=0.7941(7) and y=0.089(1) at 20.6 GPa (McMahon *et al.* 2006). The guest atoms are confined to positions (0.5, 0, 0). The atomic displacement parameters (ADPs) were refined for the host and guest respectively and may be seen in Table 5.1.

Upon refining the guest structure, it was observed that the U_{33} parameter

was significantly larger than the U_{11} parameter. The U_{11} guest parameter refined to be similar in value to the U_{11}, U_{22} and U_{33} host parameters within error, and so to directly compare the host and guest ADPs, the guest U_{11} parameter was constrained to be approximately the same as the host at 0.03 Å^2. The guest U_{33} parameter is larger than its U_{11} parameter by a factor of ∼5.6 indicating that there is significantly more disorder along the *c*-axis. As the square-root of the ADP corresponds to the root-mean-squared (RMS) physical displacement of the atom from its average expected position, it is determined that along the *a*/*b* axes, the approximate displacement is similar in the host and the guest structures at ∼0.18 Å. Applying the same analysis to the U_{33} parameter, the RMS displacement of the guest atom along *c* is 0.41(6) Å. Figure 5.14 is a plot of the thermal ellipsoids obtained from the ADPs of the host and the guest structures respectively. One can clearly see that the displacement of the guest atoms along the *c*-axis is significant.

Figure 5.14: The host-guest structure of K at 21 GPa and room temperature as viewed along the incommensurate *c*-axis. The host and guest atoms are plotted as thermal ellipsoids as determined by the atomic displacement parameters. Blue ellipsoids indicate the host atoms and purple ellipsoids indicate the guest atoms. The host ellipsoids are approximately spherical, indicating uniform displacement in all directions. The guest ellipsoids are clearly elongated along the *c*-axis, indicating a large degree of disorder at room temperature along the incommensurate axis.

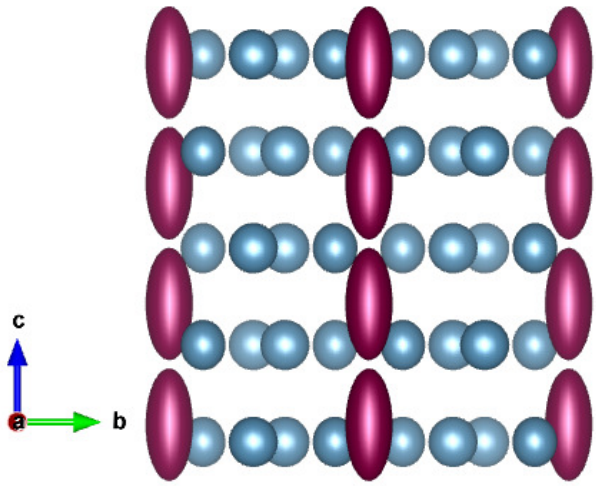

One may consider this data in the context of the Lindemann criterion

for melting, where one considers a solid to have melted when its average mean square displacement is approximately 10-15 % of the nearest neighbour (n.n.) distance (Lindemann 1910), as cited by Martinez-Canales & Bergara (Martinez-Canales & Bergara 2008). The n.n. distance for the guest atoms is along the *c*-axis, and is in fact the *c*-lattice parameter, determined to be 2.989 Å at 21 GPa and RT, and is illustrated in Figure 5.15 by the green arrow. The average displacement of the guest atom is therefore 13.8 % of the n.n. distance, and so one may consider, in the context of the Lindemann criterion, that the guest chains are liquid-like, even at room temperature. Upon increasing temperature above RT, it was not possible to refine the guest structure due to the large increase in thermal motion, which already considerable at RT. The n.n. distance in the host at this pressure is 2.845 Å and the closest approach for the host atoms is illustrated in Figure 5.15 by the blue arrow. Therefore, the average displacement of the host atom from its average position (0.18 Å) is just 6 % of the n.n. distance.The red arrow in Figure 5.15 indicates the interchain spacing in the guest structure, as discussed in Section 5.4.4, and determined to be 7.00 Å at 21 GPa.

5.5 Quasi-Single Crystal and Powder Studies

While single-crystal diffraction studies provided a wealth of information on the order-disorder phenomenon at 21 GPa, single-crystals of *tI*19-K at higher pressures were extremely difficult to grow due to the steep gradient of the melting curve; the melting temperature has been measured to increase at a rate of ∼65 K/GPa up to 750 K at 24 GPa (Chapter 4). To investigate the order-disorder transition in the guest chains at higher pressures, both powder and quasi-single crystal samples were utilised. Details of sample preparation and diamond cells used may be seen above in Section 5.2.

Powder diffraction data were collected at beamline I15 at the Diamond Light Source (DLS), and at beamline ID09a at the European Synchrotron Radiation Facility (ESRF). The X-ray wavelengths and beam diameters were ∼0.33 Å and 40 μm ; and ∼0.414 Å and 15 μm respectively. Samples were oscillated ±5° during each exposure to improve powder averaging. Typical exposure times at DLS were 180 s, and at ESRF were 1 s. The Perkin Elmer

Figure 5.15: The host-guest structure viewed in the a-b plane (upper image) and the guest structure, depicted in perspective, along the c-axis (lower image). The host atoms are represented by the light grey atoms, and the guest atoms, residing the channels formed by the host structure, are represented by the dark grey atoms. The red arrow indicates the interchain spacing between the guest chains, the blue arrow indicates the nearest neighbour distance of atoms in the host structure, and the green arrow indicates the nearest neighbour distance of atoms in the guest structure.

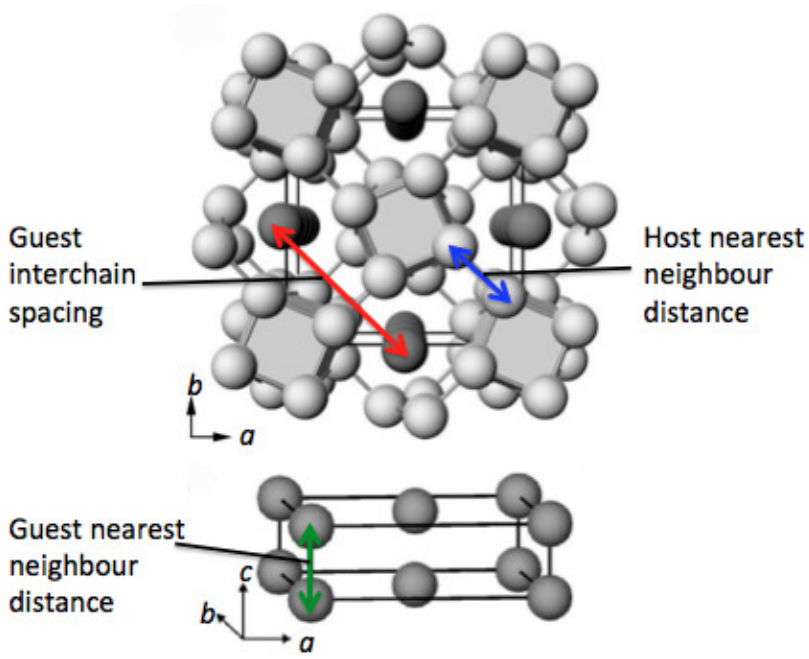

flatpanel detector was used at DLS, and the MAR555 image plate was used at the ESRF. The 2D diffraction images were integrated azimuthally using Fit2D (Hammersley *et al.* 1996), and the resulting integrated profiles were analysed using Jana2006 (Petricek *et al.* 2006). It should be stressed here that even the powder samples were not of sufficiently good quality (they had a reasonable degree of preferred orientation) to perform a Rietveld refinement, and so Le Bail fits were performed on all the data.

The onset of the order-disorder transition was identified by the disappearance of Bragg scattering from the guest structure. An example of 2D diffraction images from quasi-single crystal samples and from polycrystalline samples may be seen in Figure 5.16 and 5.17 respectively. In Figure 5.16

Figure 5.16: A section of the 2D diffraction images illustrating the order-disorder transition in the guest chains from a quasi-single crystal of *tI*19-K at 25.3 GPa. The guest reflections are highlighted by the open squares. The guest reflections decrease in intensity as temperature increases from room temperature (293 K), and the Bragg scattering disappears entirely leaving only the line of diffuse scattering in Figure (c) at T=369 K

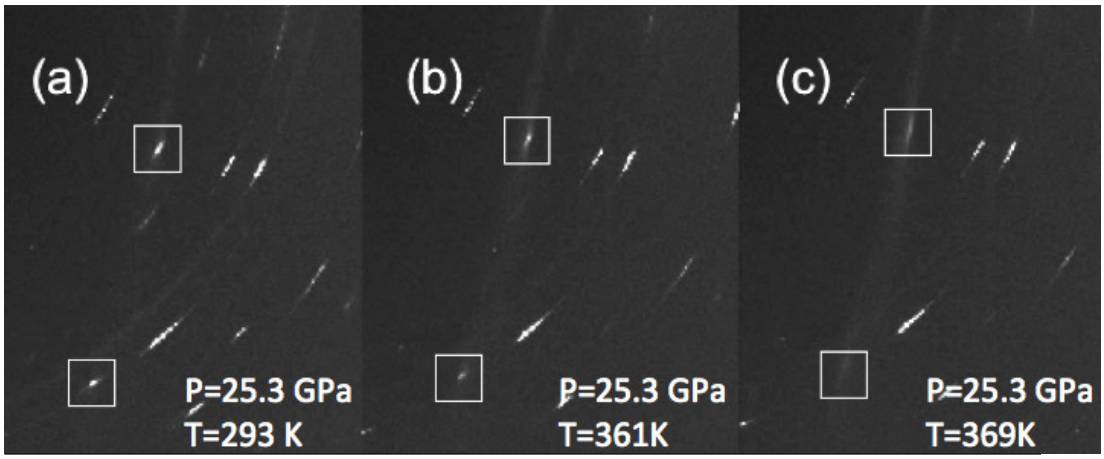

Figure 5.17: 2D diffraction images from polycrystalline samples. Here the diffuse scattering from the disordered guest chains is not observable. The order-disorder transition in polycrystalline samples was determined by the complete disappearance of Bragg scattering from the guest component. Bragg scattering from the guest substructure is highlighted by the open ovals. Furthermore this Figure demonstrates a change in the gradient of the order-disorder transition – as pressure is increased from 30.0 GPa (a) to 31.1 GPa (b) at T∼375 K the guest chains reorder.

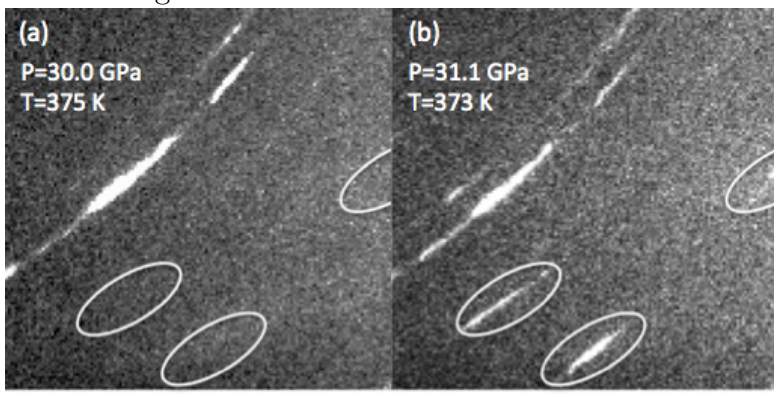

(a), the sample is at room temperature and the guest reflections, highlighted by the open squares, are sharp, with the Bragg reflections lying along the Debye-Scherrer ring. In this instance, the diffuse scattering is weak but it is still possible to observe the line of scattering. The temperature is increased to 343 K in Figure 5.16 (b) and one can see a reduction in the intensity of the Bragg reflections. It is important to note that this is the temperature at which the guest peaks were determined to disappear entirely at 21 GPa, yet clearly at 25.3 GPa, some Bragg scattering from the guest component is clearly still observed.

Figure 5.18: Azimuthally integrated 1D diffraction patterns from a quasi-single crystalline sample of *tI*19-K at 25.3 GPa on temperature increase. The guest peaks (peaks (*1101*) and (*2001*)) are highlighted by the dashed red line, and disappear at 365 K, some 20 K above the order-disorder transition temperature at 21 GPa. The host peaks are also labelled with their (*hklm*) indices.

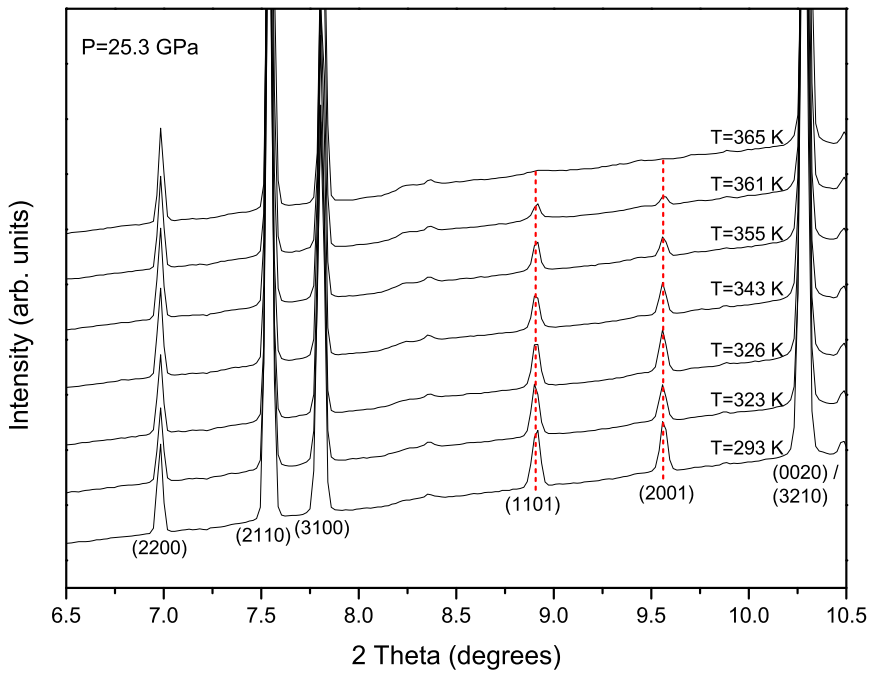

On increasing the temperature slightly to 365 K, in Figure 5.16 (c), the

Bragg reflections have disappeared completely and only the diffuse scattering remains. The order-disorder transition temperature increases by 20 K when the pressure is increased 3 GPa. Figure 5.18 is an example of azimuthally integrated 1D patterns from quasi-crystalline samples. It is clear from the Figure that the Bragg reflections from the guest completely disappear at ∼365 K at 25 GPa.

In Figure 5.17, the images represent a much more polycrystalline sample than that shown in Figure 5.16. Here, the guest reflections are highlighted by the open ovals. As the sample consists of numerous similarly-sized single-crystals, the line of diffuse scattering observed in the single-crystal and quasi-single crystal samples has been "washed out". Therefore, the only contribution of the guest peaks in Figure 5.17 is from Bragg scattering. The data shown in Figure 5.17 (a) is at 30.0 GPa and 375 K, and Figure 5.17 (b) is at 31.1 GPa and 373 K. By increasing pressure just 1.1 GPa, the guest reflections recrystallise. In the polycrystalline samples of *tI*19-K, the Bragg scattering from the guest component was significantly weaker than the host component and so azimuthal integrations were performed around only the guest peaks, excluding the host peaks, to obtain accurate *d*-spacings. Numerous P-T points at which the order-disorder transition occurred were cross-checked with quasi-single crystal and polycrystalline samples. Good agreement on the onset of the order-disorder transition was found between different samples.

By making small increases in pressure and temperature, the order-disorder transition line was measured up to 50 GPa using two polycrystalline samples and two quasi-single crystal samples. The order-disorder transition line is shown in Figure 5.19, where the dot-dash line is drawn between the order and disorder data points as a guide to the eye. Beginning at 20 GPa, the transition line has a positive gradient of ∼10 K/GPa, before levelling out at ∼26 GPa and ∼365 K. At 27.5 GPa, the previously-reported phase transition occurs in the host structure where it loses the *c*-glide symmetry; a major indication of this transition in the host is seen in the emergence of the (*1010*) host reflection, denoted by the ∗ symbol in Figure 5.20.

The order-disorder transition temperature (Figure 5.19) remains constant at 365 K indicating that the change in host structure alone has little effect

Figure 5.19: The order-disorder transition temperature with increasing pressure. Ordered guest chains are represented by the green closed triangles and disordered guest chains are represented by red open circles. The dot-dash line represents the order-disorder transition line and is drawn as a guide to the eye. The melting curve of K, as described in Chapter 4, is represented by the solid line, and solid-solid phase transition lines are represented by dashed lines. Note the short dashed lines indicate the phase change in guest structure only, and do not take into account the change in host symmetry. There are significant changes in gradient of the transition temperature, which may be influenced by intra-phase transitions occurring in both the host and guest structures.

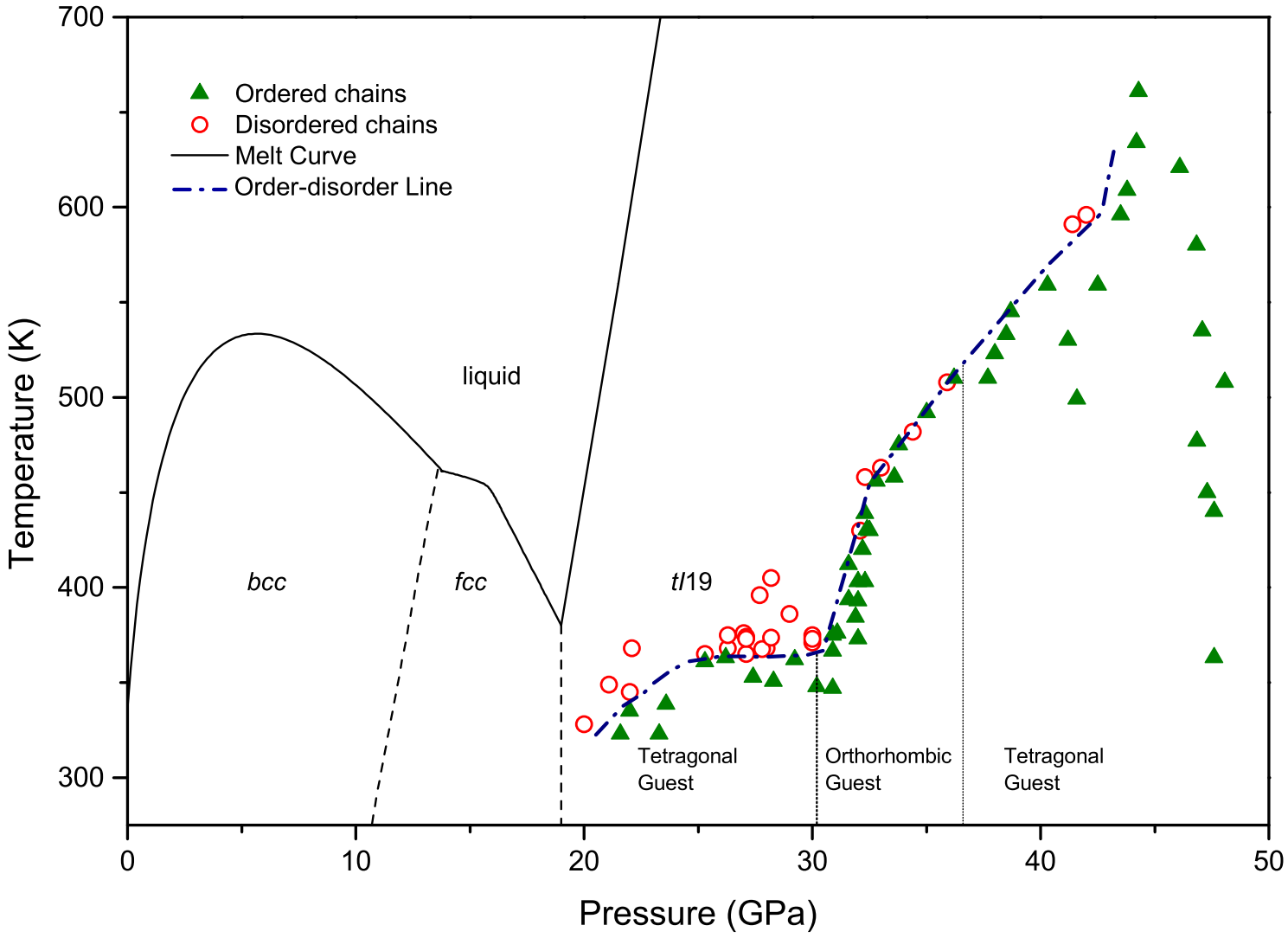

on the transition temperature. However, at 30.2 GPa and 365 K, the chains abruptly become ordered once more, and there is a sharp change in gradient of the melting transition temperature, increasing at a rate of at least 35 K/GPa. The gradient of the order-disorder transition line increases steeply until 32.3 GPa, where the gradient reduces, increasing at ∼15 K/GPa. At pressures above 37.7 GPa the guest structure in the ordered phase transforms back to the tetragonal structure it assumed below 30 GPa, and at ∼42 GPa the host regains its *c*-glide symmetry, signified by the disappearance of the (*1010*) host reflection. Above 42 GPa the host-guest phase is isostructural once more with the phase it adopted below 28 GPa.

Interestingly, the re-entrant guest transition appears to have no influence on the order disorder transition temperature – between 32.3 GPa and 42.5 GPa the gradient appears to be constant at ∼15 K/GPa, though it should be noted here that the absence of order-disorder points in the pressure range 37 to 42 GPa means we cannot exclude the possibility that there is another increase in the gradient of this transition line that we have not detected. Finally, at 42.5 GPa, there once more appears to be a sharp rise in the order-disorder transition temperature – it was not possible to disorder the guest chains at 660 K at pressures in excess of 43 GPa. This increase in the gradient of the order-disorder transition temperature may be influenced by the host undergoing the re-entrant transition at 42 GPa.

Further evidence for the change in the guest structure is provided in Figures 5.21 and 5.22. Figure 5.21 is a plot of the c_{Guest} lattice parameter and Figure 5.22 is a plot of the c_{Host}/c_{Guest} ratio. In each plot the purple triangles are the values of c_{Guest} and c_{Host}/c_{Guest} obtained if one assumes that the guest is tetragonal, and the blue circles indicate where it has been indexed on an orthorhombic lattice. Clearly, if one assumes that the guest structure does not undergo a phase transition then there are significant discontinuities in both the c_{Guest} lattice parameter and the c_{Host}/c_{Guest} ratio.

The c_{Host}/c_{Guest} ratio initially decreases, passing through a commensurate value of c_{Host}/c_{Guest}=8/3 at 22 GPa. The c_{Host}/c_{Guest} ratio reaches a minimum value of 1.58 at 30 GPa, and varies slowly when in the orthorhombic phase, becoming gradually more positive. Following the transformation in the guest back to a tetragonal structure the c_{Host}/c_{Guest} ratio once

Figure 5.20: 1D integrated diffraction profile indicating the change in both the host and guest structure. The † symbol indicated guest peaks that are indexed using a tetragonal lattice whereas the ‡ symbol represent the guest peaks that are indexed on an orthorhombic lattice. The host undergoes a loss of *c*-glide symmetry as indicated by the emergence of the (*1010*) host reflection highlight by the ∗ symbol.

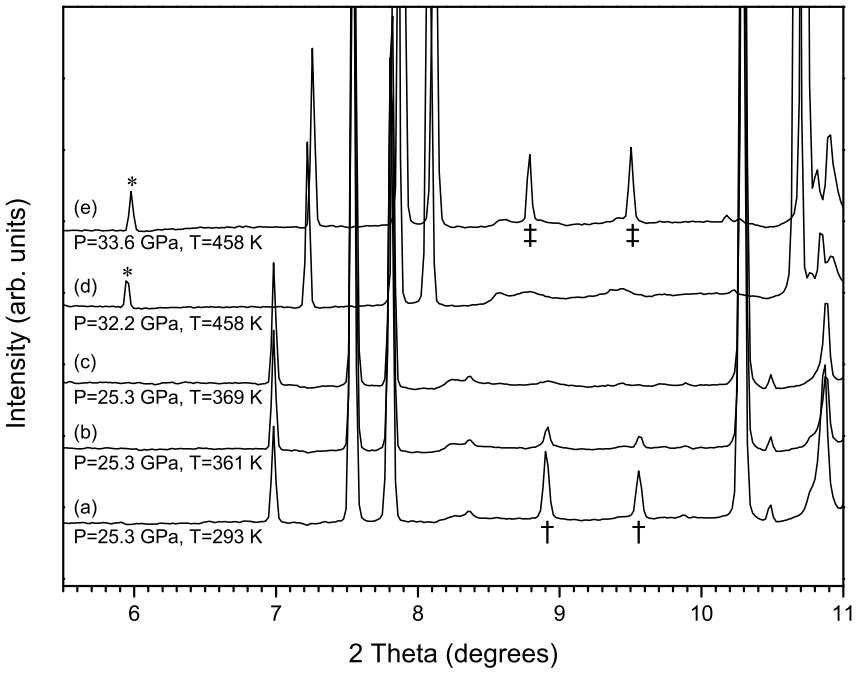

more passes through a commensurate value before increasing steeply from 1.60 at 38 GPa, to almost 1.66 at 47 GPa, in stark contrast to its behaviour below 30 GPa where it decreases with increasing pressure. The c_{Host}/c_{Guest} ratio increases steeply, approaching a second commensurate value of c_{Host}/c_{Guest}=5/3 at pressures of approximately 47 GPa.

What is curious is that the transition in the guest from a tetragonal-to-orthorhombic structure appears to have a significant influence upon the order-disorder transition temperature, while there is no evidence that the reverse phase transition at 37 GPa has any influence on this order-disorder transition whatsoever. Furthermore, at above 42 GPa, after the

Figure 5.21: The variation of the c_{Guest} lattice parameter of *tI*19-K with pressure, indexed using a tetragonal lattice – purple triangles – and an orthorhombic lattice – blue circles. The smooth variation of the c_{Guest} lattice parameter when the guest is indexed using both a tetragonal and orthorhombic lattice indicates it undergoes a series of tetragonal-orthorhombic-tetragonal phase transitions.

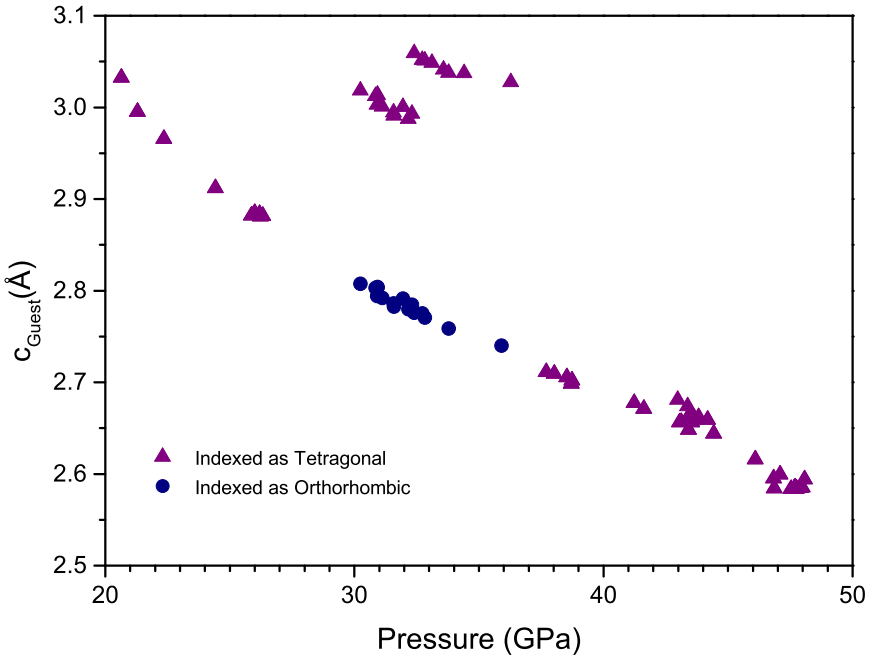

host undergoes a transition whereby it regains the previously lost *c*-glide symmetry, the order-disorder temperature undergoes yet another change in gradient, with no chain disordering observed up to 660 K.

One way to interpret the changing gradients in the order-disorder transition line is through considering the changes in the interaction between the host and guest components of the structure. A simple model to construct to understand the host and guest interaction would be to consider how fast the diameter of the host channel closes relative to how quickly the K atoms decrease in size with increasing pressure. See Figures 5.1 or 5.15 for an illustration of the host channel. The light grey guest atoms reside within channels formed by the dark grey host atoms. One would expect that if the

Figure 5.22: The variation of the c_{Host}/c_{Guest} ratio of *tI*19-K with pressure. The purple triangles represent the guest structure indexed on a tetragonal lattice; the blue circles indicate the guest structure indexed using an orthorhombic lattice. To avoid discontinuities and to have a smoothly varying c_{Host}/c_{Guest} ratio the guest must undergo a tetragonal-orthorhombic-tetragonal phase transition series

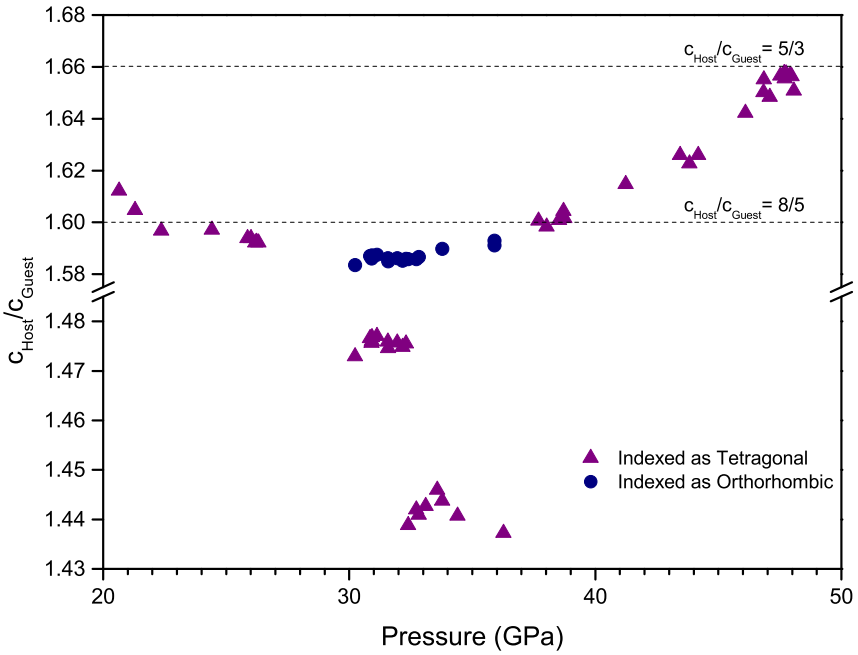

channels became smaller at a faster rate than the atoms decreased in size as pressure was increased, then the host would have more of an effect on the guest, due to their increased proximity and hence increased interaction, making it more difficult to disorder the guest structure, and hence causing the gradient of the order-disorder transition line to increase.

Several assumptions are required in this model. One such assumption is that the distance of closest approach in the composite structure is effectively the diameter of the atom. In the host-guest structure, the shortest distance is the nearest-neighbour (n.n.) distance in the host structure, and is indicated in Figure 5.15 by the blue arrow.

To extract the n.n. distance, one needs to perform Rietveld refinements (on powder diffraction data), or perform single-crystal refinements, at small (1 GPa) pressure intervals between 21 GPa and 50 GPa, and extract the $16k$ Wyckoff positions of the host structure. These Wyckoff positions have two refinable positions (x and y) which vary with pressure (McMahon *et al.* 2006). Obtaining these positions at different pressures will allow the calculation of the distance of closest approach of the host atoms (the atom size in this model), and will furthermore, allow the calculation the diameter of the channels, as this also depends on the atomic positions.

Unfortunately, the powder diffraction data obtained in this study was of insufficient quality to perform Rietveld refinements, and, due to the steep gradient in the melting temperature, it has not yet been possible to grow a single-crystal of *tI*19-K at pressures above 21 GPa. As a consequence, neither the size of the channel nor the n.n. distance can be obtained, and hence the atom size, can be obtained. Higher-quality powder diffraction data is required to test this model.

5.6 Conclusion

An order-disorder transition in the incommensurate host-guest phase of K has been investigated using single-crystal, quasi-single crystal and polycrystalline samples and *in situ* X-ray diffraction techniques. A single-crystal refinement was performed on the host and guest structure at room temperature and atomic displacement parameters determined. It was discovered that the average displacement of the guest atoms along the incommensurate *c*-axis is $\sim$14 % of the nearest neighbour distance. In the context of the Lindemann criterion (Lindemann 1910), this suggests that the guest chains are liquid-like along the *c*-axis, exhibiting a large degree of disorder even at room temperature.

Furthermore, in agreement with a study conducted by Lundegaard *et al.* (Lundegaard 2013) the incommensurate host-guest phase of K undergoes a series of complex phase transitions with increasing pressure, with both the host and guest structure undergoing phase transitions. The intra-phase transitions in the guest structure appear to have some influence over the

gradient of the order-disorder transition temperature, though it should be noted that the re-entrant orthorhombic-to-tetragonal transition appears to have no effect on the order-disorder transition temperature.

Importantly, the variation of the c_{Host}/c_{Guest} ratio, the fact that it passes through two commensurate values with increasing pressure, and approaches a third commensurate value before the transition to the $oP8$ phase, means that there are several different pressure points at which it would be meaningful to perform full electronic structure calculations on tI19-K, perhaps providing insight into the mechanism for the intra-phase transitions described here, and the changing gradient in the order-disorder line.

Section II:

Dynamic Compression Studies on Sodium

Chapter 6

Dynamic Compression of Sodium

6.1 The Limits of Static Compression Techniques

The diamond anvil cell is an extremely useful tool in high-pressure science. In the last decade it has revealed a wealth of unexpected and complex physical phenomena. The low-symmetry, open-packed crystal structures and unusual melting behaviour observed in the alkali elements under compression using this technique is described in detail in Chapters 2, 4 and 5. This technique does, however, have its limits.

Due to mechanical stability of the diamond anvils, the pressures that can be achieved with this technique have been typically limited to a maximum of ∼400 GPa. Recently, advances have been made in developing a double-stage diamond anvil cell (dDAC), whereby diamond spheres, 20-50 μm in diameter are embedded on the flat diamond culets, and samples are compressed between the small spheres. For example, in their development of this technique, Dubrovinsky *et al.* have recently reported the compression of rhenium to pressures in excess of 640 GPa at room temperature (Dubrovinsky & Dubrovinskaia 2012).

However, it should be stressed that, according to the developers of the dDAC, it seems unlikely that this technique could be readily applied to

studying the alkali elements (Dubrovinsky 2012). An alternative technique to reach states beyond the limits of the diamond anvil cells is to use shock and quasi-isentropic (QI) compression (also known as ramp-compression) techniques.

There are several techniques that may be used to generate shock wave e.g. flyer plates, magnetic fields, and lasers. This Chapter will focus on the use of high-powered lasers to generate extreme pressures in Na.

6.2 Laser-Driven Compression Techniques

High-energy lasers are used to create a pressurising wave by ablating the surface of a sample. In laser-driven ablation, the absorbed laser energy rapidly heats a few microns of the target material, causing the material to expand outwards at a high velocity. Due to conservation of momentum, a high-velocity wave is generated in the sample material, causing it to rapidly compress. Laser-driven shock-compression techniques, combined with optical velocimetry and reflectivity measurements, have allowed the investigation of phase transitions at multi-megabar pressures and thousands of Kelvin. By combining laser-driven shock-compression techniques with optical reflectivity measurements, for instance, an insulator-to-metal transition has been reported in quartz (SiO_2) (Hicks *et al.* 2006), an insulating-to-conducting transition has been reported in helium (He) (Celliers *et al.* 2010), and a liquid-liquid transition has been reported in magnesium silicate ($MgSiO_3$) (Spaulding *et al.* 2012). This liquid-liquid transition will be discussed later in this Chapter.

Laser-driven shock-compression studies on iron (Fe) demonstrate the utility of high-energy lasers as a means to investigate phase transitions at extreme compressions, and, moreover, demonstrate the complimentary nature of static and dynamic compression techniques. Dynamic compression of Fe dates back to the 1950s when, in 1956, using explosive detonation to generate shock waves in Fe, Bancroft *et al.* suggested that due to observations in wave-profile measurements, a phase transition occurred at 13 GPa (Bancroft *et al.* 1956). Using static compression techniques combined with X-ray diffraction, Jamieson & Lawson directly observed this phase

transition, and described it as a body-centred cubic (*bcc*) to hexagonal close-packed (*hcp*) phase transition (often referred to as an α-to-ϵ transition in the literature) (Jamieson & Lawson 1962).

However, the question of whether the phase transition observed in static compression studies, which typically take place on minute-to-day time scales, was the same phase transition observed under shock-compression, which occur on picosecond to nanosecond time scales, remained unanswered until the last decade. Kalantar *et al.* used high-energy lasers not only to shock-compress Fe, but also to generate X-rays to probe the phase transition under dynamic loading *in situ*, and indeed observed the α-to-ϵ transition on shock-compression (Kalantar *et al.* 2005).

Shock-compression studies, however, do have a disadvantage when it comes to studying solid materials at extreme conditions. Under shock conditions, generation of entropy leads to extreme heating – discussed in detail in Section 6.4.2 – and so when materials are shock-compressed to pressures in excess of 200 GPa, they are in the liquid or plasma state. The last decade has seen the development of QI-compression techniques using lasers. By combining pulse shaping of the drive laser pulse with careful target design, one may more gradually compress materials to multi-megabar pressures, avoiding the associated sample heating involved in shock-compression (Higginbotham *et al.* 2012). In the last decade this technique has been applied to numerous materials including diamond, which was QI-compressed to 800 GPa (Bradley *et al.* 2009).

An example of the different paths in P-T space that aluminium would follow under shock, multi-shock and isentropic compression, superimposed on the melt curve of aluminium may be seen in Figure 6.1 (Lorenz *et al.* 2006). It is expected that under QI-compression, the point in P-T space a material will reach will be intermediate between the isentrope and the multi-shock trajectory, or Hugoniot, reaching multi-megabar pressures yet a temperature significantly below the melting temperature.

Rygg *et al.* combined *in situ* X-ray diffraction generated by a laser-plasma source with QI-compression techniques to measure crystalline diffraction up to pressures of 900 GPa (Rygg *et al.* 2012). Importantly, in their study of tantalum (Ta), Rygg *et al.* demonstrate *solid* diffraction at pressures in excess

Figure 6.1: An example of the predicted trajectories of aluminium under shock-compression, multi-shock compression and isentropic compression, superimposed with the melt curve. Under isentropic compression it is possible to compress far beyond the shock-melt pressure of the material yet remain in the solid state (Lorenz *et al.* 2006)

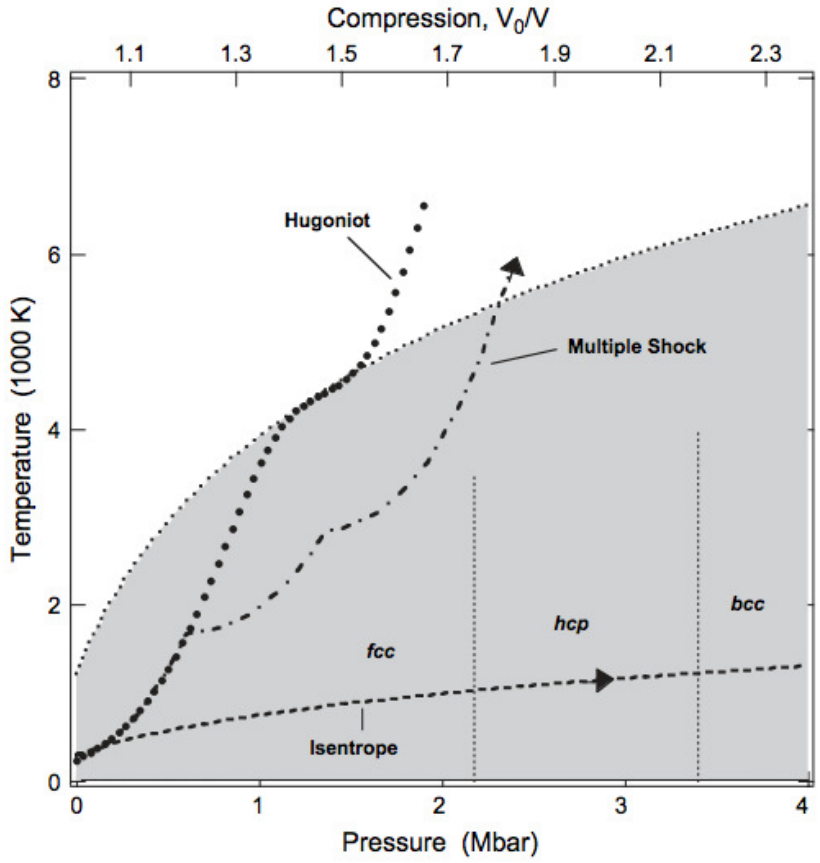

of the pressure at which melting had been observed along the Hugoniot. Figure 6.2 compares the volumetric compression of tantalum under QI- and shock-compression conditions. The thermal energy generated under shock conditions causes Ta to shock-melt at 240 GPa. Under QI-compression, solid-diffraction was obtained above this pressure, at 260 GPa. Perhaps the most striking and significant result of this study is that under QI-compression, the volumetric data measured lie closer to the cold curve, as determined by room-temperature DAC experiments, than the Hugoniot, indicating that the sample is at significantly lower temperature than would be reached on the Hugoniot.

Figure 6.2: Volumetric data for quasi-isentropically compressed tantalum as determined using *in situ* X-ray diffraction. This work by Rygg *et al.* demonstrates that it is possible to compress tantalum beyond the Hugoniot melting pressure, yet measure solid diffraction. Furthermore, their volumetric data lies much closer to the cold curve as determined by room-temperature diamond anvil cell experiments than the shock-compression curve, indicated that the quasi-isentropically compressed sample is considerably cooler than its shocked counterpart (Rygg *et al.* 2012)

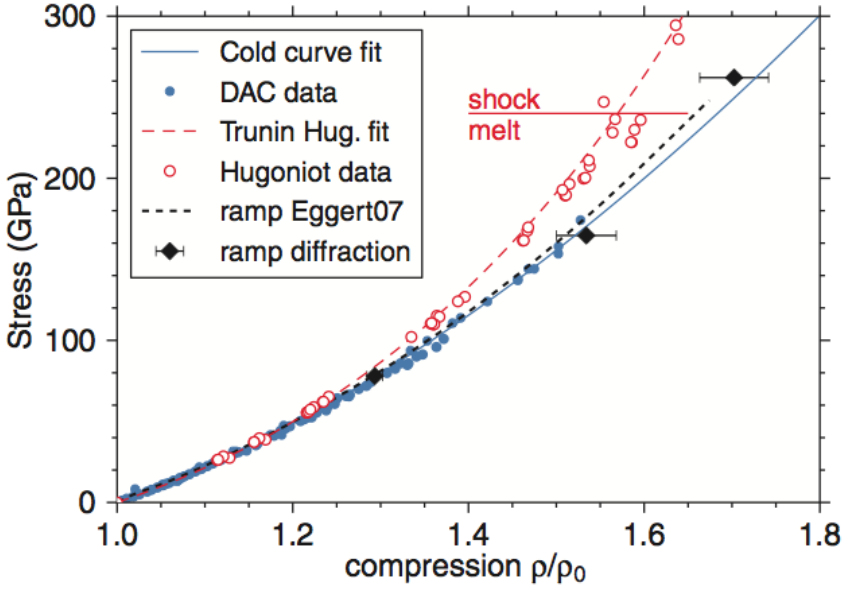

6.3 Motivation for Laser-Driven Compression of Na

Na is a model system to investigate the emergence of complex behaviour at extreme compressions. As explained in detail in Chapter 2, the alkali elements, at ambient conditions, are well described by the nearly-free electron model, and Na is perhaps the best example of a nearly-free electron alkali metal, calculated to maintain a spherical Fermi surface under compression in both the *bcc* and *fcc* phases which are stable up to 105 GPa (Degtyareva & Degtyareva 2009) (Hanfland *et al.* 2002).

At further compressions, beyond a megabar, Na crystallises into complex low-symmetry structures and is an example of unusual and unexpected bonding under pressure (McMahon *et al.* 2007) (Gregoryanz *et al.* 2008).

At megabar pressures, crystalline phases of Na are characterised by electrons becoming increasingly localised into interstitial regions, at which point the phase may be considered to be pseudo-ionically bonded, with the interstitial electrons playing the role of near massless negative ions (Ma *et al.* 2009).

The most striking example of this electron localisation effect in Na occurs at 200 GPa when the electrons are sufficiently localised that it transforms to a transparent electrical insulator. This phase is predicted to be stable up to 600 GPa, far beyond the limits of current diamond anvil cell techniques – dDAC techniques are currently not applicable to the alkali elements (Dubrovinsky 2012). Furthermore, the melting curve of Na is striking (Gregoryanz *et al.* 2005). The melting minimum, now observed in all the alkali elements, occurs in Na at pressures of a megabar, following which the melting temperature appears to increase at a rapid rate. It should be noted, however, that the melting curve has not been experimentally determined above 140 GPa due to the difficulties associated with containing a highly-reactive element at megabar pressures, heating it, and studying it with *in situ* diffraction.

With regards to performing high-pressure structural studies of Na using X-ray diffraction and DAC techniques, as one increasingly compresses the sample to achieve higher pressures, its thickness decreases. Therefore, the ratio of coherent scattering from the thin sample may be overwhelmed by the Compton scattering from the diamond anvils, particularly if it is a low-Z element like Na. The recent development of laser-driven QI-compression techniques are arguably the only available method to create extreme pressure states in such highly-reactive materials, while keeping the temperature sufficiently low so as to remain in the solid state. Importantly, Marqués *et al.* calculate that it requires temperatures in excess of 3,500 K to melt Na at 200 GPa (Marqués *et al.* 2011b). Furthermore, shock- or QI-compression may be the only way to investigate the nature of the liquid at 200 GPa, and by conducting a combination of QI- and shock-compression experiments it may be possible to map out the melting curve in at pressures on excess of a megabar.

This Chapter details target design, manufacture and an initial proof-of-principle study on laser-driven compression experiments on Na. This study

is part of an ongoing campaign to develop techniques to study the alkali elements at multi-megabar, if not gigabar, pressures.

6.4 Shock vs. Quasi-Isentropic Compression

The most important difference between shock and QI-compression is the associated heating due to a shock wave that is less significant in QI-compression experiments. To explain this we first appeal to several important concepts in shock-compression such as the Hugoniot and the Rankine-Hugoniot relations (Zel'dovich & Raizer 2002).

6.4.1 Rankine-Hugoniot Relations

For a given initial density, the locus of P-T states achieved following shock-compression is called the Hugoniot. At a shock front, conservation of mass, energy and momentum must be obeyed. These conservation relations are known as the Rankine-Hugoniot relations.

Consider a sample initially with density ρ_0, and moving at velocity u_0. If a shock travels through the sample from an initial position $x(t)$ to position $x(t+dt)$, in time interval dt, then the initial mass in this volume may be written as $\rho_0(U_s - u_0)Adt$, where U_s is the shock propagation velocity, and A is the cross sectional area of the shock front. Furthermore, in a time interval dt the location of this shock front has propagated a distance $u_p dt$, where u_p is the particle velocity. It is therefore simple to write an expression for conservation of mass:

$$\rho_0(U_s - u_0)Adt = \rho_1(U_s - u_p)Adt \tag{6.1}$$

where ρ_1 is the density of the sample at the shock front. Therefore, one obtains the relation:

$$\rho_0(U_s - u_0) = \rho_1(U_s - u_p) \tag{6.2}$$

This mass, $\rho_0(U_s - u_0)Adt$, acquires a momentum which is also conserved and may be expressed as $\rho_0(U_s - u0)Adt \cdot u_p$. This momentum may be related to a pressure via Newton's second law, where it is understood that force is

equal to the rate of change of momentum, and pressure is force per unit area. Therefore:

$$P_1 - P_0 = \frac{\rho_0(U_s - u_0)Adtu_p}{Adt} = \rho_0(U_s - u_0)u_p \tag{6.3}$$

Finally, energy is also conserved at the shock front, and so one may write that the increase in the sum of the kinetic and internal energies of the compressed sample is equal to the work done (W.d.) on the sample by the external force:

$$W.d. = P_1 Adtu_p - P_0 Adtu_0 = [\rho_1(U_s - u_p)Adt(E_1 + \frac{1}{2}u_p^2) - \rho_0(U_s - u_0)Adt(E_0 + \frac{1}{2}u_0^2)] \tag{6.4}$$

where here the kinetic and internal energies are expressed per unit mass. Here, $\frac{1}{2}u_p^2$ and E_1 is the kinetic and internal energy of the shocked material, and $\frac{1}{2}u_0^2$ and E_0 is the kinetic and internal energy of the unshocked material. By appealing to Equations 6.2 and 6.3, and by writing the volume in terms of the specific density i.e. $V = 1/\rho$, internal energy may be written as:

$$E_1 - E_0 = \frac{1}{2}(P_1 + P_0)(V_1 - V_0) \tag{6.5}$$

Frequently, one assumes that the initial pressure, P_0, and velocity, u_0, of the material are zero, simplifying these relations.

For most materials, U_s and u_p are related by a linear relationship, $U_s = c_0 + su_p$, where c_0 is the speed of sound of the material at ambient conditions and s is a parameter determined from a fit to experimentally measured U_s and u_p data. Knowing this relationship, and through use of Equation 6.3, it should be clear that it is possible to determine the pressure state a sample reaches under shock conditions if one can measure u_p. The technique used to determine pressure in the experiments detailed in this Chapter was optical velocimetry, which will be explained in detail below. What is important to note is that although pressure may be determined through use of the Rankine-Hugoniot relations, it is not possible to determine temperature in this manner. The difference in temperatures achieved under shock- and QI-compression will be discussed below.

6.4.2 Heating due to Shock

There are distinct differences between shock and QI-compression. QI-compression is so-called as the P-T states a material may access under this type of compression lie closer to those it would achieve had it been isentropically compressed rather than shock-compressed (Higginbotham *et al.* 2012). Under shock-compression, materials will reach a point along their Hugoniot, and this type of compression has associated with it a considerable amount of heating. As can be seen from Equation 6.5, the change in internal energy on shock-compression is related to both pressure and volume. An example of a Hugoniot and an isentrope in P-V space may be seen in Figure 6.3, labelled P_H and P_i respectively. The dashed line is the Rayleigh line, connecting the initial and final states along the Hugoniot.

For a reversible process, such as compression along an isentrope, the increase in internal energy (ΔE_i) is equal to the area under the P-V curve mapped out by points V_0, V_1 and P_i in Figure 6.3:

$$\Delta E_i = -\int_{V_1}^{V_0} P_i dV \tag{6.6}$$

This is the increase in internal energy due to an elastic process, and is illustrated by the blue shaded region in Figure 6.3. In an irreversible process e.g. on shock-compression, the increase in internal energy is given by Equation 6.5, where $P_0 = 0$ and $P_1 = P_H$ in Figure 6.3. It is composed of both an elastic component and a thermal component. This is equivalent to the area traced out by the triangle V_0, V_1, P_H in Figure 6.3. The shaded red region on Figure 6.3 is the increase in internal energy due to the thermal energy only i.e. the difference in the increase in internal energy on shock-compression as opposed to QI-compression (Zel'dovich & Raizer 2002).

Alternatively, one may write:

$$\Delta E_i = \int_{V_1}^{V_0} TdS - \int_{V_1}^{V_0} PdV = \frac{1}{2}(P_H)(V_1 - V_0) \tag{6.7}$$

Comparing Equation 6.7 with Equation 6.6 demonstrates that the generation of entropy is responsible for an additional contribution to the internal energy, which is responsible for heating on shock-compression.

Figure 6.3: A Hugoniot (labelled P_H) and isentrope (labelled P_i in P-V space. The area shaded in blue is the increase in internal energy on isentropic compression (a reversible process). The area shaded in red is the difference in the increase in internal energy on shock-compression compared with the increase in internal energy on isentropic compression. This increase in internal energy leads to a large increase in sample temperature on shock-compression. The increase in internal energy on quasi-isentropic compression is intermediate between the two cases detailed here.

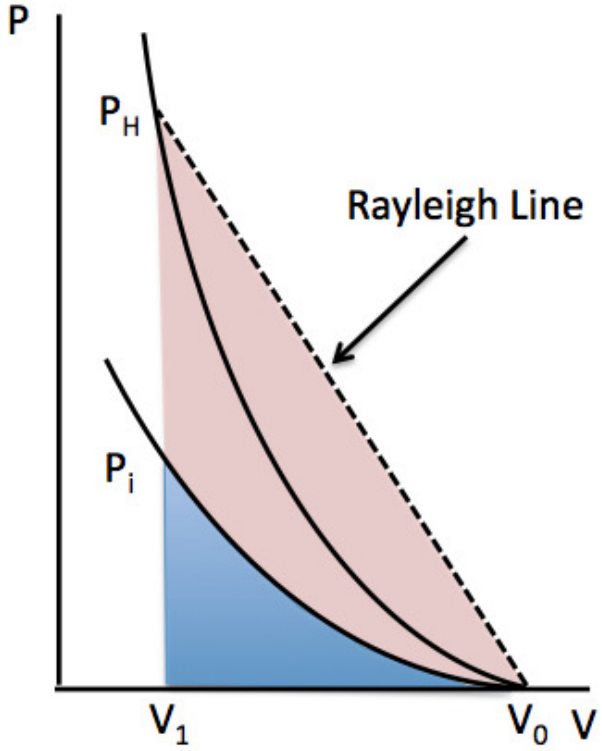

In reality, a material under QI-compression follows a path somewhere intermediate between the isentrope and the Hugoniot. The large contribution to the entropy that a material experiences on shock-compression is avoided, i.e. heating is minimal, and so it is possible to maintain sufficiently low temperatures to probe materials in the solid state at multi-megabar pressures.

6.5 Target Design

Careful considerations must be made to create targets for QI-compression experiments. Unlike a shock, which propagates unchanged through a material provided it is sufficiently supported by the drive, a QI-compression wave is initially more gradual. As the QI-compression wave progresses through the material, it steepens continually. If this compression wave steepens sufficiently, the sample can "shock-up", and hence sample thickness is a key consideration in target design (Swift & Johnson 2005). One requires a sample to be sufficiently thin so as to avoid steepening up and shocking, but also sufficiently thick to avoid complex reverberation effects which can lead to a misinterpretation of the data.

Target development and design was a key focus of this Thesis research, and improvement and development of target design is still ongoing. For instance, the target design detailed here was used in August 2011 on the Janus laser at the Jupiter Laser Facility, LLNL. At the time of writing, an additional campaign (June 2013) has been completed. This involved minor changes to the target design, and improvements to the target-loading techniques.

The target design used in the August 2011 experiments consisted of 20 μm thick nanocrystalline diamond (Diamond Materials), squares of tantalum foil (Goodfellows) with a 1.5x1.5 mm square laser drilled out of the centre to act as a gasket material (frame) and set the target thickness, and a single-crystal of 500 μm lithium fluoride (LiF). The drive laser would be incident on the surface of the diamond, ablating it, and hence driving a pressurising wave through the sample. The single-crystal of LiF acts as a window material. The probe laser (used for optical velocimetry and optical reflectivity measurements) passes through the window, and what is measured is the LiF/sample interface.

The diamond and the LiF have a flash coating of $\sim$0.1 μm of aluminium (Al). As Na was expected to undergo significant changes of reflectivity throughout the experiment (see Section 6.8), the Al coatings would ensure that part of the LiF/sample interface, or the diamond/sample interface would remain reflecting even if Na transformed to the transparent insulating phase, ensuring that optical velocimetry techniques could be used to measure

Figure 6.4: A schematic of the target design used for laser driven compression experiments on Na. A typical target consists of a 20 μm thick nanocrystalline diamond (Diamond Materials), squares of tantalum foil (Goodfellows) with a 1.5x1.5 mm square laser drilled out of the centre to act as a gasket material (frame) which set the target thickness, and a single-crystal of 500 μm lithium fluoride.

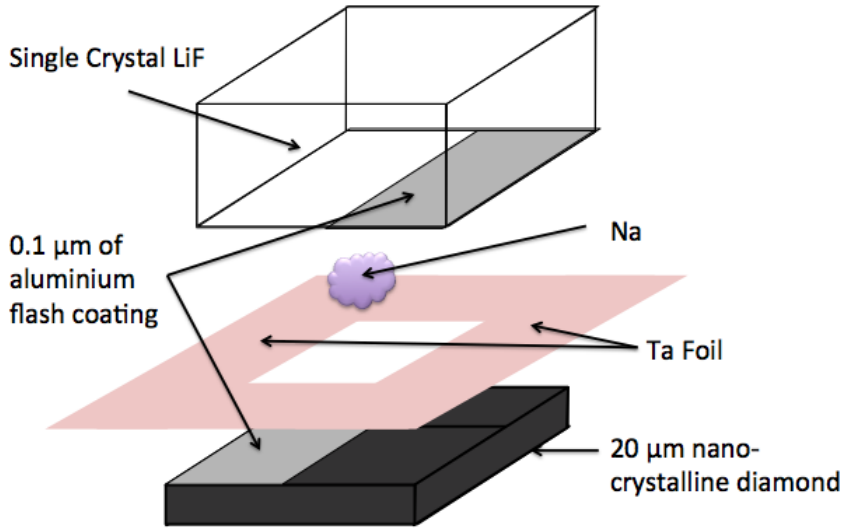

the velocity of the moving interface, and hence that the pressure could be determined. Optical velocimetry (VISAR) will be explained in Section 6.7.

The surface of the LiF window (without the Al flash coating) which faced the probe laser, i.e. the LiF/vacuum interface, had an anti-reflection coating to ensure that reflections from the rear surface of the LiF did not interfere with reflections of interest i.e. to ensure that the reflections measured arose from the LiF-sample interface rather than the free-surface of the LiF. A schematic of the target design is illustrated in Figure 6.4.

6.5.1 Sample Loading

Na, like all of the alkali elements, is highly reactive, and so great care was required to be taken with sample preparation. Modified diamond anvil cells ("jigs") with large sapphire anvils were used for sample loading. Pieces of LiF with frames of Ta foil, attached with micron-thick layers of epoxy (Araldite), were secured to the bottom anvil, as illustrated in Figure 6.5. All

LiF pieces have the flash coating of Al described above. A piece of 2×2 mm nanocrystalline CVD diamond was attached to the top anvil and the pieces were offset with respect to each other to obtain a ∼100 μm gap between the aluminium coatings. The gap between the Al layers would ensure that when Na transformed to the transparent insulating phase, part of the target would lose reflectivity entirely. An example of how the aluminium coatings were offset with respect to each other may be seen in Figure 6.5 (a).

Figure 6.5: Target alignment and loading techniques: (a) An illustration of how the ∼0.1 μm flash coating of aluminium which coated half of the diamond ablator and half of the lithium fluoride window were aligned and offset with respect to each other. The aluminium flash coating was to ensure good reflectivity at extreme compressions. (b) An illustration of how targets were loaded. Target materials were secured to large sapphire anvils, and small pieces of Na were loaded rapidly in a high-quality glovebox, and squeezed to a thickness set by the tantalum frame. Quick-curing epoxy was used to seal the targets from oxygen and moisture.

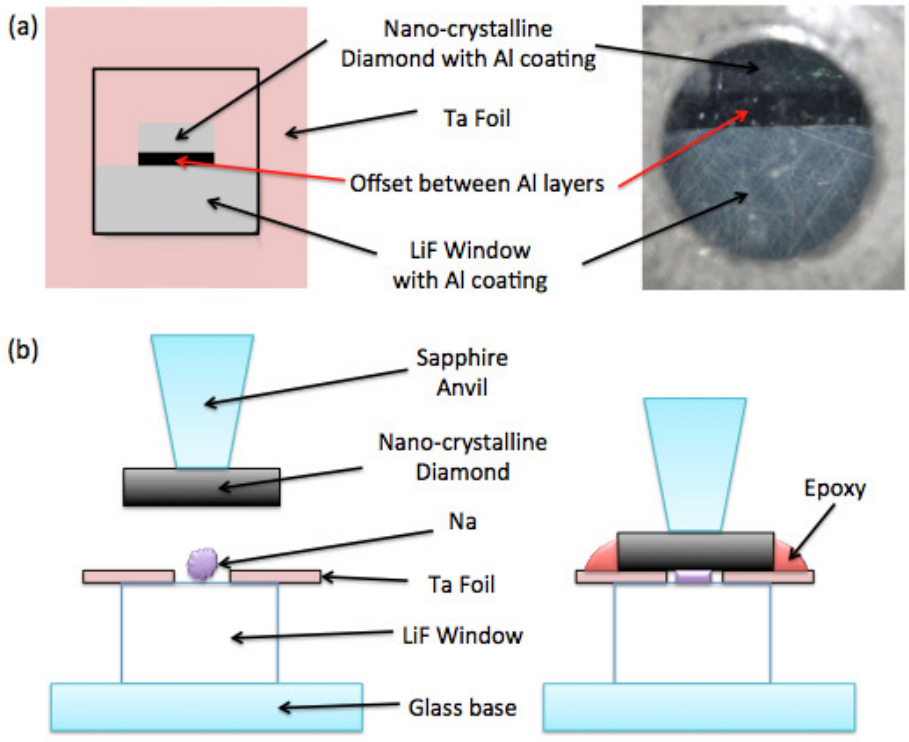

The jigs and target materials were place in a high-quality glove box with O_2 <1 ppm and H_2O <1 ppm. High-purity samples of Na (99.8 % Alfa Aesar)

were loaded, rapidly, under argon in this dry, oxygen-free environment, directly onto the LiF surface. Good contact between the Na and the diamond/LiF surfaces was achieved by closing the jig securely, squeezing the Na down to a thickness set by the Ta foil. The diamond-Ta interface was then sealed with quick curing epoxy (Araldite) to prevent sample reaction when removed from the argon atmosphere. The target jig and loading technique is summarised in Figure 6.5 (b).

Despite taking precautions to prevent Na reacting (e.g. loading in a glovebox), its highly reactive nature means that even in such a dry, oxygen-free environment an oxide layer may form on the surface throughout the loading process. From experience, the oxide layer is a few nm in thickness – a surface effect only. However, the experiments contained within this Chapter rely on diagnostics which measure reflectivity changes of the Na-LiF interface to determine the onset of phase transitions, and so it was vitally important to ensure that the targets had no such oxide layer.

The presence or lack of an oxide layer may be clearly seen through visual inspection of the completed targets. Figure 6.6 shows two completed targets that have been removed from the glovebox. Figure 6.6 (a) shows target without any reaction. The Na is highly reflective and in fact is of comparable reflectivity to the Al flash coating, as expected at ambient conditions. Figure 6.6 (b) is a target with an oxide layer on the surface of the Na. The Na is visibly duller than the Al flash coating, a clear indication that a reaction has occurred.

All targets were visually inspected prior to each experimental shot, and only results from targets that were determined to have no oxide layer are described in this Chapter.

6.6 Janus Experimental Setup

The experiments were carried out at Janus at the Jupiter Laser Facility (JLF), LLNL. Janus is a two-beam system Nd:glass laser system which is capable of delivering ∼1 kJ in 0.35-20 ns at λ=1053 nm. In the experiments described here, frequency-doubling crystals were employed, capable of delivering ∼500 J at λ=527 nm. Typical maximum energies

Figure 6.6: Examples of completed Na targets for laser driven compression experiments: (a) The Na and Al layers pictured are of comparable reflectivity, as expected at ambient conditions, indicating that the Na has not tarnished or reacted. (b) Here the surface of the Na is considerably less reflecting than the Al. This is due to the formation of an oxide layer on the Na surface, indicating a reaction has taken place. All targets were inspected and only those that showed no signs of reaction were shot (used for experiment).

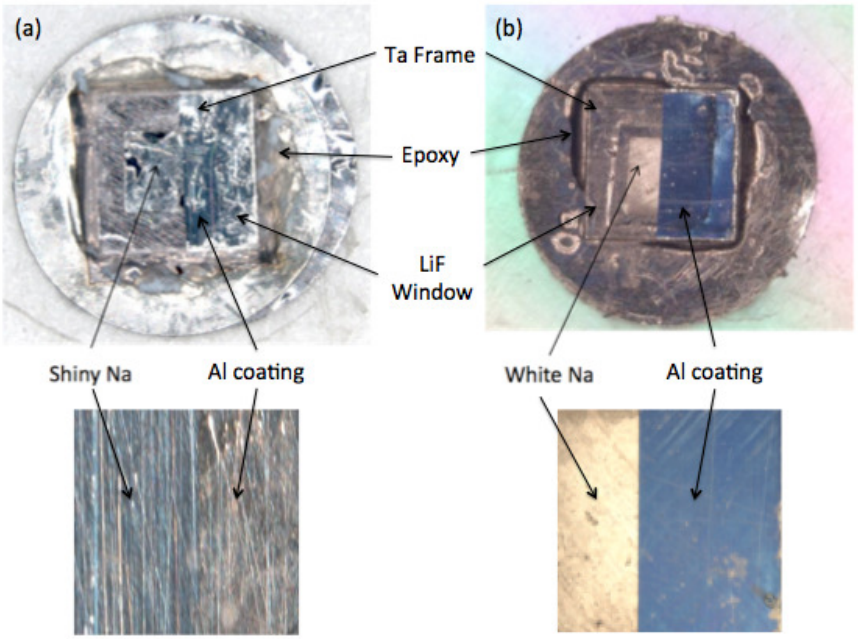

on target throughout this campaign, however, were ∼350 J. This facility has pulse-shaping capabilities and both 10 ns ramp pulses and 2 ns square pulses were utilised throughout this campaign for QI- and shock-compression, respectively. Pressure was determined using optical velocimetry (VISAR) and temperature gauged using streaked optical pyrometry (SOP). Optical reflectivity of the sample was measured using the 532 nm VISAR probe laser. These techniques will be expanded upon in subsequent Sections (Sections 6.7, 6.8, and 6.9).

A schematic of the Janus target chamber may be seen in Figure 6.7, and a photograph of the chamber setup used in these experiments is shown in Figure 6.8. The 527 nm drive beams enter the chamber, one normal to the target (West beam), and one entering the chamber at 27 degrees to target normal (East Beam). Phase plates were used to ensure a uniform laser spot

Figure 6.7: A schematic of the Janus target chamber, indicating the East and West beams of the 527 nm Janus laser, and the 532 nm VISAR laser beam, incident on a target.

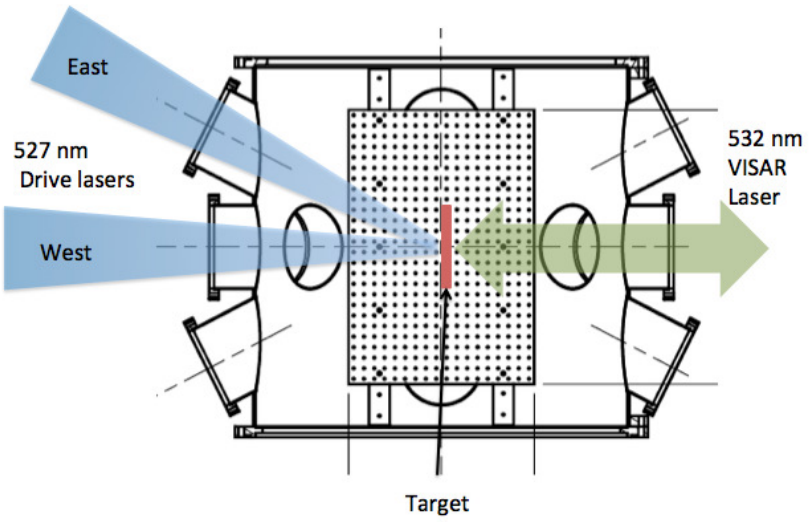

and hence uniform ablation of the sample. For the majority of shots, 1,000 μm phase plates were used. To achieve the highest pressures in this study, 600 m phase plates were employed. VISAR and SOP were normal to the sample/LiF interface.

6.7 VISAR

One of the principle diagnostic methods for investigating samples in shock experiments is by optical observations. Pressure is a key variable to be determined in these experiments, and this is done so typically through use of VISAR – Velocity Interferometry from the Surface of Any Reflector – which measures the velocity of the moving reflecting surface. In these experiments, the VISAR laser passed through a transparent (LiF) window, and the reflecting surface measured was the Na/Al-LiF interface, as shown in Figure 6.9.

This technique relies on the relativistic Doppler effect: when a moving object is illuminated with light of wavelength λ_0, the reflected wavelength, λ, is given by:

Figure 6.8: Photograph of the Janus target chamber indicating the incident drive and VISAR laser beams

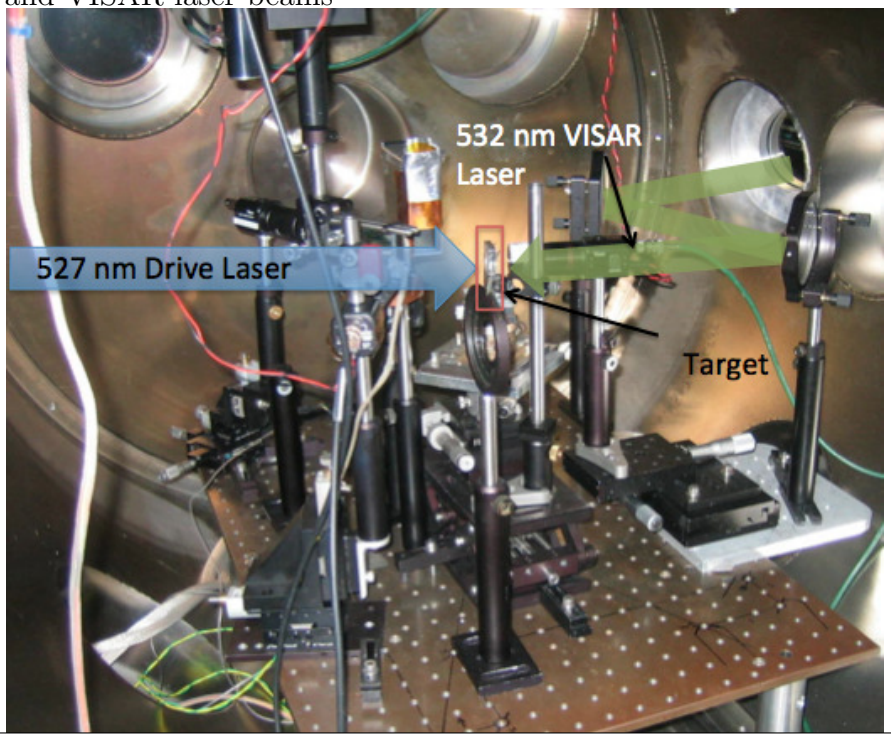

Figure 6.9: An illustration of the VISAR laser incident on a target. The VISAR beam passes through the transparent LiF window and reflects off the Na/LiF interface. The velocity of this interface under shock or QI-compression, is measured, and used to determine pressure.

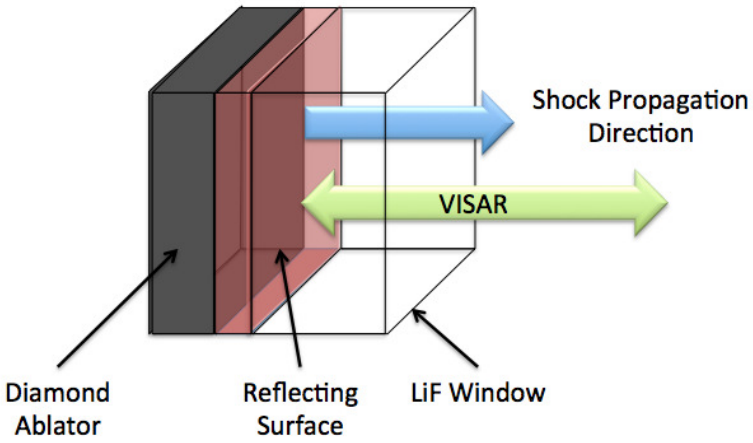

$$\lambda = \lambda_0 \left[\frac{1 - v/c}{1 + v/c}\right]^2 \approx \lambda_0(1 - 2v/c) \tag{6.8}$$

where v is the velocity of the moving surface, and c is the speed of light in a vacuum. The approximation in Equation 6.8 is due to the fact that typical velocities measured are less than a factor of 0.001 of c.

6.7.1 VISAR Setup at Janus

The composition of a VISAR setup has been described in detail by Barker & Hollenbach (Barker & Hollenbach 1972), and by Celliers *et al.* (Celliers *et al.* 2004), and a simplified example may be seen in Figure 6.10. The VISAR setup at Janus at the Jupiter Laser Facility, LLNL, consists of a λ=532 nm probe laser, which reflects off the surface of a target. This light is then directed to a Mach-Zender interferometer. The coherent light is then split up into equal parts, and one part is passed through a leg which has a well-defined time-delay offset, τ, produced by a well-characterised etalon with a high index of refraction. The etalons used in these experiments were composed of fused silica, with an index of refraction $n = 1.46071$ at 532 nm. The light is then recombined, and upon recombination, the offset in the arms of the interferometer produces a fringe pattern.

The fringes formed by the time-delay in the interferometer are streaked in time using a Hamamatsu C7700 streak camera over an interval specific to the experiment, typically of order ∼10-50 ns in these experiments. The change in frequency, $\Delta\omega$, of the light due to being Doppler shifted is related to a change in phase, $\Delta\phi$, and velocity, u by: $\Delta\omega/\omega = \Delta\phi/\phi = 2u/c$. The VISAR approximation, vital for extracting useful information relating fringe shifts to velocities, relies on the fact that the change in velocity of the moving surface is slow compared to the time-delay, and therefore allows us to write an expression for a velocity per fringe (VPF) relation:

$$VPF = \frac{\lambda_0}{2\tau(1 + \delta)} \tag{6.9}$$

where the δ term takes into account the dispersion due to the etalon.

A change in the velocity of the reflecting surface, therefore, causes motion of the fringes. It should be noted that multiple fringe shifts are possible and

Figure 6.10: A simplified schematic of the VISAR setup used at Janus, JLF, indicating the dual interferometer beds used, with different etalons (grey rectangles), to resolve any ambiguity in the velocity of the moving surface. Beamsplitters are represented by the purple rectangles, and mirrors are indicated by the blue rectangles.

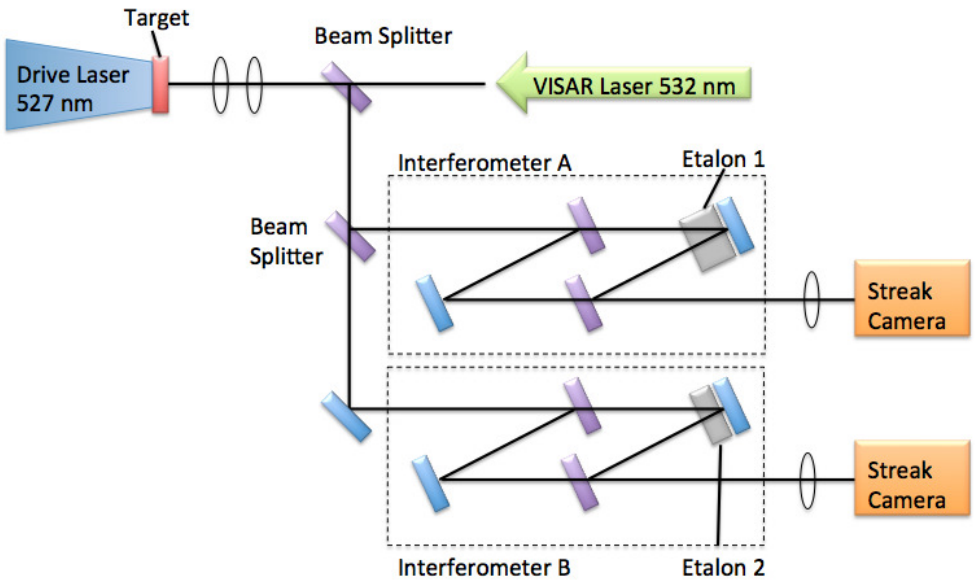

so to resolve ambiguities in the velocity, two interferometers are used at Janus, each with a different time-delay and hence a different sensitivity. It is vital that the one etalon is not an integer multiple of the other, such that when one analyses the data there is only one point when the velocity-time profiles agree.

As the VISAR laser will be reflecting from the Na/Al-LiF interface, rather than the LiF/vacuum interface, a correction to the VPF relation is required to take into account not only the refractive index of the shocked window (Celliers *et al.* 2004). The thickness of the etalons used in these experiments, and their associated time-delays and VPF relations, in vacuum and including the LiF correction, are shown in Table 6.1.

6.7.2 Extracting the Velocity

The phase difference, $\Delta\phi$, of the fringe shifts streaked over time is required to determine the velocity, and hence pressure, of the Na-LiF interface. To

Table 6.1: Thicknesses of etalons used in the Janus campaign on Na, including their time-delays, and values of velocity per fringe both in vacuum and with a correction for the LiF window

Etalon (mm)	Time-delay (ns)	VPF$_{vac}$(μm/ns)	VPF$_{LiF}$(μm/ns)
28.7722	0.1488	1.732	1.347
11.6399	0.0602	4.281	3.329
Later replaced with:			
11.3441	0.0587	4.392	3.415

extract the phase, one needs to perform a series of Fourier transforms. This analysis was originally described by Takeda *et al.* (Takeda *et al.* 1982) and is additionally described by Celliers *et al.* (Celliers *et al.* 2004). For these experiments the phase extraction was performed using a code written in IgorPro (WaveMetrics Inc.), and kindly provided, by J. H. Eggert, and will be briefly summarised here. Figure 6.11 is a summary of the data analysis techniques employed.

One may write an expression for the fringe intensity as:

$$g(x,t) = b(x,t) + c(x,t)\exp[2\pi i f_0 x] + c^*(x,t)\exp[-2\pi i f_0 x] \tag{6.10}$$

where f_0 is the frequency, $c(x,t) = \frac{1}{2}a(x,t)\exp[i\phi(x,t)]$, and all other symbols used have their conventional definition. By performing a Fast Fourier Transform (FFT), one obtains:

$$G(f,t) = B(f,t) + C(f - f_0, t) + C^*(f + f_0, t) \tag{6.11}$$

The spectra obtained following the FFT may be observed in Figure 6.11 (b). By filtering, i.e. removing the background function from the phase by selecting C, and performing an Inverse Fast Fourier Transform (IFFT), one may extract a "wrapped" phase:

$$W[\phi(x,t) + 2\pi f_0 x] = \arctan[Re(C(x,t)), Im(C(x,t))] \tag{6.12}$$

This so-called wrapped phase is bounded by the values $[-\pi, \pi]$ and so

Figure 6.11: A summary of analysis for extracting velocity of a moving surface from VISAR (optical velocimetry) data. (a) Is an example of raw data, (b) the Fourier transform, (c) an example of a "wrapped" phase, (d) the extracted velocity, and (e) a lineout of said velocity. The image is taken from Celliers *et al.* (Celliers *et al.* 2004)

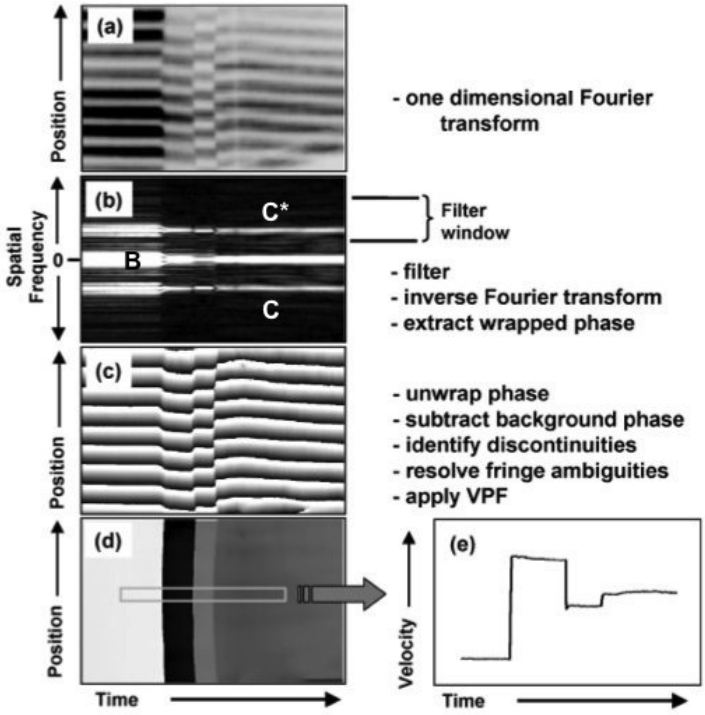

discontinuities occur when ϕ passes through odd multiples of π. Therefore, an offset is added to remove these discontinuities and a background is subtracted. The VPF relation is then applied to this unwrapped phase and the fringe ambiguities are resolved. An example of an unwrapped phase and the velocity-time profile obtained may be seen in Figures 6.11 (d) and (e).

6.8 Optical Reflectivity

Numerous diamond anvil cell studies have noted changes in the reflectivity of Na as it undergoes solid-solid phase changes, including the transformation to a transparent insulating phase ($hP4$) at pressures in excess of 180 GPa (Ma *et al.* 2009) (Marqués *et al.* 2011b) (Lazicki *et al.* 2009). Photomicrographs of Na in a DAC at various pressures may be seen in Figure 6.12 and one

can clearly see significant changes in reflectivity in visible light prior to the transformation to the transparent phase. In Figures 6.12 (a) and (b), Na is in the *cI*16 phase at 120 Pa, and the *oP*8 phase at 124 GPa respectively. Both phases are shiny and highly reflective under visible light. At 156 GPa, Figure 6.12 (c), Na is in the stability field of the *tI*19 phase, and one can clear see that the sample is considerably less reflecting and is in fact black, indicating a departure from metallic behaviour. Finally, Figure 6.12 (d) is shown in transmitted light and one can see that at 199 GPa Na is now transparent.

Figure 6.12: Photomicrographs of Na in a diamond anvil cell at various pressures Photomicrographs of Na at different pressures in a diamond anvil cell. Images (a) and (b) illustrate that Na is still a reflective metal in the *cI*16 phase at 120 GPa (a) and the *oP*8 phase at 124 GPa (b). When Na undergoes a transition to the *tI*19 phase (c), the sample becomes black indicating a departure from metallic behaviour. Finally, at 200 GPa (d) Na is observed to be a transparent insulator (Ma *et al.* 2009).

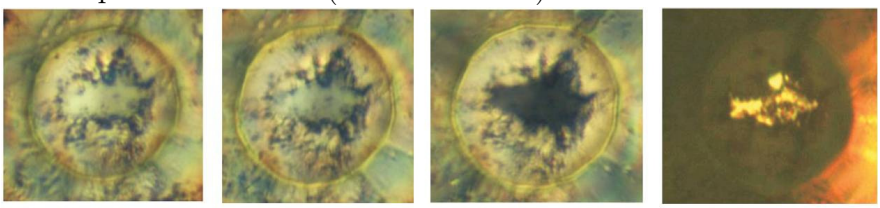

To further quantify the changes in reflectivity that Na exhibits between ambient pressure up to and including the *tI*19 phase (125 GPa at room temperature), Lazicki *et al.* used optical reflectivity and synchrotron infrared absorption techniques to make a comprehensive investigation on changes in optical properties (Lazicki *et al.* 2009). Figure 6.13 is a summary of the changing optical reflectivity of Na in different phases over a wide range of photon energies. The vertical dashed line indicates the photon energy of the VISAR probe laser – 2.33 eV. Clearly, as Na departs from the high symmetry *bcc* and *fcc* phases and transforms to lower symmetry structures, these complex phase changes are accompanied by electronic transitions that are manifested in distinct changes in reflectivity.

Lazicki *et al.* observe a slight drop in reflectivity, by approximately 15 % in the visible range, on transforming from *fcc* to *cI*16 at 105 GPa. Further

Figure 6.13: The reflectivity of Na at room temperature and at various pressures as determined using synchrotron infrared absorption spectroscopy and optical reflectivity techniques. The experimental data is shown as solid lines, the dot dashed lines indicated Lorentz oscillator fits to the data. The wavelength of the 532 nm VISAR laser used to measure optical reflectivity of Na in the dynamic compression experiments contained within this Chapter is indicated by the vertical purple dot dashed line at 2.33 eV. Following the *bcc* and *fcc* solid phases, there are significant reflectivity changes at 2.33 eV as Na undergoes a series of phase transitions, prior to the onset of the transparent phase a 200 GPa (Lazicki *et al.* 2009)

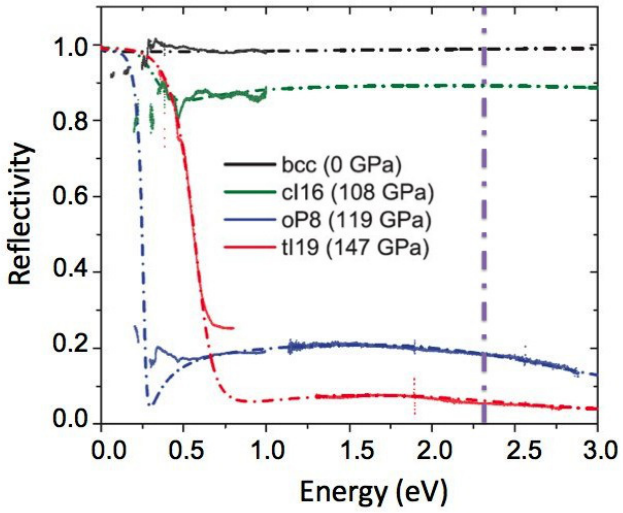

transformations to *oP*8 at 118 GPa and *tI*19 at 125 GPa have associated significant decreases in reflectivity at 2.33 eV (Lazicki *et al.* 2009). Therefore, one would expect that upon QI-compression one would observe significant changes in the reflectivity of Na, prior to the onset of the transparent phase where reflectivity would be lost entirely.

Optical reflectivity of Na was measured directly at 532nm (2.33 eV) using the VISAR probe layer and streaked over time. The reflectivity of Na over time was normalised to an average of the reflectivity of the uncompressed (Na) sample. Furthermore, the reflectivity of the Na prior to compression was compared directly to that of the Al flash coating at ambient conditions, as a check to determine whether the Na had reacted. At ambient conditions, the reflectivity of Na and Al is comparable, whereas if an oxide layer has formed on the Na surface, the reflectivity of Na would be greatly reduced

compared to Al.

The reflectivity of the sample, streaked over time is given by:

$$R_{Na} = \frac{I_{Na_t}}{I_{Na_i}} F \tag{6.13}$$

where I_{Na_t} is the intensity of the light reflecting from Na, streaked over time, and I_{Na_i} is the intensity of the light reflecting from unshocked Na. F is a normalisation factor, adjusted so that $R_{Na} \sim 1$ prior to breakout at the Na/LiF interface.

Upon the transformation to the transparent phase, the expectation is that one would see through the Na to the surface of the diamond ablator. This would be made evident by the loss of VISAR fringes as the laser passes through the transparent sample. The VISAR laser would then reflect off the layer of aluminium on the back of the diamond ablator, and so fringes would return. The offset between the Al layers on the LiF and the diamond ablator would give a region where no fringes exist.

6.9 Streaked Optical Pyrometry

As described in Section 6.4.2, under shock-compression the generation of entropy leads to a large increase in the temperature of the sample. One method to determine temperature in shock-compression experiments is through use of streaked optical pyrometry (SOP). The setup used at Janus, JLF, was developed and described in detail by Spaulding *et al.* (Spaulding *et al.* 2007), and is similar to apparatus developed on the OMEGA facility, described by Miller *et al.* (Miller *et al.* 2007).

SOP operates by collecting the self-emission of the target, streaked over time, throughout a shock-compression experiment. This self-emission is calibrated to a temperature; the streak camera output may be calibrated to the source radiance of a standard material e.g. α-SiO_2.

Radiance, $L(\lambda)$, is then related to a temperature via Planck's law:

$$L(\lambda, T) = \varepsilon \frac{2hc^2}{\lambda^5} \frac{1}{e^{hc/\lambda T} - 1} \tag{6.14}$$

where T is temperature, λ is wavelength of the radiation, h is Planck's

constant, c is the speed of light and ε is the emissivity of the sample. In such temperature calibrations a "grey body" assumption is often made, whereby $\varepsilon<1$ is assumed to be constant.

During this initial campaign, an attempt was made to calibrate the SOP diagnostic using α -SiO_2. However, this calibration was unsuccessful due to issues relating to the drive laser, and so it was not possible to extract sample temperatures in this campaign. Therefore, throughout this preliminary study, SOP signal was used to place an upper limit on the temperatures reached during QI-compression – the SOP setup at Janus is sensitive to temperatures of 4,000 K and above (Spaulding *et al.* 2007). Under QI-compression conditions the sample temperatures were below this temperature limit, as determined by the absence of any signal on the SOP. Sample temperatures reached under shock-compression were expected to follow the calculated Hugoniot by Wang & Sun (Wang & Sun 2001).

6.10 Shock and Quasi-Isentropically Compressed Na

This Section contains the results of preliminary experiments conducted on Na using laser-driven compression techniques. The aim of these experiments was to QI-compress Na to pressures in excess of 200 GPa, observing the onset of the transparent insulating phase through monitoring changes in reflectivity of the sample at 532 nm (2.33 eV). QI-compression of the targets was achieved through direct-drive of the diamond ablator.

Direct-drive techniques utilise pulse shaping of the drive lasers to directly apply a ramped irradiance profile to a diamond ablator, which in turn would send a QI-compression wave through the sample (Swift & Johnson 2005). An alternative method to this would be to use indirect drive, whereby there is a vacuum gap between the ablator and the sample. A laser would be used to create a shock in the ablator, causing the material to expand outward. Material from the ablator would rarefy across the vacuum gap and impact against the sample surface, causing a QI-wave to be generated through the sample. This method is particularly useful as it decouples the laser pulse-shape from the compression wave (Smith *et al.* 2008). The current target

design for laser driven compression of Na, however, is designed for direct-drive only.

The ramped laser pulse shapes used varied from shot to shot. Examples of typical pulse shapes delivered to the target may be seen in Figure 6.14. The red trace in Figure 6.14 shows a ramp-pulse, a gradual rise in laser intensity with time. The blue trace in Figure 6.14 illustrates a sharp jump in the pulse shape at early time, followed by a gradual rise. This early feature can cause samples to shock-up.

Figure 6.14: Examples of the different ramped laser pulse shapes as delivered to the target. The red line represents a smooth ramp pulse. The blue line represents a pulse with a sharp jump in laser energy at early time, which can cause samples to be shock-compressed, rather than QI-compressed.

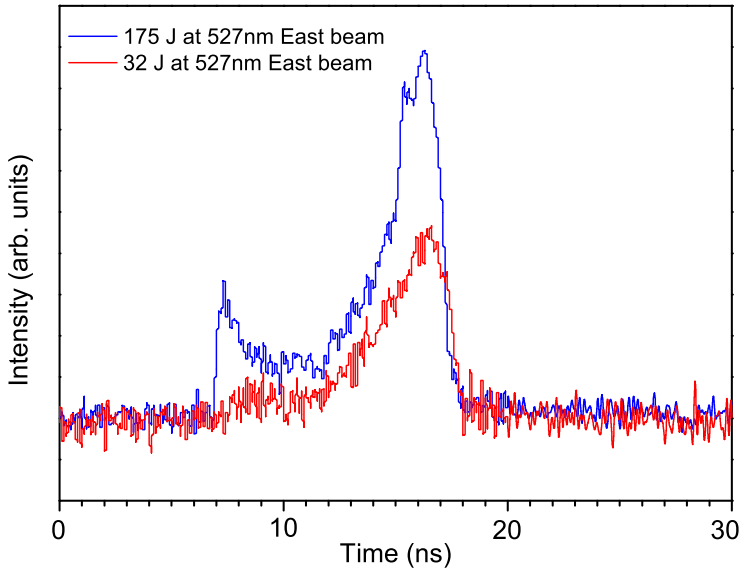

Due to Na being highly compressible, despite attempting to QI-compress the samples, many of the samples were shock-compressed. This is because both sound velocity and particle velocity increase as pressure and density increase. In a highly compressible material both pressure and density increase rapidly. This "shocking up" is illustrated in Figure 6.15. A shaped compression pulse is sent into a sample. At point A, the pressure is low, and so the wave velocity and the particle velocity is low. At point B, the

pressure is higher and likewise the particle and wave velocities are higher; at point C the pressure and velocities are higher still. The consequence of this is that at point C the wave travels fast than at point A, and so if the sample is sufficiently thick, the wave can steepen into a shock front, as illustrated by the vertical line in Figure 6.15.

Figure 6.15: An illustration of how thick targets can "shock up". As Na is highly compressible the wave speed and particle velocity both increase significantly as pressure (and density) is increased. As a consequence, a wave at higher pressure will travel at a higher velocity than a wave at lower pressure, and can eventually steepen into a shock front if the target is sufficiently thick.

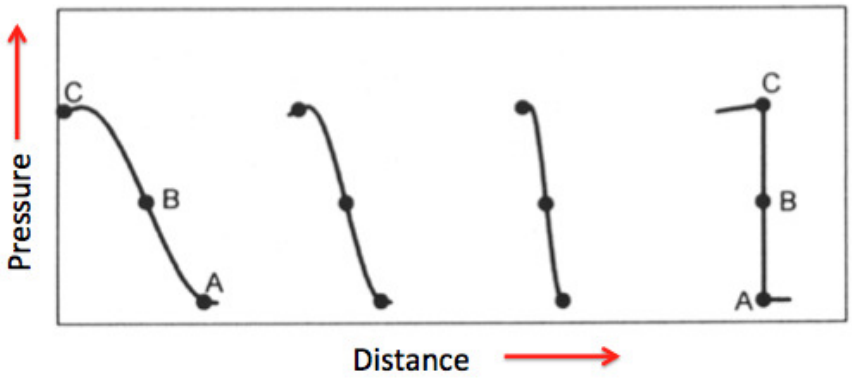

6.10.1 Shock-Compressed Na

It was originally assumed that the pressure in shock-compressed Na was the same as the pressure measured in the LiF. However, following simulations performed by one of the collaborators on this project, A. Lazicki, LLNL, on a similar target configuration (tin with a diamond ablator and LiF window), it was concluded that the pressure of Na would instead considerably lower, and would be therefore be obtained through impedance-matching techniques.

Determining Pressure Through Impedance Matching

Determining pressure using impedance-matching techniques has been described in detail by Celliers *et al.* (Celliers *et al.* 2005). The shock impedance is given by:

$$Z = \rho_0 U_s \tag{6.15}$$

where ρ_0 is the density of the uncompressed material and U_s is the shock velocity. The shock impedances of Na and LiF are considerably different. Therefore, as the compression wave passing through the Na reaches the Na/LiF interface, the impedance mismatch causes not only a shock wave to be transmitted into the LiF, but also a wave to be reflected back into the Na. As Na has a lower impedance than LiF, the reflected wave is a re-shock, rather than a release.

The key assumption made in this analysis is that the re-shock into the Na may be approximated by the reflected Na Hugoniot. Therefore, the intersection of the reflected Na Hugoniot with the LiF and Na principle Hugoniots will give the common pressure state at the Na/LiF interface. Figure 6.16 is an illustration of this technique. The particle velocity of the Na/LiF interface was measured using optical velocimetry techniques and was determined to be ∼2.7 km/s. The Na re-shock is plotted intersecting the LiF and Na Hugoniots, giving a pressure in the Na of 34.5 GPa.

6.10.2 Results from Shock-compressed Na

Representative velocimetry and pyrometry data from shock-compressed Na may be seen in Figure 6.17. This particular sample was initially shocked to a peak pressure of 57 GPa, as determined using the impedance-matching technique described in Section 6.10.1 (pressure in the LiF was determined to be 103 GPa). On the decaying shock, there is a two-wave feature in both the velocimetry and the pyrometry data, and this feature was repeatable. This feature is highlighted in the VISAR and SOP data in Figure 6.17 by the black arrows. Six targets of varying thickness – between 9 to 12.5 μm – were shock-compressed to peak pressures of between 40 and 57 GPa, and this two-wave feature was observed in all. Such observations in both the velocity and temperature data have typically been interpreted as a phase transition (Bancroft *et al.* 1956) (McWilliams *et al.* 2012) (Spaulding *et al.* 2012) (Smith *et al.* 2008).

Upon examination of the calculated Hugoniot in P-T space, shown in

Figure 6.16: An example of the impedance matching technique used to determine pressure in shock-compressed Na. The Na and LiF Hugoniots are shown in blue and red respectively. Na and LiF have different impedances, and as the shock wave is transmitted from the Na into the LiF, a re-shock is transmitted back into the Na. The Na re-shock is approximated by the reflected Na Hugoniot, represented by the dashed line. The velocity of the LiF interface is measured using optical velocimetry – here it is 2.7 km/s. The intersection of the reflected Na Hugoniot with the LiF and Na principle Hugoniots gives the pressure in the Na. In this example the pressure in the Na is 34.5 GPa.

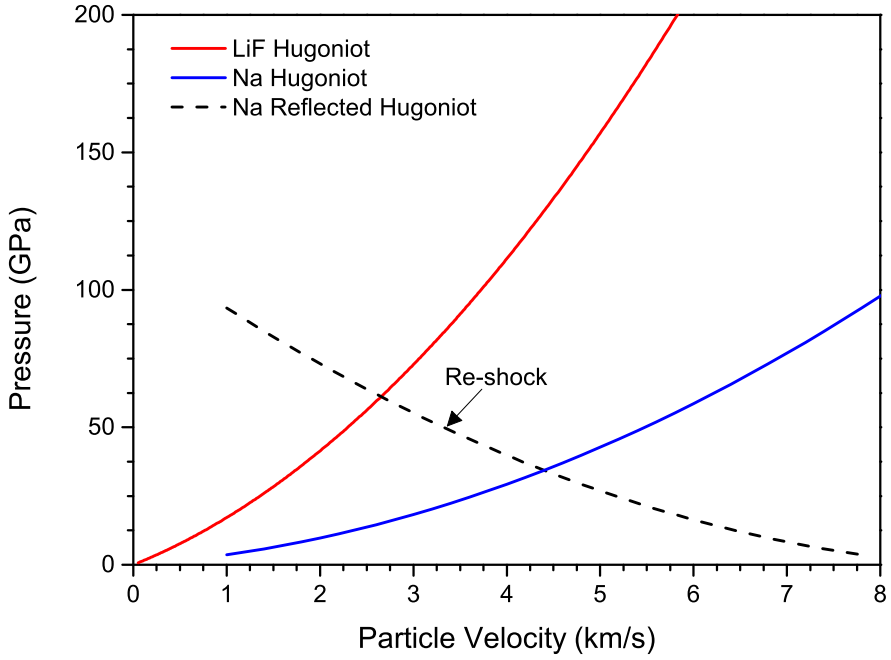

Figure 6.18, one may see that at 57 GPa, the sample is at T∼8,000 K. As discussed in Section 6.9, it was not possible to calibrate the SOP in this campaign, and so all temperatures from shock-compressed samples are determined from the Na Hugoniot, calculated by Wang & Sun (Wang & Sun 2001). At 47 GPa, if one assumes the release is still following the Na Hugoniot, a typical assumption in low-pressure shocks (below 1 Mbar) (Celliers *et al.* 2005), the temperature is still many thousands of Kelvin above

Figure 6.17: Optical velocimetry and streaked optical pyrometry data of Na on shock-compression. This sample was shock-compressed to a peak pressure of 57 GPa. The SOP data indicates that the sample is at elevated temperature, and according to the P-T Hugoniot calculations from Wang & Sun, it is expected to be at T∼8,000 K. There is a two-wave feature on the decaying shock in both the pyrometry and the velocimetry data, which may be an indication of a phase transition. This is highlighted by the black arrows. The insets show the raw VISAR and SOP data.

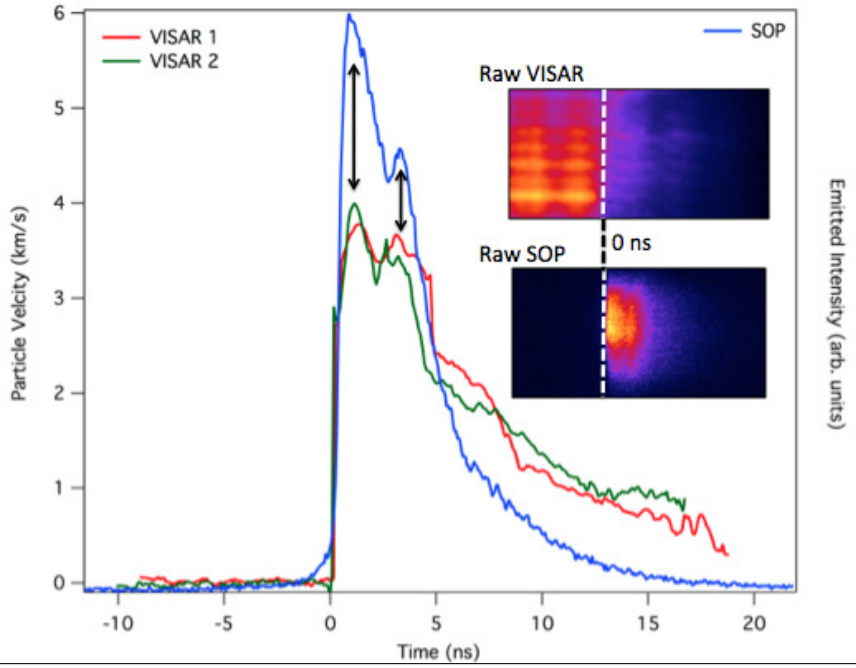

the melting curve, as determined through static compression techniques (Gregoryanz *et al.* 2005), and also shown on Figure 6.18. Therefore, one may conclude that this two-wave feature is not a signature of re-crystallisation from the liquid phase.

One possible interpretation of this data is the occurrence of a liquid-liquid transition. In their 2012, study Spaulding *et al.* performed laser-driven shock-compression experiments on $MgSiO_3$ to pressures and temperatures of between 300-800 GPa and 10,000-16,000 K (Spaulding *et al.* 2012). They observed a distinct two-wave feature in their velocimetry and pyrometry data on the decaying shock. An example of their data may be seen in Figure 6.19, and the similarities between it and the shocked-Na data presented here are notable. The pressure and temperature conditions achieved by Spaulding

Figure 6.18: The calculated Na Hugoniot by Wang & Sun (Wang & Sun 2001), superimposed on the melting curve of Na as determined using diamond anvil cell techniques by Gregoryanz *et al.* (Gregoryanz *et al.* 2005). The room-temperature solid-solid phase transitions are also indicated. The shaded region in the liquid is a suggested liquid-liquid phase transition, which may coincide with the maximum in the melting temperature. See text for further details.

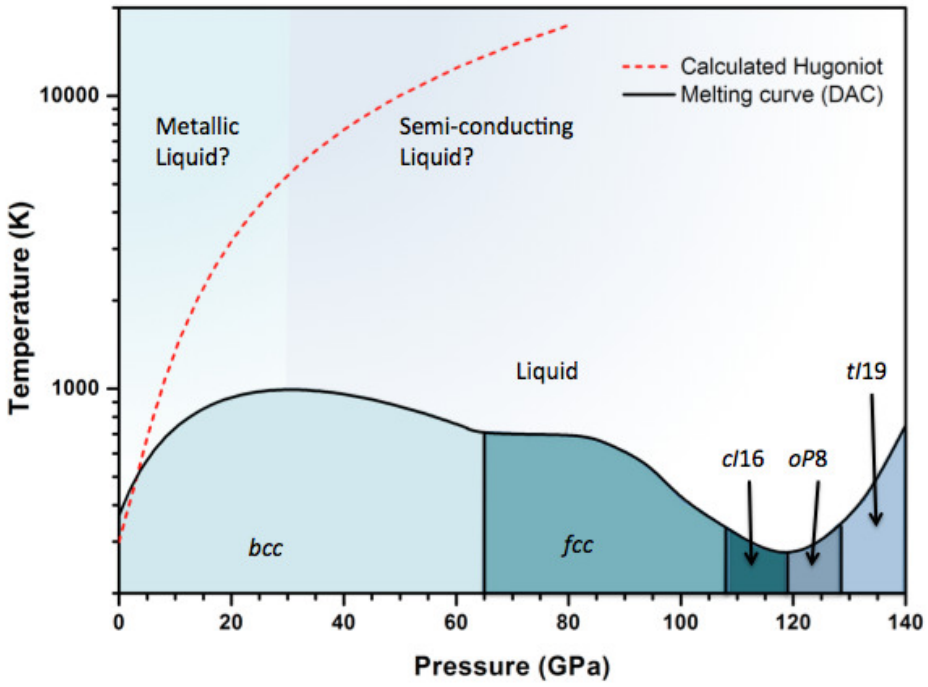

et al. are far above the calculated melting curve of $MgSiO_3$ (Belonoshko *et al.* 2005), and so the authors (Spaulding *et al.* suggest the two-wave feature is a signature of an abrupt liquid-liquid phase transition, assigning it to a transition from a high-density liquid to a low-density liquid (Spaulding *et al.* 2012).

In their 2013 theoretical study, Boates and Bonev indicate that liquid-liquid phase transitions are extremely rare, and are often driven by distinct changes in electronic character or bonding properties (Boates & Bonev 2013). Rather than a liquid-liquid transition they suggest that the features that Spaulding *et al.* (Spaulding *et al.* 2012) observe in their velocimetry and pyrometry data are in fact due to $MgSiO_3$ dissociating into MgO and SiO_2. Such dissociation, however, would *not* explain the features observed in

Figure 6.19: Optical velocimetry and pyrometry data for $MgSiO_3$. This data has been interpreted by the authors, Spaulding *et al.* (Spaulding *et al.* 2012), as a transition from a high-density liquid to a low-density liquid. This data bears striking similarities to the optical velocimetry and pyrometry data observed on the shock-compression of Na, as illustrated in Figure 6.17

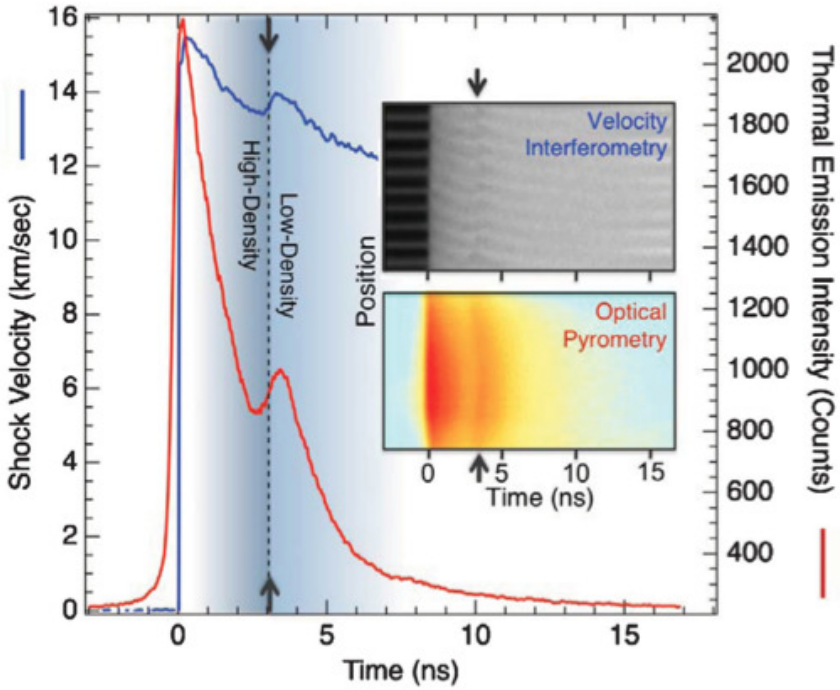

shock-compressed Na (Figure 6.17). Additionally, Na is known to undergo numerous striking structural and electronic transitions in the solid phases up to 200 GPa (McMahon *et al.* 2007) (Gregoryanz *et al.* 2008) (Lazicki *et al.* 2009) (Ma *et al.* 2009) (Marqués *et al.* 2011b). Could such transitions be mirrored in the liquid phase?

Raty *et al.* (Raty *et al.* 2007) predict the occurrence of structural and electronic liquid-liquid transitions in Na as a mechanism to explain the anomalous melting curve of Na (Gregoryanz *et al.* 2005). They (Raty *et al.* performed molecular dynamics simulations on liquid-Na and predict that transitions similar to those taking place in the underlying solid, occur in the liquid at lower pressures (Raty *et al.* 2007). They suggest an increase in the density of the liquid phase occurs, coinciding with the maximum in the melting temperature at 30 GPa, where the liquid co-ordination is

expected to undergo a change from a *bcc*-like co-ordination to an *fcc*-like co-ordinated liquid. Following the maximum in the melting curve, the melting temperature has been determined to decrease down to a deep minimum at 118 GPa and 300 K (Gregoryanz *et al.* 2005). This minimum in the melting temperature has been found to coincide with both complex structural and electronic transitions occurring in the solid phase (Gregoryanz *et al.* 2005) (Lazicki *et al.* 2009) (Marqués *et al.* 2011b). For example, at 105 GPa, Na transforms to the *cI*16 phase and a pseudo-gap opens at the Fermi level. At higher compressions this gap opens further, and Na becomes an indirect semi-conductor in the *oP*8 phase. The band gap increases in the (visibly) black *tI*19 phase at 125 GPa, before opening entirely as Na transforms to the transparent insulating phase *hP*4 at ∼180 GPa (Lazicki *et al.* 2009) (Ma *et al.* 2009).

Moreover, Raty *et al.* (Raty *et al.* 2007) predict that the conductivity in the liquid decreases significantly, reducing by a factor of 3 between 40 and 80 GPa, suggesting that the conductivity in this pressure range deviates away from a Drude-like shape towards a semi-conductor shape. The underlying solid in this same pressure range is determined to have Drude-like conductivity, and indeed solid-Na in this pressure interval is still well described by the nearly-free electron model (Lazicki *et al.* 2009) (Degtyareva & Degtyareva 2009) (Hanfland *et al.* 2002).

To monitor the onset of electronic transitions throughout the shock- and QI-compression experiments, the reflectivity of Na was measured using the 532 nm VISAR laser. The reflectivity of the Al flash coating and the Na sample may be seen in Figure 6.20. Prior to shock breakout at the Na/LiF interface, the reflectivity of Al and Na are comparable at 532nm, as expected at ambient conditions. After breakout (defined here as occurring at t=0 ns) the reflectivity of Al and Na both decrease. Al has been demonstrated to decrease significantly in reflectivity on increasing pressure, dropping to approximately 60 % of its initial value at approximately 40 GPa (Tups & Syassen 1984). The reflectivity of Na is notably reduced compared with that of the Al flash coating.

In a more thorough analysis, the reflectivity of the Na sample was normalised to a value obtained from undriven Na. The reflectivity of the

Figure 6.20: The reflectivity of Na and Al prior to and after shock breakout at the Na/LiF interface. This sample was compressed to a peak pressure of 57 GPa, and the corresponding velocimetry and pyrometry data may be seen in Figure 6.17. Breakout is defined as occurring at t=0 ns. Prior to shock breakout the Al and Na are both highly reflective. After shock breakout, both Na and Al decrease significantly in reflectivity, with Na notably decreasing by a larger amount.

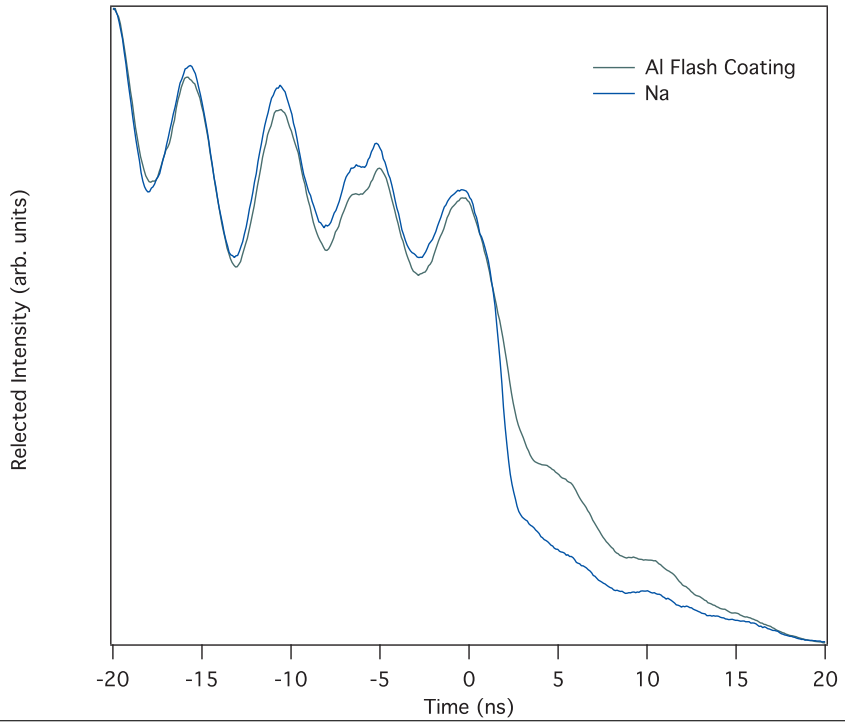

57 GPa shot discussed above may be seen in Figure 6.21. Once more, t=0 ns is defined as when the shock breaks out at the Na-LiF interface. At breakout, the reflectivity of both Na drops to between 10-20 % of its initial value. Inspection of Figure 6.13, showing the reflectivity of solid-Na at room temperature on increasing pressure, indicates that solid-Na drops to approximately ∼20 % of its ambient pressure value when it transforms to the *oP*8 phase at 119 GPa. Upon transforming to the *tI*19 phase, Na undergoes an additional ∼10 % drop in reflectivity at 532 nm.

Electronic band structure and structure calculations performed on the *oP*8 by both Lundegaard *et al.* (Lundegaard *et al.* 2009a) and Lazicki *et*

Figure 6.21: The reflectivity of Na on shock-compression to a peak pressure of 57 GPa, normalised to the reflectivity of Na prior to shock breakout. Following shock breakout, the reflectivity of Na was observed to drop by ∼85 % of its value at ambient conditions. This reflectivity is of a similar value to the reflectivity of (solid) *oP*8-Na at room temperature. This is possibly an indication that electronic transitions are occurring in liquid-Na, similar to those taking place in the underlying solid at higher pressure (Lazicki *et al.* 2009)

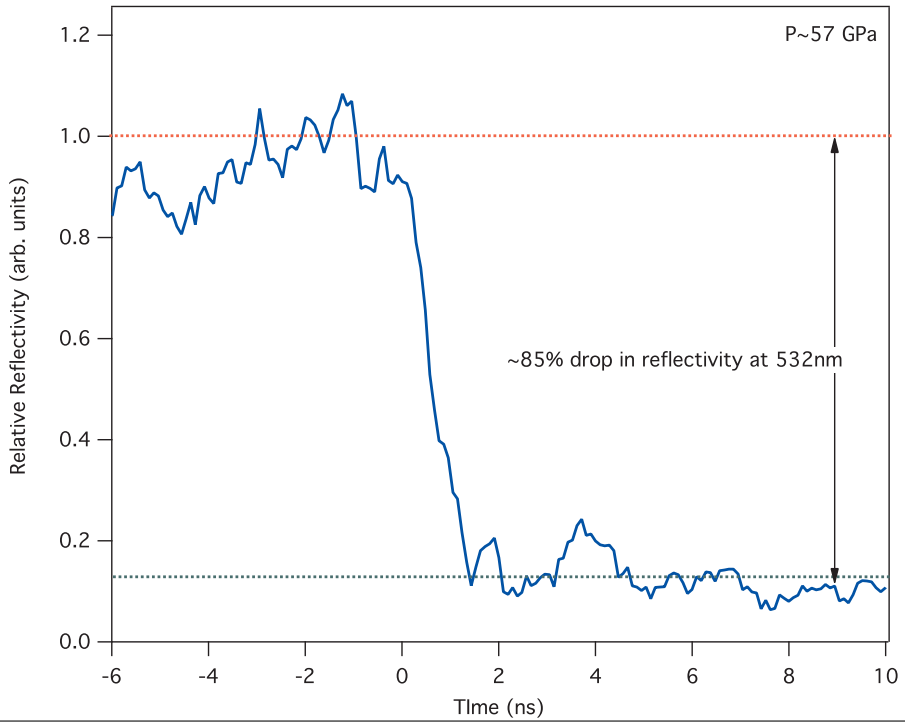

al. (Lazicki *et al.* 2009) have determined this phase to be a semi-metal. Furthermore Lazicki *et al.* performed band structure calculations on a commensurate analogue to the *tI*19 phase and revealed that Na is also a semi-conductor in this phase. It should be stressed, however, that the band structure calculations for *tI*19-Na were performed assuming a commensurate analogue i.e. that at some pressure the host and guest structures would become commensurate with each other, and so could this phase could be modelled at a certain pressure as a commensurate supercell. There has been no experimental observation of such an occurrence for *tI*19-Na to-date, and

so the physical basis of these calculations is questionable.

Utilising multi-shock flyer-plates to achieve off-Hugoniot P-T states, Golyshev *et al.* made *in situ* measurements of the resistivity of liquid-Na (Golyshev *et al.* 2011). They measured a marked increase in the resistivity of liquid-Na with respect to ambient-pressure liquid-Na, increasing by a factor of 25, from 9.57 $\mu\Omega$m at ambient pressure and 371 K, to 246 $\mu\Omega$m at 200 GPa and T$\sim$8,000 K. What is interesting to note in this study is that they observe a deviation away from Drude-like conductivity towards a semi-conductor-type model at significantly lower pressures and elevated temperatures than the analogous phase transition in the underlying solid. Between 28-46 GPa, Golyshev *et al.* suggest that there is a transformation from a metallic liquid to a semi-conducting liquid, in broad agreement with the observations discussed here.

These preliminary measurements on laser-shocked Na could suggest that electronic transitions may be occurring in liquid-Na, similar to those occurring in the underlying solid at much higher pressures. Further experiments are required to determine if this is the case, and will be discussed following the Section on QI-compression of Na.

6.10.3 Quasi-isentropic Compression of Na

The main aim of the August 2011 campaign at Janus, JLF, was to QI-compress Na into the stability field of the transparent *hP*4 phase at 200 GPa (Ma *et al.* 2009). As described in Section 6.10.1, due to the significant compressibility of Na it was very prone to "shocking-up". Therefore, in order to QI-compress Na to pressures in excess of 200 GPa, the samples were required to be extremely thin – typical target thicknesses for when Na was successfully QI-compressed were determined to be between 2 and 6 μm. In this Section, two shots will be discussed in detail, one QI-compressed to a peak pressure of 45 GPa and one QI-compressed to peak pressure of 120 GPa.

An example of velocimetry data and raw VISAR data from a sample that underwent QI-compression may be seen in Figure 6.22. It is important to note that the rise on the velocity profile has numerous features, or "kinks". Typically, such kinks in the velocity-time profile are indications of the occurrence of phase transitions. The numerous phase transitions

that Na has been observed to undergo using static compression techniques could suggest that these kinks correspond to numerous solid-solid transitions (Gregoryanz *et al.* 2008). However, upon inspection of Figure 6.18, due to the solid-solid phase transitions occurring at the minimum in the melting temperature, which occurs at 118 GPa and 300 K (Gregoryanz *et al.* 2005), it is clear that for the kinks in the velocity profile to correspond to solid-solid phase transitions the compression would have to occur at room temperature, which is not possible under these compression conditions.

Figure 6.22: Optical velocimetry data from quasi-isentropically compressed Na. The gradual rise on the velocity-time profile is indicative of QI-compression as opposed to shock-compression. The inset shows an example of raw VISAR data. The kinks on the rise of the velocity-time profile could be indicative of Na undergoing a series of phase transitions. However, the absence of similar features on the decaying wave suggests that the source is instead reverberations occurring within the target. This sample was compressed to a peak pressure of 120 GPa, as determined from the LiF isentrope.

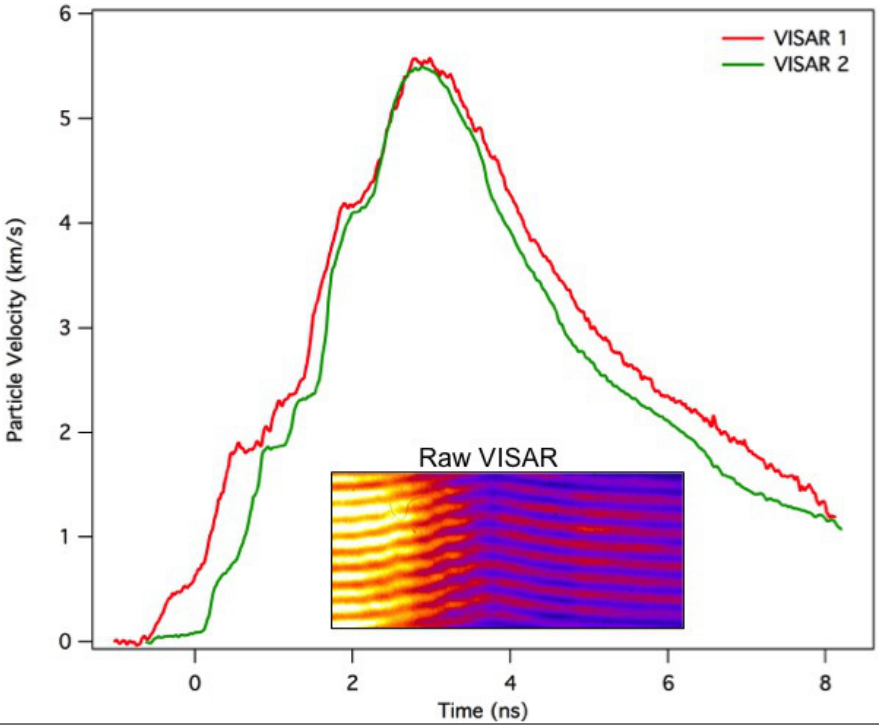

Furthermore, if these kinks in the velocity profile were due to Na undergoing a series of phase transitions on the rising compression wave, then one would expect to see similar features on the release wave. It is clear that on inspection of Figure 6.22 there is an absence of any such features or kinks on the decaying wave, adding further weight to the suggestion that the kinks on the rise are not due to phase transition occurring in the Na. A probable source of these features is the occurrence of reverberations within the target.

It was assumed that the pressure achieved during QI-compression was closer to that of the LiF isentrope rather than that of the Na isentrope, due to the large number of shocks and re-shocks that the sample undergoes. The target in Figure 6.22 was therefore determined to be compressed to a peak pressure of P$\sim$120 GPa, as determined from the LiF isentrope.

The difference in the amount of heating a material experiences under shock- and QI-compression has been discussed in Section 6.4.2, and an example of SOP data from shock- and QI-compressed samples may be seen in Figure 6.23. Clearly the thermal emission from the shock and QI-compressed samples is significantly different. No signal was detected on the SOP for the sample compressed to 120 GPa (Figure 6.22), indicating that this sample was below 4,000 K (see Section 6.9). It is interesting to note that when a sample was QI-compressed, as indicated by the VISAR data, to $\sim$130 GPa, a signal was observed on the SOP, indicating that the temperature is at least several thousand Kelvin. One supposes, therefore, that the sample that is QI-compressed to 120 GPa is also at elevated temperature, yet below the detection limit of the SOP.

Inspection of the Na phase diagram in Figure 6.18 indicates that on QI-compression, the states that are accessed are off-Hugoniot. For example, the temperature on the Hugoniot at P$\sim$100 GPa is expected to be in excess of 10,000 K, whereas an absence of signal on the SOP lets us constrain the temperature to be T<4,000 K (Spaulding *et al.* 2007). For the QI-compressed shot where the pressure achieved was determined to be $\sim$120 GPa, it is clear that most probably we are in the liquid phase as Na melts at just above room temperature (300 K) at this pressure. Figure 6.23 further illustrates that a sample was QI-compressed to P$\sim$45 GPa – there was also no signal detected on the SOP, indicating that Na remained (relatively) cool. This shot is of

Figure 6.23: Typical streaked optical pyrometry data from different targets under shock- and QI-compression. The detection limit of this apparatus is 4,000 K (Spaulding *et al.* 2007). The red line is data taken from a shock-compressed sample, and the large signal indicates a significant amount of thermal emission from the target. According to the calculated Hugoniot this sample is expected to be at temperatures in excess of 10,000 K. The yellow, blue, and green lines are all from QI-compressed samples. The green and blue lines, compressed to peak pressures of 45 and 120 GPa, do not register on the SOP, indicating that their temperature is below 4,000 K. The yellow line is a target QI-compressed to 130 GPa, and a significant signal is observed on the SOP indicating that the temperature is above 4,000 K.

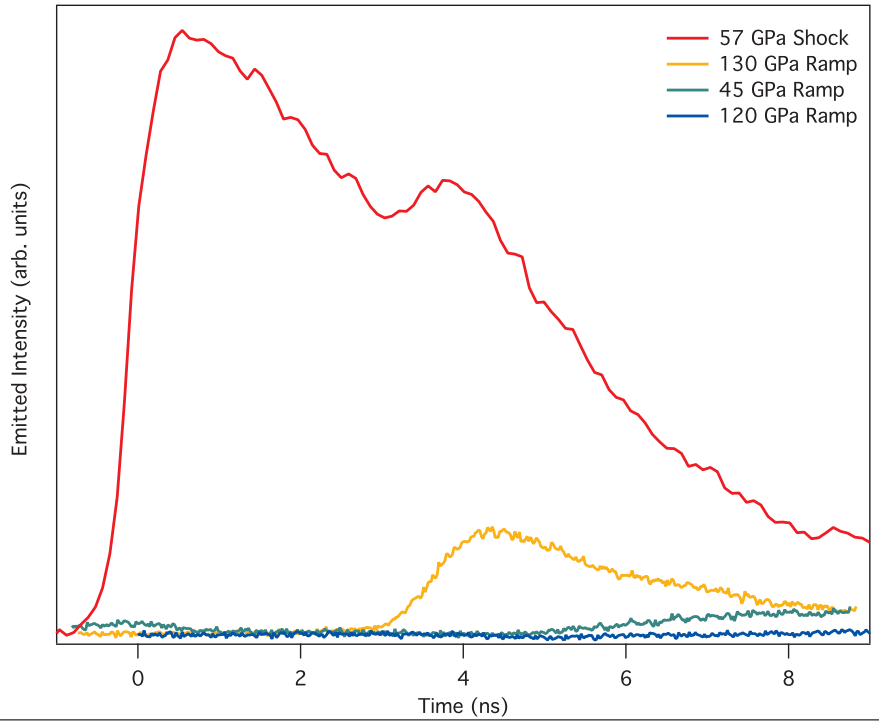

particular interest as the peak pressure reached makes it directly comparable with the shock-compression data described above in Section 6.10.2, which were compressed to similar peak-pressures. Returning once more to the Na phase diagram, at 45 GPa the melting temperature, as determined by static compression techniques, is 800 K. It is therefore possible that at 45 GPa, the melting curve has not been crossed, and the sample is still in the solid state. This point will be returned in the discussion of the reflectivity measurements.

The reflectivity of Na at 532 nm during QI-compression to 45 GPa may be seen in Figure 6.24. Once more, t=0 ns is defined as the time that breakout occurs at the Na-LiF interface. After breakout, there is a continual decrease in the reflectivity of Na (relative to the unshocked sample), decreasing down to ∼70-80 % of its initial value. Returning to the static reflectivity data of Lazicki *et al.* (Lazicki *et al.* 2009), shown in Figure 6.13, the *bcc*- and *fcc*-solid phases in Na are nearly indistinguishable in optical reflectivity measurements as both are highly reflective at 532 nm (2.33 eV). If at 45 GPa we are *not* traversing the melting curve, and Na is a solid, it will be in the *fcc* phase, and one would expect that there would be no significant decrease in reflectivity. The drop in reflectivity we observe could therefore be interpreted as due to crossing the melting curve.

According to Raty *et al.* (Raty *et al.* 2007), at P∼45 GPa, the liquid is predicted to undergo structural and electronic transitions, such that it behaves similarly to the *cI*16 solid, stable at higher pressures. These transitions will be manifested by a decrease in reflectivity as Na departs from nearly-free electron behaviour. Further, the reflectivity of solid-*cI*16 is ∼80 % of the ambient value and so one could tentatively ascribe this drop in reflectivity at 45 GPa to a melting transition to a *cI*16-like liquid phase (Lazicki *et al.* 2009). Clearly, additional experiments are necessary to determine the nature of this transition.

The optical reflectivity at 532 nm at P∼120 GPa may be seen in Figure 6.25. At this pressure we are confident that we are in the liquid phase, as remaining in the solid would involve isothermal compression at 300 K (Gregoryanz *et al.* 2005). Here we observe a more significant drop in reflectivity than that observed at 45 GPa; the reflectivity drops to ∼45 % of its initial value. Interpreting these changes in reflectivity in terms of electronic transitions occurring in the liquid, which are similar to those in the underlying solid, gets somewhat complicated. The reflectivity observed here is intermediate between the *cI*16-solid and the *oP*8-solid phases at 300 K (Lazicki *et al.* 2009). One could interpret this as gradual electronic changes occurring in the liquid phase, as opposed to the abrupt changes measured in the underlying solid.

Figure 6.24: The reflectivity of Na on QI-compression, plotted relative to the reflectivity of the same sample at ambient conditions. This sample was compressed to a peak pressure of 45 GPa, and SOP data indicate that the temperature of the sample is below 4,000 K. Breakout from the Na/LiF interface is defined to occur at t=0 ns, and following this the sample reflectivity drops to ∼70 % of its ambient value over 2 ns. This may be an indication of crossing the melt curve.

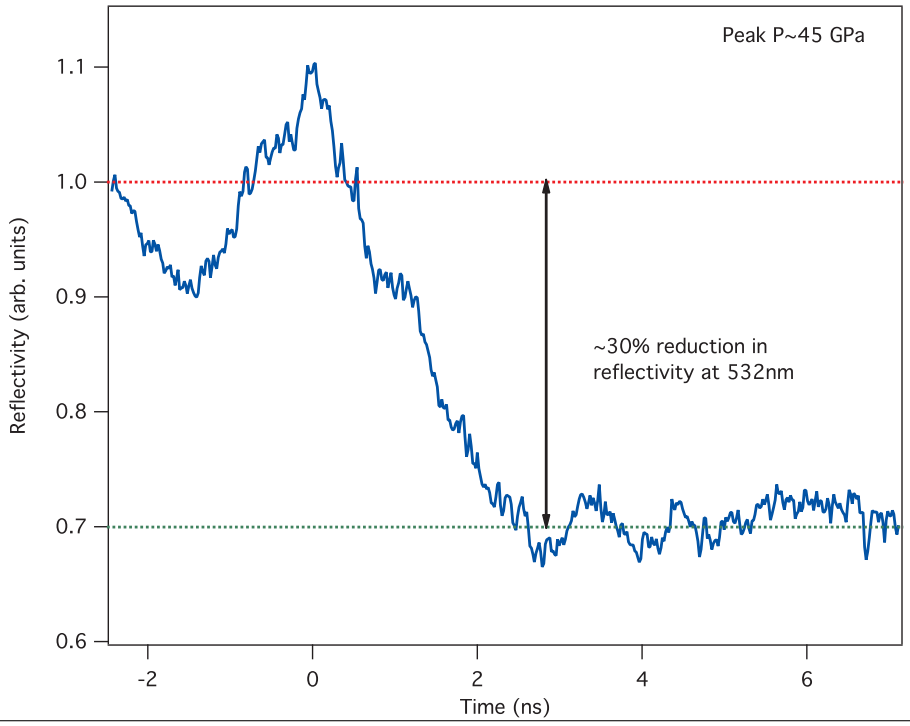

6.11 Conclusion

This Chapter describes preliminary experiments on laser-driven compression of Na. A large amount of time was devoted to target development as it was extremely challenging to construct thin targets that were sealed from reaction with air and moisture. The successful target design is evident here in this preliminary study. The target design is easily extended to the other alkali elements. At the time of writing (August 2013) we have successfully completed a month-long Janus campaign (June 2013) where we made additional measurements on shock and QI-compressed Na, and

Figure 6.25: The reflectivity of Na on QI-compression, normalised to the reflectivity of the same sample at ambient conditions (unshocked). This sample was compressed to a peak pressure of 120 GPa, and SOP data indicate that the temperature of the sample is below 4,000 K. Breakout at the Na/LiF interface is defined to occur at t=0 ns, and following this the sample reflectivity drops to ∼45 % of its ambient value over 2.5 ns. The reflectivity here is intermediate between the *cI*16-solid and the *oP*8-solid phases at 300 K and could be an indication of electronic changes occurring in liquid Na (Raty *et al.* 2007).

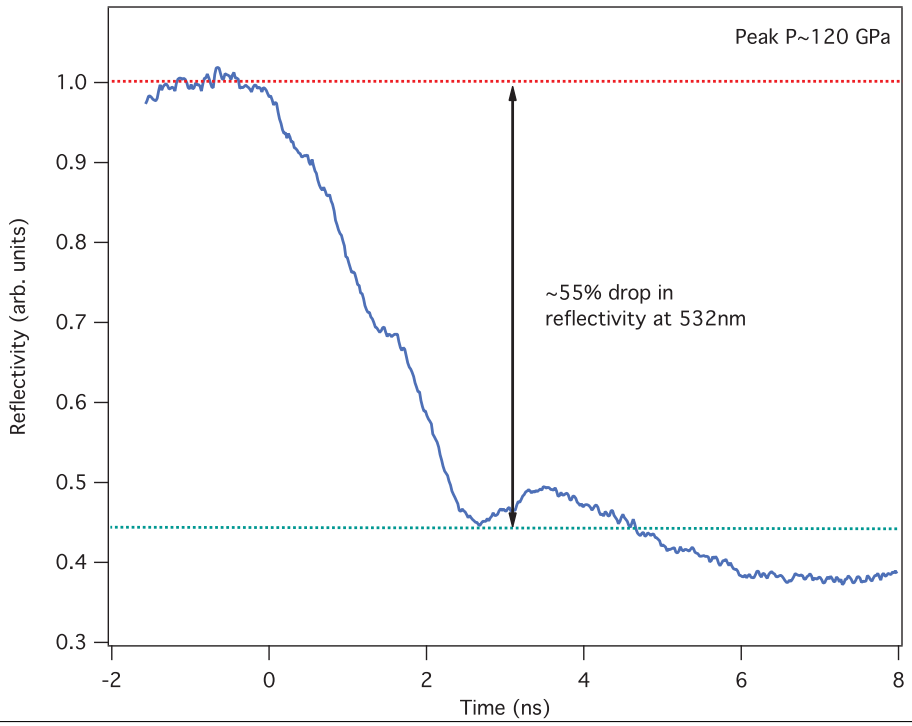

extended the target design to study potassium (K).

The preliminary results in the shock-compression study whereby we observe a significant decrease in reflectivity of liquid-Na is in qualitative agreement with the study conducted by Golyshev *et al.* (Golyshev *et al.* 2011). These observations suggest that a liquid-liquid phase transition may occur in liquid-Na under shock-compression, signified by a change in optical properties, and hence the electronic character, of the liquid phase.

However, it should be noted that there is a strong possibility that the two-

wave feature in the decaying shock may be due to complex wave interactions within the targets – the targets consist of thin layers of Na sandwiched between nanocrystalline diamond and single-crystals of LiF. It is possible that reverberation effects due to the reflection of waves at the Na-LiF or Na-diamond interface would account for the two-wave feature in the velocimetry data, though it is unclear as to why these reverberation effects would cause an increase in temperature.

Several steps may be taken (and have been undertaken in the June 2013 campaign which is not described here) to eliminate reverberation effects. To eliminate the two-wave feature, described in Section 6.10.2, being due to the Equation of State of the diamond ablator, which has a strong elastic-plastic wave (McWilliams *et al.* 2010), a CH ablator with an Al coating on the drive surface to prevent the drive light penetrating through the transparent plastic and interacting with the Na-CH interface was used. Furthermore, by shock-compressing very thick targets one can attempt to eliminate the reverberation effects between the ablator and the LiF crystal by creating at target that is sufficiently thick that by the time the VISAR measurement has been made, the compression wave has not yet reverberated. Due to the compressibility of Na, however, this will prove very challenging.

The significant changes in the reflectivity of Na on shock- and QI-loading are promising, but one must be wary of over-interpreting these results. Although significant changes occur on compression, it is unclear whether these changes are due to a departure from metallic behaviour towards a more semi-conductor like behaviour suggested by Raty *et al.* (Raty *et al.* 2007), or observed in the multi-shock flyer plate experiments by Golyshev *et al.* (Golyshev *et al.* 2011) on Na. Additional and more detailed measurements (i.e. measure reflectivity at various wavelengths) are required to understand these preliminary observations.

There have been numerous observations in the last decade of materials undergoing an insulator-to-metal or semi-conductor transition, and perhaps the experiments discussed here are observing the reverse of such a transition. To better understand the nature of the changes in reflectivity observed on shock- and QI-compressed Na, analysis like that described by Hicks *et al.* could be performed (Hicks *et al.* 2006). Such analysis relies on using

both measured temperature and changes in reflectivity to extract band gaps. Unfortunately it was not possible to calibrate the SOP in these experiments, and so it was not possible to determine temperature values.

Furthermore, to more thoroughly investigate the change in reflectivity under dynamic compression a broad-band reflectivity diagnostic, developed by S. Ali (Berkley/LLNL) as part of her thesis work, was used in the most recent campaign (June 2013), which monitors reflectivity from 400-800 nm (visible), or from 840-1150 nm (near-IR). Due to time constraints the most recent campaign is not contained in this Thesis, but the preliminary results, and the results from the June 2013 campaign, are certainly promising.

Chapter 7

Conclusions & Future Work

7.1 Conclusions

The focus of the work contained within this Thesis was the investigation of the behaviour of sodium (Na) and potassium (K) at high-pressures and high-temperatures, using both static and dynamic compression techniques. The following is a summary of the major observations discussed in this Thesis.

7.1.1 Section I: Static Compression Studies on Potassium

The first, and to the author's mind most striking, observation is that K is a somewhat overlooked element, particularly when compared with its immediate neighbours in the periodic table. Residing in the middle of the alkali elements, it has received comparatively little attention than the rest of the group-I elements. The first two results Chapters (4 and 5) in this Thesis aim to amend that imbalance.

The Revised Melting Curve of Potassium

Using diamond anvil cell techniques combined with external resistive heating both in-air and in-vacuum, the melting curve of K has been reinvestigated, and extended to 24 GPa and 750 K. The onset of melting was determined using *in situ* synchrotron X-ray diffraction techniques, determined by the observation of a diffuse halo of scattering from the liquid phase, and by

the simultaneous disappearance of crystalline Bragg scattering. Unlike the previous studies in the literature, where the melting temperature was observed to continually rise with increasing pressure, in this study, a maximum in the melting temperature was observed in the stability field of the *bcc*-solid phase. It was located by performing a fit to the data using the Kechin Equation, and was determined to be at 5.6 GPa and 534 K.

Following the maximum this maximum, the melting temperature becomes negative, decreasing down to a minimum at 19 GPa and 390 K at the *fcc*-*tI*19-liquid triple point. Following this, as pressure is increased further, the melting temperature regains a positive gradient, increasing steeply at a rate of ∼65 K/GPa. At the maximum P-T conditions reached in this study – 24 GPa and 750 K – the gradient of the melting temperature showed no signs of becoming more gradual. The melting curve of K, therefore, was determined to be in-keeping with the general trend of anomalous melting observed in its alkali neighbours, and in fact is remarkably similar to that of Na, but occurring at significantly lower pressures and temperatures.

Finally, there appears to be a shift in the *d*-spacing of the first liquid peak from a *bcc*-like position to an *fcc*-like position close to the maximum in the melting temperatures. Several GPa below the *fcc*-*tI*19-liquid triple point there is a shift away from an *fcc*-like position. This shift in the liquid peak position is indicative of a change in compressibility of the liquid, ahead of a phase change occurring in the underlying solid.

An Order-Disorder Transition in Composite Incommensurate Host-Guest Potassium

Upon conducting studies on the melting curve of K, an interesting temperature-dependent phenomenon was observed in the composite incommensurate host-guest structure *tI*19. The Bragg scattering from the guest component grew weaker as temperature was increased at a constant pressure of 22 GPa. The Bragg scattering eventually disappeared entirely, while the scattering from the host structure remained intact. This indicated a disordering transition occurring in the guest substructure, while the host substructure retained long-range order.

This order-disorder transition was investigated using single crystal, quasi-

single crystal and polycrystalline samples and *in situ* X-ray diffraction techniques. A single-crystal refinement was performed on the host and guest substructures at room temperature, and atomic displacement parameters were refined. It was discovered that the average displacement of the guest atoms along the incommensurate *c*-axis is ∼14 % of the nearest neighbour distance. In the context of the Lindemann criterion, this suggests that the guest chains are close to liquid-like along the *c*-axis, exhibiting a large degree of disorder even at room temperature.

Powder and quasi-single crystal diffraction studies were performed on *tI*19-K up to 50 GPa and 650 K, and the pressure and temperature dependence of the order-disorder transition was carefully mapped out. Furthermore, the powder and quasi-single crystal diffraction studies confirm that the host and guest structures undergo a series of complex (re-entrant) phase transitions with increasing pressure. It was observed that these transitions in the guest structure appear to have some influence over the gradient of the order-disorder transition temperature.

Importantly, the c_{Host}/c_{Guest} ratio passes through two commensurate values as pressure is increased from 20 GPa to 50 GPa, and approaches a third commensurate value prior to the transition to the *oP*8 phase. This means that there are several different pressure points at which it would be meaningful to perform full electronic structure calculations on *tI*19-K using an analogous supercell, perhaps providing insight into the mechanism for the intra-phase transitions in the host and the guest.

7.1.2 Section II: Dynamic Compression Studies on Sodium

The alkali elements are highly reactive, and so performing static compression experiments on them at elevated temperatures is experimentally challenging. Moreover, static compression techniques are limited by the mechanical stability of the diamonds, and so investigating the behaviour of the alkali elements beyond ∼300 GPa is impossible with this technique. One solution is to use dynamic, specifically laser-driven, compression techniques to shock or quasi-isentropically compress material to multi-megabar pressures, far beyond the limits of the diamond anvil cell. Chapter 6 describes, to the best

of the author's knowledge, the first laser-driven compression experiments performed on an alkali element.

Laser Driven Shock- and Quasi-Isentropic Compression Studies of Sodium

A key result of this Thesis research was the design and implementation of a target design for laser-driven compression experiments on sodium, and this design can be easily extended to the other alkali elements. Indeed, to-date it has been implemented in further laser-driven compression experiments on K. Furthermore, preliminary measurements were made on shock- and quasi-isentropic (QI) compression of Na, monitoring optical velocimetry, streaked optical pyrometry and optical reflectivity to diagnose the sample.

In the shock-compression measurements, the reflectivity of liquid-Na decreases to ∼20 % of its ambient pressure value at 57 GPa. All shock-compressed samples were shocked to pressures in excess of 40 GPa, and in all a drop in reflectivity of a similar magnitude was observed. Furthermore, on the decaying shock, a two-wave feature in the velocimetry and pyrometry data is observed. Such a feature is typically interpreted as a phase transition. These observations suggest that a liquid-liquid phase transition occurs, signified by the changes in reflectivity, and hence electronic character, of liquid-Na under shock compression conditions above 40 GPa.

The successful laser-driven QI-compression of Na has also been demonstrated. The highest pressure Na has been QI-compressed to was 130 GPa, significantly lower than the transition to the transparent insulating phase. Changes in reflectivity of QI-compressed Na have been observed, and it is notable that the changes in reflectivity on QI-compression are less dramatic than the changes on shock compression. Finally, a gradual drop in the reflectivity of Na under QI-compression was observed at 45 GPa, which may be an indication of crossing the melting curve. *In situ* diffraction is required to determine whether this is the case.

7.2 Future Work

This Thesis has been divided into two distinct sections, a static compression section and a dynamic compression section, highlighting the long-held view that these techniques are very different. It is the author's view, and the view of an increasing number in the high-pressure community, that these techniques are highly complimentary, rather than unrelated or dissimilar. In combining static and dynamic compression techniques it is possible to probe a large region of P-T space that is inaccessible to one technique alone.

Of particular interest to the author is the extension of both static and dynamic compression techniques to experiments at X-ray Free Electron Lasers (XFELs). XFELs are an extremely brilliant source of coherent, short-pulse – of order 100 fs – high-intensity, hard X-rays. As a direct comparison with synchrotron sources, the European XFEL, due to come online in late 2015-early 2016, is expected to have a peak brilliance 10^{12} times, and an average brilliance 10^4 times, that of the most brilliant synchrotron source, which, at the time of writing, is the Petra-III synchrotron at the Deutsches Elektronen Synchrotron. The European XFEL will operate at photon energies ranging from 3 keV up to 24 keV in the fundamental, offering an extremely bright, time-resolved source, operating at photon energies that are ideal for diamond anvil cell studies, in addition to combining brilliant, time-resolve X-rays with dynamic compression techniques.

The High Energy Density (HED) instrument, one of six instruments proposed at the European XFEL, will allow the combination of a high-powered pulse-shaped ∼100 J nanosecond laser with the extremely bright and time-resolved X-rays available at this facility to achieve pressures of tens of megabar. It is key to note here, however, that a major requirement for the success of dynamic compression studies is the repeatability and reproducibility of the laser pulse shape and energy on target. The effect that an unreliable pulse shape has on a target was demonstrated in Chapter 6, where a small jump in laser intensity at early time resulted in the shock-, rather than QI-compression, of the Na target.

At the time of writing there, arguably, exists only one laser in the world that provides the desired reproducibility and fidelity in pulse shape and energy – the National Ignition Facility at LLNL. In the author's opinion,

an important requirement for the advancement of the field of structural studies under dynamic compression conditions requires a laser with such properties, though undeniably lower energy and higher repetition rate, to be implemented at the European XFEL. By conducting combined static and dynamic compression experiments at XFELs, one can see the potential for revolutionising our understanding of matter at extreme conditions, obtaining, for example, synchrotron-quality X-ray diffraction of crystalline solids at tens of megabar. This is a field in which the author intends to play a key role.

"I always believed that whatever had to be written would somehow get itself written"

– Seamus Heaney

Appendix A
List of Publications

Several studies detailed in this Thesis have been published to-date and an additional manuscript is in preparation concerning the work contained in Chapter 5. Moreover, throughout this Ph.D., the author has played a key role and participated in numerous additional studies. These studies were outwith the scope of this Thesis, and are expected to yield additional publications in the near future. The studies that have been published are bound with this Thesis after the Bibliography and are listed below.

E.E. McBride, O. Narygina, G.W. Stinton and M.I. McMahon. *'Melting of Potassium to 22 GPa'*, Journal of Physics: Conference Series, **377**, 012040 (2012).

O. Narygina, E.E. McBride, G.W. Stinton, and M.I. McMahon. *'Melting Curve of Potassium to 22 GPa'*, Physical Review B, **84**, 054111, (2011).

Bibliography

Alexander, S. & McTague, J. (1978), 'Should all crystals be bcc? Landau Theory of solidification and crystal nucleation', *Physical Review Letters* **41**(10), 702.

Badding, J., Mao, H. & Hemley, R. (1991), 'High-pressure synchrotron X-ray diffraction of Cs IV and Cs V', *Solid State Communications* **77**(10), 801.

Bancroft, D., Peterson, E. L. & Minshall, S. (1956), 'Polymorphism of iron at high pressure', *Journal of Applied Physics* **27**(3), 291.

Barker, L. M. & Hollenbach, R. E. (1972), 'Laser interferometer for measuring high velocities of any reflecting surface', *Journal of Applied Physics* **43**(11), 4669.

Belonoshko, A. B., Skorodumova, N. V., Rosengren, A., Ahuja, R., Johansson, B., Burakovsky, L. & Preston, D. L. (2005), 'High-pressure melting of $MgSiO_3$', *Physical Review Letters* **94**, 195701.

Boates, B. & Bonev, S. A. (2013), 'Demixing instability in dense molten $MgSiO_3$ and the phase diagram of MgO', *Physical Review Letters* **110**(13), 135504.

Boehler, R. & De Hantsetters, K. (2004), 'New anvil designs in diamond-cells', *High Pressure Research* **24**(3), 391.

Boehler, R. & Zha, C.-S. (1986), 'Systematics in the melting behavior of the alkali metals from DAC measurements', *Physica B+C* **139**, 233.

Bradley, D., Eggert, J., Smith, R., Prisbrey, S., Hicks, D., Braun, D., Biener, J., Hamza, A., Rudd, R. & Collins, G. (2009), 'Diamond at 800 GPa', *Physical Review Letters* **102**(7), 075503.

Briggs, R., Daisenberger, D., Salamat, A., Garbarino, G., Mezouar, M., Wilson, M. & McMillan, P. F. (2012), 'Melting of Sn to 1 Mbar', *Journal of Physics: Conference Series* **377**(1), 012035.

Bundy, F. P. (1959), 'Phase Diagram of rubidium to 150 000 kg/cm^2 and 400°C', *Physical Review* **115**(2), 274.

Celliers, P. M., Bradley, D. K., Collins, G. W., Hicks, D. G., Boehly, T. R. & Armstrong, W. J. (2004), 'Line-imaging velocimeter for shock diagnostics at the OMEGA laser facility', *Review of Scientific Instruments* **75**(11), 4916.

Celliers, P. M., Collins, G. W., Hicks, D. G. & Eggert, J. H. (2005), 'Systematic uncertainties in shock-wave impedance-match analysis and the high-pressure equation of state of Al', *Journal of Applied Physics* **98**(11), 113529.

Celliers, P. M., Loubeyre, P., Eggert, J. H., Brygoo, S., McWilliams, R. S., Hicks, D. G., Boehly, T. R., Jeanloz, R. & Collins, G. W. (2010), 'Insulator-to-conducting transition in dense fluid helium', *Physical Review Letters* **104**(18), 184503.

Christensen, N. E., Boers, D. J., van Velsen, J. L. & Novikov, D. L. (2000), '*Ab initio* thermodynamics of body-centred cubic and face-centred cubic Cs', *Journal of Physics: Condensed Matter* **12**(14), 3293.

Cohen, R. E. & Gülseren, O. (2001), 'Thermal equation of state of tantalum', *Physical Review* B **63**, 224101.

Dass, N. (1995), 'Melting maximum in alkali metals', *Physical Review* B **52**(5), 3023.

Datchi, F., Dewaele, A., Loubeyre, P., Letoullec, R., Godec, Y. L. & Canny, B. (2007), 'Optical pressure sensors for high-pressure high-temperature studies in a diamond anvil cell', *High Pressure Research* **27**(4), 447.

Datchi, F., LeToullec, R. & Loubeyre, P. (1997), 'Improved calibration of the SrB_4O_7:Sm^{2+} optical pressure gauge: Advantages at very high pressures and high temperatures', *Journal of Applied Physics* **81**(8), 3333.

Degtyareva, V. F. & Degtyareva, O. (2009), 'Structure stability in the simple element sodium under pressure', *New Journal of Physics* **11**(6), 063037.

Dewaele, A., Loubeyre, P. & Mezouar, M. (2004), 'Refinement of the equation of state of tantalum', *Physical Review* B **69**, 092106.

Dubrovinsky, L. (2012), Private Communication.

Dubrovinsky, L. & Dubrovinskaia, N. (2012), 'Implementation of micro-ball nanodiamond anvils for high-pressure studies above 6 Mbar', *Nature Communications* **3**, 1163.

Emery, V. & Axe, J. (1978), 'One-dimensional fluctuations and the chain-ordering transformation in $Hg_{3-\delta}AsF_6$', *Physical Review Letters* **40**(23), 1507.

Falconi, S., McMahon, M. I., Lundegaard, L. F., Hejny, C., Nelmes, R. J. & Hanfland, M. (2006), 'X-ray diffraction study of diffuse scattering in incommensurate rubidium-IV', *Physical Review* B **73**, 214102.

Giacovazzo, C., Monaco, H. L., Artioli, G., Viterne, D., Ferraris, G., Gilli, G., Zanotti, G. & Catti, M. (2002), *Fundamentals of crystallography*, Oxford University Press.

Glötzel, D. & McMahan, A. K. (1979), 'Relativistic effects, phonons, and the isostructural transition in cesium', *Physical Review* B **20**(8), 3210.

Golyshev, A. A., Shakhray, D. V., Kim, V. V., Molodets, A. M. & Fortov, V. E. (2011), 'High-temperature resistivity of shocked liquid sodium at pressures up to 230 GPa', *Physical Review* B **83**(9), 094114.

Goncharov, A. F., Beck, P., Struzhkin, V. V., Hemley, R. J. & Crowhurst, J. C. (2008), 'Laser-heating diamond anvil cell studies of simple molecular systems at high pressures and temperatures', *Journal of Physics and Chemistry of Solids* **69**(9), 2217.

Gregoryanz, E., Degtyareva, O., Somayazulu, M., Hemley, R. J. & Mao, H.-k. (2005), 'Melting of dense sodium', *Physical Review Letters* **94**, 185502.

Gregoryanz, E., Lundegaard, L. F., McMahon, M. I., Guillaume, C., Nelmes, R. J. & Mezouar, M. (2008), 'Structural diversity of sodium', *Science* **320**(5879), 1054.

Guillaume, C. L., Gregoryanz, E., Degtyareva, O., McMahon, M. I., Hanfland, M., Evans, S., Guthrie, M., Sinogeikin, S. V. & Mao, H.-K. (2011), 'Cold melting and solid structures of dense lithium', *Nature Physics* **7**(3), 211.

Hall, H. T., Merrill, L. & Barnett, J. D. (1964), 'High pressure polymorphism in cesium', *Science* **146**(3649), 1297.

Hammersley, A. P., Svensson, S. O., Hanfland, M., Fitch, A. N. & Häusermann, D. (1996), 'Two dimensional detector software: From real detector to idealised image or two-theta scan', *High Pressure Research* **14**, 235.

Hanfland, M., Loa, I. & Syassen, K. (2002), 'Sodium under pressure: bcc to fcc structural transition and pressure-volume relation to 100 GPa', *Physical Review* B **65**, 184109.

Hanfland, M., Loa, I., Syassen, K., Schwarz, U. & Takemura, K. (1999), 'Equation of state of lithium to 21 GPa', *Solid State Communications* **112**(3), 123.

Hanfland, M., Syassen, K., Christensen, N. E. & Novikov, D. L. (2000), 'New high-pressure phases of lithium', *Nature* **408**, 174.

Hernández, E. R. & Íñiguez, J. (2007), 'First-principles simulations on the nature of the melting line of sodium', *Physical Review Letters* **98**, 055501.

Hicks, D. G., Boehly, T. R., Eggert, J. H., Miller, J. E., Celliers, P. M. & Collins, G. W. (2006), 'Dissociation of liquid silica at high pressures and temperatures', *Physical Review Letters* **97**(2), 025502.

Higginbotham, A., Hawreliak, J., Bringa, E. M., Kimminau, G., Park, N., Reed, E., Remington, B. A. & Wark, J. S. (2012), 'Molecular dynamics simulations of ramp-compressed copper', *Physical Review* B **85**(2), 024112.

Jamieson, J. C. & Lawson, A. W. (1962), 'X-ray diffraction studies in the 100 kilobar pressure range', *Journal of Applied Physics* **33**(3), 776.

Jayaraman, A. (1983), 'Diamond anvil cell and high-pressure physical investigations', *Review of Modern Physics* **55**(1), 65.

Jenei, Z., Visbeck, K., Cynn, H., Yoo, C.-S. & Evans, W. (2009), 'High-temperature experiments using a resistively-heated high-pressure membrane diamond anvil cell', *Review of Scientific Instruments* **80**(10), 104501.

Kalantar, D., Belak, J., Collins, G., Colvin, J., Davies, H., Eggert, J., Germann, T., Hawreliak, J., Holian, B., Kadau, K., Lomdahl, P., Lorenzana, H., Meyers, M., Rosolankova, K., Schneider, M., Sheppard, J., Stölken, J. & Wark, J. (2005), 'Direct observation of the $\alpha - \epsilon$ transition in shock-compressed iron via nanosecond X-ray diffraction', *Physical Review Letters* **95**(7), 075502.

Katsnelson, M. I., Sinko, G. V., Smirnov, N. A., Trefilov, A. V. & Khromov, K. Y. (2000), 'Structure, elastic moduli, and thermodynamics of sodium and potassium at ultrahigh pressures', *Physical Review* B **61**(21), 14420.

Kechin, V. V. (2001), 'Melting curve equations at high pressure', *Physical Review* B **65**, 052102.

Kennedy, G. C., Jayaraman, A. & Newton, R. C. (1962), 'Fusion curve and polymorphic transitions of cesium at high pressures', *Physical Review* **126**(4), 1363.

Lazicki, A., Fei, Y. & Hemley, R. J. (2010), 'High-pressure differential thermal analysis measurements of the melting curve of lithium', *Solid State Communications* **150**(13), 625.

Lazicki, A., Goncharov, A. F., Struzhkin, V. V., Cohen, R. E., Liu, Z., Gregoryanz, E., Guillaume, C., Mao, H.-K. & Hemley, R. J. (2009), 'Anomalous optical and electronic properties of dense sodium', *Proceedings of the National Academy of Sciences* **106**(16), 6525.

LeToullec, R., Pinceaux, J. P. & Loubeyre, P. (1988), 'The membrane diamond anvil cell: A new device for generating continuous pressure and temperature variations', *High Pressure Research* **1**(1), 77.

Lindemann, F. A. (1910), 'The calculation of molecular vibration frequencies', *Physikalische Zeitschrift* **11**, 609.

Loa, I., Nelmes, R. J., Lundegaard, L. F. & McMahon, M. I. (2012), 'Extraordinarily complex crystal structure with mesoscopic patterning in barium at high pressure', *Nature Materials* **11**(7), 627.

Lorenz, K. T., Edwards, M. J., Jankowski, A. F., Pollaine, S. M., Smith, R. F. & Remington, B. A. (2006), 'High pressure, quasi-isentropic compression experiments on the OMEGA laser', *High Energy Density Physics* **2**(3), 113.

Luedemann, H. D. & Kennedy, G. C. (1968), 'Melting curves of lithium, sodium, potassium, and rubidium to 80 kilobars', *Journal of Geophysical Research* **73**(8), 2795.

Lundegaard, L. F. (2007), High-Pressure Diffraction Studies of Rubidium Phase IV, PhD thesis, The University of Edinburgh.

Lundegaard, L. F. (2013), 'Observation of a re-entrant phase transition in incommensurate potassium', *Physical Review* B **88**, 054106.

Lundegaard, L. F., Gregoryanz, E., McMahon, M. I., Guillaume, C., Loa, I. & Nelmes, R. J. (2009a), 'Single-crystal studies of incommensurate Na to 1.5 Mbar', *Physical Review* B **79**, 064105.

Lundegaard, L. F., Marqués, M., Stinton, G., Ackland, G. J., Nelmes, R. J. & McMahon, M. I. (2009b), 'Observation of the oP8 crystal structure in potassium at high pressure', *Physical Review* B **80**, 020101.

Ma, Y., Eremets, M., Oganov, A. R., Xie, Y., Trojan, I., Medvedev, S., Lyakhov, A. O., Valle, M. & Prakapenka, V. (2009), 'Transparent dense sodium', *Nature* **458**(12), 07786.

Mao, H. K., Bell, P. M., Shaner, J. W. & Steinberg, D. J. (1978), 'Specific volume measurements of Cu, Mo, Pd, and Ag and calibration of the ruby *R1* fluorescence pressure gauge from 0.06 to 1 Mbar', *Journal of Applied Physics* **49**(6), 3276.

Marqués, M., Ackland, G. J., Lundegaard, L. F., Stinton, G., Nelmes, R. J., McMahon, M. I. & Contreras-García, J. (2009), 'Potassium under pressure: A pseudobinary ionic compound', *Physical Review Letters* **103**, 115501.

Marqués, M., McMahon, M. I., Gregoryanz, E., Hanfland, M., Guillaume, C. L., Pickard, C. J., Ackland, G. J. & Nelmes, R. J. (2011a), 'Crystal structures of dense lithium: A metal-semiconductor-metal transition', *Physical Review Letters* **106**, 095502.

Marqués, M., Santoro, M., Guillaume, C. L., Gorelli, F. A., Contreras-García, J., Howie, R. T., Goncharov, A. F. & Gregoryanz, E. (2011b), 'Optical and electronic properties of dense sodium', *Physical Review* B **83**, 184106.

Martinez-Canales, M. & Bergara, A. (2008), 'Lindemann criterion and the anomalous melting curve of sodium', *Journal of Physics and Chemistry of Solids* **69**(9), 2151.

McMahan, A. (1984), 'Alkali-metal structures above the *s*-*d* transition', *Physical Review* B **29**(10), 5982.

McMahon, M. I., Gregoryanz, E., Lundegaard, L. F., Loa, I., Guillaume, C., Nelmes, R. J., Kleppe, A. K., Amboage, M., Wilhelm, H. & Jephcoat,

A. P. (2007), 'Structure of sodium above 100 GPa by single-crystal X-ray diffraction', *Proceedings of the National Academy of Sciences* **104**(44), 17297.

McMahon, M. I. & Nelmes, R. J. (2006), 'High-pressure structures and phase transformations in elemental metals', *Chemical Society Reviews* **35**, 943.

McMahon, M. I., Nelmes, R. J. & Rekhi, S. (2001a), 'Complex crystal structure of cesium-III', *Physical Review Letters* **87**(25), 255502.

McMahon, M. I., Nelmes, R. J., Schwarz, U. & Syassen, K. (2006), 'Composite incommensurate K-III and a commensurate form: Study of a high-pressure phase of potassium', *Physical Review* B **74**(14), 140102.

McMahon, M. I., Rekhi, S. & Nelmes, R. J. (2001b), 'Pressure dependent incommensuration in Rb-IV', *Physical Review Letters* **87**(5), 055501.

McMahon, M. & Nelmes, R. (2004), 'Chain "melting" in the composite Rb-IV structure', *Physical Review Letters* **93**(5), 055501.

McWilliams, R. S., Eggert, J. H., Hicks, D. G., Bradley, D. K., Celliers, P. M., Spaulding, D. K., Boehly, T. R., Collins, G. W. & Jeanloz, R. (2010), 'Strength effects in diamond under shock compression from 0.1 to 1 TPa', *Physical Review* B **81**(1), 014111.

McWilliams, R. S., Spaulding, D. K., Eggert, J. H., Celliers, P. M., Hicks, D. G., Smith, R. F., Collins, G. W. & Jeanloz, R. (2012), 'Phase transformations and metallization of magnesium oxide at high pressure and temperature', *Science* **338**(6112), 1330.

Merrill, L. & Bassett, W. A. (1974), 'Miniature diamond anvil pressure cell for single crystal X-ray diffraction studies', *Review of Scientific Instruments* **45**(2), 290.

Miller, J. E., Boehly, T. R., Melchior, A., Meyerhofer, D. D., Celliers, P. M., Eggert, J. H., Hicks, D. G., Sorce, C. M., Oertel, J. A. & Emmel, P. M. (2007), 'Streaked optical pyrometer system for laser-driven shock-wave experiments on OMEGA', *Review of Scientific Instruments* **78**(3), 034903.

Neaton, J. B. & Ashcroft, N. W. (2001), 'On the constitution of sodium at higher densities', *Physical Review Letters* **86**(13), 2830.

Nelmes, R. J., McMahon, M. I., Loveday, J. S. & Rekhi, S. (2002), 'Structure of Rb-III: Novel modulated stacking structures in alkali metals', *Physical Review Letters* **88**(15), 155503.

Olijnyk, H. & Holzapfel, W. B. (1983), 'Phase transitions in K and Rb under pressure', *Physical Letters A* **99**(8), 381.

Pecharsky, V. K. & Zavalij, P. Y. (2009), *Fundamentals of powder diffraction and structural characterization of materials*, Springer.

Petricek, V., Dusek, M. & Palatinus, L. (2006), *Jana2006: The crystallographic computing system*, Institute of Physics, Praha, Czech Republic.

Pickard, C. J. & Needs, R. J. (2010), 'Aluminium at terapascal pressures', *Nature Materials* **9**(8), 624.

Piermarini, G. J., Block, S., Barnett, J. D. & Forman, R. A. (1975), 'Calibration of the pressure dependence of the *R1* ruby fluorescence line to 195 kbar', *Journal of Applied Physics* **46**(6), 2774.

Raty, J.-Y., Schwegler, E. & Bonev, S. A. (2007), 'Electronic and structural transitions in dense liquid sodium', *Nature* **449**(7161), 448.

Rygg, J. R., Eggert, J. H., Lazicki, A. E., Coppari, F., Hawreliak, J. A., Hicks, D. G., Smith, R. F., Sorce, C. M., Uphaus, T. M., Yaakobi, B. & Collins, G. W. (2012), 'Powder diffraction from solids in the terapascal regime', *Review of Scientific Instruments* **83**(11), 113904.

Sanloup, C., Gregoryanz, E., Degtyareva, O. & Hanfland, M. (2008), 'Structural transition in compressed amorphous sulfur', *Physical Review Letters* **100**, 075701.

Schaeffer, A. M. J., Talmadge, W. B., Temple, S. R. & Deemyad, S. (2012), 'High pressure melting of lithium', *Physical Review Letters* **109**, 185702.

Schwarz, U., Grzechnik, A., Syassen, K., Loa, I. & Hanfland, M. (1999a), 'Rubidium-IV: A high pressure phase with complex crystal structure', *Physical Review Letters* **83**(20), 4085.

Schwarz, U., Syassen, K., Grzechnik, A. & Hanfland, M. (1999b), 'The crystal structure of rubidium-VI near 50 GPa', *Solid State Communications* **112**(6), 319.

Schwarz, U., Takemura, K., Hanfland, M. & Syassen, K. (1998), 'Crystal structure of cesium-V', *Physical Review Letters* **81**(13), 2711.

Singh, A. K. & Kenichi, T. (2001), 'Measurement and analysis of nonhydrostatic lattice strain component in niobium to 145 GPa under various fluid pressure-transmitting media', *Journal of Applied Physics* **90**(7), 3269.

Siringo, F., Pucci, R. & Angilella, G. G. N. (1997), 'Are light alkali metals still metals under high pressure?', *High Pressure Research* **15**(4), 255.

Smith, R., Eggert, J., Saculla, M., Jankowski, A., Bastea, M., Hicks, D. & Collins, G. (2008), 'Ultrafast dynamic compression technique to study the kinetics of phase transformations in bismuth', *Physical Review Letters* **101**(6), 065701.

Spaulding, D. K., Hicks, D. G., Smith, R. F., Eggert, J. H., McWilliams, R. S., Collins, G. W., Jeanloz, R., Elert, M., Furnish, M. D., Chau, R., Holmes, N. & Nguyen, J. (2007), 'New optical diagnostics for equation of state experiments on the JANUS laser', *AIP Conference Proceedings* **955**(1), 1071.

Spaulding, D. K., McWilliams, R. S., Jeanloz, R., Eggert, J. H., Celliers, P. M., Hicks, D. G., Collins, G. W. & Smith, R. F. (2012), 'Evidence for a phase transition in silicate melt at extreme pressure and temperature conditions', *Physical Review Letters* **108**(6), 065701.

Swift, D. & Johnson, R. (2005), 'Quasi-isentropic compression by ablative laser loading: Response of materials to dynamic loading on nanosecond time scales', *Physical Review E* **71**(6), 066401.

Takeda, M., Ina, H. & Kobayashi, S. (1982), 'Fourier-transform method of fringe-pattern analysis for computer-based topography and interferometry', *Journal of the Optical Society of America* **72**(1), 156.

Takemura, K., Christensen, N. E., Novikov, D. L., Syassen, K., Schwarz, U. & Hanfland, M. (2000), 'Phase stability of highly compressed cesium', *Physical Review* B **61**(21), 14399.

Takemura, K., Minomura, S. & Shimomura, O. (1982), 'X-ray diffraction study of electronic transitions in cesium under high pressure', *Physical Review Letters* **49**(24), 1772.

Takemura, K. & Syassen, K. (1983), 'High-pressure phase transitions in potassium and phase relations among heavy alkali metals', *Physical Review* B **28**(2), 1193.

Tamblyn, I., Raty, J.-Y. & Bonev, S. A. (2008), 'Tetrahedral clustering in molten lithium under pressure', *Physical Review Letters* **101**, 075703.

Tateno, S., Hirose, K., Ohishi, Y. & Tatsumi, Y. (2010), 'The structure of iron in Earth's inner core', *Science* **330**(6002), 359.

Taxak, M., Kumar, S., Krishnamurthy, N., Suri, A. K. & Tiwari, G. P. (2012), 'Change in lattice parameter of tantalum due to dissolved hydrogen', *Processing and Application of Ceramics* **6**(2), 73.

Tups, H. & Syassen, K. (1984), 'Effect of pressure on the optical absorption in aluminium', *Journal of Physics F: Metal Physics* **14**(11), 2753.

Wang, Y. & Sun, Y.-F. (2001), 'Thermodynamic properties of sodium: A first-principles study', *Chinese Physics Letters* **18**(7), 864.

Winzenick, M., Vijayakumar, V. & Holzapfel, W. B. (1994), 'High-pressure X-ray diffraction on potassium and rubidium up to 50 GPa', *Physical Review* B **50**(17), 12381.

Young, D. A. (1991), *Phase Diagrams of the Elements*, University of California Press, Berkeley, CA.

Young, D. A. & Ross, M. (1984), 'Theoretical high-pressure equations of state and phase diagrams of the alkali metals', *Physical Review* B **29**(2), 682.

Zel'dovich, Y. B. & Raizer, Y. P. (2002), *Physics of shock waves and high-temperature hydrodynamic phenomena*, Dover Publications Inc.

Zha, C.-S. & Boehler, R. (1985), 'Melting of sodium and potassium in a diamond anvil cell', *Physical Review* B **31**(5), 3199.

PHYSICAL REVIEW B **84**, 054111 (2011)

Melting curve of potassium to 22 GPa

O. Narygina,* E. E. McBride, G. W. Stinton, and M. I. McMahon
SUPA, School of Physics and Astronomy, and Centre for Science at Extreme Conditions, The University of Edinburgh, Mayfield Road, Edinburgh EH9 3JZ, United Kingdom
(Received 17 January 2011; revised manuscript received 24 April 2011; published 12 August 2011)

The melting curve of potassium has been measured experimentally to 22 GPa using *in situ* X-ray diffraction and gas-membrane diamond anvil cells equipped with external resistive heating. The evolution of the melting temperature with pressure is similar to that of sodium, but it is different to that reported previously. A melting maximum is found in the stability field of the *bcc*-phase, at 5.8(5) GPa, followed by a decrease in the melting temperature down to a melting minimum at the *fcc*-host-guest (*tI*19) transition at 19(1) GPa. The *bcc*-*fcc*-liquid and *fcc*-*tI*19-liquid triple points are found to be at 466(10) K and 13.6(3) GPa and at 390(10) K and 19.0(3) GPa, respectively.

DOI: 10.1103/PhysRevB.84.054111 PACS number(s): 61.50.Ks, 64.70.dj

I. INTRODUCTION

The high-pressure behavior of the alkali metals remains a "hot topic" in both experimental and theoretical physics. Despite the apparent simplicity of these metals (a single *s* electron in the valence band), they exhibit quite peculiar properties at high pressures, such as the formation of composite and/or open-packed structures,[1] low melting temperatures,[2,3] and both a decrease in electrical conductivity and the appearance of superconductivity.[4] The pressure-induced structural behavior of the different alkali metals is broadly similar, with the main trend being transitions between simple, cubic phases (body-centered-cubic [*bcc*] and face-centered-cubic [*fcc*]) before transitions to open-packed phases with decreased structural symmetry.[1,5] Potassium (K), like the other alkali metals, crystallizes in the *bcc* structure at ambient conditions before transforming to the *fcc* phase at 11 GPa at 300 K.[6,7] Further increase of pressure leads first to a transition at 19 GPa to the incommensurate host-guest composite structure with 19.2 atoms per unit cell (hereafter referred to as *tI*19),[7] and then to the orthorhombic *oP*8 structure at 54 GPa, which is stable up to 90 GPa, where it transforms to the tetragonal *tI*4 structure, which in turn transforms to the orthorhombic *oC*16 structure at 96 GPa.[8] There is also evidence of the stabilization of the hexagonal *hP*4 structure at pressures between 25 and 35 GPa.[9] The *oP*8 and *hP*4 structures are otherwise observed only in sodium (Na), but at much higher pressures,[10,11] while the *oC*16 and *tI*4 structures are observed in both cesium (Cs) and rubidium (Rb) at high pressures.[12] The high-pressure structural behavior of K therefore has similarities to each of its group-I neighbors (Na, Rb, and Cs).

One of the common features of most of the alkali metals is complex melting behavior. The melting temperature of Na reaches a maximum of ~1000 K at about 31 GPa in the *bcc* phase, followed by a dramatic decrease down to approximately room temperature at ~120 GPa.[2] The appearance of one or more melting-curve maxima has also been observed in lithium (Li), Rb, and Cs,[3,13,14] but not, however, in K, at least not up to 14.5 GPa.[15] The melting curve of K has been measured to 8 GPa in a piston-cylinder apparatus.[16] Later experiments, performed up to 3 GPa using the piston piezometer method[17] and a modified piston-cylinder apparatus with a hydrostatic pressure medium,[18] have revealed that this earlier study was performed under nonhydrostatic conditions. Later, Zha and Boehler[15] extended the melting curve of K to 14.5 GPa by optical observations of a sample enclosed in a diamond anvil cell (DAC). They reported a continuous increase of the melting temperature in both the *bcc* and *fcc* phases, up to 649 K at 14.5 GPa. However, theoretical calculations of the melting temperature of K have suggested the presence of a melting maximum in the interval of 4–8 GPa.[19–21] To resolve this apparent discrepancy between experimental and theoretical results, and to extend the measurements of potassium melting curve into the incommensurate *tI*19 phase above 19 GPa, we performed an *in situ* X-ray diffraction (XRD) study of the melting curve of K at pressures up to 22 GPa using DAC techniques.

II. EXPERIMENT

High-purity (99.95+%) samples of K (Aldrich Chemical Company), along with a few small pieces of SrB_4O_7:Sm^{2+} for pressure calibration, were loaded into membrane pressure cells equipped with 300 μm-culet-size diamond anvils in a dry, oxygen-free atmosphere (<1 ppm O_2 and <1 ppm H_2O) to prevent sample oxidation. In order to avoid contamination, no pressure transmitting medium was used. While the stated purity of the sample refers to the metal content, such samples may contain nonmetallic contaminants such as oxygen. However, in a previous room-temperature study of potassium using both as-purchased and distilled samples, we observed no difference in their high-pressure behavior.[7] Diffraction patterns of the low-pressure *bcc* and *fcc* phases in the present study showed no discernible contaminant peaks, confirming that the sample was pure K.

Initial experiments conducted with rhenium (Re) gaskets showed that the K reacted with the gasket material immediately upon melting. Gold-lined Re gaskets also showed evidence of reaction. However, no reactions were observed between the liquid-K and tungsten (W) or iridium (Ir). Therefore, we employed W and composite Re-Ir gaskets in our experiments, pre-indented to 20 μm, and with an initial sample-chamber diameter of 80 to 125 μm, depending on the gasket material. For pressure measurements, the shift of the $^7D_0$–$^5F_0$ fluorescence line of SrB_4O_7:Sm^{2+} was used.[22] In

several runs, once the melting point of K was first reached, the fluorescence signal from the $SrB_4O_7:Sm^{2+}$ became very weak or disappeared entirely. In this case, the pressure was determined from the room-temperature K equation-of-state (EOS),[7] with a correction for the effects of thermal expansion, as obtained from the ambient-pressure thermal expansion,[23] and our own high-pressure, high-temperature measurements of the crystalline phases when the pressure could be directly determined from $SrB_4O_7:Sm^{2+}$. In these cases, the maximum correction that needed to be applied to the pressure determined from the room-temperature EOS was 0.5 GPa.

In order to heat the sample to the desired temperatures, we used external resistive heating K-rings (Watlow Ltd.), which allow sustained, stable, and homogeneous heating of the sample up to at least 600 K. A K-type (chromel/alumel) thermocouple, placed on the back of the diamond anvils, was used for temperature measurements; the uncertainty in temperature was estimated to be not more than 10 K. At each experimental point, the temperature before and after the X-ray exposure was the same within 2–3 K.

In situ high-pressure XRD measurements were performed on beamline ID09a at the European Synchrotron Radiation Facility (ESRF), and on beamline I15 at the Diamond Light Source (DLS). The incident X-ray wavelengths were 0.4143 Å and 0.4140 Å, and the X-ray beam sizes were approximately 10 μm and 30 μm in diameter, respectively. The XRD data were collected on a MAR555 detector (exposure time 1 s) on ID09a, and on a MAR 345 image-plate detector (exposure time 120 s) on I15. In both cases, the detectors were placed approximately 350 mm from the sample. During each X-ray exposure, the sample was oscillated $\pm 7^\circ$ around a vertical axis in order to improve the powder-averaging of the XRD patterns from polycrystalline samples, and to obtain a sufficient number of reflections to identify the crystal structure of K when the sample had annealed into a single crystal, as is discussed in the following section. The resulting two-dimensional (2D) XRD images were integrated azimuthally using Fit2D,[24] and subsequent analysis was performed either with the GSAS package,[25] or by least-squares fitting of the measured *d*-spacings.

Diffraction data were collected from ten different samples, and consistent results were obtained from all of them. In all experimental runs, the K samples were initially precompressed to a desired pressure at room temperature and then heated until melting was observed. The pressure and/or temperature of the sample were then changed to bring it back into a crystalline phase (*bcc*, *fcc*, or *tI*19 depending on the pressure). Melting was judged both from the complete disappearance of the crystalline Bragg scattering and by the simultaneous appearance of a diffuse halo of scattering from the liquid phase.

III. RESULTS

A representative set of high-pressure, high-temperature 2D XRD images, and their integrated XRD profiles, is shown in Fig. 1. They demonstrate the sharp transition from *fcc*-K to liquid-K at 18.3(3) GPa, which is induced by the small increase in temperature of only 4 K. A subsequent pressure increase of about 2 GPa at the same temperature (408[10] K) brings the sample into the stability field of the incommensurate *tI*19 phase, and results in the recrystallization of the sample. It should be noted that upon heating, K samples tend to anneal into high-quality single crystals, and, therefore, many of the high-temperature diffraction patterns collected from the solid phases during this experiment were single-crystal–like (see Fig. 1(a)). The Bragg peaks from such samples tend to rapidly saturate the detector, and hence azimuthal integration results in diffraction profiles that do not have accurate relative peak intensities. Therefore, the analysis of the integrated XRD patterns (see Fig. 1(d)) was performed using the Le Bail method. On the raw diffraction image collected from the incommensurate *tI*19-K phase at 408(10) K and 22.3(3) GPa (Fig. 1(c)), the reflections from the "host" component of the structure are sharp (Miller indices for some of which are given), while the (*hk*1) layer of "guest" reflections is extremely broad and diffuse, and appears to form an almost continuous line of diffuse intensity in the 2D images, with several weak intensity maxima. In the integrated profile, the strong (001) guest peak then appears as a broad bump (marked in Fig. 1(d) by the black arrow). The diffuse nature of the guest reflections arises from a temperature-induced reduction in the correlation length between the guest-atom chains, resulting in the broadening of the guest reflections in the *hk*-plane. We have observed such broadening previously in the composite phases of both Rb and Na.[26,27]

Integrated diffraction profiles of liquid-K collected at different pressures, with the background from the pressure cell subtracted, are shown in Fig. 2(a). In order to subtract the background, which includes both Compton scattering and thermal diffuse scattering (TDS) from the diamond anvils, we utilized the procedure described by Sanloup *et al.*[28] In this procedure, a background baseline for a diffraction profile from the liquid is obtained by the integration of a pattern collected from the solid phase immediately prior to melting, once all Bragg reflections from the solid phase have been masked. As one can see in Fig. 2(a), at pressures below 11 GPa, only the first diffraction maximum from the liquid-K is well defined; however, above 11 GPa, the much weaker second diffuse halo becomes more pronounced as pressure increases. Observation of the second diffuse halo of scattering is made more difficult by the fact that it lies at the same *d*-spacing as the TDS from the diamond anvils.

The *d*-spacing of the first diffraction maximum from the liquid is plotted as a function of pressure in Fig. 2(b) (solid circles), along with the *d*-spacing of the (110) and (111) reflections from the *bcc* (unfilled triangles) and *fcc* phases (unfilled squares), respectively. The *d*-spacing of the first diffraction maximum of the liquid at 2.2(5) GPa agrees well with the *d*-spacing of the (110) reflection from *bcc*-K, while from 5 to 15 GPa the position of the first liquid diffraction peak closely follows the *d*-spacing of the (111) *fcc*-K reflection. The kinks in the liquid data at about 5 and 15 GPa suggests changes in the compressibility of liquid-K at these pressures, the possible origin of which is discussed in the next section.

The melting curve of potassium measured to 22 GPa is shown in Fig. 3. It appears to be strikingly similar to that of Na,[2] but with the phases appearing at significantly lower pressures. All XRD patterns collected below 11(1) GPa showed the presence of single-phase *bcc*-K; and at 11–13.6 GPa (depending on the temperature), we detected the

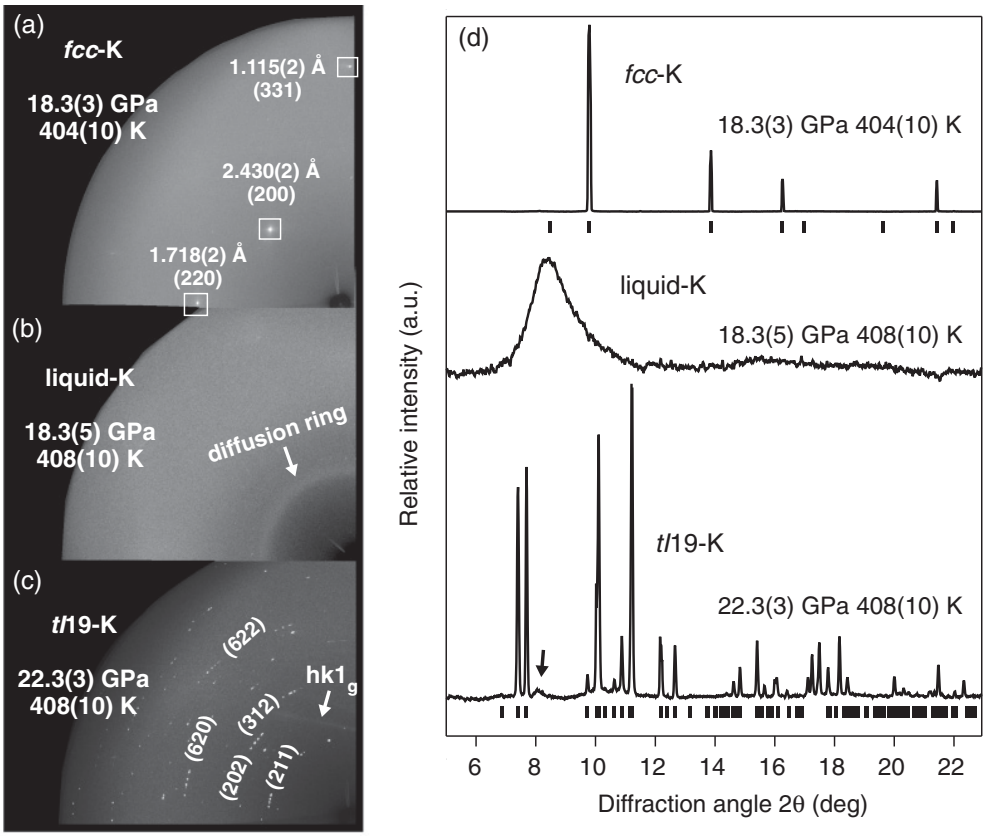

FIG. 1. (a)–(c) Representative quadrants of XRD images from the solid and liquid phases of K. Three d-spacings of *fcc*-K and Miller indices for some reflections of *tI*19-K are marked in the images (a,c), and the diffuse line of ($hk1$) reflections from the guest component of the *tI*19 phase is identified with the white arrow in image (c). (d) The corresponding integrated XRD profiles. The crystalline phases are indexed to the *fcc* and "host-guest" *tI*19 structures, and vertical bars show the fitted positions of the diffraction reflections of *fcc*-K ($a_{fcc} = 4.856(1)$ Å) and the "host" phase of *tI*19-K ($a_{host} = 9.769(1)$ Å, $c_{host} = 4.730(1)$ Å). The black arrow shows the position of the (001) "guest" reflection of *tI*19-K. The XRD profile of liquid-K obtained at 18.3(5) GPa and 408(10) K is plotted with the background subtracted; the background baseline was obtained by integration of the pattern collected for *fcc*-K at 404(10) K and 18.3(3) GPa after all Bragg reflections had been masked (see text for the details).

appearance of *fcc*-K. The *bcc-fcc* phase boundary was tracked using a series of small changes in pressure/temperature up to the *bcc-fcc*-liquid triple point (the area highlighted in Fig. 3), which we found to be at 466(10) K and 13.6(3) GPa. Using the ambient temperature phase transition pressure, 11 GPa[6,7] (highlighted by a star in Fig. 3), the gradient of the *bcc-fcc* phase boundary is determined to be +64(5) K/GPa. Note that the *bcc-fcc* phase boundary for K was previously reported to be almost vertical, or even to have a slightly negative gradient,[15,21] and the *bcc-fcc*-liquid triple point was previously reported to be at 566 K and 11 GPa.[15]

Within the *bcc* stability region of the phase diagram, we traversed the melting line five times, at ambient pressure, 2.2(3), 5.1(3), 7.4(3) GPa, and 11.6(3) GPa, obtaining melting temperatures of 338(2) K, 496(10) K, 536(10) K, 526(10) K, and 498(10) K, respectively. With further increases of pressure above 11.6 GPa, the melting temperature continues to fall, decreasing to 466(10) K at the *bcc-fcc*-liquid triple point at 13.6(3) GPa. At pressures above the triple point, in the *fcc* phase, the melting temperature is almost constant up to 15.6(3) GPa. Note, that we cannot rule out the presence of a second melting maximum in the *fcc*-K stability field between 13.6 and 15.6 GPa, (the presence of a second maximum was also discussed for the case of the Na melting curve,[29] and it clearly exists in the *fcc* phase of Cs[14]). However, if such a maximum exists in K, it would be very small. Above 15.6 GPa, the melting curve again changes its behavior, descending to a clear minimum at 390(10) K and 19.0(3) GPa at the *fcc-tI*19-liquid triple point. The *fcc-tI*19 phase boundary is found to be almost vertical. In the *tI*19 phase, the melting temperature increases very rapidly with pressure, changing by some 65(5) K/GPa (Fig. 3). Similar behavior is observed in Na, where the melting temperature, after passing through a deep minimum at 300 K and 118 GPa, increases again after the transition to the *tI*19 phase at 125 GPa, although the increase does not seem as rapid as in K.[10,30] This difference is most probably related to the substantial volume change of 4.1(1)% observed at the *fcc-tI*19 transition in K, which is significantly larger than the volume change of 0.5(2)% observed at the *oP*8-*tI*19 transition in Na.[7,10]

Our measured melting temperatures up to the *bcc-fcc*-liquid triple point, combined with all previous melting curve

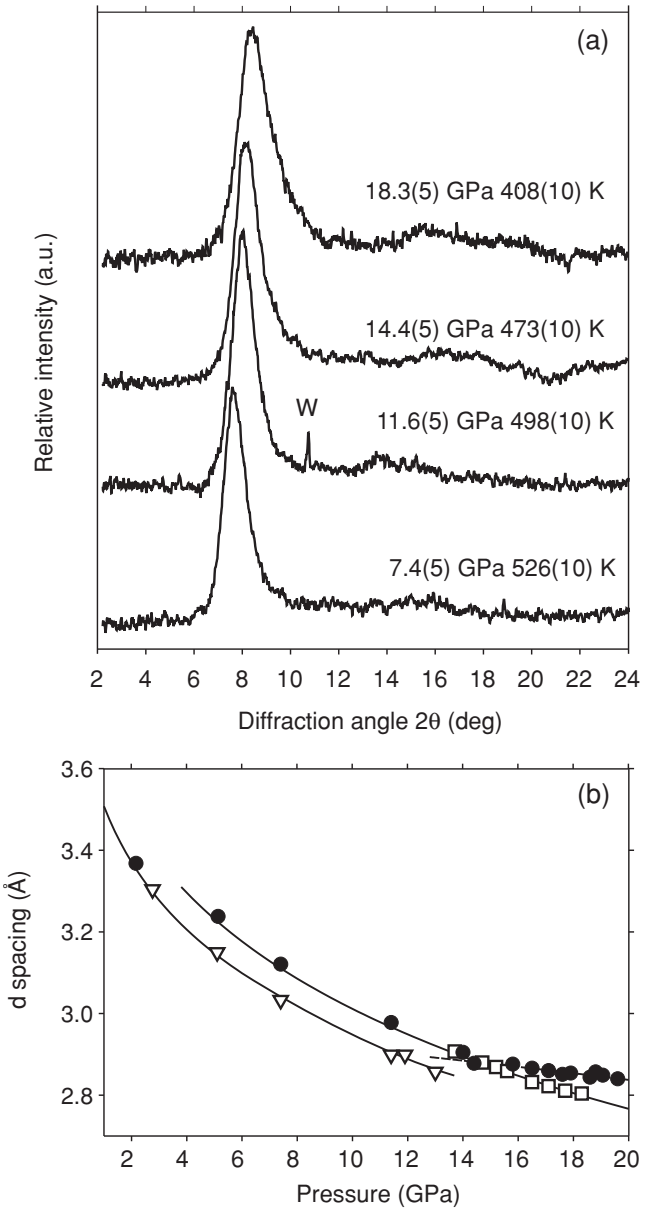

FIG. 2. (a) Integrated XRD profiles from liquid K obtained at different pressures. The background has been subtracted using the procedure described in Sanloup *et al.*[28] (see text for the details). A weak diffraction peak from the tungsten (W) gasket is marked. (b) The pressure-induced shift of the first diffraction peak from liquid-K (solid circles) and the (110) (open triangles) and (111) (open squares) diffraction peaks from *bcc*- and *fcc*-K, respectively. The lines through the data points are guides to the eye.

measurements up to 3 GPa,[16–18] suggest the presence of a melting maximum in the *bcc* phase. To locate it, we fitted these data to the Kechin equation,[31] using the following parameters: $a = 0.527(27)$, $b = 0.288(10)$, and $c = 0.045(1)$. The resulting curve (shown by the solid black line in Fig. 3) gives an excellent fit to the observed melting temperatures and suggests the maximum melting point is at 530(10) K and 5.8(5) GPa, which is in good agreement with theoretical calculations by Young and Ross[19] and Katsnelson *et al.*[21] (the dotted and dash-dotted lines in Fig. 3, respectively). Note that the existence of a melting maximum in the *bcc* phase is not dependent on the fit to the Kechin equation, as we clearly see the melting temperature of the *bcc* phase decrease between 5.1(5) GPa and 13.6(3) GPa. We use the fit simply to provide a best estimate of where the maximum is located.

As evidenced from Fig. 3, our diffraction results are in strong disagreement with the melting curve of K reported by Zha and Boehler.[15] Although some differences might arise from the use of different pressure calibrants (Zha and Boehler used ruby fluorescence, the spectrum of which gets broader and weaker at high temperatures[15]) and different sample preparation techniques (Zha and Boehler loaded their samples under mineral oil), it seems unlikely that these factors alone can explain such a significant misfit between the two data sets; the temperature difference between the two melting curves at 14.5 GPa is more than 180 K. The most likely explanation is the different way of defining the observation of melting. Zha and Boehler determined melting by visual observation of the sample, through monitoring changes in sample shape, surface texture, and reflectivity in both transmitted and reflected light. The very large differences between the melting temperatures reported in that study, and the results we report here through direct observation of melting using X-ray diffraction, strongly suggest that the changes observed by Zha and Boehler were not a result of melting.

IV. DISCUSSION

K, like Na, Rb, and Cs, is found to have a melting maximum in the *bcc* phase. The *bcc* phases of the neighboring alkaline earth elements also exhibit either a maximum, as in Ba,[32] or flat melting curves over extended pressure ranges, as in Ca and Sr.[33] The recently-observed maximum in the Li melting curve at 10 GPa may be in the *bcc* phase.[34] The appearance of a melting maximum, without the presence of a phase transition within the solid phase, is itself a manifestation of anomalous behavior of a system. According to the Clausius-Clapeyron equation, a change in the gradient of the melting slope from positive to negative suggests a change in the relative densities of the solid and liquid phases, with the liquid becoming the denser of the two at pressures above the melting maximum. This effectively means structural changes either in the liquid or solid phase, or both. In Na, it has been shown that above 30 GPa (the pressure at which the maximum melting temperature is observed), the liquid phase of Na is less compressible than the underlying *bcc* phase.[2] Molecular dynamics simulations by Hernandez and Iniguez[29] confirmed the higher compressibility of the liquid phase and suggested that while there is no dramatic change in the liquid structure on compression, there is a higher probability of *fcc*-like local order in liquid Na at higher pressures.[29] Further molecular dynamic simulations of liquid and solid Na by Raty *et al.*[35] showed changes in the second coordination shell of the liquid phase above 30 GPa. They assigned these to a change from a *bcc*-like to a *fcc*-like liquid, resulting in a negative slope of the melting curve between 30 and 65 GPa, where the solid Na itself adopts the *fcc* structure. The reason for structural and/or electronic changes to occur in a liquid state earlier than in a solid state has been discussed by several authors and is assumed to be related

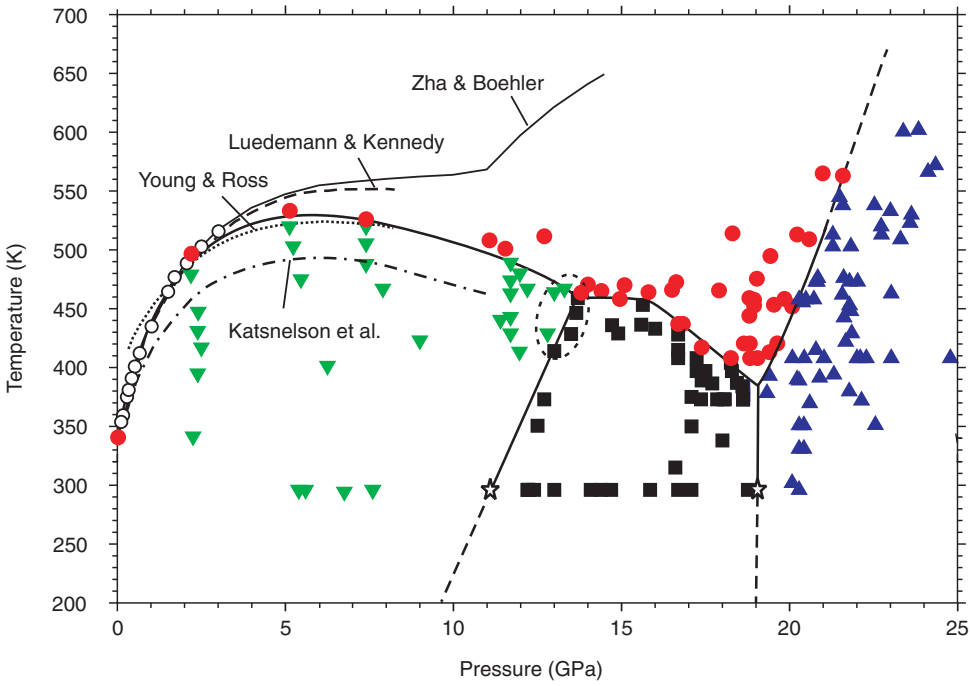

FIG. 3. (Color online) The melting curve of K measured to 22 GPa. Filled symbols represent the data from this study: downward-pointing triangles correspond to *bcc*-K, squares to *fcc*-K, upward-pointing triangles to *tI*19-K, and circles to the liquid phase. The melting temperature at ambient pressure was obtained by observation of the K sample sealed in a glass capsule. Solid and dashed lines represent the measured phase boundaries and their extrapolations, respectively. The data points marked with stars show the locations of the *bcc-fcc* and *fcc-tI*19 phase transitions at room temperature.[6,7] Open circles are data points from references 16–18. The melting curve in the pressure range from ambient up to the 13.6(3) GPa (the location of the *bcc-fcc*-liquid triple point) represents the fit of the experimental data using the Kechin equation.[31] Some previously-reported experimental and theoretically calculated melting curves of K are from references 15, 16, 19, and 21.

to the finite-temperature fluctuations in liquids, which allow changes to occur continuously over a large pressure range. In solids, they occur discretely at a definite pressure.[35,36]

Similarities in the melting curves of K and Na,[2] as well as the other similarities in the structural behavior of these two alkali elements at high compressions (discussed previously), may suggest a similar origin for the melting maximum in the stability field of *bcc*-K, namely, a decrease of compressibility of the liquid phase above 6 GPa and increasing probability of *fcc*-like local ordering. Detailed measurements of the relative compressibilities of the *bcc* and liquid phases of K along with molecular dynamics simulations are required to confirm this. However, a plot of the *d*-spacing of the first diffraction peak in liquid K implies a change in its compression behavior at about 5 GPa [Fig. 2(b)]. While at 2.2 GPa the *d*-spacing of the first diffraction peak of the liquid agrees very well with the *bcc*-K equation of state, at pressures between 5 and 14 GPa it closely follows the *fcc*-K equation of state. This suggests that the local ordering in liquid-K may change from *bcc*- to the denser *fcc*-like at about 5 GPa, i.e., almost 8 GPa below the *bcc-fcc* transition pressure in the solid phase (13.6 GPa at 455 K).

While the melting maximum in the *bcc* phase might be explained by different compressibilities of the solid and liquid phases, and an increased likelihood of *fcc*-like local ordering, this cannot explain the behavior of the K melting curve above 13.6 GPa, where the solid K itself adopts the *fcc* structure, and the melting curve remains essentially flat to 15.6 GPa before decreasing to its minimum value of 390(10) K at 19.0(3) GPa, just before the transition to *tI*19 phase (Fig. 3). Raty *et al.*[35] reported that the similar behavior of the melting curve of *fcc*-Na results from electronic and structural changes in the liquid phase that are similar to those that occur at the *fcc*-to-*cI*16 transition in the solid phase at higher pressures.[37,2] As a result, the liquid local order changes from *fcc*-like to *cI*16-like, altering the compressibility of the liquid phase. This is then reflected in the negative gradient of the melting curve of Na between 80 and 100 GPa. Above 100 GPa, where the solid transforms to the *cI*16 phase, the melting curve recovers its positive slope.[10] Since the melting behavior of *fcc*-K and *fcc*-Na is very similar, we suggest it can be explained in the same manner, namely by electronic and structural changes, which, in the case of K, result in the liquid local order changing from *fcc*-like to *tI*19-like. Figure 2(b) shows the pressure dependence of the *d*-spacing of the first diffraction peak in liquid K and the (111) diffraction peak from the *fcc*-K phase. While below 15.6 GPa both the *d*-spacing and compressibility of the peaks are the same, there is a clear change in liquid-K above that pressure, with the compressibility of the first liquid diffraction peak being somewhat less than that of the (111) diffraction peak [Fig. 2(b)]. This change in compressibility results in the negative slope of the melting curve of K between 15.6 and 19 GPa. Above 19 GPa, where the solid itself assumes the denser *tI*19 structure, the slope of the melting curve recovers a positive gradient.

However, anomalous melting behavior can also be related to structural changes in a solid. Thus, the melting of *bcc*- and *fcc*-Na can be explained in the framework of the Lindeman melting criterion, without consideration of a liquid phase. Several authors have calculated softening of the elastic moduli of solid Na above 30 GPa and a consequent decrease of the Debye temperature,[38] which, according to the Lindeman criterion, results in a negative slope of a melting curve. A strong softening of elastic moduli was also found in *fcc*-Cs,[39] the melting temperature of which also decreases with pressure.[14] The theoretical work by Katsnelson *et al.*[21] did show softening of elastic constants in both *bcc*- and *fcc*-K. Using the Lindeman criterion, they also calculated the melting curve of K, which they found to have a maximum at about 5 GPa (in good agreement with the 5.8(5) GPa presented here). However, the same calculation underestimates the melting temperature over a large pressure range (dash-dotted line in Fig. 3). The possible softening of elastic moduli in *bcc*- and *fcc*-K, and its effect on the melting curve of K, will require further experimental work.

Finally, the marked minimum of the K melting curve, just before the transition to the incommensurate *tI*19 phase, is also not unique: the melting curves of Cs, Rb, Na, and Li also reach their high-pressure minima at the transition to their high-pressure, low-symmetry phase.[2,3,13,14] In the case of Cs, superconductivity was discovered in the low-symmetry Cs-IV phase,[40] while Li becomes superconducting in the *fcc* phase, with $T_c \approx 10$ K at ∼21 GPa, which increases to 17 K at 40 GPa, i.e., the same pressure at which the melting temperature of Li reaches its minimum of 190 K, just before the transition to the *cI*16 phase.[3] Therefore, one might also expect superconducting behavior in Na, Rb, and K at pressures near the melting minimum. Indeed, theoretical work from Shi and Papaconstantopoulos[41] has predicted superconductivity in K with $T_c \approx 2$–12 K at 14 GPa (within the *fcc*-K stability field), while Sanna *et al.*[42] and Profeta *et al.*,[43] using *ab initio* electronic structure calculations, have predicted superconductivity in K with T_c increasing from 1–2 K at 21–23 GPa (within stability field of *tI*19-K) to 11 K at 29 GPa. There is to date, however, no experimental evidence of superconductivity in any phase of K, apart from a weak anomaly observed at 1.7 K at 35 GPa.[4] Further work at lower temperatures is required.

V. CONCLUSIONS

In conclusion, the melting temperature of K has been measured to 22 GPa, and it is found to be very different to that reported previously. The *bcc* phase exhibits a melting maximum like that observed previously in Na, Rb, and Cs, while the melting curve of the *fcc* phase is found to be very similar to that observed previously in Na. Using similar arguments to those put forward previously to explain the melting curve of Na, we suggest that the behavior of the K melting curve is due to structural and electronic changes in the liquid phase at about 5 and 14 GPa, which mirror those that occur in the solid phase at 13.6 and 19 GPa, respectively. However, the anomalous melting of *bcc*- and *fcc*-K may also suggest a softening of elastic moduli of these phases as pressure increases. Further work is required to understand the complex nature of dense potassium.

ACKNOWLEDGMENTS

We thank the European Synchrotron Radiation Facility (ESRF) and Diamond Light Source (DLS) for provision of synchrotron time and support. We thank A. K. Kleppe, H. Wilhelm, and A. P. Jephcoat of I15 (DLS), and S. Evans and M. Hanfland of ID09a (ESRF) for their help with the experiment. We also thank E. Gregoryanz for discussions. This work was supported by a research grant from the UK Engineering and Physical Sciences Research Council.

*Olga.Narygina@ed.ac.uk

[1] M. I. McMahon and R. J. Nelmes, Chem. Soc. Rev. **35**, 943 (2006), and references therein.
[2] E. Gregoryanz, O. Degtyareva, M. Somayazulu, R. J. Hemley, and H.-K. Mao, Phys. Rev. Lett. **94**, 185502 (2005).
[3] C. L. Guillaume, E. Gregoryanz, O. Degtyareva, M. I. McMahon, M. Hanfland, S. Evans, M. Guthrie, S. V. Sinogeikin, and H.-K. Mao, Nature Phys. **7**, 211 (2011).
[4] J. S. Schilling, High Pres. Res. **26**, 145 (2006), and references therein.
[5] K. Syassen, in *Proceedings of International School of Physics. Enrico Fermi Course CXLVII*, edited by R. J. Hemley *et al.* (IOS Press, Amsterdam, 2002), p. 251.
[6] H. Olijnyk and W. B. Holzapfel, Phys. Lett. **99**, 381 (1983).
[7] M. I. McMahon, R. J. Nelmes, U. Schwarz, and K. Syassen, Phys. Rev. B **74**, 140102 (2006).
[8] L. F. Lundegaard, M. Marqués, G. Stinton, G. J. Ackland, R. J. Nelmes, and M. I. McMahon, Phys. Rev. B **80**, 020101 (2009).
[9] M. Marqués, G. J. Ackland, L. F. Lundegaard, G. Stinton, R. J. Nelmes, M. I. McMahon, and J. Contreras-Garcia, Phys. Rev. Lett. **103**, 115501 (2009).
[10] E. Gregoryanz, L. F. Lundegaard, M. I. McMahon, C. Guillaume, R. J. Nelmes, and M. Mezouar, Science **320**, 1054 (2008).
[11] Y. Ma, M. Eremets, A. R. Oganov, Y. Xie, I. Trojan, S. Medvedev, A. O. Lyakhov, M. Valle, and V. Prakapenka, Nature **458**, 182 (2009).
[12] U. Schwarz, K. Takemura, M. Hanfland, and K. Syassen, Phys. Rev. Lett. **81**, 2711 (1998); U. Schwarz, A. Grzechnik, K. Syassen, I. Loa, and M. Hanfland, *ibid.* **83**, 4085 (1999).
[13] R. Boehler and C.-S. Zha, Physica B+C **139–140**, 233 (1986).
[14] G. C. Kennedy and P. N. La Mori, J. Geophys. Res. **67**, 851 (1962); A. Jayaraman, R. C. Newton, and J. M. McDonough, Phys. Rev. **159**, 527 (1967); I. N. Makarenko, V. A. Ivanov, and S. M. Stishov, JETP Lett. **18**, 187 (1973).
[15] C.-S. Zha and R. Boehler, Phys. Rev. B **31**, 3199 (1985).
[16] H. D. Luedemann and G. C. Kennedy, J. Geophys. Res. **73**, 2795 (1968).

[17]I. N. Makarenko, A. N. Nikolaenko, and S. M. Stishov, in *High Pressure Science and Technology, Sixth AIRAPT Conference (1977) 347*, edited by K. D. Timmerhaus and M. C. Barber (Plenum, New York, 1979).
[18]R. Boehler, Phys. Rev. B **27**, 6754 (1983).
[19]D. A. Young and M. Ross, Phys. Rev. B **29**, 682 (1984).
[20]N. Dass, Phys. Rev. B **52**, 3023 (1995).
[21]M. I. Katsnelson, G. V. Sinko, N. A. Smirnov, A. V. Trefilov, and K. Yu. Khromov, Phys. Rev. B **61**, 14420 (2000).
[22]A. Lacam and C. Chateau, J. Appl. Phys. **66**, 366 (1989).
[23]D. R. Schouten and C. A. Swenson, Phys. Rev. B **10**, 2175 (1974).
[24]P. Hammersley, *Reference Manual V3.1 ESRF Internal Report ESRF98HA01T*, ESRF, Grenoble (1998).
[25]C. Larson and R. B. Von Dreele, Los Alamos National Laboratory Report LAUR 86 (2004), p. 748.
[26]M. I. McMahon, S. Rekhi, and R. J. Nelmes, Phys. Rev. Lett. **87**, 055501 (2001).
[27]L. F. Lundegaard, E. Gregoryanz, M. I. McMahon, C. Guillaume, I. Loa, and R. J. Nelmes, Phys. Rev. B **79**, 064105 (2009).
[28]C. Sanloup, E. Gregoryanz, O. Degtyareva, and M. Hanfland, Phys. Rev. Lett. **100**, 075701 (2008), and reference therein.
[29]E. R. Hernandez and J. Iniguez, Phys. Rev. Lett. **98**, 055501 (2007).
[30]M. Marqués, M. Santoro, C. L. Guillaume, F. Gorelli, J. Contreras-García, R. Howie, A. F. Goncharov, and E. Gregoryanz, Phys. Rev. B **83**, 184106 (2011).
[31]V. V. Kechin, J. Phys. Condens. Matter **7**, 531 (1995); Phys. Rev. B **65**, 052102 (2001).
[32]M. Winzenick and W. B. Holzapfel, Phys. Rev. B **55**, 101 (1997).
[33]D. Errandonea, R. Boehler, and M. Ross, Phys. Rev. B **65**, 012108 (2001).
[34]A. Lazicki, Y. Fei, and R. Hemley, Solid State Commun. **150**, 625 (2010).
[35]J.-Y. Raty, E. Schwegler, and S. A. Bonev, Nature **449**, 448 (2007).
[36]S. A. Bonev, E. Schwegler, T. Ogitsu, and G. Galli, Nature **431**, 669 (2004).
[37]V. F. Degtyareva, High Press. Res. **23,** 253 (2003), and references therein.
[38]M. Martinez-Canales and A. Bergara, J. Phys. Chem. Solids **69**, 2151 (2008); L. Koči, R. Ahuja, L. Vitos, and U. Pinsook, Phys. Rev. B **77**, 132101 (2008); S. V. Lepeshkin, M. V. Magnitskaya, and E. G. Maksimov, JETP Lett. **89**, 688 (2009).
[39]V. G. Vaks, M. I. Katsnelson, A. I. Likhtenstein, G. V. Peschanskikh, and A. V. Trefilov, J. Phys. Condens. Matter **3**, 1409 (1991).
[40]J. Wittig, Phys. Rev. Lett. **24**, 812 (1970); in *Superconductivity in d- and f-Band Metals*, edited by W. Buckel and W. Weber (Kernforschungszentrum, Karlsruhe, 1982), p. 321.
[41]L. Shi and D. A. Papaconstantopoulos, Phys. Rev. B **73**, 184516 (2006).
[42]A. Sanna, C. Franchini, A. Floris, G. Profeta, N. N. Lathiotakis, M. Lüders, M. A. L. Marques, E. K. U. Gross, A. Continenza, and S. Massidda, Phys. Rev. B **73**, 144512 (2006).
[43]G. Profeta, C. Franchini, N. N. Lathiotakis, A. Floris, A. Sanna, M. A. L. Marques, M. Lüders, S. Massidda, E. K. U. Gross, and A. Continenza, Phys. Rev. Lett. **96**, 047003 (2006).

Melting of potassium to 22 GPa

E E McBride, O Narygina, G W Stinton and M I McMahon
SUPA, School of Physics and Astronomy, and Centre for Science at Extreme Conditions, The University of Edinburgh, Edinburgh EH9 3JZ, UK

E-mail: e.mcbride@ed.ac.uk

Using *in-situ* x-ray diffraction, the melting curve of potassium was determined to 22 GPa and was found to be remarkably similar to that of sodium, and strikingly different to that reported previously. The existence of a maximum in the *bcc* phase was determined at 5.8(5) GPa and 530(10) K; the melting temperature was then observed to decrease over several GPa, flattening out at the *bcc*-*fcc*-liquid triple point at 13.6(3) GPa and 466(10) K, before further decreasing from 15.6(3) GPa to a minimum at 19(1) GPa and 390(10) K. It then regained a positive slope and increased rapidly at a rate of 65(5) K/GPa In the *tI*19 phase it was observed that the guest chains "melted" before the host structure at 20.3(3) GPa and 420(10) K, but were solid at 22.5(3) GPa and 350(10) K.

1. Introduction

The alkali metals at ambient conditions are well described by the nearly-free electron (NFE) model but show a significant departure from this behaviour with increasing pressure. Anomalous melting, where the gradient of the melting curve becomes negative over large pressure regions, has been observed in rubidium (Rb) and caesium (Cs) [1], sodium (Na) [2] and lithium (Li) [3]. To-date, potassium (K) appears to be an exception to this trend, with no observed melting maximum, at least not to 14.5 GPa [4].

Further evidence of a departure from the NFE model is seen in the emergence of structural complexity with pressure. At atmospheric pressure, the alkali elements are all body-centred cubic (*bcc*), and with increasing pressure they all transform to the closer-packed face-centred cubic (*fcc*) structure. Further application of pressure, however, sees them depart from this "simple" behaviour, with the emergence of low-symmetry open-packed structures [5-11]. The high-pressure phases of K have much in common with its group-I neighbours, with the incommensurate host-guest structure *tI*19.2 (hereafter referred to as *tI*19) being observed in Na, K and Rb [6-8], and the *oP*8 and *hP*4 forms observed in both Na and K [6, 9-11].

Given the similar structural transitions of K and the other alkali metals, and given that anomalous melting has been observed in all others, it is remarkable that K does not follow this trend of a melting maximum. We have therefore reinvestigated its melting temperature using diamond anvil cell (DAC) techniques and *in-situ* x-ray diffraction.

2. Experiment

All experiments were conducted using high-purity (99.95+%) samples of K (Aldrich Chemical Company) which were loaded under argon in a dry, oxygen-free atmosphere (< 1 ppm O_2, < 1 ppm H_2O), without a pressure transmitting medium to prevent contamination. Samples were loaded into

membrane DACs with tungsten or composite rhenium-iridium gaskets. $SrB_4O_7:Sm^{2+}$ was used as a pressure calibrant.

The sample temperature was controlled using external resistive heaters and measured using a thermocouple on the back of one of the diamonds. *In-situ* x-ray diffraction measurements were performed at beamlines ID09a and I15 at the European Synchrotron Radiation Facility and Diamond Light Source, respectively, using MAR 555 and MAR 345 area detectors. For each x-ray exposure, the samples were rocked ±7° to ensure good powder diffraction images, and to ensure that very few crystalline Bragg reflections were missed if the sample had annealed into a single crystal.

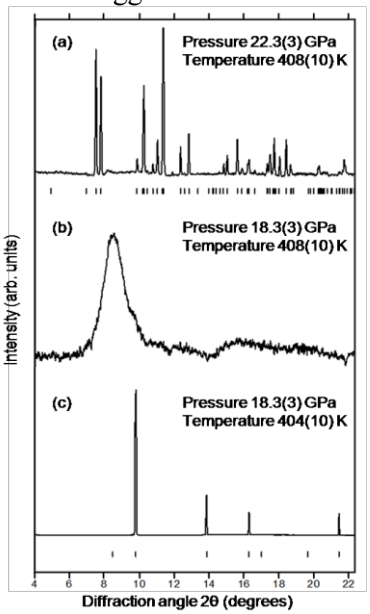

Figure 1. Representative integrated profiles from the crystalline (a) *tI*19 and (c) *fcc* phases, and the (b) liquid phase. The background in the liquid profile has been subtracted, using the method of Sanloup *et al*. [12]. Tick marks below profiles (a) and (c) show the calculated peak positions for the *tI*19 and *fcc* phases, respectively. The lowest angle (111) peak from the *fcc* phase is absent, as the sample was a single crystal and this reflection was not observed during the ±7° oscillation during the x-ray exposure.

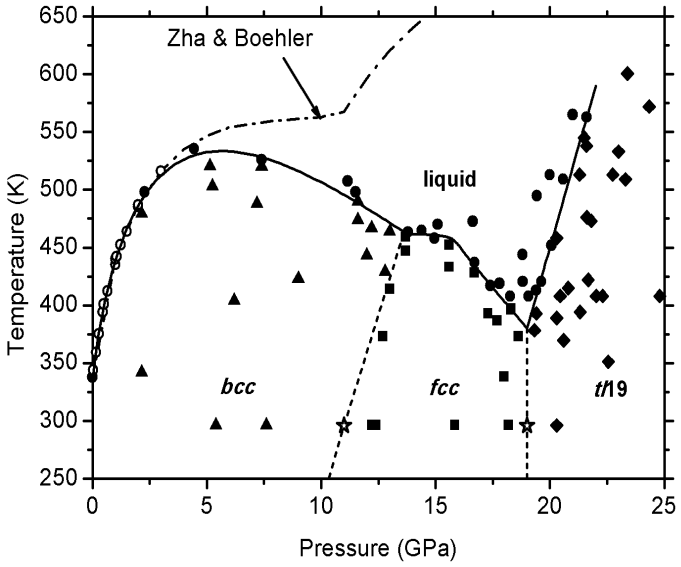

Figure 2: The melting curve of K to 22 GPa. Unfilled circles are data to 3 GPa from refs. [4] and [13], and the solid black line below 13.6 GPa is a fit to the Kechin equation [14] using this data combined with our own. The continuation of the solid line above 13.6 GPa is a guide to the eye. Stars indicate room temperature phase transition pressures [7], and the dashed lines are proposed phase boundaries based on this study. The dot-dashed line is the previously determined melting temperature [4].

3. Results

Representative integrated x-ray diffraction profiles in figure 1 show evidence of melting. It is clear that there is a sharp transition from the *fcc* structure at 18.3(3) GPa and 404(10) K to the liquid phase at 18.3(3) GPa and 408(10) K. By maintaining the temperature at 408(10) K and increasing pressure by 4 GPa potassium then recrystallises in the *tI*19 phase. At high temperatures, K anneals easily into single crystals. As a result, integrated profiles have missing reflections, and inaccurate peak intensities. Integrated profiles were thus analysed using Le Bail rather than Rietveld methods.

The melting curve of K, as determined by our measurements, is shown in figure 2, along with the previously-determined melting curve of Zha & Boehler [4]. Our results indicate the clear presence of a melting maximum in the *bcc* phase. Melting of the *bcc* phase was observed at ambient pressure,

2.2(3) GPa, 4.5(3) GPa, 7.4(3) GPa, and 11.5(3) GPa at 338(10) K, 498(10) K, 536(10) K, 526(10) K and 498(10) K, respectively. There is clearly a maximum in the melting temperature between 4.5(3) GPa and 7.4(3) GPa.

Up to 3 GPa, our melting results are in good agreement with previous studies (see refs. [4] and [13]); these results are shown by the unfilled circles in figure 2. Combining these previous results with our own, and using our *bcc*-*fcc*-liquid triple point at 13.6(3) GPa and 466(10) K, we performed a fit using the Kechin equation [14] to determine the location of the melting maximum in the *bcc* phase. This fit locates the maximum at 5.8(5) GPa and 530(10) K.

Above the triple point the melting temperature remains (almost) flat for several GPa. It should be noted that the presence of a second maximum, like that observed in Cs [1], cannot be ruled out, but it was too slight to be observed in this study. This region of nearly constant melting temperature ends as the melting curve decreases from 15.6(3) GPa and 462(10) K to a minimum at 19.0(3) GPa and 390(10) K. The location of this minimum coincides with the transformation from *fcc*-K to *tI*19-K; the phase boundary can be seen to be almost vertical. In the *tI*19-K phase the melting temperature rises very rapidly, increasing at a rate of 65(5) K/GPa.

Upon heating the *tI*19 phase, it was observed that the guest chains "melted" before the sample, consistent with a weak host-guest interaction. This is illustrated in figure 3, which shows 2D diffraction images collected from the *tI*19 phase both below and above the chain-melting transition. At 22.5(3) GPa and 350(10) K (figure 3(a)) Bragg reflections from the guest phase are clearly visible, although elongated perpendicular to the chain direction, indicating only short-range inter-chain correlations. The (101) guest reflection is circled. Figure 3(b) shows the 2D image from the same sample at 20.3(3) GPa and 420(10) K. The Bragg reflections from the guest chains have disappeared, as a result of the loss of long range order, and only some diffuse scattering remains. The calculated position of the (101) reflection is circled. The change in the guest reflections is quantified in figure 4, which shows 1D integrations of the 2D images in figure 3, performed over the same small regions encompassing the (101) reflection. At 22.5(3) GPa and 350(10) K there is a distinct Bragg peak and this has clearly disappeared at 20.3(3) GPa and 420(10) K. Initial observations at higher pressures indicate the chain melting temperature is almost independent of pressure.

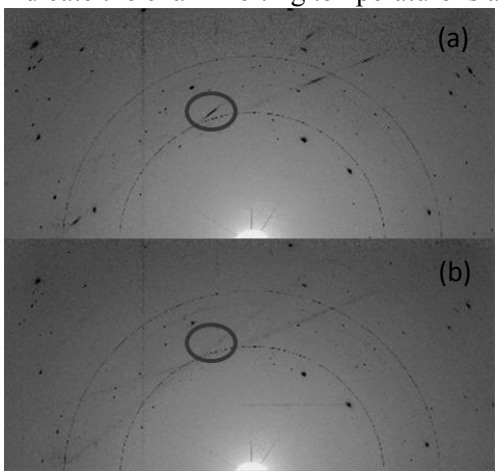

Figure 3: 2D diffraction images of the *tI*19 phase collected at (a) 22.5 GPa and 350 K, and at (b) 20.3 GPa and 420 K. The position of the (101) guest reflection is circled in both images.

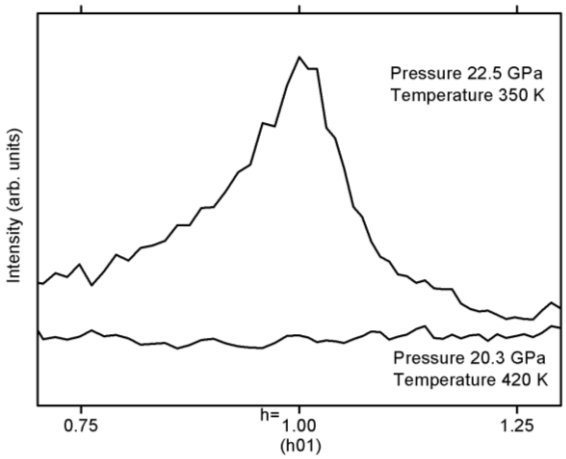

Figure 4: 1D profiles obtained by integrating the 2D diffraction images over the same small region encompassing the (101) reflection. There is a distinct Bragg peak at 22.5(3) GPa and 350(10) K which is absent at 20.3(3) GPa and 420(10) K.

4. Discussion

The melting behaviour of K is remarkably similar to that of Na, where there is also a melting maximum in the *bcc* phase followed by a decrease in the melting temperature to a dramatic minimum

of 300 K at 118 GPa. After this, the gradient of the melting curve regains a positive slope and increases rapidly [2], although the increase does not appear to be as rapid as in K. From the Clausius-Clapeyron relation, a change in the melting curve gradient from positive to negative is an indication of densification of the liquid phase relative to the underlying solid. A change in the sign of the gradient might thus imply a structural change in either the liquid or the solid phase. In Na, as in K, the maximum in the melting temperature occurs in the *bcc* phase, several GPa (approximately 6 GPa in K and 30 GPa in Na) before the transition in the solid from the *bcc* to the *fcc* phase.

To further understand this anomalous melting behaviour, Raty *et al*. performed *ab initio* calculations on the evolution of the melting temperature of Na [15]. They showed that the anomalous melting could be explained by a sequence of structural and electronic transitions in the liquid phase. They found that at the maximum in the melting temperature, *bcc*-like to *fcc*-like structural transitions were occurring in the liquid. Furthermore, their study attributed the negative slope of the melting temperature above the crystalline *bcc* to *fcc* transition to electronic and structural transitions in the liquid. Not only did they report a drop in calculated co-ordination number above 60 GPa, to that of the solid above 103 GPa, but they also detailed a three-fold drop in conductivity, indicating electronic changes occurring in the liquid.

Due to the remarkable similarity of the melting curves of Na and K, we suggest that similar mechanisms to those detailed above for Na could explain the melting behaviour of K. The advantage of K is that the anomalous melting behaviour occurs at much lower, and hence experimentally accessible, pressures than Na, and so additional studies are planned to investigate the co-ordination and electronic properties of liquid-K.

Acknowledgements
We thank S Evans and M Hanfland of ID09a at the European Synchrotron Radiation Facility, and A K Kleppe, H Wilhelm, and A P Jephcoat of I15 at the Diamond Light Source, for provision of synchrotron time and support. We also thank E Gregoryanz for discussions. This work was supported by a research grant from the UK Engineering and Physical Sciences Research Council.

References

[1] Boehler R and Zha C-S 1986 *Physica B+C* **139-140** 233
[2] Gregoryanz E, Degtyareva O, Somayazulu M, Hemley R J and Mao H-K 2005 *Phys*. *Rev*. *Lett*. **94** 185502
[3] Guillaume C L, Gregoryanz E, Degtyareva O, McMahon M I, Hanfland M, Evans S, Guthrie M, Sinogeikin S V and Mao H-K 2011 *Nature Physics* **7** 211
[4] Zha C-S and Boehler R 1985 *Phys*. *Rev*. *B* **31** 3199
[5] Marqués M, McMahon M I, Gregoryanz E, Hanfland M, Guillaume C L, Pickard C J, Ackland G J and Nelmes R J 2011 *Phys*. *Rev*. *Lett*. **106** 095502
[6] Gregoryanz E, Lundegaard L F, McMahon M I, Guillaume C L, Nelmes R J and Mezouar M 2008 *Science* **320** 1054
[7] McMahon M I, Nelmes R J, Schwarz U and Syassen K 2006 *Phys*. *Rev*. *B* **74** 140102
[8] McMahon M I and Nelmes R J 2001 *Phys*. *Rev*. *Lett*. **87** 055501
[9] Lundegaard L F, Marqués M, Stinton G, Nelmes R J and McMahon M I 2009 *Phys*. *Rev*. *B* **80** 020101
[10] Marqués M, Ackland G J, Lundegaard L F, Stinton G, Nelmes R J and McMahon M I 2009 *Phys*. *Rev*. *Lett*. **103** 115501
[11] Ma Y, Erements M, Oganov A Rm Xie Y, Trojan I, Medvedev S, Lyakhov A O, Valle M and Prakapenka V 2009 *Nature* **458** 07786
[12] Sanloup C, Gregoryanz E, Degtyareva O and Hanfland M 2008 *Phys*. *Rev*. *Lett*. **100** 075701
[13] Luedemann H D and Kennedy G C 1968 *Journal of Geophysical Research* **73** 2795
[14] Kechin V V 2001 *Phys*. *Rev*. *B* **65** 052102
[15] Raty J-Y, Schwegler E and Bonev S A 2007 *Nature* **449** 448